FACULDADE DE ENGENHARIA DA UNIVERSIDADE DO PORTO

# Load-Bearing Plates for Orthopaedic Implants: Design, Simulation and Topology Optimization

**Luís Miguel Bouça Rego**

FINAL VERSION




**Master's in Bioengineering**

Supervisor: Prof. Jorge Lino Alves

Supervisor: Prof. Marco Parente

Supervisor: Engº Pedro Miguel Lopes

September 5, 2026

© Luís Miguel Bouça Rego, 2026

# Resumo

Os implantes metálicos densos convencionais sofrem de uma discrepância de rigidez acentuada face ao osso envolvente, uma disparidade que provoca stress shielding e leva à reabsorção progressiva do tecido ósseo ao longo do tempo. Os metais biodegradáveis, como o ferro, enfrentam um obstáculo diferente, uma vez que a sua forma maciça degrada-se demasiado lentamente para funcionar como um implante verdadeiramente temporário. A introdução de uma arquitetura porosa controlada foi proposta como forma de resolver ambos os problemas em simultâneo, reduzindo a rigidez aparente para níveis fisiológicos e acelerando ao mesmo tempo a corrosão através de uma maior exposição do material aos fluidos envolventes.

Duas geometrias celulares foram investigadas para este efeito, cada uma escolhida pelas vantagens distintas que o seu design oferece. A natureza estocástica da geometria *Voronoi* representa a morfologia irregular do osso trabecular natural, enquanto a geometria *Gyroid* apresenta uma topologia suave e totalmente isenta de junções discretas. Foi desenvolvido um pipeline computacional open source para gerar ambas as arquiteturas ao longo de um vasto espaço morfológico, sendo que, posteriormente, um estudo paramétrico construído sobre esse pipeline relacionou os parâmetros de geração com a densidade relativa e a área de superfície. Com base nestas relações, um subconjunto representativo de espécimes, abrangendo uma ampla gama de densidades relativas, foi fabricado em ferro puro por L-PBF, fornecendo a base física para a caracterização de biodegradação e mecânica que se seguiu.

Os ensaios de biodegradação, combinando medições de perda de massa, quantificação da libertação de iões e análise morfológica de superfície, confirmaram que a porosidade consegue de facto acelerar a corrosão do ferro. Contudo, a extensão dessa aceleração revelou depender sobretudo da acessibilidade dos fluidos e do confinamento dos canais e não apenas da área de superfície nominal. As simulações por elementos finitos, por sua vez, mostraram que a densidade relativa é o principal preditor do módulo de elasticidade aparente, com a lei de Gibson–Ashby a verificar-se com boa concordância em ambas as arquiteturas, assim como um regime dominado por flexão confirmado em cada caso. Além disso, a *Gyroid* apresentou sistematicamente maior rigidez do que a *Voronoi* para densidades equivalentes e várias configurações atingiram módulos aparentes dentro dos intervalos do osso trabecular e cortical.

Em conjunto, estes resultados sugerem que as estruturas celulares arquitetadas em ferro representam um caminho promissor e genuinamente verificável rumo a implantes metálicos biodegradáveis, sustentando a hipótese inicial de que a porosidade pode conciliar compatibilidade mecânica com degradação acelerada. Ainda assim, é necessária mais otimização e validação a longo prazo antes de esta abordagem poder ser considerada pronta para aplicação clínica.

**Palavras-chave**: Implantes Metálicos Biodegradáveis • Stress Shielding • Estruturas Celulares Porosas em Ferro • *Voronoi* e *Gyroid* (TPMS) • Fabrico Aditivo (L-PBF) • Biodegradação e Caracterização Mecânica

# Abstract

Conventional dense metallic implants suffer from a pronounced stiffness mismatch relative to the surrounding bone, a disparity that drives stress shielding and leads to the progressive resorption of bone tissue over time. Biodegradable metals such as iron face a different obstacle, since their bulk form degrades far too slowly to function as a genuinely temporary implant. Introducing a controlled porous architecture was proposed as a way of addressing both problems simultaneously, reducing the apparent stiffness towards physiological levels while accelerating corrosion through greater exposure of the material to the surrounding fluids.

Two cellular geometries were investigated for this purpose, each chosen for the distinct advantages its design offers. The stochastic nature of the *Voronoi* geometry represents the irregular morphology of natural trabecular bone, whereas the *Gyroid* geometry presents a smooth topology entirely free of discrete junctions. An open-source computational pipeline was developed to generate both architectures across a broad morphological space, and a parametric study built on this pipeline subsequently related the generation parameters to relative density and surface area. Based on these relationships, a representative subset of specimens, spanning a wide range of relative densities, was fabricated in pure iron by L-PBF, providing the physical basis for the biodegradation and mechanical characterisation that followed.

The biodegradation assays, combining mass loss measurements, ion release quantification and surface morphological analysis, confirmed that porosity can indeed accelerate the corrosion of iron. However, the extent of this acceleration proved to depend chiefly on fluid accessibility and channel confinement rather than on nominal surface area alone. The finite element simulations, in turn, showed that relative density is the primary predictor of the apparent elastic modulus, with the Gibson–Ashby law verified with good agreement in both architectures, as well as a bending-dominated regime confirmed in each case. Moreover, the *Gyroid* consistently exhibited higher stiffness than *Voronoi* at equivalent densities, and several configurations reached apparent moduli within the trabecular and cortical bone ranges.

These results suggest that architected cellular iron structures represent a promising and genuinely verifiable pathway towards biodegradable metallic implants, supporting the initial hypothesis that porosity can reconcile mechanical compatibility with accelerated degradation. Further optimisation and long-term validation nonetheless remain necessary before this approach can be considered ready for clinical application.

**Keywords**: Biodegradable Metallic Implants • Stress Shielding • Porous Iron Cellular Structures • *Voronoi* and *Gyroid* (TPMS) • Additive Manufacturing (L-PBF) • Biodegradation and Mechanical Characterisation

# Scientific Dissemination

Part of the work developed in this dissertation was presented at the following scientific conference:

- *Computational analysis of compressive behaviour of Gyroid and Voronoi cellular structures in pure iron for biodegradable bone implant applications*. **6th International Conference on Materials Design and Applications (MDA 2026)**, Porto, Portugal, July 2026.

# The United Nations Sustainable Development Goals

The United Nations Sustainable Development Goals (SDGs) provide a global framework for achieving a better and more sustainable future for all. It includes 17 goals (https://sdgs.un.org/goals) to address the world's most pressing challenges, including poverty, inequality, climate change, environmental degradation, peace, and justice.

This dissertation is highly aligned with the UN agenda, as it seeks to develop advanced biomedical solutions that directly impact human health while driving technological innovation in advanced manufacturing. The specific Sustainable Development Goals addressed by this work are:

**SDG 3** Good Health and Well-Being.
**SDG 9** Industry, Innovation and Infrastructure.

| SDG | Target | Contribution | Performance Indicators and Metrics |
|---|---|---|---|
| 3 | 3.4 | The development of biodegradable porous orthopaedic implants directly improves patients' quality of life. By matching the stiffness of human bone to prevent stress shielding and bone resorption, and by degrading safely over time, these implants eliminate the clinical need for secondary removal surgeries, significantly reducing patient trauma and enhancing overall well-being. | Reduction in the requirement for secondary removal surgeries; improvement in bone regeneration and patient recovery rates. |
| 9 | 9.5 | This research fosters innovation through the application of cutting-edge additive manufacturing (L-PBF). The development of an open-source computational design pipeline, combined with topology optimisation and finite element simulation, upgrades the technological capabilities of the biomedical manufacturing industry and promotes advanced engineering research. | Development of adaptable open-source computational design tools; successful application of advanced additive manufacturing in biomedical engineering. |

# Acknowledgements

A chegada do fim de uma vida académica pode trazer sentimentos amargos ao fazer-nos aperceber que rotinas simples que existem há cerca de 17 anos irão deixar de existir, parecendo aproximar-se um temível desconhecido. No entanto, é acompanhada de um grande sentido de realização por ter sido possível atingir o final deste caminho com a ambição de possíveis novas experiências que estarão por vir. Desta forma, apenas poderei agradecer a uma pequena porção de pessoas que tornaram tudo isto uma realidade.

Em primeiro lugar, agradecer ao Profº Jorge Lino Alves por dar a oportunidade de poder aplicar, na prática e num tema que me despertava muita curiosidade e agrado, todo o conhecimento que o percurso académico foi fornecendo, assim como garantir que tinha as melhores condições possíveis para desenvolver o melhor trabalho. No mesmo sentido, ao Profº Marco Parente por aconselhar e disponibilizar as ferramentas para que a parte computacional deste trabalho se tornasse possível de executar.

Muito obrigado Pedro por todo o acompanhamento praticamente diário e por toda a motivação dada para esticar os limites do que era possível desenvolver durante os 6 meses desta dissertação, de forma a que pudesse extrair o máximo desta experência, quer em termos de dinâmica quer em conhecimento.

À Profª Maria Pia Ferraz por toda a prontidão e apoio numa parte adicional deste trabalho, sem o qual era impossível de realizar. Apesar de nada lhe ser exigido e com os vários constrangimentos que foram surgindo, esteve sempre disponível para ajudar. Juntamente com todos os momentos em aula, ficará sempre muito marcado na minha memória destes tempos.

Aos meus pais, ao meu irmão e toda a minha família, uma vez que são estes que estiveram integralmente presentes durante todo o percurso, vivenciando todas as fases boas e menos boas a ele associado, fornecendo sempre o maior apoio e suporte, torcendo sempre pelo melhor.

Em particular neste anos de faculdade, à Ana por ter sido o maior apoio em todos os momentos, mesmo quando parecia difícil.

Por fim, agradecer a todos os meus amigos e amigas que forneceram toda a estabilidade social para que esta longa jornada fosse mais leve, divertida e, acima de tudo, memorável.

A todos, um enorme muito obrigado.

Luís Rego

# Declaration of Honour

I declare that this dissertation is my own work and has not previously been submitted or assessed at this or any other institution. References to other authors (statements, ideas, thoughts), as well as the use of published works, strictly comply with the rules of attribution and are duly identified in the text and in the bibliographic references, in accordance with the applicable referencing standards. I am aware that the practice of plagiarism or self-plagiarism constitutes an academic offence, as established in the U.Porto Code of Ethics.

I also declare that I have used Artificial Intelligence tools to complete part(s) of this dissertation, and that this use and its results are duly noted and have been carefully checked, having been used for writing assistance in detecting errors, inaccuracies, unfounded attributions or other forms of bias in content and arguments, as well as in coding tasks.

Luís Rego



*"Life is a playground — or nothing"*

*Mr. Nobody*

# Contents

**Scientific Dissemination** v

**1 Introduction** 1

1.1 Context and Motivation . . . 3

1.2 Objectives . . . 4

1.3 Dissertation Structure and Organization . . . 4

**2 State of the Art** 7

2.1 Bone Tissue: Composition, Structure, and Biomechanics . . . 9

2.1.1 Physicochemical Composition and Hierarchical Structure . . . 9

2.1.2 Macroscopic and Microstructural Morphology . . . 9

2.1.3 Characterization of Biomechanical Behavior and Properties . . . 11

2.1.4 Fracture Behavior and Bone Repair Mechanisms . . . 12

2.2 Metallic Implants and Architectural Strategies for Bone Repair . . . 13

2.2.1 Clinical Failure of Bone Repair . . . 13

2.2.2 Conventional Metallic Implants and the Challenge of Stress Shielding . . . 14

2.2.3 Porous Metallic Implants: Architectural Strategies for Bone Repair . . . 15

2.3 Architected Cellular Materials . . . 17

2.3.1 Periodic strut-based lattice structures . . . 18

2.3.2 Triply Periodic Minimal Surface Structures . . . 21

2.3.3 Voronoi Lattice Structures . . . 23

2.4 Graded Lattice Structures . . . 26

2.5 Additive Manufacturing of Metallic Scaffolds . . . 27

2.5.1 Manufacturing Processes of Complex Architectures . . . 27
2.5.2 Support Structures in L-PBF . . . 29
2.5.3 Biodegradable Metallic Materials . . . 29

**3 Design and Additive Manufacturing 31**
3.1 Generation of the Voronoi Structures . . . 34
3.2 Generation of the Gyroid Structures . . . 46
3.3 Parametric Study . . . 55
3.3.1 Voronoi Lattice . . . 55
3.3.2 Gyroid (TPMS) . . . 63
3.4 Additive Manufacturing . . . 70
3.4.1 Manufacturing Constraints and Design Boundaries . . . 70
3.4.2 Selection of Specimens for Manufacture . . . 73
3.4.3 Fabrication . . . 76

**4 Biodegradation Testing 79**
4.1 Methodology . . . 82
4.1.1 Specimen preparation . . . 82
4.1.2 Immersion conditions and solution volume . . . 83
4.1.3 Specimen retrieval and mass measurement . . . 84
4.1.4 Corrosion rate calculation . . . 85
4.1.5 Iron Ion Release . . . 85
4.1.6 Scanning Electron Microscopy and Energy-Dispersive X-ray Spectroscopy 86
4.2 Results . . . 86
4.2.1 Mass loss and corrosion rate analysis . . . 86
4.2.2 Iron ion release . . . 99
4.2.3 Surface morphology and corrosion product characterisation . . . 101

**5 Numerical Finite Element Simulation 107**
5.1 Surface mesh pre-processing . . . 109
5.1.1 Open-source processing attempt . . . 109

5.1.2 Global repair and remeshing in Geomagic . . . . . 110
5.2 Simulation setup . . . . . 112
5.2.1 Material Definition . . . . . 113
5.2.2 Boundary conditions . . . . . 117
5.2.3 Analysis procedure and output requests . . . . . 120
5.2.4 Mesh Convergence Study . . . . . 122
5.2.5 Mesh Quality Assessment . . . . . 128
5.3 Results and Discussion . . . . . 129
5.3.1 Apparent Stress–Strain Response . . . . . 129
5.3.2 Mechanical Properties Evaluation . . . . . 131
5.3.3 Comparison with Bone Mechanical Properties . . . . . 135

**6 Conclusions and Future Work** **139**
6.1 Conclusions . . . . . 141
6.2 Future Work . . . . . 142

**References** **145**

**A Supplementary Parametric Data** **157**
A.1 Additional Voronoi Realisations . . . . . 159

# List of Figures


2.1 Hierarchical organization of bone tissue from macrostructure to nanostructure. Adapted from [27]. . . . . 10

2.2 Anatomical distribution of cortical and trabecular bone in a long bone. Adapted from [32]. . . . . 11

2.3 Schematic representation of stages of bone fracture healing. Adapted from [34]. . 12

2.4 Representative unit cell geometries of strut-based lattice. Adapted from [57]). . . 19

2.5 Geometry of the five unit cell types investigated Adapted from Nogueira et al. [67]. 20

2.6 Von Mises effective stress distribution (MPa) in a Cubic unit cell at 5% relative density, illustrating pronounced stress concentrations at nodal junctions under compressive loading. Adapted from [68]. . . . . 21

2.7 Representative Triply Periodic Minimal Surface (TPMS) unit cell geometries used in scaffold design: Gyroid, Split P, Diamond, Primitive, Neovius, and Lidinoid. Adapted from [81]. . . . . 23

2.8 Illustration of the Voronoi scaffold generation process: (left) random seed point distribution within a cylindrical domain and (right) the resulting three-dimensional open-cell Voronoi lattice structure. Adapted from [87]. . . . . 25

2.9 Functionally graded lattice structure for biodegradable bone implants based on strut-based lattice structures. Adapted from [97]. . . . . 26

2.10 Schematic representation of additive manufacturing techniques explored for metallic scaffold fabrication: (a) Selective Laser Sintering (SLS) [100], (b) Electron Beam Melting (EBM) [101], and (c) Selective Laser Melting (SLM)/Laser Powder Bed Fusion (L-PBF) [102]. Adapted from the respective sources. . . . . 28

3.1 Flowchart of the Voronoi generation pipeline, from the seeding of the domain through to the morphological characterisation of the final mesh. . . . . 35

3.2 Cubic bounding box enclosing the cylindrical specimen used in this work. The box edge is the largest target dimension, here the 15 mm height, increased by a 5 mm margin, which gives a 20 mm cube. The resulting clearance is 2.5 mm at each end of the cylinder and 5 mm around its radius, the asymmetry arising from sizing the cube to the largest dimension alone. . . . . 37

3.3 Top view of the seeding domain with seed points placed at random. The points gather in some regions and leave others empty, the unevenness that the controlled-irregularity scheme is introduced to avoid. . . . . 37

3.4 Derivation of the grid spacing $d$ from the box edge $L$ and the point count $n$ (here $n = 5$, for illustration). The regular grid populates each edge of the cubic bounding box with $n$ points, each centred on its own cell of width $d = L/n$; the first and last points are consequently set back by $d/2$ from the corresponding faces of the box, rather than coinciding with them. . . . . 39

3.5 Simple Cubic (SC) (a) and Body-Centred Tetragonal (BCT) (b) seed grids, shown within the box enclosing the cylindrical domain of this work (top) with the corresponding front views beneath, on which the grid spacing $d$ is marked. In the simple cubic grid each layer sits directly above the last, forming the continuous aligned columns that act as cleavage planes; in the body-centred grid alternate layers are offset by half a cell, staggering the columns and breaking up those planes. 40

3.6 Illustration of the seed displacement scheme. Perturbation cubes of edge $2r$ around the front-top row of seeds in the regular grid ($n = 5$, spacing $d$), the remaining seeds shaded by depth for context; the value of $i$ shown here sits close to the upper bound $i = 0.5$, beyond which neighbouring cubes would begin to overlap (left). The resulting seed distribution once this displacement is applied throughout the volume, obtaining final seeds distribution (centre). Top view of the same distribution (right). . . . . 42

3.7 Voronoi tessellation of the perturbed seeds, shown here for a reduced seed count for clarity. (a) The tessellation as formed within the enlarged bounding box, before any trimming. (b) The same tessellation after intersection with the reduced cylinder ($R_c = R - D/2$, $H_c = H - D$); no thickness has yet been assigned to the resulting skeleton. . . . . 43

3.8 Final thickened specimen obtained from the pipeline described above, generated with $n = 8$, $i = 0.4$ and $D = 0.4$ mm. . . . . 44

3.9 Flowchart of the Gyroid generation pipeline, from the definition of the cylindrical domain through to the morphological and hydraulic characterisation of the final mesh. . . . . 49

3.10 Discretised rectangular bounding domain of dimensions $2R \times 2R \times H$, showing the uniform voxel grid at resolution $\Delta x = 0.02$ mm used to evaluate the Gyroid implicit function. . . . . 50

3.11 Comparison of two Gyroid unit cell sizes. Top row: three-dimensional views of the sheet-based Gyroid for $l = 5.0$ mm, $C = 0.2$ (left) and $l = 3.5$ mm, $C = 0.6$ (right). Bottom row: corresponding $xy$ cross-sections at $z = 0$, showing the reduction in spatial period as $l$ decreases, together with the corresponding increase in wall thickness $t$ resulting from the higher value of $C$. . . . . 51

3.12 Cylindrical masking of the sheet-based Gyroid array. Left: three-dimensional view of the masked structure within its original rectangular bounding domain. Right: corresponding $xy$ cross-section, with the circular boundary of radius $R = 5.0$ mm outlined for reference. . . . . 52

3.13 Final triangulated mesh of the sheet-based Gyroid lattice after marching cubes extraction and post-processing. . . . . 53

3.14 Relative density of the Voronoi lattice as a function of the strut-to-spacing ratio $D/d$, for all five values of $D$ explored. The dashed line is the quadratic fit of Equation (3.18). . . . . 59

3.15 Specific surface area of the Voronoi lattice. Left: as a function of grid spacing $d$ for the three values of $D$ explored, with the fit of Equation (3.19) shown dashed. Right: the same fit evaluated over the full $(d, D)$ plane, with the 32 valid observations overlaid; dotted lines mark the three sections shown on the left. . . . . 61

3.16 Relative density of the sheet-based Gyroid as a function of the level-set constant $C$, for all eight unit cell sizes explored. The dashed line is the quadratic fit of Equation (3.20). . . . . 65

3.17 Specific surface area of the sheet-based Gyroid as a function of unit cell size $l$, with each curve corresponding to a fixed value of $C$. . . . . 67

3.18 Layer-by-layer analysis in the L-PBF machine preparation software of a Voronoi specimen with nominal strut diameter $D = 0.2\,\text{mm}$ ($n = 12$). Blue indicates the nominal contour defined by the Standard Triangle Language (STL) geometry, while pink indicates the actual laser scan path the machine would trace. Several struts show no corresponding scan path at all, confirming that their thickness falls below what the current process parameters can reproduce, a pattern consistent across the layers shown (heights 3.95 and 4.05 mm). . . . . 71

3.19 Computational renders of the sheet-based Gyroid for increasing values of $C$, at a fixed unit cell size. Pore openings on the top face progressively close as $C$ increases, from fully resolved at $C = 0.8$ to fully suppressed at $C = 1.0$. On this basis, $C = 0.8$ was adopted as the upper bound for fabrication. . . . . 72

3.20 Build-preparation software view of three Voronoi specimens with the 0.5 mm base pedestal incorporated into the STL geometry, shown together with the cylindrical support structures generated to anchor each part to the build platform. The same pedestal design was applied to the Gyroid specimens. . . . . 73

3.21 Design space of the Voronoi lattice architecture in the $(D, n)$ parametric plane, showing top-surface renderings of all candidate configurations. The nine specimens selected for fabrication (highlighted) span the accessible morphological space across all three strut diameters and a broad range of cell densities, subject to the minimum-feature-size constraint ($D \geq 0.3\,\text{mm}$), estabilished in Section 3.4.1. 74

3.22 Design space of the sheet-based Gyroid architecture in the $(C, l)$ parametric plane, showing top-surface renderings of all candidate configurations. The nine specimens selected for fabrication (highlighted) were chosen to jointly cover the accessible ranges of density and surface area, respecting the upper bound $C \leq 0.8$ established in Section 3.4.1 and the minimum of two unit cells per specimen dimension established in Section 3.3.2. . . . . 75

3.23 Build platforms following extraction from the L-PBF machine, showing both the Gyroid batch (a) and the Voronoi batch (b). . . . . 77

3.24 Correspondence between the designed and as-built geometry for representative Voronoi (n=10 D=0.5 mm) and Gyroid (l=2.5 mm c=0.5) specimens, viewed from the top face. . . . . 78

4.1 Mean pH at each Simulated Body Fluid (SBF) renewal interval for Gyroid, Voronoi and dense reference specimens. Error bars show the full range (min–max) of individual readings. The dashed line marks the initial pH (7.4); the green band marks the ±0.5-unit acceptance range. . . . . 87

4.2 Mass loss (%, mean ± SD) over 30 days of immersion for all nine Gyroid (a) and Voronoi (b) conditions. Colour encodes $\rho_r$ within each architecture. . . . . 89

4.3 The three Gyroid conditions at $C = 0.8$ ($\rho_r \approx 52\%$), isolating the contribution of surface area at constant density. (a) Mass loss evolution over 30 days for the three configurations, with the $l = 1.5$ mm condition ($A = 45.1$ cm$^2$) plotted with a dashed line and triangular markers, denoting the exclusion of one replicate. (b) Day-30 mass loss plotted against surface area $A$ for the same three configurations. Error bars represent ±1 SD. . . . . 91

4.4 CR (mm yr$^{-1}$), mean, as a function of immersion time for all nine Gyroid (a) and Voronoi (b) conditions and the dense reference (dashed line with square markers). The legend orders conditions from lowest to highest relative density, with colour encoding $\rho_r$ (lighter shades correspond to lower density). ($l = 1.5$, $C = 0.8$: $n = 2$, one replicate excluded.) . . . . . 92

4.5 The three Gyroid conditions at $C = 0.8$ ($\rho_r \approx 52\,\%$): (a) Temporal evolution of CR over 30 days. (b) Day-30 CR against nominal surface area $A$; the dashed reference marks the common value of 0.107 mm yr$^{-1}$ reached by $l = 5.0$ and $l = 2.5$. . . . 94

4.6 Day-30 corrosion rate (mm yr$^{-1}$, mean) for all conditions of both architectures and the dense reference, ranked in descending order. The vertical dashed line marks the dense reference value (0.103 mm yr$^{-1}$). $^{\dagger}l = 1.5$, $C = 0.8$: $n = 2$; one replicate excluded. . . . . 95

4.7 As-built digital stereomicroscope images of two Voronoi configurations prior to immersion in SBF. (a) The $n = 10$, $D = 0.3$ mm condition retains a clearly open, well-resolved channel network. (b) Magnified detail of the strut surface in (a), where rounded protrusions along the strut edges (blue boxes), consistent with partially fused powder particles, are directly visible. (c) The narrower nominal pore size of the $n = 18$, $D = 0.5$ mm condition results in near-complete pore closure. . 98

4.8 Comparison of the dense reference and the highest-density Voronoi condition ($n = 18$, $D = 0.7$, $\rho_r = 76.4\,\%$) at Day 30. (a) Mass loss (%): both specimens record virtually identical values (0.44 and 0.41 %). (b) Corrosion rate (mm yr$^{-1}$): despite the equivalent mass loss, the CR differs by nearly a factor of five. . . . . 98

4.9 Soluble iron concentration (mg L$^{-1}$, mean ± measurement uncertainty) measured by Flame Atomic Absorption Spectrometry (FAAS) in the spent SBF collected at each of the six renewal intervals (Days 5, 10, 15, 20, 25 and 30) for the dense reference, the Voronoi specimen ($n = 14$, $D = 0.3$ mm) and the Gyroid specimen ($l = 3.5$ mm, $C = 0.3$). . . . . 101

4.10 Scanning Electron Microscopy (SEM) micrographs (50×) of corrosion product distribution after 30 days of immersion in SBF. (a) HV = 15 kV, WD = 11.7 mm. (b) HV = 15 kV, WD = 14.5 mm. Red boxes indicate representative regions of rounded, semi-spherical protrusions consistent with partially fused powder particles. 102

4.11 SEM micrographs (100×) showing the contrast between exposed metallic iron regions and corrosion product zones after 30 days of immersion in SBF. (a) HV = 15 kV, WD = 12.0 mm. (b) HV = 15 kV, WD = 14.5 mm. . . . . 103

4.12 SEM micrographs (500–1000×) showing surface depressions on exposed metallic regions and the thickness of the corrosion product layer at crack edges after 30 days of immersion in SBF. (a) HV = 15 kV, WD = 11.8 mm. (b) HV = 15 kV, WD = 14.8 mm. . . . . 103

4.13 SEM micrographs with identified Energy-Dispersive X-ray Spectroscopy (EDS) analysis zones and corresponding point spectra acquired at 15 kV following 30 days of immersion in SBF. (a) Voronoi ($n = 10$, $D = 0.3$). (b) Gyroid ($l = 5.0$ mm, $C = 0.2$). . . . . 105

5.1 Overview of the Geomagic processing workflow, from the post-design STL mesh to the final processed output. . . . . 110

5.2 Comparison of surface triangulation before and after isotropic remeshing. . . . . 111

5.3 Manual correction sequence applied to localised boundary anomalies in a Voronoi specimen. . . . . 112

5.4 Bridge-guided reconstruction strategy applied to residual open boundaries in a Gyroid specimen. . . . . 112

5.5 Tensile test results used to characterise the plastic behaviour of pure iron: (a) curves of all three specimens, and (b) mean curve computed from the two retained specimens. . . . . 114

5.6 True stress-strain curve obtained from the mean engineering curve via Equation 5.1, with identification of the main deformation regimes. The dashed vertical line marks the onset of necking, beyond which the conversion is no longer physically valid. . . . . 115

5.7 Plastic flow curve supplied to Abaqus as a function of true plastic strain, overlaid with the full true stress-strain curve. The input data are limited to the region of valid engineering-to-true conversion and monotonically non-decreasing flow stress, beyond which perfect plasticity is assumed by the solver. . . . . 117

5.8 Node sets defined for the application of boundary conditions, shown for a representative Voronoi specimen. . . . . 117

5.9 Boundary conditions applied to each specimen. . . . . 119

5.10 Symmetry reduction applied to the Gyroid specimens: (a) lateral view of the full cylindrical domain, and (b) top view of the one-quarter model with the symmetry boundary conditions used to reproduce the response of the full geometry. . . . . 120

5.11 Comparison between the linear tetrahedral element (C3D4, 4 nodes) and the quadratic tetrahedral element (C3D10, 10 nodes). . . . . 123

5.12 Mesh convergence study for the Voronoi $n$=10, $D$=0.3 mm specimen using C3D10 elements. Left: peak apparent stress as a function of element size; the dashed vertical line at $e = 0.075$ mm marks the refinement level at which the simulation could not be completed due to computational resource constraints. Right: apparent stress-strain curves for the two simulated refinement levels. . . . . 124

5.13 Mesh convergence study for the Voronoi $n$=10, $D$=0.3 mm specimen using C3D4 elements. Left: peak apparent stress as a function of element size, with the difference between each pair of consecutive refinement levels indicated. Right: apparent stress-strain curves for all five refinement levels, with the two finest levels shown as solid lines. . . . . 125

5.14 Cross-validation of the discretisation criterion for the Voronoi $n$=10 specimens with $D = 0.5$ mm (left) and $D = 0.7$ mm (right). In each panel, the dashed line corresponds to five elements per strut diameter and the solid line to six elements per strut diameter. The percentage difference between the two levels is indicated in the lower right corner of each panel. . . . . 126

5.15 Mesh convergence study for the Gyroid $l$=5.0 mm, $C$=0.2 specimen using C3D4 elements. Left: peak apparent stress as a function of element size, with the difference between each pair of consecutive refinement levels indicated. Right: apparent stress-strain curves for all three refinement levels, with the two finest levels shown as solid lines. . . . . 127

5.16 Apparent stress–strain curves for the nine Voronoi specimens. . . . . 130

5.17 Apparent stress–strain curves for the nine Gyroid specimens. . . . . 130

5.18 Gibson–Ashby scaling of apparent elastic modulus (a) and apparent yield strength (b) as a function of relative density for both architectures in log–log scale. Dashed lines represent the power-law regressions; exponents and $R^2$ values are indicated in the legend. . . . . 133

5.19 Apparent elastic modulus (a) and yield strength (b) of both architectures at matched relative densities, obtained by interpolation from the fitted Gibson–Ashby scaling laws. Ratios indicate the Gyroid-to-Voronoi values at each density level. . . . . 134

5.20 Apparent elastic modulus and yield strength of all eighteen specimens plotted against the mechanical property windows of trabecular and cortical bone. The shaded vertical band identifies the cortical modulus range (18–30 GPa) independently of strength. The dotted line indicates the constant yield strain shared by all iron lattice specimens ($\varepsilon_y = 0.26\,\%$). Voronoi specimens are shown as squares and Gyroid specimens as circles. . . . . 135

# List of Tables


2.1 Mechanical properties of bone tissue at the apparent level, under compressive loading [28, 29]. . . . . 12

2.2 Elastic modulus of cortical bone and common orthopaedic alloys. [1, 2]. . . . . 14

2.3 Indicative architectural parameters for porous metallic implants targeting bone repair and their corresponding target ranges [2, 49, 50]. . . . . 16

2.4 Comparison of additive manufacturing techniques in terms of energy source, atmosphere, and surface roughness [9, 12, 52, 98, 101, 103]. . . . . 28

3.1 Summary of the parameters governing the generative pipeline. . . . . 46

3.2 Summary of the parameters governing the Gyroid generative pipeline. . . . . 54

3.3 Fraction of total variance ($\eta^2$) in relative density and specific surface area attributable to each parameter, computed across all 128 valid observations. . . . . 56

3.4 Relative density $\rho_r$ (%) of the Voronoi lattice as a function of $n$ ($N$) and $D$. The grid spacing $d = L/n$ is included alongside $n$. . . . . 57

3.5 Groups of configurations sharing an identical value of $D/d$ despite differing individually in $n$ and $D$, with the resulting spread in relative density. . . . . 58

3.6 Specific surface area $A$ ($\mathrm{cm}^2$) of the Voronoi lattice as a function of $n$ ($N$) and $D$. The grid spacing $d = L/n$ is included alongside $n$. . . . . 60

3.7 Pore volume statistics (mean $\pm$ standard deviation, $\mathrm{mm}^3$) of the Voronoi lattice as a function of $n$ ($N$) and $D$. The grid spacing $d$ is included alongside $n$. . . . . 61

3.8 Equivalent pore diameter $d_{\mathrm{pore}}$ (mm) derived from the mean pore volume of Table 3.7 via Equation (3.6). . . . . 62

3.9 Percentage error of the realised strut diameter relative to nominal $D$ for each Voronoi configuration. The grid spacing $d = L/n$ is included alongside $n$. . . . . 63

3.10 Relative density $\rho_r$ (%) of the sheet-based Gyroid across all 80 configurations. . . 64

3.11 Specific surface area $A$ ($\mathrm{cm}^2$) of the sheet-based Gyroid across all 80 configurations. 66

3.12 Average wall thickness $t$ (mm) of the sheet-based Gyroid — lower density range ($C = 0.2$–$0.6$). . . . . 68

3.13 Average wall thickness $t$ (mm) of the sheet-based Gyroid — upper density range ($C = 0.7$–$1.1$). . . . . 68

3.14 Equivalent pore diameter $d_p$ (µm) of the sheet-based Gyroid. . . . . 69

3.15 Hydraulic diameter $d_h$ (µm) of the sheet-based Gyroid. . . . . 69

3.16 Fixed bulk L-PBF processing condition adopted throughout fabrication. . . . . 76

3.17 Contour processing condition adopted for the boundary of each specimen. . . . . 76

4.1 Voronoi specimens: design parameters, relative density, surface area and assigned SBF volume. $n$ denotes the number of cells and $D$ the density parameter. . . . . 83

4.2 Gyroid specimens: design parameters, relative density, surface area and assigned SBF volume. $l$ denotes cell size and $C$ the level-set constant. . . . . 84

4.3 Gyroid specimens: mean mass loss ($\pm$ SD, %) at Days 10, 20 and 30, ordered by relative density. Values of $\rho_r$ and $A$ are from the parametric study (Section 3.3.2). 88

4.4 Voronoi specimens: mean mass loss ($\pm$ SD, %) at Days 10, 20 and 30, ordered by relative density. Values of $\rho_r$ and $A$ are from the parametric study (Section 3.3.1). 88

4.5 Gyroid specimens: mean Corrosion Rate (CR) ($\pm$ SD, mm yr$^{-1}$) at Days 10, 20 and 30, ordered by relative density. $\rho_r$ and $A$ values are from Section 3.3.2. . . . 93

4.6 Voronoi specimens: mean CR . . . . . 93

4.7 Day-28/30 corrosion rates from static immersion tests for Additive Manufacturing (AM) pure iron scaffolds in physiological solutions. All CR values are mass-loss-based and normalised by the nominal geometric surface area according to ASTM G31. $\rho_r$: relative density. . . . . 97

4.8 Corrosion rate comparison at matched relative density between the present study and Li et al. (2018) [126], the latter reporting $\rho_r = 22$–$27\,\%$. No Gyroid condition falls exactly within this window, so the two closest configurations are included for reference. . . . . 99

4.9 Soluble iron concentration (mg L$^{-1}$, mean $\pm$ measurement uncertainty) determined by FAAS in the spent SBF collected at each renewal interval for the three specimens selected for chemical analysis. The SBF blank returned a concentration below the detection limit of the technique ($< 0.6$ g L$^{-1}$). The Day 10 value for the dense reference is unavailable owing to loss of the sample during transit. . . . . 100

5.1 Mesh integrity metrics across the stages of the open-source repair pipeline, for a representative Voronoi specimen. . . . . 110

5.2 Elastic properties of pure iron adopted in the finite element simulations. . . . . 113

5.3 Summary of the finite element simulation setup adopted for all specimens. . . . . 121

5.4 Mesh convergence study for the Voronoi $n$=10, $D$=0.3 mm specimen using quadratic tetrahedral elements (C3D10). Peak apparent stress is taken as the convergence indicator. The third refinement level ($e = 0.075$ mm) could not be completed owing to computational resource constraints. . . . . 123

5.5 Mesh convergence study for the Voronoi $n$=10, $D$=0.3 mm specimen using linear tetrahedral elements (C3D4). Peak apparent stress is taken as the convergence indicator. . . . . 124

5.6 Cross-validation of the discretisation criterion for the Voronoi $n$=10 specimen at strut diameters $D$=0.5 mm and $D$=0.7 mm. Peak apparent stress is taken as the convergence indicator. . . . . 126

5.7 Mesh convergence study for the Gyroid $l$=5.0 mm, $C$=0.2 specimen using linear tetrahedral elements (C3D4). Peak apparent stress is taken as the convergence indicator. . . . . 127

5.8 Summary of the converged discretisation criteria adopted for each architecture. . 128

5.9 Mesh quality metrics for the nine Voronoi simulation meshes. Jac. mean: mean scaled Jacobian; Jac. $< 0.2$: fraction of elements with scaled Jacobian below 0.2 (%); AR mean: mean aspect ratio; AR $> 10$: fraction of elements with aspect ratio above 10 (%). . . . . 128

5.10 Mesh quality metrics for the nine Gyroid simulation meshes. Column definitions as in Table 5.9. . . . . 129

5.11 Apparent elastic modulus and yield strength for the nine Voronoi specimens. The cell size $d = L/n$, with $L = 20$ mm. . . . . 131

5.12 Apparent elastic modulus and yield strength for the nine Gyroid specimens. . . . 132

5.13 Gibson–Ashby power-law parameters for both architectures. $P^*/P_s = C_1 \cdot (\rho^*)^{n_1}$. 132

5.14 Configurations satisfying the trabecular and cortical elastic modulus windows, together with the intermediate configurations lying between them, and the corresponding generation parameters and apparent mechanical properties. . . . . 137

A.1 Relative density $\rho_r$ (%) of the Voronoi lattice — realisation $i = 0.25$, Seed = 42. . 159

A.2 Relative density $\rho_r$ (%) of the Voronoi lattice — realisation $i = 0.25$, Seed = 100. 159

A.3 Relative density $\rho_r$ (%) of the Voronoi lattice — realisation $i = 0.40$, Seed = 100. 160

A.4 Specific surface area $A$ (mm$^2$) of the Voronoi lattice — realisation $i = 0.25$, Seed = 42. . . . . 160

A.5 Specific surface area $A$ (mm$^2$) of the Voronoi lattice — realisation $i = 0.25$, Seed = 100. . . . . 160

A.6 Specific surface area $A$ (mm$^2$) of the Voronoi lattice — realisation $i = 0.40$, Seed = 100. . . . . 161

# List of Acronyms

| | |
|---|---|
| **AM** | Additive Manufacturing |
| **BCC** | Body-Centred Cubic |
| **BCT** | Body-Centred Tetragonal |
| **CAD** | Computer-Aided Design |
| **CEMUP** | Centro de Materiais da Universidade do Porto |
| **CR** | Corrosion Rate |
| **EBM** | Electron Beam Melting |
| **EDS** | Energy-Dispersive X-ray Spectroscopy |
| **FAAS** | Flame Atomic Absorption Spectrometry |
| **FCC** | Faced-Centred Cubic |
| **FEA** | Finite Element Analysis |
| **$HNO_3$** | Nitric acid |
| **ICP-OES** | Inductively Coupled Plasma Optical Emission Spectrometry |
| **L-PBF** | Laser Powder Bed Fusion |
| **RCO** | Rhombicuboctahedron |
| **RP** | Reference Point |
| **RTCO** | Rhombitruncated Cuboctahedron |
| **SBF** | Simulated Body Fluid |
| **SC** | Simple Cubic |
| **SDG** | Sustainable Development Goal |
| **SEM** | Scanning Electron Microscopy |
| **SLM** | Selective Laser Melting |
| **SLS** | Selective Laser Sintering |
| **STL** | Standard Triangle Language |
| **TO** | Truncated Octahedron |
| **TPMS** | Triply Periodic Minimal Surface |

Chapter 1

# Introduction

## 1.1 Context and Motivation

The treatment of critical bone defects has historically relied on dense metallic implants [1, 2]. The primary biomechanical limitation inherent to this solid design is a pronounced stiffness mismatch relative to the surrounding bone tissue [3–5]. This disparity gives rise to an undesirable phenomenon known as *stress shielding*, a process that deprives the bone of required mechanical stimulation and ultimately drives progressive tissue resorption [6].

In order to mitigate this complication, the introduction of porosity in architectural design has emerged as a highly promising structural strategy. Substituting a dense material with an interconnected cellular network makes it feasible to reduce the apparent stiffness of the component to levels compatible with physiological requirements [2, 7].

Beyond offering mechanical benefits, porosity presents a valuable opportunity to explore the viability of biodegradable metallic implants. Several promising alloys possess excellent strength, but they degrade too slowly in their bulk form to be clinically practical [8, 9]. Creating a porous internal structure naturally might solve this issue by exposing a much larger portion of the material to the surrounding bodily fluids. This increased exposure accelerates the degradation process, providing a pathway to investigate their potential as temporary implants [10, 11].

Realizing this clinical potential essentially requires exploring the viability of these biodegradable devices across promising porous geometries. Additive manufacturing currently provides the technological foundation to produce such complex internal architectures [2, 12], thereby enabling the evaluation of distinct structural hypotheses that show promise for orthopedic applications. Within this context stochastic Voronoi lattices achieve topological similarity by closely emulating the irregular architecture of natural trabecular bone [13–15]. Alternatively continuous regular surfaces such as the Triply Periodic Minimal Surface (TPMS) geometry present a fundamentally different spatial paradigm by offering a smooth boundary entirely devoid of discrete junctions [16, 17].

Evaluating how these topological strategies translate into actual mechanical strength and degradation behavior remains an open challenge in the field. The present work addresses this challenge by subjecting both promising geometries to the exact same experimental and computational framework, enabling a direct comparative study focused specifically on these biomedical applications. Determining how each structural design resolves the balance between mechanical stability under compression and the permeability required for effective tissue regeneration constitutes the aim pursued throughout this research.

## 1.2 Objectives

Following the motivation outlined previously this dissertation requires the completion of four specific objectives

- **Computational Design:** Generating parts with a well defined structure, based on the purpose of this research, for both geometries using an adaptable open source pipeline. Afterwards, a comprehensive parametric study allows to understand the relationship between generation parameters and morphological characteristics across a vast parametric space.
- **Additive Manufacturing:** Selecting a representative subset of architectures that encompasses a broad spectrum of morphological characteristics to ensure a representative comparative study regarding mechanical properties and degradation behavior and subsequently fabricating these selected specimens via additive manufacturing.
- **Biodegradation Behavior:** Investigating the degradation behavior of the printed structures by tracking their physical and chemical degradation profiles alongside a characterization of the specimen surface morphology
- **Mechanical Properties Characterization:** Simulating the compressive mechanical response of the geometries through Finite Element Analysis (FEA) to extract apparent mechanical properties and determine their compatibility with human bone properties.

## 1.3 Dissertation Structure and Organization

This dissertation is organized into six chapters, structured to guide the reader progressively from the clinical motivation to the final conclusions of the research.

- **Chapter 2.** Reviews the biomechanical foundation of natural bone from its hierarchical composition to the distinct roles of cortical and trabecular tissue before examining the clinical failure of conventional dense implants caused by stress shielding. The chapter subsequently explores the architectural strategies developed to address this limitation detailing the most suitable porous geometries alongside the additive manufacturing processes that make these complex structures physically realizable.
- **Chapter 3.** Outlines the computational pipelines established to generate the structural models by detailing the specific methods employed. Following this structural definition a parametric study investigates how input variables govern the resulting morphological properties aiming to establish empirical formulations that enable future reverse engineering applications. The chapter concludes by defining the selection criteria for the representative test specimens and detailing the additive manufacturing procedures used to fabricate them.

- **Chapter 4.** Presents the experimental study of the degradation behavior by analyzing physical mass loss alongside chemical ion release profiles. A central element of this chapter is the comparative assessment between the porous specimens and a dense control sample aiming to validate the theoretical assumption that cellular architectures effectively accelerate corrosion. Nonetheless, a surface morphological characterization is performed to identify and evaluate the resulting solid corrosion products.

- **Chapter 5.** Details the complete finite element workflow, from the post-design mesh processing required to prepare the specimens to the simulation setup configured in Abaqus, and highlights a mesh convergence study, conducted on a single specimen per geometry, in order to improve the reliability of the obtained results. The chapter concludes by analyzing the resulting mechanical properties, evaluating their structural compatibility with natural bone and consequently their suitability for biomedical applications.

- **Chapter 6.** Synthesizes the conclusions withdrawn from this research and discusses potential directions for future work.

Chapter 2

# State of the Art

## 2.1 Bone Tissue: Composition, Structure, and Biomechanics

### 2.1.1 Physicochemical Composition and Hierarchical Structure

From the perspective of engineering and materials science, bone tissue can be described as a highly heterogeneous natural composite [18]. Its architecture is organized hierarchically, extending from the nanoscale to the macroscale, which accounts for its exceptional combination of low weight, high stiffness, and toughness [19, 20]. This mechanical performance results from the synergistic interaction of three main components: an inorganic mineral phase, an organic matrix, and a fluid phase [21, 22]. The inorganic phase provides the primary structural reinforcement and is composed mainly of nanometric carbonated hydroxyapatite crystals [23, 24]. This mineral component is the main determinant of the macroscopic stiffness of bone and contributes strongly to its resistance to compressive loading [22]. However, when considered in isolation at the nanoscale, hydroxyapatite behaves as a brittle ceramic and is therefore highly susceptible to fracture [19].

To compensate for this fragility, bone incorporates a flexible organic matrix that represents approximately 30% of the total tissue weight [25]. This matrix is predominantly composed of type I collagen molecules, which assemble into fibrils of approximately 100 nm in diameter, within which the rigid mineral platelets are intercalated, together with smaller amounts of lipids and non-collagenous proteins [18, 23]. From a biomechanical standpoint, collagen governs the post-yield response of bone by promoting deformation and energy dissipation through inelastic mechanisms such as fibrillar sliding [19, 22]. The interaction between the rigid mineral phase and the compliant collagen network is therefore essential for the intrinsic toughness of bone and for its resistance to microcrack propagation [26].

Finally, the fluid phase, composed mainly of water and bone marrow, also plays an essential biomechanical role [21]. Water acts as a plasticizer within the structural matrix and, together with proteoglycans, helps preserve the overall toughness of the tissue under mechanical loading [26]. Under rapid compressive loading, especially when the marrow is confined within the porous structure, the semifluid phase can increase the apparent stiffness of bone through hydraulic stiffening. Under impact conditions, this dynamic effect may raise the apparent rigidity of the structure by approximately 20% to 30% [21]. As shown in Figure 2.1, this hierarchical interplay between mineral, collagen, and fluid phases sets the structural basis for the distinct macroscopic organization of bone.

### 2.1.2 Macroscopic and Microstructural Morphology

The spatial organization of the physicochemical and nanometric constituents determines bone morphology at the micro and macroscopic scales [18]. At this hierarchical level, bone tissue

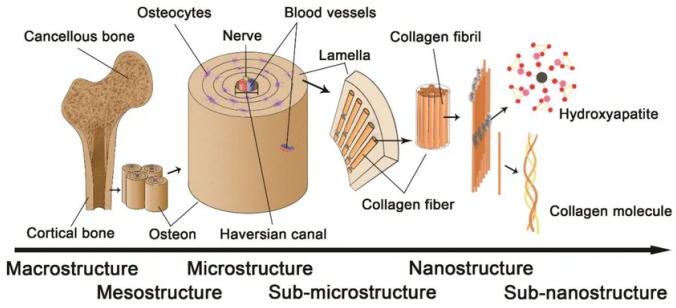



Figure 2.1: Hierarchical organization of bone tissue from macrostructure to nanostructure. Adapted from [27].

is generally divided into two main architectures that satisfy distinct mechanical and functional requirements: cortical bone and trabecular bone [18, 22].

Cortical bone forms the protective outer shell of all bones and constitutes the entire diaphysis, or central shaft, of long bones [28]. Structurally, it is a highly dense material with very low porosity, typically ranging from 5% to 15% [28, 29]. Its microstructure is largely dominated by osteons, or Haversian systems, which consist of cylindrical units formed by concentric lamellae of bone matrix surrounding a central canal responsible for the vascular supply of the tissue [25, 30]. Embedded within this lamellar arrangement is the lacuno-canalicular network, in which osteocytes reside and account for approximately 90% to 95% of all bone cells [18, 31]. These cells are the principal mechanosensors of bone and play a central role in detecting applied mechanical loads, thereby coordinating the biological response associated with bone adaptation and remodeling [31]. This hierarchical organization also explains the mechanical role of osteons, which reinforce the compact bone layer along the longitudinal axis and confer high resistance to compressive and flexural loading [23].

In contrast, trabecular bone is located within the epiphyses and metaphyses of long bones, as well as in the vertebral bodies [28]. Unlike the solid cortical shell, this tissue exhibits a highly porous architecture, with porosity values that can vary widely, typically ranging from 40% to 95% of the total volume [28, 29]. Rather than forming a continuous mass, it consists of a three-dimensional interconnected stochastic network of thin plates and struts, known as trabeculae [20]. From the perspective of engineering and materials mechanics, trabecular bone is commonly modeled as a cellular solid with a high surface-area-to-volume ratio [22]. Its primary structural function is not to provide maximal direct load-bearing, but rather to act as a buffer that absorbs energy and promotes a more gradual and homogeneous transfer of mechanical stresses toward the stiffer cortical shell[21]. This structural organization is schematically illustrated in Figure 2.2, which shows the anatomical distribution of cortical and trabecular bone in a long bone.

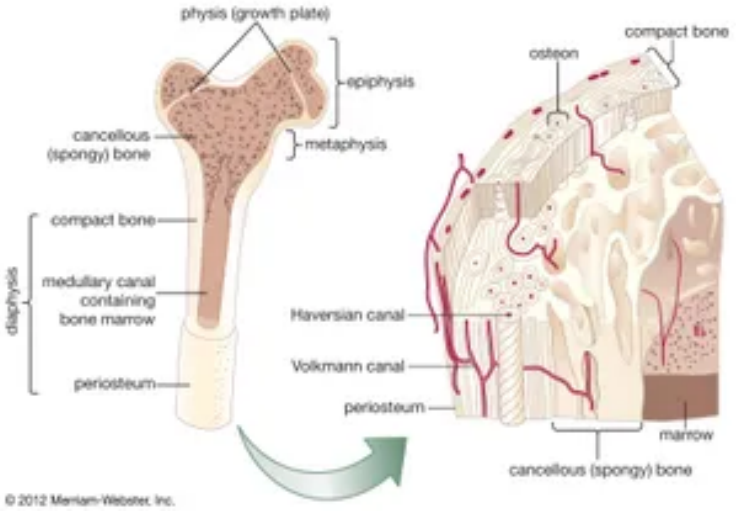



Figure 2.2: Anatomical distribution of cortical and trabecular bone in a long bone. Adapted from [32].

### 2.1.3 Characterization of Biomechanical Behavior and Properties

The mechanical behavior of bone tissue exhibits a markedly anisotropic and viscoelastic nature, depending critically on the direction of loading, the scale of observation, and the strain rate to which the material is subjected [26, 28]. Cortical bone, due to the organization of its matrix and the alignment of its osteons, is mechanically optimized to resist high compressive stresses along its longitudinal axis [28]. Its stiffness typically ranges from 18 to 30 GPa in young healthy adults, decreasing in older populations to values between 10 and 25 GPa [21]. This stiffness, however, introduces a pronounced asymmetry between tensile and compressive behavior [28, 30]. Microscale biomechanical tests show that, although the lamellar compressive yield stress can be very high, reaching 490 MPa along the axial direction, the same tissue fails under tension at substantially lower stress levels, making it susceptible to fracture under such loading conditions [30].

In contrast, the biomechanical resistance of trabecular bone is not governed by a compact mass but by its apparent density and the architecture of its three-dimensional pore network [20]. Owing to this porous architecture, its apparent stiffness is orders of magnitude lower than that of adjacent cortical bone, with apparent elastic moduli that vary substantially with anatomical site, loading direction, and apparent density, typically ranging from approximately 0.1 to 3 GPa [22, 28]. The major mechanical advantage of this network lies in its ability to behave as a cellular solid, prioritizing mechanical energy absorption over rigid load support [22, 25]. Although trabecular bone begins to yield plastically at relatively low strain levels, its macroscopic structure can sustain compressive deformations of up to 50% without completely losing its load-bearing capacity [28].

Table 2.1 consolidates the principal structural parameters of healthy adult human bone discussed throughout the previous subsections [21, 28, 29]. This mechanical framework is also central to understanding how bone responds once its structural integrity is exceeded, which leads

directly to fracture and repair.

Table 2.1: Mechanical properties of bone tissue at the apparent level, under compressive loading [28, 29].

| Tissue | Porosity (%) | Elastic modulus (GPa) | Compressive yield strength (MPa) |
|---|---|---|---|
| Cortical Bone | 5 – 15 | 18 – 30[†] | 100 – 200 |
| Trabecular Bone | 40 – 95 | 0.1 – 3[‡] | 2 – 20 |

[†]Young healthy adults; decreases to 10–25 GPa in older populations [21].
[‡]Apparent-level, compressive; site-dependent [28].

### 2.1.4 Fracture Behavior and Bone Repair Mechanisms

Bone fracture occurs when the applied mechanical loads exceed the toughness and structural resistance of the tissue [28, 29]. In contrast to most soft tissues, which heal predominantly through the formation of fibrous scar tissue, bone possesses the exceptional capacity to regenerate and restore its original form and function [33]. The vast majority of fractures consolidate through indirect healing, which involves the formation of a bone callus driven by a combination of endochondral and intramembranous ossification, as illustrated in Figure 2.3 [31, 33].

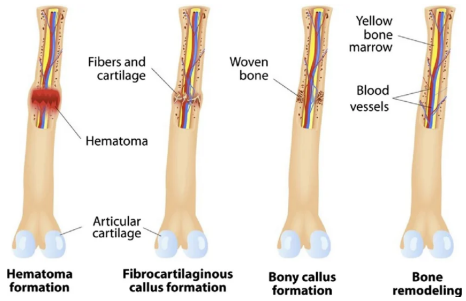



Figure 2.3: Schematic representation of stages of bone fracture healing. Adapted from [34].

The efficacy of this regenerative process is critically governed by the local mechanical environment and the physical stresses applied to the injury site [29, 31]. At the cellular level, this response is mediated by mechanotransduction, a process in which cells act as sensors that convert mechanical stimuli into biochemical signals [31]. This broader biological response not only regulates cell proliferation and the synthesis of new bone matrix, but also acts in synergy with angiogenesis, stimulating vascularization, which is vital to ensure nutrient supply to the repair site [31, 33]. When vascularization is insufficient, nutrient deprivation can impair callus maturation and contribute to delayed union or non-union outcomes, a challenge of particular relevance in the design of bone implants that must promote vascular ingrowth [35]. From a biomechanical standpoint, the magnitude and direction of movement dictate stress distribution and the success of fracture consolidation. Studies show that moderate axial movements improve biological repair by promoting callus formation, whereas excessive shear or tensile movements tend to inhibit the

healing process, corresponding to a mechanosensory framework that forms the biological basis of what is formally described by Wolff's Law [28, 31, 35].

This principle states that bone dynamically remodels itself in response to the mechanical loads to which it is subjected, distinguishing between physiological remodeling, which maintains structural integrity, and pathological remodeling, which arises when loading conditions deviate from normal physiological ranges [6, 36]. Under normal conditions, a dynamic equilibrium is maintained between osteoblasts, responsible for new bone formation, and osteoclasts, responsible for bone resorption [1]. When this mechanical homeostasis is preserved, bone mass and structural integrity are sustained. Conversely, the absence of adequate mechanical stimulation disrupts this balance, suppressing osteoblastic activity while promoting osteoclastic resorption, ultimately leading to a progressive loss of bone density [1, 36].

## 2.2 Metallic Implants and Architectural Strategies for Bone Repair

### 2.2.1 Clinical Failure of Bone Repair

Bone tissue is a remarkably dynamic organ, capable of detecting mechanical stimuli, resorbing damaged matrix, and depositing new mineralized tissue through a tightly regulated cellular dialogue. Yet this regenerative capacity is not without boundaries. When skeletal homeostasis is severely disrupted, by high-energy trauma, aggressive surgical resection, or chronic metabolic disease, the biological machinery of repair fails to bridge the deficit, and clinical intervention becomes unavoidable [37].

The clearest expression of this failure is the critical-size bone defect, defined as a bone loss that will not heal spontaneously within the patient's lifetime [38]. Gaps exceeding twice the diaphyseal diameter of a long bone carry a near-zero probability of spontaneous union, as the absence of a structural scaffold permanently disrupts the coupled processes of osteogenesis and angiogenesis. These massive defects arise most commonly from high-energy trauma, bone tumour resection, or severe infection such as osteomyelitis and without clinical intervention evolve inevitably into non-unions [37, 38]. Beyond acute trauma, degenerative and metabolic conditions impose an equally vast burden. Osteoporosis affects approximately 200 million women worldwide, generating over 8.9 million fragility fractures annually and a first fracture increases the risk of a subsequent one by 86% [39]. Concurrently, osteoarthritis drives progressive cartilage degradation and joint deformity, with demand for total hip and knee arthroplasty in the United States projected to grow by 174% and 673%, respectively, by 2030, a trend expected to intensify through 2040 as populations continue to age [40, 41].

Between 1990 and 2019, deaths and disability-adjusted life years attributable to low bone mineral density increased by over 111% and 93%, respectively [42]. In Europe, fragility fractures

already rank as the fourth leading cause of chronic disease morbidity, surpassing ischaemic stroke, with first-year mortality following hip fracture reaching 20–24% [39].

The collective burden of these medical conditions places an overwhelming and growing demand on orthopaedic care systems worldwide, underscoring the urgent need for effective and scalable treatment strategies [39, 42].

### 2.2.2 Conventional Metallic Implants and the Challenge of Stress Shielding

Meeting this demand has historically relied on a class of materials selected above all for their mechanical reliability. Metallic alloys such as titanium alloys (Ti-6Al-4V), cobalt-chromium-molybdenum (Co-Cr-Mo), and 316L stainless steel became the gold standard for load-bearing orthopaedic implants owing to their exceptional mechanical strength, favourable biocompatibility, and high corrosion resistance in physiological environments [1, 2].

Despite their durability, conventional dense metallic implants carry a fundamental biomechanical flaw: a pronounced stiffness mismatch with the host tissue they are designed to support [3–5]. As established in Section 2.1.3, cortical bone possesses an elastic modulus of 18–30 GPa, whereas standard metallic implants far exceed this range, as summarised in 2.2. Ti-6Al-4V presents a modulus of approximately 110 GPa, 316L stainless steel around 200 GPa, and Co-Cr-Mo alloys up to 230 GPa, rendering them four to ten times stiffer than the surrounding bone [1, 2].

Table 2.2: Elastic modulus of cortical bone and common orthopaedic alloys. [1, 2].

| **Material** | **Elastic Modulus (GPa)** |
|---|---|
| Cortical bone | 18–30 |
| Ti-6Al-4V | ∼110 |
| 316L Stainless Steel | ∼200 |
| Co-Cr-Mo | 210–230 |

This disparity triggers a phenomenon known as stress shielding. Mechanically, the implant and surrounding bone act as parallel load-bearing elements; since load distribution between parallel structures is proportional to their relative stiffness, the metallic stem, being far stiffer, attracts the dominant share of the applied force, leaving the adjacent bone chronically under-loaded [43]. As a direct consequence of the remodelling principles described in Section 2.1.4, the under-stimulated host bone adapts to this reduced mechanical stimulus by suppressing osteoblastic activity and accelerating osteoclastic resorption, resulting in progressive periprosthetic bone loss [6].

Clinically, this altered load distribution carries significant consequences. Studies consistently report progressive reductions in bone mineral density in the bone surrounding the implant, with loss intensifying over time in direct proportion to the degree of stiffness mismatch [6, 44]. Over

time, this sustained reduction in bone mineral density progressively compromises implant stability and culminates in aseptic loosening [6].

The excessive stiffness of fully dense metallic implants thus constitutes the central design limitation of conventional orthopaedic reconstruction. Addressing it requires not merely a change of material, but a fundamental rethinking of implant architecture, reconciling sufficient mechanical strength with a structural compliance closer to that of native bone [2, 5].

### 2.2.3 Porous Metallic Implants: Architectural Strategies for Bone Repair

As established in Section 2.2.2, the inherent stiffness mismatch between conventional dense metallic implants and natural host bone induces stress shielding, which ultimately compromises long-term implant stability [3]. To address this, the introduction of intentional porosity serves a dual architectural role: mechanically, it acts as a structural tool to actively tune the apparent stiffness of the implant down to physiological levels, while biologically, it provides an interconnected open space necessary for vascularisation and direct bone tissue ingrowth [2, 7]. Furthermore, in the specific context of biodegradable metals, such as iron, zinc, and magnesium alloys, porosity is uniquely relevant because it transforms intrinsic material limitations into a controllable parameter, by drastically increasing the specific surface area exposed to physiological fluids and thereby accelerating the material's degradation kinetics [45, 46].

The primary mechanical objective of introducing porosity is to bridge the elastic gap between rigid metals and the surrounding bone tissue. The theoretical relationship between the relative density of a cellular solid and its apparent mechanical properties is classically described by the Gibson–Ashby scaling law [47, 48]:

$$\frac{E^*}{E_s} = C_1 \left( \frac{\rho^*}{\rho_s} \right)^n \tag{2.1}$$

where $E^*$ and $E_s$ are the elastic moduli of the porous structure and the fully dense bulk material, respectively, $\rho^*/\rho_s$ is the relative density, and $C_1$ and $n$ are topology-dependent constants. By adjusting internal porosity according to this relationship, rigid alloys can be engineered to mimic the biomechanics of natural bone across the full skeletal spectrum. As a concrete illustration, finite element analyses of Ti-6Al-4V porous structures report a reduction in apparent Young's modulus from approximately 19.6 GPa to 1.85 GPa as porosity increases from 50% to 80%, placing the lower-porosity configurations within the cortical bone range and the higher-porosity ones within the trabecular bone range established in Section 2.1.3 [49].

For a porous implant to succeed in vivo, its internal architecture must satisfy stringent biological criteria to support osteoconduction and cellular proliferation. However, it is important to note that the literature lacks a universal consensus on strictly defined optimal values for these architec-

tural parameters, meaning that the values reported typically serve as indicative reference ranges rather than absolute rules. For instance, pore sizes ranging from 100 to 600 µm are broadly considered suitable for mineralised bone ingrowth, with a strict minimum of approximately 125 µm required to permit the formation of the capillary networks essential for tissue vascularisation [49, 50]. A total porosity of 30 to 50% is typically necessary to provide sufficient spatial volume for cellular infiltration, extracellular matrix deposition, and unobstructed fluid transport [50]. Regardless of pore size or total void volume, high structural interconnectivity remains a non negotiable requirement. Closed or dead end pores obstruct cellular migration and isolate internal regions from biological exchange, giving rise to localised necrotic zones that actively impair tissue regeneration [2, 49].

Beyond its role as a static scaffold, the porous network governs the implant's overall permeability, which is a determining parameter for dynamic fluid transport throughout the structure [50]. Adequate permeability sustains the continuous delivery of oxygen and nutrients to the scaffold's interior while enabling the clearance of metabolic waste and cellular debris [2, 49]. Computational fluid dynamics and experimental measurements indicate that optimal permeability coefficients for porous metallic scaffolds range from $1.10 \times 10^{-10}$ m$^2$ to $9.26 \times 10^{-7}$ m$^2$, mirroring the physiological permeability of human trabecular bone [2, 50]. As physiological fluid moves through these tortuous microchannels, it exerts wall shear stress on adhered cell populations, a mechanical stimulus that, at the micro environmental level, actively promotes the osteogenic differentiation of mesenchymal stem cells and drives angiogenesis throughout the implant's core [50, 51].Table 2.3 summarises the key architectural parameters — pore size, porosity, interconnectivity, and permeability — typically targeted in the design of porous metallic scaffolds for bone repair.

Table 2.3: Indicative architectural parameters for porous metallic implants targeting bone repair and their corresponding target ranges [2, 49, 50].

| **Parameter** | **Target Range** |
|---|---|
| Pore Size | 100 to 600 µm |
| Total Porosity | ∼30 to 50% |
| Interconnectivity | High |
| Permeability | $\sim 10^{-10}$ to $10^{-7}$ m$^2$ |

These theoretical advantages are well supported by experimental evidence. Extensive in vitro and in vivo studies consistently demonstrate that porous implants achieve superior osseointegration and deeper biological fixation compared to their fully dense counterparts [3, 7]. The presence of an interconnected architecture enhances cell spreading, sustains osteoblast proliferation across internal surfaces, and results in a significantly greater bone-to-implant contact area during the healing phase [45, 50].

Despite these clear biological advantages, an unavoidable mechanical trade-off emerges. Increasing porosity to reduce apparent stiffness and enhance fluid transport simultaneously and markedly compromises the implant's compressive strength and structural stability [45, 47]. Under the cyclic physiological loading typical of load-bearing sites, excessive or poorly distributed voids act as stress concentrators that nucleate micro-cracks and accelerate fatigue failure [2, 49].

Historically, the fabrication of open-cell porous metals relied on conventional processing routes, predominantly liquid-state foaming, powder metallurgy, and the space-holder method [7, 49]. While these techniques successfully introduced voids to reduce bulk stiffness, they offered virtually no control over the resulting internal architecture, producing stochastic structures with irregular pore shapes, broad size distributions, and inconsistent connectivity [2, 7]. Crucially, these stochastic architectures cannot resolve the fundamental biomechanical trade-off: the random distribution of material inevitably introduces localised weaknesses and unpredictable stress concentrations, making it impossible to reliably optimise the structure for complex loading without simultaneously compromising fluid transport [2, 49].

Overcoming this inherent limitation requires moving beyond randomised networks toward architectures in which the internal geometry is precisely and algorithmically defined. This necessity motivates the adoption of controlled lattice structures, which are examined in the following section [2, 47].

## 2.3 Architected Cellular Materials

To transcend the inherent topological limitations of stochastic foams, architected cellular materials, commonly known as lattice structures, have emerged as a mathematically rigorous alternative [52]. Lattice structures are architected cellular materials characterised by complex spatial patterns, whether periodic, non-periodic, or stochastic, in which material is placed according to a mathematically prescribed rule to simultaneously govern mechanical response, fluid transport, and surface properties [53, 54]. Unlike traditional stochastic foams, which possess random internal porosity, lattice structures are defined by an algorithmically controlled internal geometry conceived prior to fabrication [12]. This deterministic design intent enables the independent and simultaneous optimisation of multiple functional requirements, including the macroscopic mechanical response, physiological fluid permeability, and osseointegration interface topology [5]. By precisely tailoring the spatial arrangement and interconnectedness of the solid network, structural stiffness can be customised independently of global porosity, thereby satisfying both the load-bearing and mass transport demands crucial for bone tissue regeneration [12, 55].

Within the domain of architected cellular materials, the primary taxonomic division separates structural designs into periodic and non-periodic architectures [52]. Periodic architectures are generated through the uniform spatial repetition of a fundamental building block, known as a unit

cell, across three dimensions, ensuring highly predictable mechanical behaviour [12, 55, 56]. Conversely, non-periodic architectures are spatially organised without translational symmetry, relying instead on mathematical spatial distributions to define the solid network [55]. By deliberately incorporating structural variability without a repetitive pattern, these designs are capable of replicating the natural heterogeneity and anisotropic character of biological tissues such as trabecular bone [55].

### 2.3.1 Periodic strut-based lattice structures

Strut-based lattice structures are fundamentally defined as periodic three-dimensional networks composed of interconnected linear struts and converging nodes [12]. By the systematic spatial tessellation of these foundational building blocks, complex macroscopic geometries are generated, whereby mechanical and physical responses are strictly governed by the internal architecture [2]. Key design parameters, principally encompassing the specific unit cell geometry, strut thickness, and relative density, are systematically varied to dictate the overall functional properties of the lattice [57]. A direct correlation is mathematically established between these structural parameters and the macroscopic mechanical properties, global porosity, and total specific surface area of the implant [2, 58]. For instance, when strut thickness is intentionally increased, a corresponding rise in the relative density of the entire network is achieved, by which the compressive yield strength and overall structural stiffness of the lattice are significantly enhanced at the direct cost of interconnecting porosity [57]. The precise manipulation of these architectural features ensures that specific load-bearing requirements and biological mass transport phenomena can be accommodated simultaneously within the regenerative environment [52]. Within the extant literature, a diverse array of unit cell geometries is frequently explored and implemented, with the most prominent topologies broadly including Body-Centred Cubic (BCC), Faced-Centred Cubic (FCC), diamond, Truncated Octahedron (TO), octet-truss, Rhombicuboctahedron (RCO) and Rhombitruncated Cuboctahedron (RTCO) structures, among numerous other topologies reported in the literature, as illustrated in Figure 2.4. [59].

The deformation mechanisms intrinsic to these architected cellular materials are classically categorised into bending-dominated and stretching-dominated regimes, a crucial division mathematically established by the Maxwell stability criterion [57, 60, 61]. This topological criterion is quantitatively evaluated by relating the total number of constituent struts to the respective number of geometric nodes within a given unit cell, whereby the overarching structural response under an externally applied load is accurately predicted [2]. When a stretching-dominated regime is identified, applied macroscopic loads are primarily accommodated by the direct axial tension or compression of the constituent linear struts, resulting in high stiffness and yield strength for any specified relative density [2]. Conversely, when a bending-dominated regime is delineated, structural deformation is accommodated predominantly through the localised bending of the individual

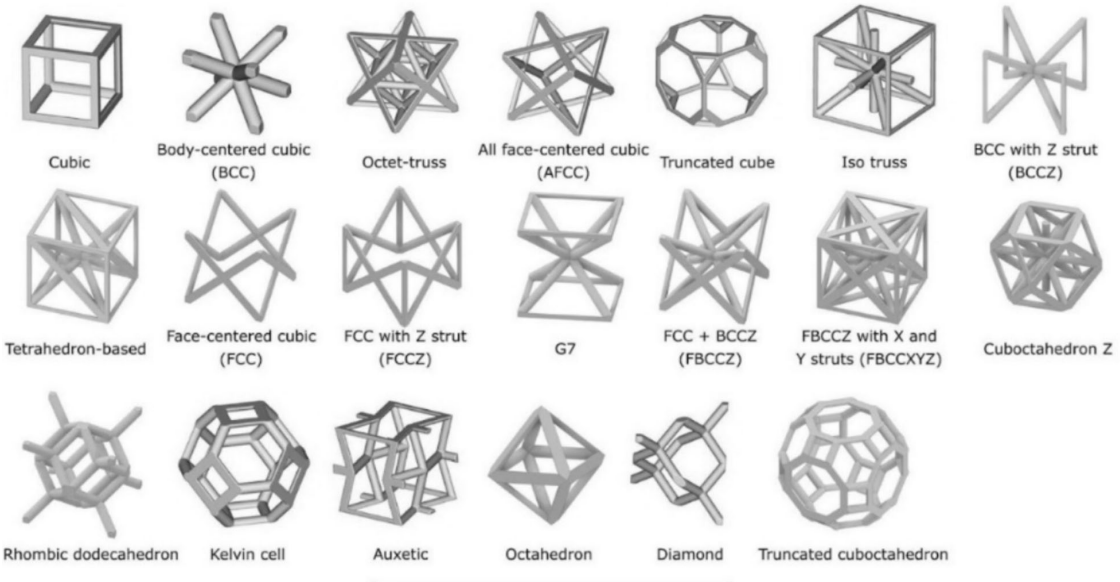



Figure 2.4: Representative unit cell geometries of strut-based lattice. Adapted from [57]).

struts, yielding a more compliant mechanical response and a progressive, stable failure mechanism associated with superior energy absorption [57, 62]. For the specialised design of bone scaffolds, bending-dominated structures are argued to be considerably more suitable than their stretching-dominated counterparts [63, 64]. This suitability is principally attributed to the fact that bending-dominated behaviour is inherently exhibited by natural trabecular bone itself; therefore, this compliant behaviour must be biomimetically emulated by a successful scaffold to effectively prevent stress shielding and to encourage healthy mechanobiological stimulation[55, 65]. Furthermore, during the gradual degradation of biodegradable implants within the physiological environment, a continuous dissolution of the solid network is experienced, by which progressively lower relative densities are inevitably reached over time [66]. Under such degraded conditions, catastrophic mechanical instabilities, such as strut buckling and layer-by-layer structural collapse, are frequently exhibited by stretching-dominated structures once their relative density is reduced beyond a critical threshold [59]. In contrast, structural stability and a reliable, uniform deformation pattern are maintained by bending-dominated architectures even at reduced relative densities, which is recognised as an essential trait for ensuring the functional integrity of a temporary implant throughout its degradation lifecycle [62].

In prior systematic investigations evaluating the compressive properties of five specific unit cell types - C, TO, TC, RCO, and RTCO (Figure 2.5)- a systematic engineering workflow was implemented to assess their biomechanical viability [67].

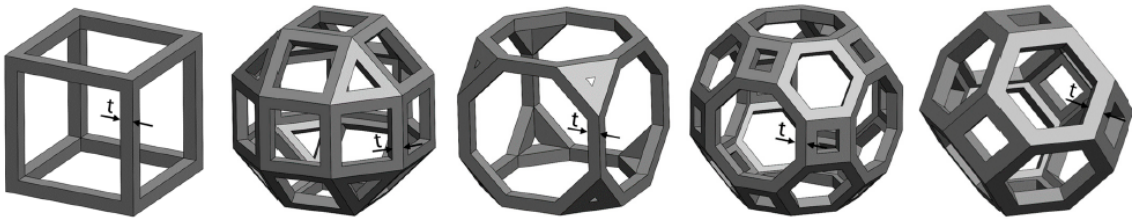


Figure 2.5: Geometry of the five unit cell types investigated Adapted from Nogueira et al. [67].

This workflow was initiated with the computational design and geometric modelling of the respective unit cells, followed by finite element analysis to numerically simulate and predict their compressive behaviour under physiological boundary conditions. These computational models were subsequently validated through the experimental uniaxial compression testing of physical metallic specimens fabricated via additive manufacturing [67]. It was computationally and empirically observed that the stretching-dominated C and TC unit cells, alongside the RCO geometry, exhibit instability at low relative densities [67, 68]. Specifically, pronounced buckling and layer-by-layer collapse were exhibited by the C and TC structures, while fabrication of the RCO structure was not achievable at a relative density of five percent. These unit cell configurations were therefore considered unsuitable for orthopaedic applications demanding high porosity and permeability. In contrast, consistent and stable deformation behaviour was demonstrated by the bending-dominated TO and RTCO architectures across the entire evaluated range of relative densities, confirming them as the only evaluated structures capable of covering the full spectrum of bone mechanical properties [67]. Moreover, the RTCO unit cell was reported to possess an approximately 25% higher specific surface area than the TO geometry, an advantage directly relevant to cellular adhesion, nutrient transport, and biodegradation rate in implant applications [67].

Despite the mechanical versatility of periodic strut-based lattice structures, several inherent geometric limitations substantially restrict their long-term viability in biomedical applications. A primary constraint arises from nodal stress concentrations: the discrete regions where multiple struts converge at sharp intersection angles are systematically identified as points of critical stress accumulation under compressive loading [12], as the von Mises stress distribution example in Figure 2.6 clearly reveals.

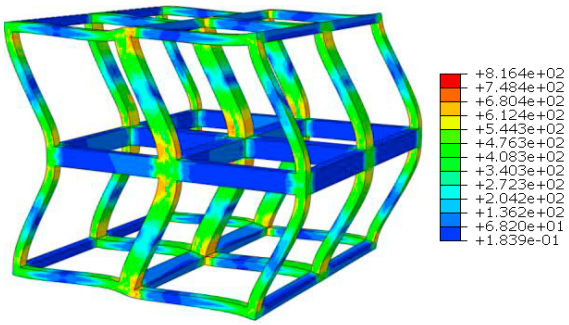



Figure 2.6: Von Mises effective stress distribution (MPa) in a Cubic unit cell at 5% relative density, illustrating pronounced stress concentrations at nodal junctions under compressive loading. Adapted from [68].

These localised stress risers are recognised as preferential initiation sites for micro-cracks, substantially deteriorating the fatigue resistance of the implant under the cyclic physiological loads characteristic of load-bearing sites [2, 57]. Sensitivity to geometric defects generated during manufacturing further compounds this vulnerability, as surface roughness, localised micro-porosity, and un-melted powder particles attached to the struts are known to exacerbate fatigue-induced failure [69, 70]. Additionally, the fluid permeability of strut-based networks is frequently limited by the abrupt angular transitions at the geometric nodes, impeding the optimal flow of physiological fluids and the vascularisation of the implant. The comprehensive fatigue characterisation of these architectures remains an open gap in the literature, and these geometric constraints thus constitute a critical consideration in the design of strut-based implants for load-bearing biomedical applications [2].

### 2.3.2 Triply Periodic Minimal Surface Structures

TPMS are mathematically rigorous architectural concepts defined as continuous, boundaryless surfaces that exhibit a mean curvature of zero at every point [71, 72]. Formulated through implicit level-set equations, these architectures partition space into interpenetrating, non-overlapping domains that repeat periodically across three orthogonal spatial directions [73, 74]. The absence of self-intersections within these implicit models produces a smooth surface topology that inherently mimics the structural configuration of natural biological formations, such as trabecular bone [75]. Within the domain of biomaterials and tissue engineering, the most relevant TPMS geometries include the Schoen Gyroid, the Schwartz Primitive (P), and the Schwartz Diamond (D) structures [16, 17]. The implicit surface of each geometry is described by a level-set equation of the general form $f(x,y,z) = C$ [73], where $f$ is a periodic trigonometric function of the spatial coordinates, $l$ defines the unit cell size, and $C$ is the isovalue constant that directly governs the resulting relative density [76]. The three principal geometries are formulated as follows [73, 76]:

$$\text{Gyroid:} \quad \sin(2\pi x/l)\cos(2\pi y/l) + \sin(2\pi y/l)\cos(2\pi z/l) + \sin(2\pi z/l)\cos(2\pi x/l) = C \quad (2.2)$$

$$\text{Primitive:} \quad \cos(2\pi x/l) + \cos(2\pi y/l) + \cos(2\pi z/l) = C \quad (2.3)$$

$$\text{Diamond:} \quad \sin(2\pi x/l)\sin(2\pi y/l)\sin(2\pi z/l) + \sin(2\pi x/l)\cos(2\pi y/l)\cos(2\pi z/l) + \\ + \cos(2\pi x/l)\sin(2\pi y/l)\cos(2\pi z/l) + \cos(2\pi x/l)\cos(2\pi y/l)\sin(2\pi z/l) = C \quad (2.4)$$

By systematically varying $C$ and $l$, the relative density and pore morphology of the TPMS architecture can be independently and precisely controlled prior to fabrication [73].These geometrical families, along with other TPMS variants, are illustrated in Figure 2.7.

Compared to conventional architected cellular materials, TPMS architectures present profound structural advantages that directly address the inherent limitations of standard strut-based lattices [77]. As explored previously, conventional lattice structures consist of discrete linear struts that converge at geometric nodes, creating sharp intersection angles that act as severe stress concentrations under macroscopic loading [12, 78]. These localised stress risers inevitably serve as initiation sites for micro-cracks, thereby deteriorating the overall fatigue resistance of the implant [78]. Conversely, TPMS structures are entirely devoid of discrete nodal junctions or sharp intersecting edges, offering a curvature-driven geometry that enables a continuous and smooth stress distribution throughout the entire bulk volume [75, 77]. Because external applied loads are distributed homogeneously across the interconnected surfaces rather than accumulating at vulnerable nodes, the occurrence of localised plastic collapse is substantially mitigated, yielding a structure inherently more resistant to fatigue-driven failure than conventional strut-based counterparts [12, 78].

The same geometry that confers mechanical advantages also delivers superior and mathematically controllable permeability, which is a critical mass transport requirement for successful osseointegration [72, 79]. The triply periodic nature of these minimal surfaces generates a highly interconnected labyrinthine network of continuous flow channels, as depicted in Figure 2.7, that closely replicates the natural pore architecture required for deep physiological fluid flow [80]. High porous interconnectivity fundamentally guarantees the unhindered diffusion of oxygen and essential nutrients into the deepest regions of the implant, whilst simultaneously facilitating the efficient removal of metabolic waste products [73, 79]. Such an environment is paramount for promoting cellular adhesion, uninhibited migration, and the rapid vascularisation of the newly forming tissue [72]. Furthermore, in the context of temporary biodegradable implants, this continuous permeability ensures uniform exposure to physiological fluids, providing a highly predictable and regulated biodegradation profile as the scaffold is progressively replaced by natural bone [66, 67].

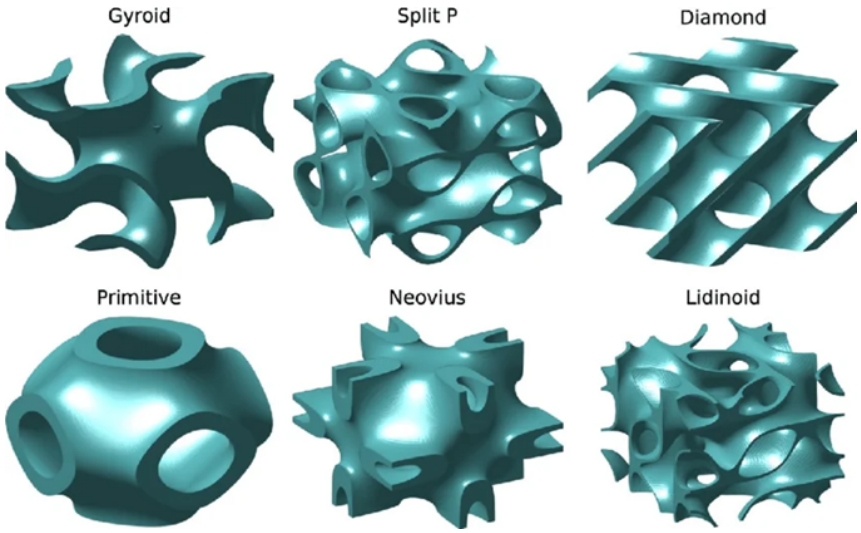



Figure 2.7: Representative TPMS unit cell geometries used in scaffold design: Gyroid, Split P, Diamond, Primitive, Neovius, and Lidinoid. Adapted from [81].

The mechanical properties of TPMS structures can be precisely engineered to cover the complete spectrum of mechanical responses exhibited by natural trabecular bone, thereby preventing deleterious stress shielding phenomena [17, 82]. Notably, several prominent TPMS geometries, including the Gyroid and Diamond surfaces, inherently exhibit bending-dominated deformation behaviour under compressive loading, a characteristic that further reinforces their biomechanical suitability for bone scaffold applications [83, 84]. Moreover, the structural stiffness and yield strength of these architectures are highly tunable through the systematic variation of relative density and sheet thickness, such that the effective elastic modulus can be tuned to match the local mechanical demands of the host tissue, ensuring simultaneous load-bearing capacity and biomechanical compatibility [72, 73].

Ultimately, the specific TPMS geometry selected for a given biomedical application must be strictly informed by the targeted functional requirements of the implantation site, as each topology presents a distinct combination of mechanical, transport, and biological properties [74, 85].

### 2.3.3 Voronoi Lattice Structures

In contrast to the strictly periodic topology of TPMS architectures, Voronoi-based lattice structures introduce a controlled stochastic geometry that more closely emulates the complex, irregular, and anisotropic morphology of natural trabecular bone [13–15]. Voronoi tessellation is mathematically defined as a spatial partitioning algorithm that divides a given Euclidean space into distinct, non-overlapping polyhedral regions based on their proximity to a predefined set of spatial coordinates, known as seed points [86]. In a three-dimensional domain, each generated Voronoi cell encapsulates all spatial coordinates that are strictly closer to its corresponding central seed point

than to any other seed in the designated set [87, 88]. Consequently, the resulting cellular geometry, encompassing the precise volume, interconnectivity, and topological shape of the individual polyhedrons, is inherently governed by the specific spatial distribution and density of these seed points [89]. This mathematical approach enables the generation of highly complex, open cellular networks that share profound topological similarities with natural biological formations [90]. While standard regular lattice arrays rely on repeating unit cells that inherently fail to capture this natural structural variability, Voronoi architectures successfully replicate the complex, heterogeneous pore distributions native to human trabecular bone microenvironments [15]. Emulating this natural trabecular architecture profoundly enhances biomechanical compatibility, as the irregular pore morphology provides a physiologically realistic structural foundation that facilitates superior cell adhesion, promotes unhindered osteoblast migration, and stimulates healthy tissue differentiation [91].

The macroscopic and microscopic architecture of these biomimetic Voronoi scaffolds is meticulously controlled through key geometrical parameters, predominantly the seed point density, the spatial distribution strategy, and the selected strut diameter, as conceptually illustrated in Figure 2.8 [89]. The deliberate manipulation of these parameters directly dictates the resultant macroscopic porosity and equivalent average pore size of the scaffold [87]. For instance, an increase in the number of seed points within a fixed volumetric domain generates a denser network of smaller Voronoi cells, which subsequently reduces the overall pore dimensions [14]. Furthermore, maintaining a constant spatial seed distribution while increasing the interconnecting strut thickness inevitably increases the relative density of the entire structure, resulting in a proportional decrease in both the interconnecting pore size and the global porosity [92]. This rigorous parametric tunability critically distinguishes Voronoi structures from conventional open-cell stochastic foams [2]. While traditional foams are characterised by uncontrolled randomness and extreme structural heterogeneity that pose significant challenges for predicting and replicating mechanical behaviour, Voronoi lattices are engineered such that their apparent irregularity is fully parametrically controllable [88]. This precise mathematical control ensures that the structural disorder can be systematically tuned to meet specific biomechanical targets without relying on unpredictable stochastic foaming processes [89].

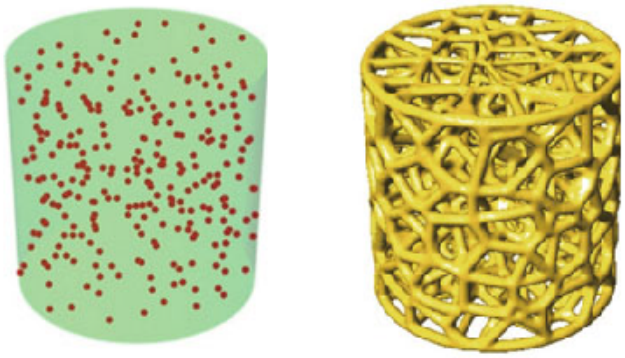


Figure 2.8: Illustration of the Voronoi scaffold generation process: (left) random seed point distribution within a cylindrical domain and (right) the resulting three-dimensional open-cell Voronoi lattice structure. Adapted from [87].

Under compressive loading, the mechanical performance of Voronoi scaffolds is fundamentally influenced by their inherent stochasticity, leading to distinct deformation mechanisms when compared to conventional strut-based or TPMS architectures [90]. Empirical and finite element evaluations demonstrate that standard, unoptimised irregular Voronoi structures generally exhibit lower ultimate compressive strength and a reduced effective elastic modulus compared to perfectly periodic designs, at equivalent porosity levels [92, 93]. Periodic architectures efficiently transfer macroscopic loads through symmetrical node-to-node connectivity, whereas random Voronoi cells often experience localised bending-dominated deformation that compromises peak strength [57]. Nevertheless, the stochastic nature of Voronoi lattices allows them to distribute compressive loads through multiple unaligned pathways, which significantly enhances energy absorption and toughness compared to conventional periodic lattices [88]. This irregular geometric arrangement suppresses premature localised buckling and promotes a stable, progressive collapse mechanism, rather than the abrupt, catastrophic failure frequently observed in uniform, rigid periodic structures [88].

Beyond mechanical stability, the stochastic geometry of Voronoi structures creates a highly interconnected, labyrinthine network of internal pore channels that critically influences the fluid permeability and mass transport capabilities of the scaffold [89]. In contrast to regular periodic architectures, which typically display a uniform and gradually increasing fluid velocity distribution, the flow of physiological fluids through the irregular internal pores of a Voronoi scaffold exhibits a highly disordered and tortuous distribution [94]. This geometrical irregularity significantly increases the frictional contact between the fluid and the irregular strut walls, which effectively reduces the overall fluid velocity and causes a corresponding pressure drop [87]. These reduced flow velocities are highly advantageous for biological mass transport, as they grant migrating cells sufficient time to adhere to the scaffold surfaces while simultaneously preventing high-shear stress damage [14]. As a consequence, the broad, tunable permeability range generated by this stochastic labyrinthine network closely matches that of natural cancellous bone, ensuring an advantageous

environment for tissue ingrowth than to highly ordered periodic architectures [94].

## 2.4 Graded Lattice Structures

Whilst strut-based, TPMS, and Voronoi-based architectures are conventionally designed as uniform structures with a single configuration replicated consistently throughout the implant volume, an alternative strategy has gained increasing attention in the literature: the deliberate spatial gradation of architectural parameters across the implant domain [94]. In functionally graded lattice structures, properties such as relative density, strut thickness, pore size, or unit cell geometry are systematically varied from region to region, rather than held constant [95, 96]. The motivation for this approach is rooted in the anatomy of natural long bones, which transition continuously from a dense, stiff cortical shell at the periphery to a highly porous, compliant trabecular core in the interior [97], as illustrated in Figure 2.9. By mimicking this heterogeneous morphology, designers can create implants that more closely replicate the spatial biomechanical gradients of the targeted host tissue [87].

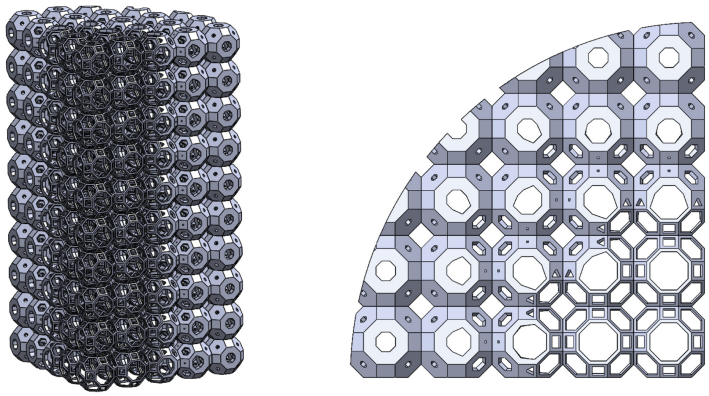


Figure 2.9: Functionally graded lattice structure for biodegradable bone implants based on strut-based lattice structures. Adapted from [97].

At the denser exterior, the graded structure provides a mechanically stiff interface that distributes applied loads compatibly with the surrounding cortical bone, reducing the risk of stress shielding-induced resorption and premature implant loosening [98]. Towards the interior, the progressive increase in porosity maintains an open, interconnected pore network that sustains nutrient diffusion, cellular infiltration, and vascularisation of the regenerating tissue [17]. These two objectives, more specifically, mechanical compatibility and biological permeability, are thus addressed simultaneously within a single continuous architecture, rather than representing competing design constraints.

Importantly, this gradation strategy is not tied to any particular scaffold topology. Its applicability has been demonstrated across strut-based periodic networks, TPMS surfaces, and stochastic

Voronoi architectures, confirming its role as a transversal design framework applicable to the full spectrum of architected cellular materials[13, 92, 99].

## 2.5 Additive Manufacturing of Metallic Scaffolds

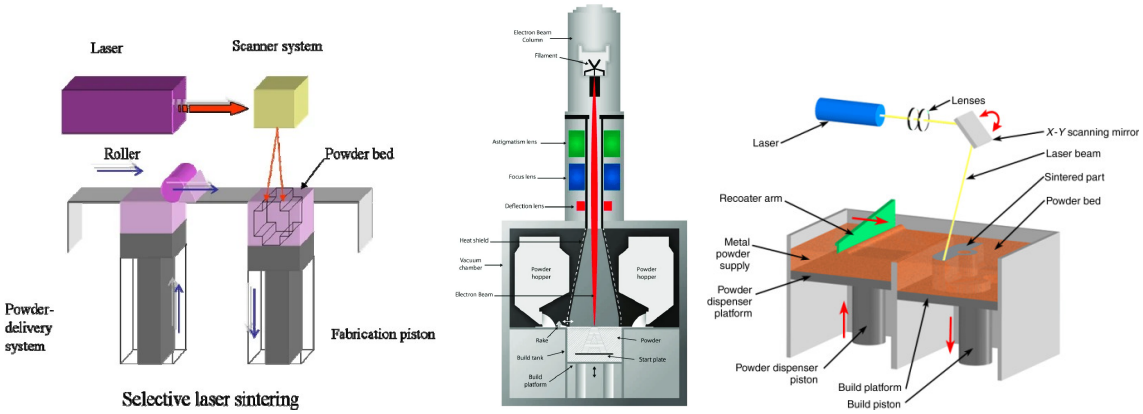
### 2.5.1 Manufacturing Processes of Complex Architectures

The advent of Additive Manufacturing (AM) has emerged as the enabling technology that renders the fabrication of complex, architected bone implants practically feasible [2]. As discussed previously, traditional manufacturing techniques, including subtractive machining, investment casting, and conventional powder metallurgy, fall short in their capacity to produce intricate, patient-specific internal geometries with the required level of architectural control. These processes lack the capability to accurately reproduce highly interconnected pore networks and internal undercuts without tool interference or mould removal constraints [9]. AM addresses these limitations by building components in a layer-by-layer fashion, enabling the direct fabrication of customised geometries with high precision and material efficiency, allowing designers to physically replicate complex anatomical structures that are unreachable through conventional processes [12].

Within the biomedical literature, several AM techniques, schematically represented in Figure 2.10, have been explored for fabricating cellular metallic scaffolds, including Selective Laser Sintering (SLS), Electron Beam Melting (EBM) and Selective Laser Melting (SLM), also widely referred to as Laser Powder Bed Fusion (L-PBF) [2]. Each presents distinct trade-offs in dimensional accuracy, surface finish, mechanical performance, and material versatility. SLS relies on thermal sintering without full melting, often resulting in residual micro-porosity and reduced mechanical strength [12]. EBM processes reactive metals effectively within a vacuum environment but yields a rougher surface finish and larger minimum feature sizes compared to laser-based systems [52]. SLM/L-PBF, by contrast, uses a focused laser to completely melt and solidify metallic powder, producing near-full density components with superior mechanical properties and surface quality. As a result, SLM/L-PBF has become the most widely adopted technique for manufacturing periodic and stochastic cellular metallic implants [2, 9].

Table 2.4 summarises these three techniques in terms of energy source, processing atmosphere, and reported surface roughness, providing a compact basis for comparison.

The operating principle of SLM/L-PBF relies on the selective, layer-by-layer consolidation of a metallic powder bed by a high-energy laser beam, guided by cross-sectional slices derived from a Computer-Aided Design (CAD) file [12]. A recoating mechanism distributes successive layers of metal powder across the build platform, maintained within an inert atmosphere; the laser selectively melts the designated areas before the platform descends to accommodate the next layer [9]. For scaffold fabrication, this process is particularly advantageous in that it offers fine




(a) SLS (b) EBM (c) SLM/L-PBF

Figure 2.10: Schematic representation of additive manufacturing techniques explored for metallic scaffold fabrication: (a) SLS [100], (b) EBM [101], and (c) SLM/L-PBF [102]. Adapted from the respective sources.

Table 2.4: Comparison of additive manufacturing techniques in terms of energy source, atmosphere, and surface roughness [9, 12, 52, 98, 101, 103].

| **Technique** | **Energy source** | **Atmosphere** | **Surface roughness** |
|---|---|---|---|
| SLS | Laser (partial sintering) | Inert gas | Rough, layered surface with residual micro-porosity; typically requires post-processing to meet implant surface requirements |
| EBM | Electron beam | High vacuum | Rougher surface finish than laser-based systems, with gas porosity and partially sintered powder particles |
| SLM/L-PBF | Laser (full melting) | Inert gas (Ar or $N_2$) | Near-full density with better surface quality than SLS/EBM, though roughness and pores of 5–300 $\mu$m are still reported on strut surfaces |

control over strut thickness, pore size, and internal topology, with adjustable process parameters enabling calibration of achievable porosity and structural fidelity [2].

### 2.5.2 Support Structures in L-PBF

The fabrication of a part by L-PBF typically relies on an auxiliary structure that is rarely part of the final design intent, the support. Its main functions are to anchor the part to the build platform and to act as the primary conduit for heat extraction, drawing thermal energy away from the melt pool [104, 105]. This thermal role is critical, since the steep temperature gradients inherent to the layer-by-layer process generate significant residual stresses which, if unsupported, can cause distortion or detachment of the part during the build [105, 106]. Supports are therefore considered an essential requirement of the process, regardless of the geometry being produced [107, 108].

Despite their functional necessity, support structures are not part of the intended component and must be removed once fabrication is complete, adding material consumption, build time, and post-processing effort to the manufacturing chain [105, 107]. This constraint becomes particularly restrictive in the fabrication of architected cellular materials. Unlike a bulk or thin-walled component, whose external surfaces form a continuous solid boundary that can be reliably anchored and, if necessary, locally supported, an open cellular architecture presents an outer surface composed by interconnected voids. This discontinuity removes the very feature that conventional support structures rely upon, namely a continuous surface capable of sustaining the anchoring load and conducting heat efficiently towards the platform [105]. As a result, generating supports directly against a porous lattice surface, or removing them once printing is complete, is markedly more difficult than for solid geometries. Therefore, for biodegradable implants intended for biomedical applications in particular, it is required that no support material or residue remain trapped within the internal architecture, since any retained metallic debris would be indistinguishable from the functional structure and could compromise both the intended porosity and the biological response of the implant [106].

### 2.5.3 Biodegradable Metallic Materials

Three main families of biodegradable metals have been explored in the literature for the development of temporary orthopaedic implants: magnesium (Mg), zinc (Zn), and iron (Fe) alloys [9, 109], where each one exhibits distinct degradation behaviours and mechanical properties [9, 109]. On one hand, magnesium possesses adequate mechanical properties to mitigate stress shielding, although it degrades excessively rapidly in physiological environments, leading to non-uniform corrosion and the undesirable accumulation of hydrogen gas [66, 110]. On the other hand, zinc offers an intermediate corrosion rate between iron and magnesium, does not generate hydrogen gas, and yields biocompatible degradation products; nonetheless, its mechanical strength is insufficient

for load-bearing applications without further alloy optimisation [9, 111]. Finally, iron-based biomaterials, by contrast, demonstrate a high elastic modulus, strength, and ductility, making them well-suited for structural load-bearing functions, though their primary disadvantage is a considerably slow degradation rate [8].

Therefore, the selection of iron-based materials for load-bearing scaffold applications is supported by three main arguments. First, pure iron and its alloys exhibit mechanical properties superior to magnesium and comparable to non-degradable metals such as titanium alloys and 316L stainless steel [66, 67]. Second, iron possesses well-established biocompatibility, as it is an essential element involved in vital biochemical processes within the human body [9], supported by in vitro assays that confirm the absence of acute cytotoxicity and acceptable cell viability levels, provided that iron ion concentrations remain below physiological tolerance limits of 0.075 mg/mL [66]. Lastly, processing iron into porous architectures leads to an intricate, interconnected pore network with high surface area which substantially increases contact with biological fluids, accelerating the corrosion rate relative to bulk material [9, 10].

Despite these advantages, the degradation rate of iron in bulk form remains too slow for clinical relevance, preventing the implant from resorbing at a pace compatible with the natural bone healing process [9, 66]. The introduction of porosity via SLM/L-PBF partially addresses this constraint, as the increased surface area exposure accelerates corrosion kinetics [11]. However, risks of localised corrosion and long-term cytotoxicity nonetheless remain as open challenges, requiring that degradation product accumulation be kept within biologically tolerable limits [112]. Iron thus emerges as the most suitable candidate among biodegradable metals for load-bearing scaffold applications, combining adequate mechanical performance, established biocompatibility, and the capacity to modulate degradation through architectural design [9, 66].

Chapter 3

# Design and Additive Manufacturing

Based on what was discussed previously, the design of a load-bearing biodegradable scaffold is, fundamentally, a problem of geometry. The implant should exhibit a stiffness comparable to that of the bone it replaces, so as not to shield the surrounding tissue from the mechanical loading required to maintain its integrity, while at the same time presenting an open and interconnected porosity, both to enable bone ingrowth and to ensure a uniform, predictable corrosion front. A dense metallic implant cannot satisfy these two requirements at once. Architected cellular materials resolve the conflict, since their apparent stiffness is governed by the internal geometry and may therefore be reduced in a prescribed and reproducible manner, largely independently of the constituent material.

The present chapter addresses this design problem for the specimens employed throughout the work. Two cellular architectures were investigated, a stochastic Voronoi lattice and an ordered gyroid drawn from the TPMS family. Generating both within a single framework, with the same domain, the same parametric ranges, and the same morphological characterisation, ensures that the two architectures are produced and characterised on a fully consistent basis.

Both architectures were generated by means of an open-source computational framework implemented in Python, an approach adopted to keep the entire design pipeline transparent, modifiable, and fully reproducible. Within this framework, a parametric study was carried out for each family, in which, beginning from the respective generation procedure, the governing design parameters were varied systematically across a broad range, producing an extensive population of structures that spans the geometric space accessible to each architecture. Each structure was then characterised through four morphological descriptors, namely relative density (and hence porosity), surface area, pore size, and the characteristic thickness of the solid phase, which together describe the resulting morphology and are all relevant to the design. By relating these descriptors to the parameters that generated them, the study established the correspondence between design input and resulting morphology, thereby quantifying how the geometry of each family responds to its controlling variables. It is this correspondence that renders the structures controllable by design rather than the outcome of arbitrary parameter choices, and it furnished the rational basis on which a representative subset was identified. From the resulting populations, nine structures were retained from each family, providing a final set of eighteen specimens.

All structures were defined within the same overall dimensions, corresponding to a cylinder of 10 mm in diameter and 15 mm in height. Both the cylindrical form and these dimensions follow the recommendations of ISO 13314, the reference standard for the compression testing of porous and cellular metals, which prescribes a cylindrical geometry with a minimum characteristic dimension of 10 mm and a height-to-diameter ratio between one and two [113]. The proportions adopted here lead to a ratio of 1.5, well within this interval and consistent with the specimen geometries commonly employed for additively manufactured cellular metals [114]. The cylindrical form is, in addition, well suited to an axially loaded specimen, as it preserves the axial symmetry of both the applied load and the finite element model. Although these standards refer to physical

compression testing, which was not performed in this work, adopting the geometry they prescribe remains justified as a design reference, since it ensures that the specimens conform to the idealised conditions those standards define. This consideration is all the more pertinent given that the compressive behaviour was reproduced numerically, so that the analysis operates on a configuration already accepted as representative for the mechanical characterisation of cellular metals.

## 3.1 Generation of the Voronoi Structures

Among the architected geometries reviewed in Chapter 2, the Voronoi tessellation was selected for this work because it most closely reproduces the irregular, anisotropic morphology of trabecular bone, a resemblance that regular lattices, built from a single repeating unit cell, cannot offer by construction. Unlike the uncontrolled stochastic foams historically used to introduce porosity into metallic implants, however, a Voronoi tessellation derives its geometry entirely from the positions of a finite set of seed points, so that its apparent disorder remains open to precise parametric control rather than being left to chance. It is this combination, an irregularity that mimics the target tissue together with a geometry that stays fully governed by the seed arrangement, that motivated its adoption here, and that the remainder of this section exploits directly.

The routine that generated the Voronoi lattices was developed with an aim broader than the specimens this work required. Although only cylindrical specimens fell within its scope, the routine was conceived as a general tool, able to fill an arbitrary target geometry rather than a single predefined shape. This adaptability was a deliberate goal rather than a by-product, and it follows from the way the lattice is built, since the structure is generated within a bounding box larger than the target and only afterwards trimmed to its boundary, so that any surface supplied as an Standard Triangle Language (STL) model can be carved from the same underlying network. The routine is, in addition, fully open, implemented without recourse to closed commercial software, which keeps every stage transparent and modifiable.

As shown in Figure 3.1, the procedure links the definition of the generative parameters to the extraction of the morphological descriptors of the designed specimen.

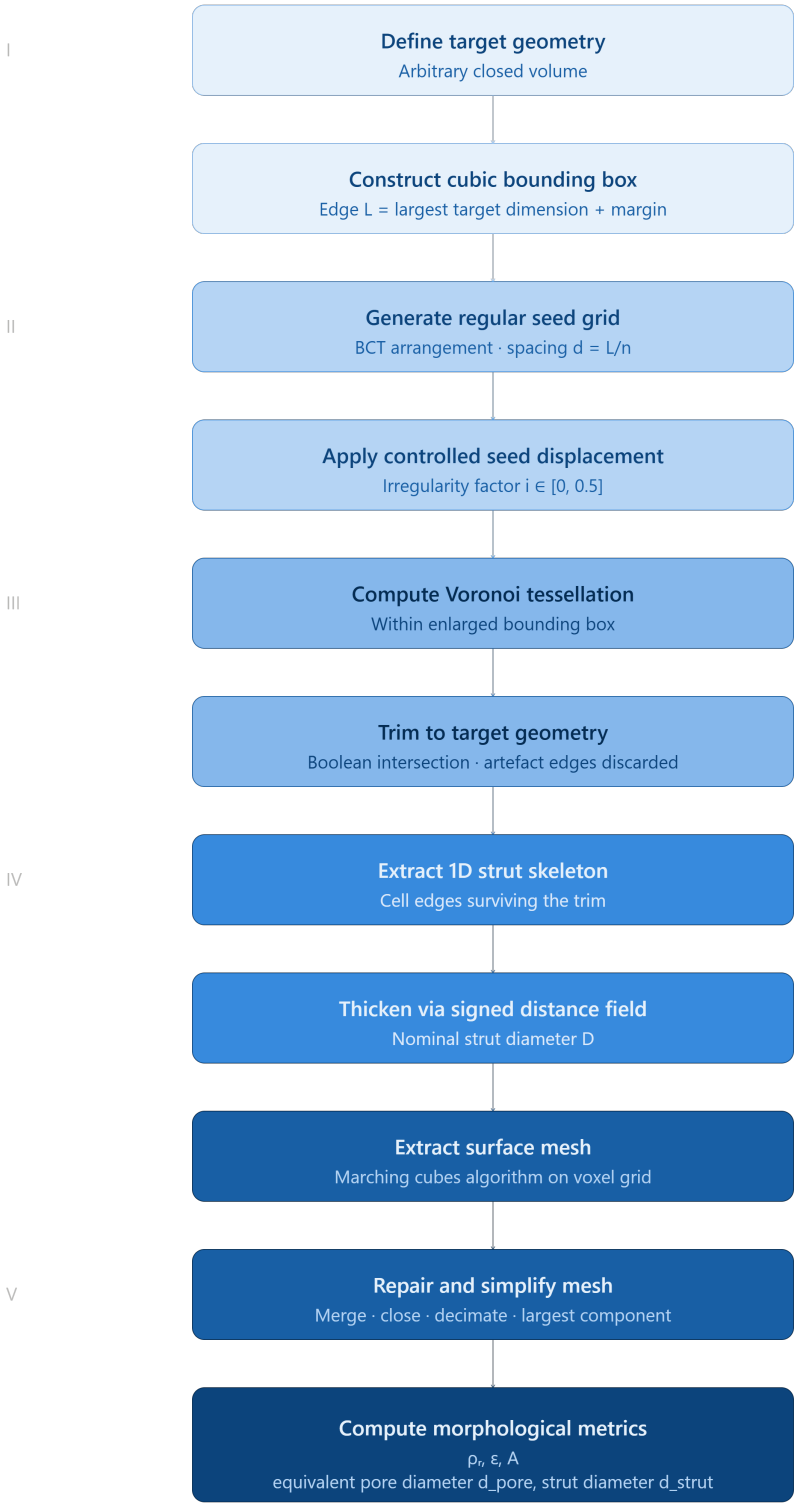



Figure 3.1: Flowchart of the Voronoi generation pipeline, from the seeding of the domain through to the morphological characterisation of the final mesh.

Every structure begins from the region in which its seed points are placed. That region is not the target geometry itself but a cubic bounding box enclosing it, its edge taken as the largest dimension of the target increased by a fixed margin. The procedure carries no units of its own and operates in whatever unit the target is supplied in; in the present work, the geometry being defined in millimetres, the margin was set to five. For the cylinder studied here, ten millimetres in diameter and fifteen in height, the largest dimension is the height, so the box becomes a cube of twenty millimetres along each edge, as illustreted in Figure 3.2. Fixing all three edges from a single dimension leaves an uneven amount of room around the part. Along the axis the clearance is 2.5 mm at each end, whereas the diameter, being the smaller dimension, sits within a wider radial gap of five millimetres. This asymmetry is no more than the consequence of fitting a cube to the largest extent of the part, and it bears no weight on the method, which requires only that every boundary cell have space to close before it is trimmed, a condition the margin satisfies on all sides.

Two considerations recommend seeding a region wider than the piece itself. The first is the integrity of the boundary, since the cells lying on the outer surface are formed by cutting the tessellation along it, and a cell can be cut cleanly only once it has grown complete. Had the seeds been confined to the cylinder, the cells against its wall would have been left open or misshapen. Seeding them across a wider volume lets each one close before the trim, so the boundary keeps the irregular character of the interior. The second consideration is generality, for the box follows from nothing more than the outer dimensions of the target and a margin, so the same procedure applies unchanged to any shape whose extent is known. A geometry as involved as a patient-specific implant could be filled by exactly the procedure described here, the cylinder being merely the case this work required.

The arrangement of these seeds within the box governs the whole structure, since the Voronoi tessellation is determined significantly by their positions. The most immediate option is to scatter a set number of points at random through the volume. However, random distribution offers no control over where those points finally come to rest. It lets them gather in some regions while leaving others sparsely filled, so the Voronoi cells inherit this unevenness as pronounced asymmetries between dense and sparse zones, as illustrated in Figure 3.3. Such uncontrolled variation moves the resulting architecture away from that of trabecular bone, which, though itself irregular, stays broadly uniform throughout rather than breaking into pronounced clusters and voids. The difficulty runs deeper than appearance, for the very randomness that makes a purely stochastic lattice attractive is also what renders it hard to control and to optimise, a limitation explicitly recognised for stochastic designs of this kind [88]. Introducing disorder in a controlled manner provides a more reliable route to a bone-like architecture than leaving the distribution of points entirely to chance.

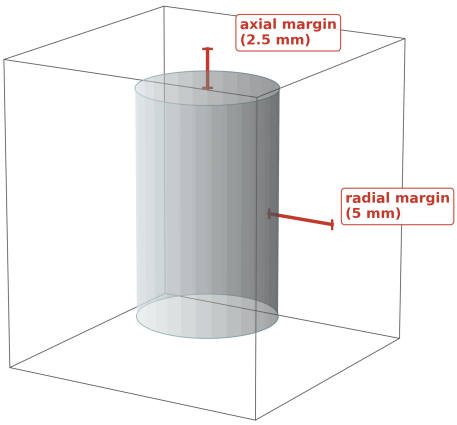



Figure 3.2: Cubic bounding box enclosing the cylindrical specimen used in this work. The box edge is the largest target dimension, here the 15 mm height, increased by a 5 mm margin, which gives a 20 mm cube. The resulting clearance is 2.5 mm at each end of the cylinder and 5 mm around its radius, the asymmetry arising from sizing the cube to the largest dimension alone.

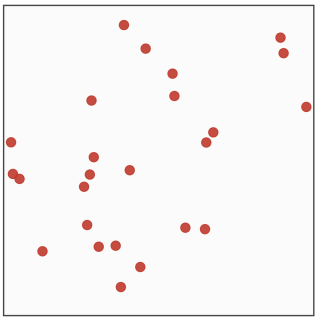


Figure 3.3: Top view of the seeding domain with seed points placed at random. The points gather in some regions and leave others empty, the unevenness that the controlled-irregularity scheme is introduced to avoid.

To bring the tessellation under control, the seeds are not scattered freely but placed on a regular grid and then displaced by a limited amount, a controlled-irregularity scheme established for bone-mimicking Voronoi scaffolds by Du et al. [115]. The scale of the cells is governed by a single quantity, the spacing $d$ between neighbouring grid points, marked on the front views of Figure 3.5, the physical length that decides how large the cells grow and, together with the strut diameter, how dense the structure becomes. It is therefore through $d$ that the morphology is ultimately controlled. Because the seeds start from a regular arrangement, the cells remain evenly spread throughout the volume even once the disorder is introduced, lending the global uniformity that random seeding cannot provide.

The grid may be built in more than one form, and the one chosen here departs from the original method. Where Du et al. lay the seeds on a Simple Cubic (SC) lattice, the present work staggers alternate layers by half the in-plane spacing, the difference resting on how successive layers are stacked, as shown in Figure 3.4. A SC grid sets each layer squarely above the last, so the seeds settle into continuous flat planes that thread the whole structure. Such aligned planes, known as cleavage planes, are a recognised frailty, offering straight surfaces along which the lattice can shear under load. Offsetting every second layer by half a spacing breaks that alignment: no plane of the grid runs uninterrupted from one face of the domain to the other, whatever the vertical spacing between layers happens to be, since it is the lateral offset alone that displaces the columns. This staggering is what defines a body-centred arrangement, as opposed to a simple one, and it is specifically this body-centred character, rather than the cubic symmetry accompanying it in the classical case, that carries the further advantage documented in the literature: the Voronoi cell of a BCC lattice is the near-spherical, Kelvin-type truncated octahedron, and the tessellation it generates remains topologically stable under perturbation, unlike that of the simple cubic lattice, which degenerates under any finite disturbance of its sites [116, 117].

Both of these properties, the removal of cleavage planes and the near-spherical cell shape, depend only on the arrangement of the seeds relative to one another, not on the absolute scale of the grid. That scale, the previously mentioned variable $d$, is set independently. It follows from a regular cubic grid, defined by populating each edge of the cubic bounding box, of side $L$, with $n$ seed points along every axis, so that the spacing between neighbouring points is given by the following Equation 3.1 and illustrated in Figure 3.4.

$$d = \frac{L}{n} \tag{3.1}$$

Each of the $n$ points along an edge is placed at the centre of its own cell of width $d$, so that the first and last points are set back by $d/2$ from the corresponding faces of the bounding box rather than coinciding with them. This regular grid is the starting point common to both topologies considered here; the SC lattice is obtained directly from it, whereas the body-centred grid is obtained by displacing every second layer of this same regular arrangement, as described above.

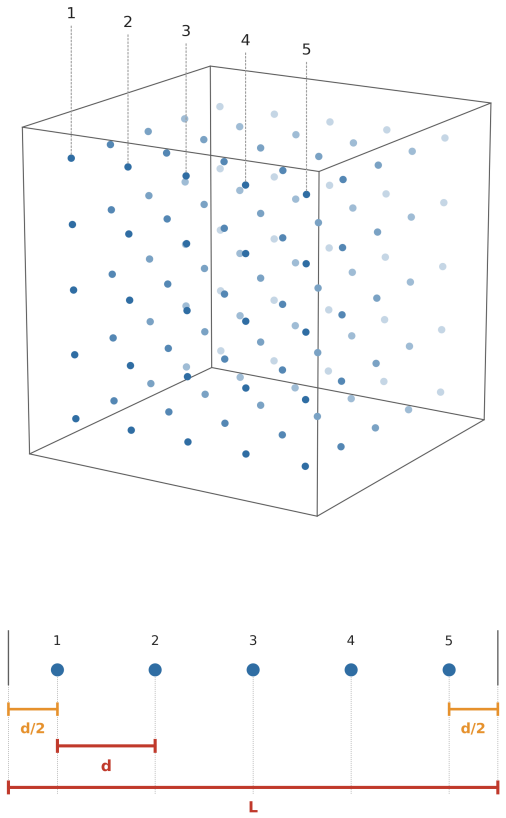



Figure 3.4: Derivation of the grid spacing $d$ from the box edge $L$ and the point count $n$ (here $n = 5$, for illustration). The regular grid populates each edge of the cubic bounding box with $n$ points, each centred on its own cell of width $d = L/n$; the first and last points are consequently set back by $d/2$ from the corresponding faces of the box, rather than coinciding with them.

In the present implementation, the layers were spaced vertically by this same distance $d$, rather than by half of it as a strictly BCC arrangement would require; the seed grid is consequently an elongated, Body-Centred Tetragonal (BCT) arrangement, stretched along the build axis by a factor of two relative to the BCC case. This departure was made deliberately. Keeping the vertical spacing equal to $d$ lets $n$ retain the meaning fixed for the regular grid, the number of points along each edge, while also matching the number of layers stacked along the build axis: with $n$ layers spaced by $d$, the vertical count coincides with the in-plane one inherited from the base grid. Spacing the layers by $d/2$ instead, as a strictly BCC arrangement would require, would break this correspondence: the vertical layer count would no longer match the number of points fixed by $n$ on the regular grid, and $n$ would cease to describe the structure consistently.

The removal of cleavage planes, discussed above, follows from the lateral offset alone and is therefore unaffected by this choice. What is no longer guaranteed is the near-perfect sphericity of the Voronoi cell reported for the cubic body-centred lattice [116]; the primary objective motivating the staggered arrangement, the elimination of through-going planes, is nonetheless achieved regardless of the vertical spacing adopted.

This displacement in consecutive layers, visible in Figure 3.5, has a direct consequence for how many seeds the grid contains, since $n$ no longer cubes as simply as it does for the regular grid. The two grids share the same $n$ layer heights along the build axis; what changes between them is the in-plane arrangement of alternate layers. Layers of even index are left exactly as in the regular grid, each an $n \times n$ array set back by $d/2$ from the walls. Layers of odd index are instead built over a narrower range, set back by $d$ rather than $d/2$ and holding $n-1$ rather than $n$ points along each in-plane axis. This narrower layer can be understood as the regular one displaced by $d/2$: the point that sat $d/2$ inside a wall would then coincide with the wall itself, and is consequently absent, with no seed placed at the opposite wall in its stead. An offset layer therefore holds $(n-1)^2$ points against the $n^2$ of a full one.

Since the first layer is always of even index, and full and offset layers alternate from it, a grid of $n$ layers comprises $\lceil n/2 \rceil$ full layers and $\lfloor n/2 \rfloor$ offset ones. The seed count for each grid follows directly:

$$N_{\mathrm{SC}} = n^3, \qquad N_{\mathrm{BCT}} = \left\lceil \frac{n}{2} \right\rceil n^2 + \left\lfloor \frac{n}{2} \right\rfloor (n-1)^2 \tag{3.2}$$

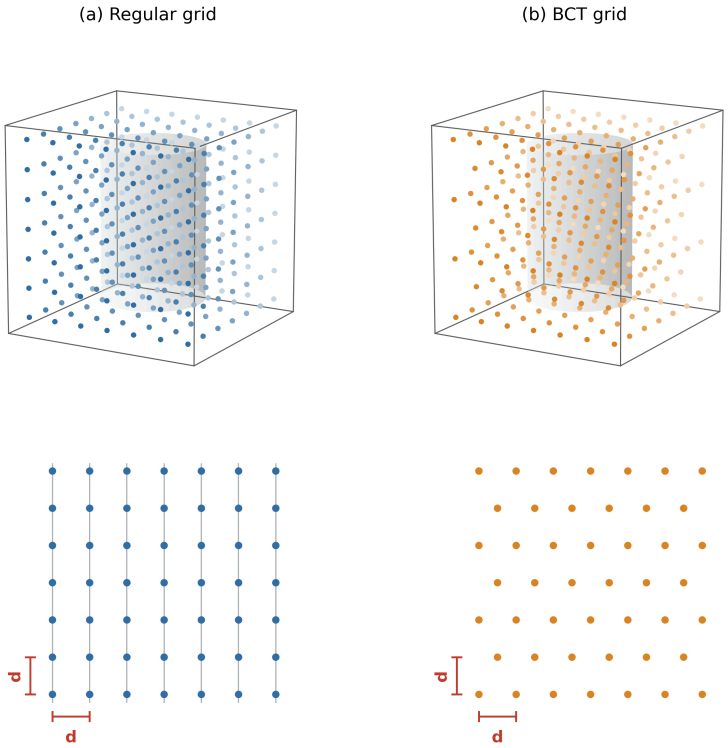



Figure 3.5: SC (a) and BCT (b) seed grids, shown within the box enclosing the cylindrical domain of this work (top) with the corresponding front views beneath, on which the grid spacing $d$ is marked. In the simple cubic grid each layer sits directly above the last, forming the continuous aligned columns that act as cleavage planes; in the body-centred grid alternate layers are offset by half a cell, staggering the columns and breaking up those planes.

Once these positions are fixed, each seed is displaced by a random amount to introduce the controlled irregularity motivating the whole scheme. The magnitude of this displacement is set by a single dimensionless quantity, the irregularity factor $i$, through

$$r = i \times d \tag{3.3}$$

so that $r$ scales with the same spacing $d$ that governs the grid itself, letting the amount of disorder be compared independently of the absolute size of the structure. The displacement is drawn independently along each of the three axes, from a uniform distribution over $[-r, r]$, and added to the seed's regular position. This draw is generated using a pseudo-random number generator, whose output sequence is fully determined by an integer parameter $S$, the random seed. Fixing $S$ guarantees reproducibility, since the same value of $S$ always produces the same sequence of per-site displacements, and therefore the same tessellation, whereas a different value produces a different, but statistically equivalent, realisation of the same controlled-irregularity scheme. The irregularity factor $i$ and the random seed $S$ thus play distinct roles, with $i$ setting the magnitude of the disorder while $S$ selects a particular instance of it.

The region within which a seed may come to rest is therefore a cube of edge $2r$ centred on that position, as shown in Figure 3.6. Setting $i = 0$ recovers the unperturbed grid exactly, and as $i$ increases, the seeds depart further from their regular positions, with the resulting cells departing correspondingly further from the ordered lattice described above.

For this displacement to remain meaningful, the cube within which a seed may move must not overlap the equivalent cube of a neighbouring seed, since doing so would let two seeds cross paths and undermine the very notion of a regular starting position. As neighbouring seeds are spaced a distance $d$ apart, this condition requires $2r \leq d$, or equivalently, from Equation 3.3, $i \leq 0.5$. The irregularity factor is therefore restricted to the range $i \in [0, 0.5]$, with $i = 0.5$ corresponding to the largest perturbation cube that still touches, without overlapping, those of its immediate neighbours.

Unlike the purely random distribution described in Figure 3.3, the perturbed grid retains a broadly even coverage of the volume even after displacement, striking the expected balance between order and disorder.

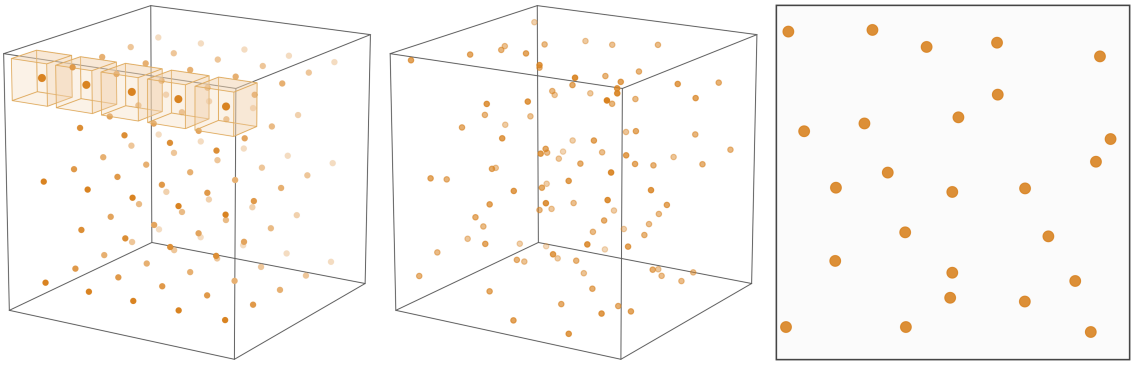


Figure 3.6: Illustration of the seed displacement scheme. Perturbation cubes of edge $2r$ around the front-top row of seeds in the regular grid ($n = 5$, spacing $d$), the remaining seeds shaded by depth for context; the value of $i$ shown here sits close to the upper bound $i = 0.5$, beyond which neighbouring cubes would begin to overlap (left). The resulting seed distribution once this displacement is applied throughout the volume, obtaining final seeds distribution (centre). Top view of the same distribution (right).

The perturbed seeds generated in the previous step are next used to construct the Voronoi tessellation, which is first formed within the enlarged bounding box and only afterwards intersected with the cylindrical target geometry, as depicted in Figure 3.7.

The intersection itself is not performed against the nominal cylinder but against a reduced one, of radius $R_c = R - D/2$ and height $H_c = H - D$, smaller than the specimen by half the strut diameter on every side. The reduction is deliberate: the skeleton is later thickened by $D/2$ in the distance-field step that follows, and starting from a domain drawn in by that same amount lets the outer surface of the finished struts land exactly on the nominal radius and height of the cylinder, rather than protruding past them. The cut is carried out as a true solid boolean operation, using CadQuery, between this reduced cylinder and a solid built directly from the polyhedral faces the tessellation returns for each cell. Applied uniformly to every candidate cell, this operation yields one of three outcomes depending on the cell's position relative to the cylinder: a cell lying entirely within the reduced cylinder is returned unchanged, one lying entirely outside it vanishes, and one straddling the boundary is clipped to the portion that remains inside.

Cutting a flat-faced polyhedron against a curved surface in this way does not simply trim its existing edges; it also introduces new ones, running wherever a face happens to be sliced by the cylindrical wall. These are not features of the cellular structure but artefacts of the cut itself, and they are readily distinguished from genuine strut edges by two properties held simultaneously: they run vertically, their two endpoints sharing the same $x$ and $y$ coordinates, and they lie exactly at radius $R_c$ from the axis. Edges meeting both conditions are discarded before the skeleton is built.

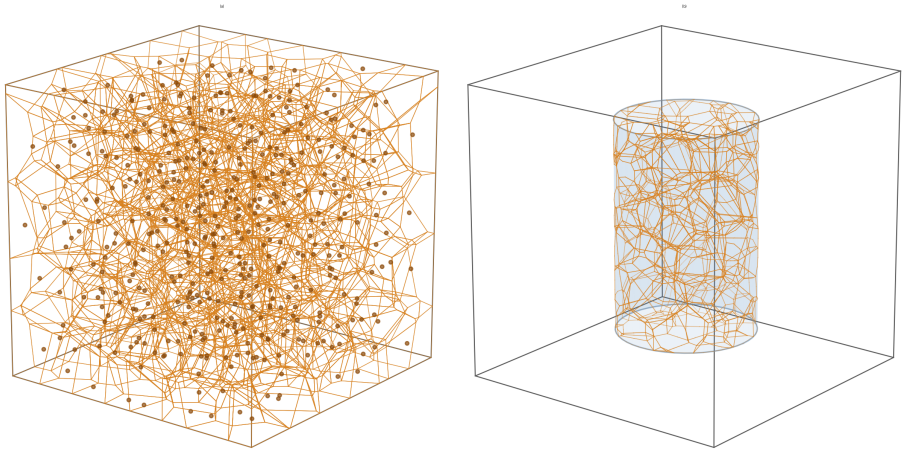


Figure 3.7: Voronoi tessellation of the perturbed seeds, shown here for a reduced seed count for clarity. (a) The tessellation as formed within the enlarged bounding box, before any trimming. (b) The same tessellation after intersection with the reduced cylinder ($R_c = R - D/2$, $H_c = H - D$); no thickness has yet been assigned to the resulting skeleton.

The frame shown on the right-hand side of Figure 3.7 is the skeleton from which the final structure is built, once thickness is assigned to it in the step described next.

This skeleton is not yet a solid, since it consists only of points sampled along the surviving edges. In order to convert it into a set of solid struts, the struts are represented through a signed distance field rather than as a union of independently generated solid segments. This choice avoids a difficulty inherent to the last approach. At nodes where several struts converge, boolean unions of separate solids readily produce overlapping or non-manifold geometry, whereas a distance field has no such notion of separate parts to begin with. Every point in space is instead assigned a single, well-defined distance to the nearest skeleton point, regardless of how many struts happen to meet there.

This distance field is computed over a regular voxel grid spanning the specimen, using a $k$-d tree for efficient nearest-neighbour search. Subtracting half the target strut diameter from the distance places the zero level of the resulting field exactly at $D/2$ from the skeleton centreline, so that the field is negative inside the material and positive outside it. The strut boundary therefore corresponds to wherever this field crosses zero. This field is then combined, through a pointwise maximum, with the signed distance field of the nominal cylinder of radius $R$ and height $H$. It is at this step that the earlier reduction of the cutting cylinder to $R_c = R - D/2$ and $H_c = H - D$ becomes relevant, since the skeleton was already confined within this smaller domain. Thickening it by $D/2$ therefore brings the outer surface of the struts to rest exactly on the nominal boundary, rather than beyond it.

The zero level set of this combined field is subsequently extracted as an explicit triangulated mesh using the marching cubes algorithm, which locates the boundary by interpolating between

adjacent voxels of opposite sign. The resulting mesh is then processed in order to remove common defects before further use. Duplicate vertices are merged, degenerate faces are discarded, and open boundaries are closed, while face orientation is checked for consistency, so that the surface remains free of inverted faces or open edges that would otherwise compromise its use in finite-element analysis or manufacture. Where the face count exceeds the target adopted for these applications, the mesh is further simplified through topology-preserving decimation. Finally, only the largest connected component is retained, and any disconnected fragments arising from local artefacts in the distance field are discarded. The resulting solid, shown in Figure 3.8 for a representative case with $n = 8$, is the specimen geometry used in the mechanical and biodegradation studies that follow.

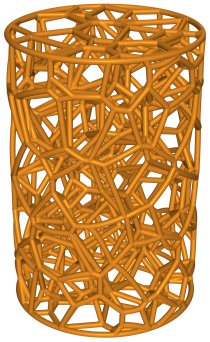


Figure 3.8: Final thickened specimen obtained from the pipeline described above, generated with $n = 8$, $i = 0.4$ and $D = 0.4$ mm.

Once the mesh has been generated, it also provides the basis for the quantitative characterisation of each specimen. The relative density $\rho_r$ and porosity $\varepsilon$ were obtained from the ratio between the enclosed mesh volume $V_{\text{mat}}$ and the total cylindrical volume of the specimen domain $V_{\text{cil}} = \pi R^2 H$, according to Equation 3.4.

$$\rho_r = \frac{V_{\text{mat}}}{V_{\text{cil}}}, \qquad \varepsilon = 1 - \rho_r \tag{3.4}$$

Pore size characterisation in a Voronoi lattice benefits from the discrete nature of the underlying tessellation, since each Voronoi cell corresponds to a well-defined polyhedral region of space. The full geometric volume of every cell, obtained directly from the Voronoi tessellation prior to strut thickening and clipped to the reduced cylindrical domain used for the boolean cut, was recorded independently of the mesh generation step. Each of these cell volumes was subsequently scaled by the specimen-wide porosity fraction $\varepsilon$ to estimate the void volume $V_{\text{pore}}$ nominally associated with that cell, as formalised in Equation 3.5.

$$V_{\text{pore}} = V_{\text{cell}} \cdot \varepsilon \tag{3.5}$$

Nevertheless, to obtain the classical diameter for each pore, the estimated void volume was converted into an equivalent pore diameter under a spherical-void approximation, from which the mean pore diameter and its standard deviation across the cell population were computed for each configuration, providing a measure of both the characteristic pore size and its dispersion within the lattice, as expressed in Equation 3.6.

$$d_{\text{pore}} = 2\sqrt[3]{\frac{3V_{\text{pore}}}{4\pi}} \tag{3.6}$$

As a validation of the input strut thickness parameter, the diameter actually realised in the final mesh was also estimated, exploiting the one-dimensional skeleton extracted during the thickening step described previously. For every vertex of the final mesh, the distance to the nearest point of this skeleton was queried, with measurements restricted to regions along the strut body while excluding nodal junctions, and doubling the mean of these distances produced the realised strut diameter $d_{\text{strut}}$, which was then compared against the nominal target diameter $D$ to assess whether the thickening process reproduces the intended input value, as expressed in Equation 3.7.

$$\text{error} = \frac{d_{\text{strut}} - D}{D} \times 100\% \tag{3.7}$$

Together with the specific surface area of the mesh, these metrics were computed systematically across the full parametric study, reported in Section 3.3.1, and provide the link between the generative parameters and the resulting morphological characteristics of each specimen.

Collectively, the parameters introduced throughout this section define a single, self-consistent pipeline running from the initial seeding domain to the final thickened specimen. Table 3.1 summarises them for reference.

Table 3.1: Summary of the parameters governing the generative pipeline.

| Symbol | Description |
|---|---|
| $R$, $H$ | Nominal radius and height of the target cylinder |
| $L$ | Edge of the cubic bounding box, set from the largest target dimension plus a fixed margin |
| $n$ | Number of seed points along each edge of the regular grid |
| $d$ | Grid spacing, $d = L/n$, setting the distance beetween neighbour seed points |
| $i$ | Irregularity factor, $i \in [0, 0.5]$, scaling the seed displacement relative to $d$ |
| $r$ | Maximum seed displacement, $r = i \times d$ |
| $S$ | Random seed, the integer initialising pseudo-random generator used to ensure reproducibility |
| $D$ | Nominal strut diameter |
| $R_c$, $H_c$ | Reduced cylinder used for the boolean cut, $R_c = R - D/2$, $H_c = H - D$ |
| $N_{\mathrm{SC}}$, $N_{\mathrm{BCT}}$ | Total seed count for the simple cubic and body-centred tetragonal grids, respectively |
| $V_{\mathrm{mat}}$, $V_{\mathrm{cil}}$ | Enclosed mesh volume and total cylindrical volume of the specimen domain |
| $\rho_r$, $\varepsilon$ | Relative density and porosity of the specimen |
| $V_{\mathrm{cell}}$ | Full geometric volume of a Voronoi cell, prior to strut thickening |
| $V_{\mathrm{pore}}$ | Void volume nominally associated with a Voronoi cell, $V_{\mathrm{pore}} = V_{\mathrm{cell}} \cdot \varepsilon$ |
| $d_{\mathrm{pore}}$ | Equivalent pore diameter, under a spherical-void approximation |
| $d_{\mathrm{strut}}$ | Strut diameter actually realised in the final mesh |
| $A$ | Specific surface area of the mesh |

## 3.2 Generation of the Gyroid Structures

TPMS architectures distinguish themselves from conventional strut-based lattices through their smooth, curvature-driven geometry that eliminates discrete nodal junctions, enables a continuous stress distribution throughout the bulk volume, and generates a highly interconnected labyrinthine network of open channels that sustains the permeability and mass transport requirements critical

for osseointegration and biodegradation. This is especially relevant for iron-based biodegradable scaffolds, since corrosion is surface-driven and geometric surface area directly governs degradation kinetics.

Among the members of the TPMS family, the Gyroid was selected for this work on the basis of three converging arguments. As introduced previously, the Gyroid surface is described by the implicit level-set equation

$$\sin\left(\frac{2\pi x}{l}\right)\cos\left(\frac{2\pi y}{l}\right)+\sin\left(\frac{2\pi y}{l}\right)\cos\left(\frac{2\pi z}{l}\right)+\sin\left(\frac{2\pi z}{l}\right)\cos\left(\frac{2\pi x}{l}\right)=C \tag{3.8}$$

where $l$ defines the unit cell size and $C$ is the isovalue constant that governs the resulting relative density. This formulation provides a single, continuously adjustable handle on both wall thickness and porosity without altering the topology of the surface, which is a practical advantage for the parametric study described in the following sections.

Comparative studies have consistently demonstrated that the Gyroid exhibits the highest fluid permeability among the principal TPMS topologies at equivalent porosity across all tested flow rates [49], a characteristic that governs both the delivery of oxygen and nutrients to cells colonising the scaffold interior and the removal of corrosion products from the degrading implant surface. This permeability advantage is accompanied by a favourable mechanical balance within the family. Moreover, stretching-dominated topologies, such as the Primitive surface, favour compressive stiffness but sacrifice permeability and risk stress shielding, while bending-dominated topologies, such as the Diamond surface, favour fluid transport but exhibit a Young's modulus as low as half that of stretching-dominated designs at equivalent density [49]. The Gyroid avoids this trade-off, since its bending-dominated regime provides a mechanical compliance close to trabecular bone, while its larger inter-channel junction area sustains permeability among the highest in the family and makes it particularly suited to graded cellular structures [118].

Beyond the choice of topology, TPMS-based lattices can further be realised in two distinct configurations, skeletal and sheet-based, depending on how the implicit surface is used to partition space into solid and void regions. The Gyroid minimal surface itself is bicontinuous, dividing space into two intertwined labyrinth-like channel networks that are congruent apart from their handedness [13, 119]. In the skeletal variant, one of these two channel networks is filled with solid material, leaving a single open channel. In the sheet-based variant, the surface is instead thickened symmetrically about its mid-plane, keeping both channel networks fully open and interpenetrating [13, 119]. This thickening is achieved by assigning the level-set constant a pair of symmetric bounding values, such that the solid domain is defined by

$$-C \leq f(x,y,z) \leq C \tag{3.9}$$

where $f(x,y,z)$ is the Gyroid implicit function and $C$ is the isovalue constant introduced previously, with the resulting wall thickness increasing monotonically with $C$. This configuration gives the sheet-based Gyroid a higher specific surface area, more homogeneous pore connectivity and greater fluid permeability than the skeletal variant at equivalent relative density. Sheet networks also exhibit higher elastic moduli than skeletal networks [83], with a compressive strength between 1.3 and 2 times greater and correspondingly higher toughness [49]. Their higher surface-area-to-volume ratio, smoother curvature and fully interconnected porosity further make them particularly suited to bone and cartilage regeneration [119]. The sheet-based Gyroid therefore meets the mechanical, degradation and biological requirements of this application simultaneously.

The complete generative pipeline described throughout this section, from the definition of the bounding domain to the extraction of the morphological metrics, is summarised in Figure 3.9 .

The generation of each cylindrical specimen began with the instantiation of the TPMS object within a cuboidal bounding domain of dimensions $2R \times 2R \times H$, where $R = 5.0\,\text{mm}$ and $H = 15.0\,\text{mm}$ correspond respectively to the target radius and height of the cylindrical specimens adopted for this study. This cuboidal domain corresponds to the native spatial format adopted by the TPMS generation tool used in this work, which evaluates the Gyroid implicit function, described in Equation 3.8, over a uniform three-dimensional Cartesian grid [120]. This grid is discretised at a user-defined voxel resolution $\Delta x$, set to $0.02\,\text{mm}$ in the present work, representing a suitable balance between geometric fidelity and computational cost, sufficient to resolve even the thinnest wall configurations. The total number of voxels spanning the domain is therefore given by Equation 3.10, producing a regular orthogonal lattice of sample points at which the implicit function will subsequently be evaluated.

$$N_{\text{voxels}} = \left\lfloor \frac{2R}{\Delta x} \right\rfloor \times \left\lfloor \frac{2R}{\Delta x} \right\rfloor \times \left\lfloor \frac{H}{\Delta x} \right\rfloor \tag{3.10}$$

Figure 3.10 illustrates this discretised rectangular domain, showing the voxel grid that defines the spatial resolution of the generation process.

Once the bounding domain and voxel grid are established, the Gyroid architecture is generated by specifying two independent geometric parameters, the unit cell size $l$ and the level-set constant $C$, already introduced in Equations 3.8 and 3.9. The unit cell size $l$ sets the spatial period of the surface, that is, the physical length over which the Gyroid pattern completes one full cycle in each coordinate direction. This effect is illustrated in Figure 3.11, which compares the three-dimensional structure and the corresponding $xy$ cross-section at $z = 0$ for two unit cell sizes, $l = 5.0\,\text{mm}$ and $l = 3.5\,\text{mm}$. Reducing $l$ from $5.0\,\text{mm}$ to $3.5\,\text{mm}$ compresses the same periodic wave pattern into a shorter spatial interval, so that a greater number of Gyroid periods are fitted within the same bounding domain.

After the parameters definition, the implicit function is evaluated at every node of the voxel




Figure 3.9: Flowchart of the Gyroid generation pipeline, from the definition of the cylindrical domain through to the morphological and hydraulic characterisation of the final mesh.

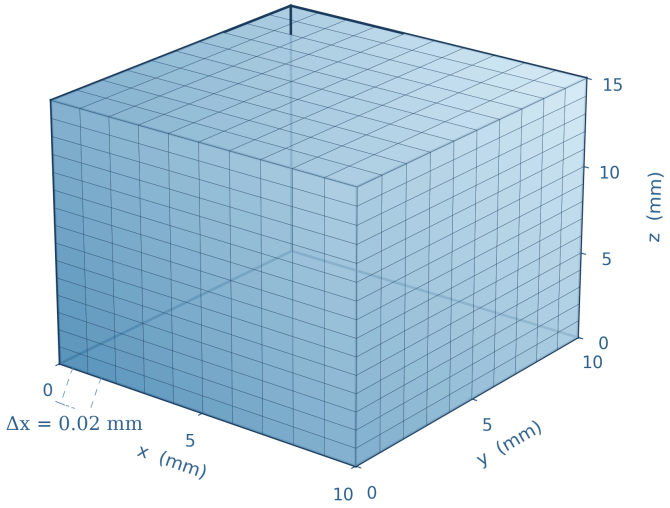



Figure 3.10: Discretised rectangular bounding domain of dimensions $2R \times 2R \times H$, showing the uniform voxel grid at resolution $\Delta x = 0.02$ mm used to evaluate the Gyroid implicit function.

grid, and each node is assigned to the solid or void phase according to the sheet-based rule of Equation 3.9. The level-set constant $C$ is the regulating factor of this equation, defining the bounds of the admissible band $[-C, C]$ within which the implicit function value is considered solid. It does not itself represent a physical dimension, but rather governs, through this band, the resulting wall thickness $t$ of the sheet, which is the quantity indicated in the cross-sections of Figure 3.11. The level-set constant $C$ governs the width of this admissible band and, consequently, the resulting wall thickness $t$, with larger values of $C$ corresponding to thicker, more solid walls, and smaller values corresponding to thinner, more slender ones. This relationship is illustrated in Figure 3.11, where the left-hand structure, generated with $C = 0.2$, exhibits a markedly thinner wall than the right-hand structure, generated with $C = 0.6$. Since $C$ governs wall thickness independently of the spatial period set by $l$, the two parameters can be adjusted separately without altering one another. Together, $l$ and $C$ therefore provide independent control over the geometric characteristics of the sheet-based Gyroid.

Having generated the binary array representing the sheet-based Gyroid within the full rectangular domain, a cylindrical mask is applied to isolate the region corresponding to the target specimen geometry. This mask is defined in the $xy$-plane by comparing the radial distance of each voxel from the domain centre to the target radius $R$, and is subsequently extruded uniformly along the $z$-axis, so that every horizontal cross-section of the domain is subject to the same circular boundary. Voxels lying outside this cylindrical boundary are set to void, regardless of whether they

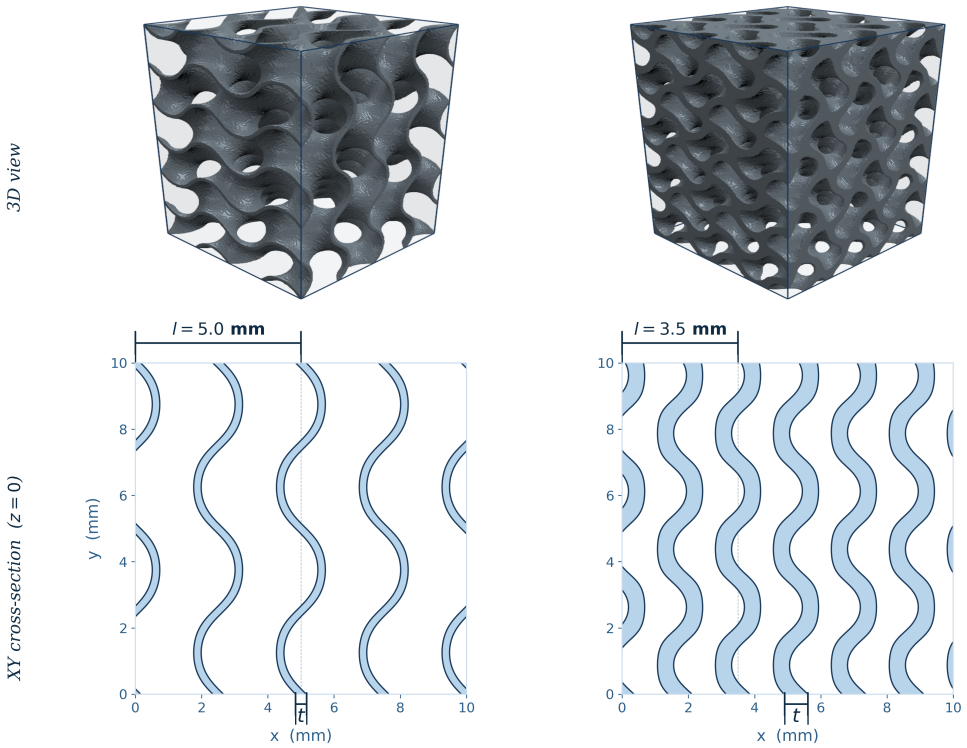



Figure 3.11: Comparison of two Gyroid unit cell sizes. Top row: three-dimensional views of the sheet-based Gyroid for $l = 5.0\,\text{mm}$, $C = 0.2$ (left) and $l = 3.5\,\text{mm}$, $C = 0.6$ (right). Bottom row: corresponding $xy$ cross-sections at $z = 0$, showing the reduction in spatial period as $l$ decreases, together with the corresponding increase in wall thickness $t$ resulting from the higher value of $C$.

were previously assigned to the solid phase by the Gyroid implicit function, while voxels lying inside the boundary retain the phase assignment established in the previous step. Figure 3.12 illustrates the outcome of this operation, showing the three-dimensional cylindrical structure obtained after masking, together with the corresponding *xy* cross-section, in which the circular boundary of the target specimen of radius $R$ is outlined for reference.

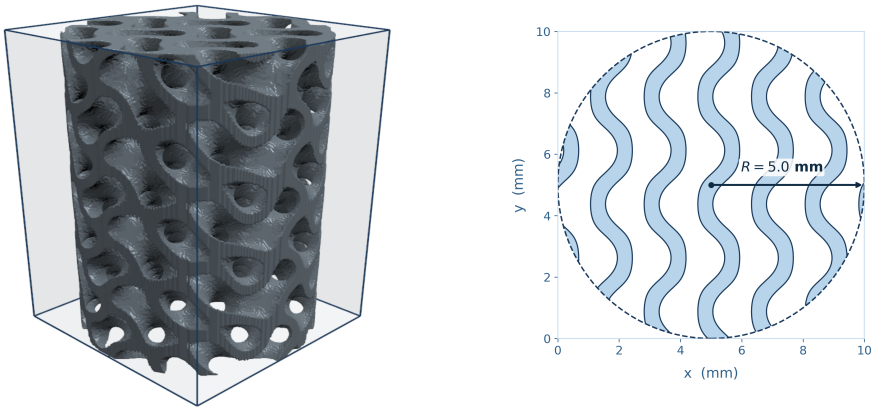



Figure 3.12: Cylindrical masking of the sheet-based Gyroid array. Left: three-dimensional view of the masked structure within its original rectangular bounding domain. Right: corresponding *xy* cross-section, with the circular boundary of radius $R = 5.0\,\text{mm}$ outlined for reference.

The masked and pedestal-augmented voxel array is subsequently converted into a triangulated surface mesh using the marching cubes algorithm, the same isosurface extraction method employed previously for the generation of the Voronoi lattice structures described in Section 3.1. This algorithm identifies the boundary between solid and void voxels throughout the array and reconstructs it as a continuous triangulated surface, with the resulting vertex coordinates translated and scaled by the voxel resolution $\Delta x$ so that the final mesh is expressed in physical millimetre units consistent with the target specimen dimensions. Nevertheless, owing to the fine voxel resolution required to resolve the thinnest wall configurations explored in this work, the resulting mesh is composed of an extremely large number of triangular faces, yielding file sizes that are impractical for further manipulation ansubsequent processing. Therefore, it is executed a decimation, whereby a simplification algorithm reduces the number of triangles to a target face count while minimising geometric deviation from the original surface, after which the mesh is validated and, where necessary, repaired to eliminate duplicate or degenerate elements and preserve a watertight, manifold geometry.

Independently of this reduction in face count, the mesh also retains a characteristic surface roughness inherited from the discrete, staircase-like nature of the underlying voxel grid, which is mitigated through the application of a Taubin smoothing filter. Unlike more classical schemes such as Laplacian smoothing, which tend to progressively shrink the geometry and erode fine features with each iteration, the Taubin filter alternates between shrinking and inflating passes,

allowing it to attenuate voxelisation artefacts on the surface while preserving the overall wall thickness and global shape of the structure, avoiding excessive volume loss during smoothing that would directly compromise the properties of each specimen. The final specimen is presented in Figure 3.13, showing the smooth, watertight Gyroid mesh obtained after decimation and Taubin smoothing, together with the integrated cylindrical pedestal.



Figure 3.13: Final triangulated mesh of the sheet-based Gyroid lattice after marching cubes extraction and post-processing.

With the mesh finalised, attention turns to the quantitative characterisation of each specimen derived directly from its geometry. The relative density $\rho_r$ and porosity $\varepsilon$ were obtained from the ratio between the enclosed mesh volume $V_{\text{solid}}$ and the total cylindrical volume of the specimen domain $V_{\text{total}} = \pi R^2 H$, according to Equation 3.11.

$$\rho_r = \frac{V_{\text{solid}}}{V_{\text{total}}}, \qquad \varepsilon = 1 - \rho_r \tag{3.11}$$

The specific surface area $A$ was extracted directly from the mesh, and the average wall thickness $t$ was estimated from the relation in Equation 3.12, which provides a global thickness measure consistent with the local level-set control exerted by the parameter $C$ [13, 119].

$$t = \frac{2V_{\text{solid}}}{A} \tag{3.12}$$

Characterising pore size, however, is not as straightforward as in strut-based or Voronoi lattices, where the void space is geometrically discrete. The Gyroid sheet is instead a continuous, bicontinuous surface dividing space into two open, mutually interpenetrating channel networks, so its pore space has no single discrete dimension to measure. Two complementary diameters were therefore derived analytically from the volume and surface area of the mesh, each addressing a distinct physical aspect of the pore space.

The equivalent pore diameter $d_p$ provides a static measure of the volumetric space available for cellular accommodation within a unit cell, and constitutes the principal indicator of pore size

used in this study, given its established relevance to osteoblast adhesion and bone ingrowth into the scaffold volume [4, 49]. It is obtained by extracting the void volume $V_{\text{pore}}$ contained within one unit cell of volume $l^3$ and idealising this void as a sphere of equal volume [74]. Equation 3.13 provides the corresponding mathematical formulation.

$$d_p = 2\sqrt[3]{\frac{3V_{\text{pore}}}{4\pi}} \tag{3.13}$$

By contrast, the hydraulic diameter $d_h$ characterises the dynamic transport behaviour of the interconnected channel network, converting its tortuous, continuously curved geometry into an equivalent straight conduit, and provides the principal indicator of the diameter of the interconnected channels typical of the Gyroid topology. It is computed from the porosity $\varepsilon$ and the specific surface area $S_v = A/V_{\text{total}}$, with the hydraulic diameter constituting the principal descriptor governing flow resistance and permeability within the scaffold [74, 119], as formalised in Equation 3.14.

$$d_h = \frac{4\varepsilon}{S_v} \tag{3.14}$$

Finally, Table 3.2 summarises the full set of parameters introduced throughout this section, together with their physical meaning within the generative pipeline.

Table 3.2: Summary of the parameters governing the Gyroid generative pipeline.

| **Symbol** | **Description** |
|---|---|
| $R, H$ | Nominal radius and height of the target cylinder |
| $\Delta x$ | Voxel resolution of the discretised bounding domain |
| $N_{\text{voxels}}$ | Total number of voxels spanning the rectangular domain |
| $l$ | Unit cell size, setting the spatial period of the Gyroid surface |
| $C$ | Level-set constant, governing the wall thickness of the sheet |
| $f(x,y,z)$ | Gyroid implicit function evaluated at each voxel node |
| $\rho_r, \varepsilon$ | Relative density and porosity of the specimen |
| $V_{\text{solid}}, V_{\text{total}}$ | Enclosed mesh volume and total cylindrical domain volume |
| $A$ | Specific surface area of the mesh |
| $t$ | Average wall thickness, $t = 2V_{\text{solid}}/A$ |
| $d_p$ | Equivalent pore diameter, under a spherical-void approximation |
| $d_h$ | Hydraulic diameter of the interconnected channel network |
| $S_v$ | Specific surface area per unit volume, $S_v = A/V_{\text{total}}$ |

## 3.3 Parametric Study

A parametric study was carried out for each architecture by varying the governing generation parameters systematically across a broad range. The aim was to map the morphological space accessible to each geometry, covering a wide spectrum of relative densities that encompasses both the trabecular and cortical bone ranges, and to establish quantitative relationships between the input parameters and the resulting morphological descriptors. Both families were generated on the same cylindrical domain ($R = 5.0\,\text{mm}$, $H = 15.0\,\text{mm}$) and characterised by relative density $\rho_r$, specific surface area $A$, and the characteristic thickness of the solid phase. For each architecture the results are organised by morphological descriptor, and closed form regression models are derived for the two primary outputs, relative density and specific surface area, providing an analytical link that supports inverse design without re running the generator. This parametric mapping also provides the basis for selecting a reduced set of nine representative geometries that span a broad range of both properties, which are then carried forward to the additive manufacturing, biodegradation testing and biomechanical simulation stages that follow.

### 3.3.1 Voronoi Lattice

The parametric space of the BCT Voronoi lattice was explored over eleven values of seed count per edge, $n \in \{10, 12, 14, 16, 18, 20, 22, 24, 26, 28, 30\}$, three values of nominal strut diameter, $D \in \{0.3, 0.5, 0.7\}$ mm, two values of the irregularity factor, $i \in \{0.25, 0.40\}$, and two random seeds, S $\in \{42, 100\}$, producing four independent realisations of each $(n, D)$ combination for a total of 132 valid observations. The total seed count $N$ associated with each value of $n$, which follows from the BCT seed geometry as described in Section 3.1, is reported alongside it in the tables that follow. One configuration ($n = 30$, $D = 0.7$ mm) could not be completed for any realisation. For this seed count, the resulting grid spacing, given by Equation (3.1), is

$$d = \frac{L}{n} = \frac{20\,\text{mm}}{30} = 0.667\text{mm}, \tag{3.15}$$

which is smaller than the specified strut diameter $D = 0.7\,\text{mm}$. Since the strut diameter cannot exceed the inter-seed spacing without the struts of adjacent cells merging into a continuous solid region, the condition $D < d$ is required for the lattice to retain a well-defined, open-pore topology; this configuration violates that condition and is therefore excluded, leaving 32 valid $(n, D)$ combinations and 128 valid observations in total.

The relative influence of all four parameters on the morphological descriptors was assessed through a variance decomposition, in which the fraction of total variance attributable to each factor is expressed as its effect size $\eta^2$, the ratio of the factor's between-group sum of squares to the total sum of squares across all observations. The results are summarised in Table 3.3.

Table 3.3: Fraction of total variance ($\eta^2$) in relative density and specific surface area attributable to each parameter, computed across all 128 valid observations.

| Descriptor | $\eta_n^2$ | $\eta_D^2$ | $\eta_i^2$ | $\eta_S^2$ |
|---|---|---|---|---|
| Relative density $\rho_r$ | 0.411 | 0.528 | $1.7 \times 10^{-5}$ | $1.1 \times 10^{-6}$ |
| Specific surface area $A$ | 0.215 | 0.397 | $7.7 \times 10^{-6}$ | $1.6 \times 10^{-6}$ |

The design parameters $n$ and $D$ jointly account for more than 93% of the total variance in both descriptors. The irregularity factor $i$ and the random seed each contribute a fraction on the order of $10^{-5}$ or smaller, several orders of magnitude below the conventional negligibility threshold of $\eta^2 = 0.01$ [121], confirming that both act as secondary parameters with no first-order influence on the resulting morphology. The raw deviation statistics support this conclusion. Across all 32 valid $(n, D)$ combinations, the maximum deviation in relative density due to changing $i$ ( $S$ held fixed) was 3.0%, with a median of 0.35%, while changing $S$ ($i$ held fixed) produced a maximum deviation of 1.6% and a median of 0.26%. A small number of combinations, concentrated at the highest densities explored ($n \geq 22$, $D = 0.7$ mm), show larger deviations in specific surface area, likely reflecting the topological sensitivity of the structure once it approaches full density. Given how low the overall variance attributable to $i$ and the random seed already is, these isolated cases are best regarded as negligible outliers rather than as evidence against the conclusion above. Across the remainder of the parameter space both sources of variation remain below 3.5%, with a median below 1%.

Given these findings, $n$ and $D$ are identified as the governing design parameters of the Voronoi lattice. The morphological results reported in the following sub-sections correspond to the reference realisation $i = 0.40$, Seed $= 42$, although the full dataset for all four realisations is provided in Appendix A.1.

Before turning to the results themselves, it is worth clarifying why $n$, rather than the grid spacing $d$, is adopted as the primary reporting variable throughout this study, even though it is $d$ that carries the direct geometric meaning established in Section 3.1. $n$ is retained here because it is the integer input actually supplied to the generator, and the quantity most directly communicated between a design intent and a specific structure, within the single bounding-box edge $L$ adopted throughout this work. This choice is a matter of convenience specific to the present study, not a claim that $n$ carries geometric meaning of its own: $n$ is meaningful only in conjunction with $L$, and the same value of $n$ would describe a different cell size, and therefore a different structure, on a bounding box of a different edge length. Consequently, should the present findings be extended to specimens of a different scale using the same generation pipeline, it is $d$, not $n$, that would need to be preserved to reproduce the same local morphology, since $d$ is the quantity that transfers unchanged across specimen geometries and overall dimensions.

#### 3.3.1.1 Relative Density

The computed values of relative density $\rho_r$ (%) are presented in Table 3.4, together with the grid spacing $d$ introduced above.

Table 3.4: Relative density $\rho_r$ (%) of the Voronoi lattice as a function of $n$ ($N$) and $D$. The grid spacing $d = L/n$ is included alongside $n$.

| $n$ | $N$ | $d$ (mm) | $D$=0.3 | $D$=0.4 | $D$=0.5 | $D$=0.6 | $D$=0.7 |
|---|---|---|---|---|---|---|---|
| 8 | 452 | 2.500 | 8.12 | 13.32 | 19.22 | 25.52 | 31.99 |
| 10 | 905 | 2.000 | 10.95 | 17.77 | 25.37 | 33.31 | 41.30 |
| 12 | 1590 | 1.667 | 14.67 | 23.57 | 33.16 | 42.89 | 52.29 |
| 14 | 2555 | 1.429 | 18.49 | 29.12 | 40.18 | 50.98 | 61.07 |
| 16 | 3848 | 1.250 | 22.18 | 34.39 | 46.72 | 58.37 | 68.68 |
| 18 | 5517 | 1.111 | 26.39 | 40.31 | 53.90 | 66.16 | 76.41 |
| 20 | 7610 | 1.000 | 30.78 | 46.31 | 60.82 | 73.26 | 83.09 |
| 22 | 10175 | 0.909 | 34.94 | 51.61 | 66.56 | 78.68 | 88.45 |
| 24 | 13260 | 0.833 | 39.25 | 57.10 | 72.41 | 84.13 | 94.47 |
| 26 | 16913 | 0.769 | 43.77 | 62.58 | 77.86 | 89.63 | 96.76 |
| 28 | 21182 | 0.714 | 48.25 | 67.66 | 82.51 | 94.57 | 98.09 |
| 30 | 26115 | 0.667 | 52.43 | 72.15 | 86.86 | 96.74 | — |

Both $d$ and $D$ exert a substantial influence on relative density, and neither can be treated as secondary to the other. Decreasing $d$ at fixed $D$ raises the total number of struts within the domain, whereas increasing $D$ at fixed $d$ thickens every strut instead, and although the two mechanisms are geometrically distinct, they produce, as the following examples illustrate, changes of comparable magnitude. Stepping from $D = 0.3$ to $D = 0.7$ mm at fixed $n = 18$ ($d = 1.111$ mm) raises $\rho_r$ from 26.4% to 76.4%, whereas stepping from $n = 8$ to $n = 30$, that is, $d$ from 2.500 mm down to 0.667 mm, at fixed $D = 0.5$ mm raises $\rho_r$ from 19.2% to 86.9%. The two length scales therefore produce changes of comparable magnitude within the domain studied here, and the resulting density cannot be attributed predominantly to either one. The accessible density range extends from 8.1% ($n = 8$, $D = 0.3$ mm) to 98.1% ($n = 28$, $D = 0.7$ mm), and at this high-density end the lattice transitions towards a near-solid body, which reinforces the exclusion of the single configuration ($n = 30$, $D = 0.7$ mm) for which strut merging prevented the open-pore topology from being retained.

Since it is $d$, and not $n$, that carries direct geometric meaning, as established above, $\rho_r$ is regressed here directly on $d$ and $D$, rather than on $n$ and $D$. A power-law model of the form $\rho_r = k\,d^a D^b$, fitted by log-linear regression to all 59 valid observations, yields

$$\rho_r = 115.5\, d^{-0.987} D^{1.013} \qquad (R^2 = 0.977) \tag{3.16}$$

where the negative exponent on $d$ simply reflects that density falls as the cell size grows, while the magnitude of both exponents remains close to unity, so that $\rho_r$ still scales approximately linearly

with each length scale taken independently. A second-order polynomial in $d$ and $D$, in turn, gives

$$\rho_r = 32.1 - 73.9\,d + 252.9\,D + 19.9\,d^2 - 43.7\,dD - 84.1\,D^2 \qquad (R^2 = 0.993) \tag{3.17}$$

with a maximum residual of 5.4 percentage points across the parameter space. Both regressions remain useful as direct empirical fits, although they still treat $d$ and $D$ as two unrelated regressors, and therefore give no indication of whether a simpler relationship underlies the data.

The existence of such a simplification can, in fact, be anticipated on physical grounds. Relative density is dimensionless, and if it depends on the local strut geometry alone, rather than on the absolute size of the specimen, it can depend on $D$ and $d$ only through their dimensionless ratio $D/d$, provided the topology of the tessellation remains unchanged as $d$ is varied. Table 3.3 already confirms that the irregularity factor and the random seed leave no detectable signature in the resulting morphology, which supports this expectation without establishing it exactly. The reduction of $D$ and $d$ to a single ratio $D/d$ is therefore treated here as a hypothesis to be tested against the data.

The data support this hypothesis directly. Table 3.5 lists the fourteen groups of configurations, covering 33 of the 59 valid cases, that share an identical value of $D/d$ despite differing individually in $n$ and $D$. For each group, the spread is reported both in absolute terms, as the difference in percentage points (pp) between the highest and lowest $\rho_r$ value in the group, and in relative terms, as that same difference expressed as a percentage of the group's own density level. Densities within each group agree to within 4.0 percentage points in absolute terms, with a relative spread below 3% in eight of the fourteen groups and never exceeding 14.1%, confirming $D/d$, rather than $d$ and $D$ separately, as the variable that governs the density response of the lattice.

Table 3.5: Groups of configurations sharing an identical value of $D/d$ despite differing individually in $n$ and $D$, with the resulting spread in relative density.

| $D/d$ | $(n, D)$ pairs | $\rho_r$ values (%) | Spread |
|---|---|---|---|
| 0.20 | (8, 0.5), (10, 0.4) | 19.22, 17.77 | 1.45 pp (7.8%) |
| 0.24 | (8, 0.6), (12, 0.4), (16, 0.3) | 25.52, 23.57, 22.18 | 3.34 pp (14.1%) |
| 0.28 | (8, 0.7), (14, 0.4) | 31.99, 29.12 | 2.87 pp (9.4%) |
| 0.30 | (10, 0.6), (12, 0.5), (20, 0.3) | 33.31, 33.16, 30.78 | 2.53 pp (7.8%) |
| 0.35 | (10, 0.7), (14, 0.5) | 41.30, 40.18 | 1.12 pp (2.7%) |
| 0.36 | (12, 0.6), (18, 0.4), (24, 0.3) | 42.89, 40.31, 39.25 | 3.64 pp (8.9%) |
| 0.40 | (16, 0.5), (20, 0.4) | 46.72, 46.31 | 0.41 pp (0.9%) |
| 0.42 | (12, 0.7), (14, 0.6), (28, 0.3) | 52.29, 50.98, 48.25 | 4.04 pp (8.0%) |
| 0.45 | (18, 0.5), (30, 0.3) | 53.90, 52.43 | 1.47 pp (2.8%) |
| 0.48 | (16, 0.6), (24, 0.4) | 58.37, 57.10 | 1.27 pp (2.2%) |
| 0.56 | (16, 0.7), (28, 0.4) | 68.68, 67.66 | 1.02 pp (1.5%) |
| 0.60 | (20, 0.6), (24, 0.5), (30, 0.4) | 73.26, 72.41, 72.15 | 1.11 pp (1.5%) |
| 0.70 | (20, 0.7), (28, 0.5) | 83.09, 82.51 | 0.58 pp (0.7%) |
| 0.84 | (24, 0.7), (28, 0.6) | 94.47, 94.57 | 0.10 pp (0.1%) |

Given this, a general quadratic regression in $D/d$, expressed in Equatioon 3.18, was fitted to all 59 valid observations, in place of the two-variable models attempted first.

$$\rho_r = -17.9 + 192.1\left(\frac{D}{d}\right) - 71.1\left(\frac{D}{d}\right)^2 \qquad (R^2 = 0.9965) \tag{3.18}$$

This fit yields a maximum residual of 4.0 percentage points across the full parameter space, with all 59 observations collapsing onto a single curve in $D/d$, as shown in Figure 3.14. It improves on both the power-law and the polynomial regressions in $d$ and $D$ (Equations (3.16) and (3.17)) while depending on one fewer regressor, confirming $D/d$ as the variable that most directly organises the density response of the lattice. The quadratic term reflects a departure from linearity towards the upper end of the explored range, where $D$ approaches $d$ and strut merging sets in, causing density to rise more slowly than at lower ratios.

Equation (3.18) is adopted as the primary result of this sub-section. For inverse design, either $D$ or $d$ can be fixed first and the other solved for, once a target density is set, although $D$ is typically the more natural choice to fix, since it is the variable most directly constrained by manufacturing or biodegradation requirements. Solving the quadratic for the corresponding $D/d$ then fixes the remaining variable, subject to $D/d < 1$, since $d < D$ would place the configuration beyond the open-pore regime characterised here. Because the result is expressed as a ratio, it also transfers, in principle, to bounding-box edges $L$ other than the one used in this work.

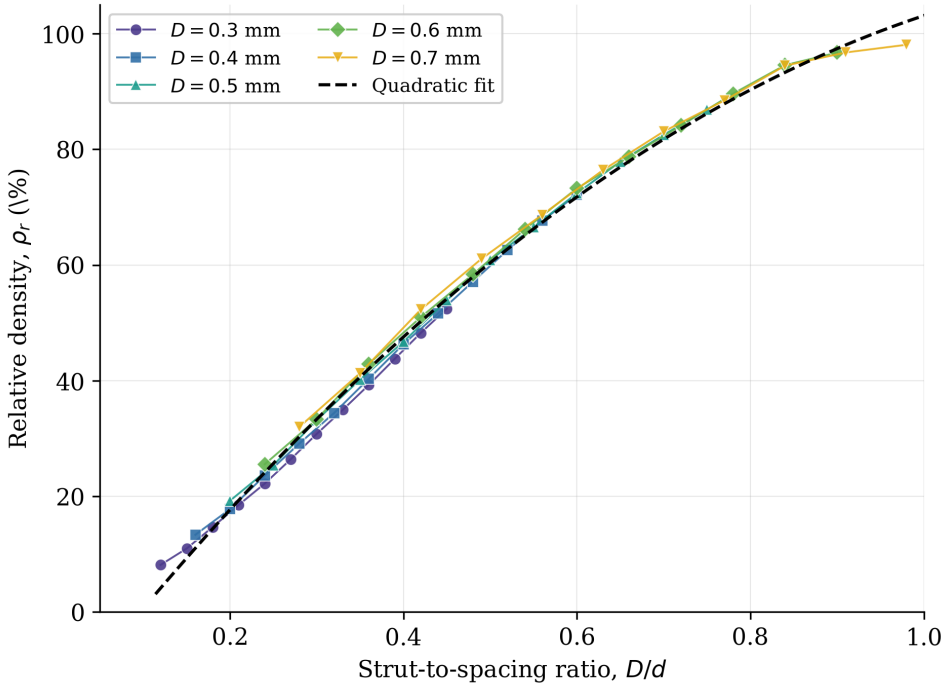



Figure 3.14: Relative density of the Voronoi lattice as a function of the strut-to-spacing ratio $D/d$, for all five values of $D$ explored. The dashed line is the quadratic fit of Equation (3.18).

#### 3.3.1.2 Specific Surface Area

The computed values of specific surface area $A$ (cm$^2$) are presented in Table 3.6.

Table 3.6: Specific surface area $A$ (cm$^2$) of the Voronoi lattice as a function of $n$ ($N$) and $D$. The grid spacing $d = L/n$ is included alongside $n$.

| $n$ | $N$ | $d$ (mm) | $D$=0.3 mm | $D$=0.5 mm | $D$=0.7 mm |
|---|---|---|---|---|---|
| 10 | 905 | 2.000 | 15.48 | 19.78 | 20.72 |
| 12 | 1590 | 1.667 | 20.32 | 24.49 | 23.85 |
| 14 | 2555 | 1.429 | 24.93 | 28.21 | 25.68 |
| 16 | 3848 | 1.250 | 29.15 | 31.04 | 26.14 |
| 18 | 5517 | 1.111 | 33.73 | 33.49 | 25.45 |
| 20 | 7610 | 1.000 | 38.23 | 35.14 | 23.81 |
| 22 | 10175 | 0.909 | 42.08 | 35.67 | 20.80 |
| 24 | 13260 | 0.833 | 45.81 | 35.53 | 12.30 |
| 26 | 16913 | 0.769 | 49.30 | 34.29 | 8.02 |
| 28 | 21182 | 0.714 | 52.27 | 32.34 | 7.23 |
| 30 | 26115 | 0.667 | 54.63 | 29.21 | — |

Surface area responds to $d$ and $D$ through a markedly non-monotonic pattern. At large $d$, where struts are well separated, thickening them with increasing $D$ adds exposed surface, whereas at small $d$, where struts sit close together, the same increase in $D$ eventually causes neighbouring struts to merge, converting exposed interfacial area into buried material. This reversal is visible directly in3 Table 3.6 and in Figure 3.15: at $d = 2.000$ mm ($n = 10$) surface area still increases with $D$, whereas from $d = 1.25$ mm ($n = 16$) onwards the $D = 0.7$ mm series falls below the $D = 0.3$ mm series at the same $d$, reaching 7.23 cm$^2$ against 52.27 cm$^2$ at $d = 0.714$ mm ($n = 28$). This reversal depends on both $D$ and $d$ jointly and sets in at a different point for each configuration, so that grouping by $D/d$ no longer yields comparable surface areas, unlike the case of relative density; surface area must therefore be modelled as a function of $d$ and $D$ individually.

As $d$ decreases, the number of struts filling the domain grows faster than each individual strut shrinks, so the resulting surface area is expected to scale approximately as $d^{-2}$. A polynomial expansion built on this scaling, with cross terms in $D$ to capture their coupling rather than a form restricted to $D/d$ alone, was fitted to all 32 valid observations:

$$A = -13.2 + \frac{17.5}{d} + \frac{25.6}{d^2} + 180.9\,\frac{D}{d} - 125.6\,\frac{D}{d^2} - 92.1\,\frac{D^2}{d} \qquad (R^2 = 0.991) \tag{3.19}$$

This form reproduces the data closely across most of the parameter space, losing accuracy only at the two most heavily coalesced configurations ($n = 26$ and $n = 28$ at $D = 0.7$ mm). Equation (3.19) is adopted as the design relationship for specific surface area, and is illustrated in Figure 3.15: the line plot shows the fit against the three explored values of $D$, while the contour shows the full $(d, D)$ plane, revealing the diagonal ridge of maximum area whose position depends on $d$ itself, which is why no single-variable reduction analogous to $D/d$ is available here.

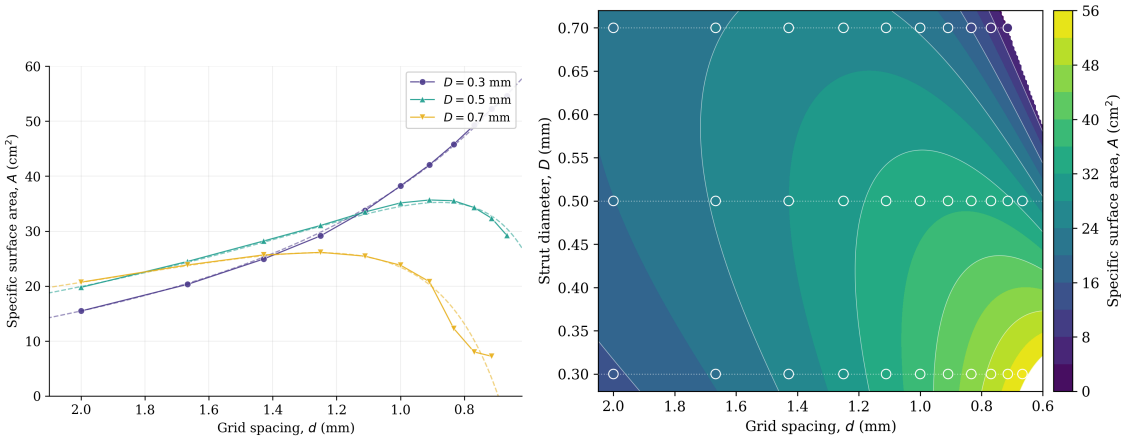



Figure 3.15: Specific surface area of the Voronoi lattice. Left: as a function of grid spacing $d$ for the three values of $D$ explored, with the fit of Equation (3.19) shown dashed. Right: the same fit evaluated over the full $(d, D)$ plane, with the 32 valid observations overlaid; dotted lines mark the three sections shown on the left.

#### 3.3.1.3 Pore Size Characterisation

The void space of each configuration is characterised through its pore volume $V_{\text{pore}}$, computed cell-by-cell across the tessellation as defined by Equation 3.6. Because every cell is evaluated individually, both the population mean and its standard deviation are available for each configuration, the latter offering a direct measure of pore size heterogeneity. These statistics are reported in Table 3.7.

Table 3.7: Pore volume statistics (mean $\pm$ standard deviation, mm$^3$) of the Voronoi lattice as a function of $n$ ($N$) and $D$. The grid spacing $d$ is included alongside $n$.

| $n$ | $N$ | $d$ (mm) | $D$=0.3 mm | $D$=0.5 mm | $D$=0.7 mm |
|---|---|---|---|---|---|
| 10 | 905 | 2.000 | $3.765 \pm 3.016$ | $3.171 \pm 2.497$ | $2.448 \pm 1.955$ |
| 12 | 1590 | 1.667 | $2.313 \pm 1.607$ | $1.780 \pm 1.271$ | $1.244 \pm 0.920$ |
| 14 | 2555 | 1.429 | $1.434 \pm 1.006$ | $1.041 \pm 0.741$ | $0.672 \pm 0.482$ |
| 16 | 3848 | 1.250 | $0.990 \pm 0.648$ | $0.678 \pm 0.439$ | $0.393 \pm 0.258$ |
| 18 | 5517 | 1.111 | $0.682 \pm 0.421$ | $0.428 \pm 0.262$ | $0.218 \pm 0.134$ |
| 20 | 7610 | 1.000 | $0.492 \pm 0.284$ | $0.272 \pm 0.165$ | $0.117 \pm 0.072$ |
| 22 | 10175 | 0.909 | $0.352 \pm 0.206$ | $0.181 \pm 0.105$ | $0.065 \pm 0.037$ |
| 24 | 13260 | 0.833 | $0.261 \pm 0.143$ | $0.119 \pm 0.063$ | $0.023 \pm 0.012$ |
| 26 | 16913 | 0.769 | $0.198 \pm 0.099$ | $0.077 \pm 0.040$ | $0.009 \pm 0.004$ |
| 28 | 21182 | 0.714 | $0.147 \pm 0.074$ | $0.049 \pm 0.026$ | $0.005 \pm 0.003$ |
| 30 | 26115 | 0.667 | $0.110 \pm 0.056$ | $0.031 \pm 0.016$ | — |

Both moments contract together across the parametric space, the domain subdividing into progressively smaller cells as $d$ falls while the concurrent thickening of struts at higher $D$ leaves proportionally less volume free within each cell. The ratio between the two moments is more informative than this joint contraction. The coefficient of variation (CV $= \sigma/\mu$) remains confined

to 0.50–0.80 across the entire grid, essentially independent of the particular $(d, D)$ combination chosen. Pore size heterogeneity is therefore not a by-product of any specific design point but a structural signature of the BCT Voronoi tessellation itself.

To compare these results against biological targets reported in the literature, the mean pore volume of each configuration is converted into an equivalent pore diameter $d_{\text{pore}}$ under the spherical-void approximation of Equation (3.6), summarised in Table 3.8.

Table 3.8: Equivalent pore diameter $d_{\text{pore}}$ (mm) derived from the mean pore volume of Table 3.7 via Equation (3.6).

| $n$ | $N$ | $d$ (mm) | $D$=0.3 mm | $D$=0.5 mm | $D$=0.7 mm |
|---|---|---|---|---|---|
| 10 | 905 | 2.000 | 1.665 | 1.588 | 1.450 |
| 12 | 1590 | 1.667 | 1.483 | 1.358 | 1.201 |
| 14 | 2555 | 1.429 | 1.248 | 1.116 | 0.961 |
| 16 | 3848 | 1.250 | 1.110 | 0.981 | 0.812 |
| 18 | 5517 | 1.111 | 0.992 | 0.854 | 0.685 |
| 20 | 7610 | 1.000 | 0.908 | 0.737 | 0.554 |
| 22 | 10175 | 0.909 | 0.802 | 0.642 | 0.460 |
| 24 | 13260 | 0.833 | 0.734 | 0.564 | 0.329 |
| 26 | 16913 | 0.769 | 0.679 | 0.495 | 0.237 |
| 28 | 21182 | 0.714 | 0.616 | 0.425 | 0.203 |
| 30 | 26115 | 0.667 | 0.556 | 0.365 | — |

The benchmark for Voronoi-based bone scaffolds in the literature is approximately 500 µm [122, 123], consistent with the general target established in Section 2.2.3. Measured against this value across the full grid of Table 3.8, only a narrow band of configurations approaches it: those at $d \approx 0.91$–$1.00$ mm with $D = 0.7$ mm ($d_{\text{pore}} = 460$–$554$ µm) and at $d \approx 0.77$–$0.83$ mm with $D = 0.5$ mm ($d_{\text{pore}} = 495$–$564$ µm), with every other $(d, D)$ combination lying further from the target in either direction.

Whether this band is actually usable, however, depends on how it sits against relative density and surface area, the two quantities the parametric study is built around. Checking the same $(n, D)$ pairs against Table 3.4 and Table 3.6 shows that both candidate regions fall within the moderately dense part of the design space, at $\rho_r \approx 83$–$98\%$ for $D = 0.7$ mm and $\rho_r \approx 72$–$78\%$ for $D = 0.5$ mm, rather than in the open, low-density regime typically sought for scaffold applications. The $D = 0.7$ mm band additionally coincides with the onset of strut merging identified in Section 3.3.1.2, where surface area collapses sharply with $d$, making that region unattractive on both density and area grounds despite its favourable pore size.

This outcome carries a practical implication for lattice design. Achieving pore sizes near the 500 µm benchmark in this architecture is only possible by moving into the denser, more heavily coalesced end of the explored range, which runs counter to the open, low-density regime that relative density and surface area considerations otherwise favour. Because $d_{\text{pore}}$ responds to the same two parameters, $d$ and $D$, that already govern those two primary characteristics, it cannot

be tuned independently to meet the pore-size target without also shifting $\rho_r$ and $A$ away from their more favourable values. Satisfying the pore-size benchmark and preserving an open, mechanically efficient lattice are therefore, within the present parameter space, competing rather than complementary design goals.

#### 3.3.1.4 Strut Diameter

Table 3.9 reports the percentage deviation of the realised strut diameter $d_{\text{strut}}$ from the nominal input value $D$, computed according to Equation 3.7, for each configuration.

Table 3.9: Percentage error of the realised strut diameter relative to nominal $D$ for each Voronoi configuration. The grid spacing $d = L/n$ is included alongside $n$.

| $n$ | $N$ | $d$ (mm) | $D$=0.3 mm | $D$=0.5 mm | $D$=0.7 mm |
|---|---|---|---|---|---|
| 10 | 905 | 2.000 | +0.31% | +0.09% | +0.02% |
| 12 | 1590 | 1.667 | +0.43% | +0.13% | +0.04% |
| 14 | 2555 | 1.429 | +0.53% | +0.17% | +0.06% |
| 16 | 3848 | 1.250 | +0.62% | +0.20% | +0.07% |
| 18 | 5517 | 1.111 | +0.71% | +0.23% | +0.08% |
| 20 | 7610 | 1.000 | +0.79% | +0.25% | +0.09% |
| 22 | 10175 | 0.909 | +0.85% | +0.26% | +0.09% |
| 24 | 13260 | 0.833 | +0.92% | +0.27% | +0.07% |
| 26 | 16913 | 0.769 | +0.96% | +0.28% | +0.04% |
| 28 | 21182 | 0.714 | +0.99% | +0.27% | +0.02% |
| 30 | 26115 | 0.667 | +1.01% | +0.26% | — |

Deviations are positive throughout the parametric space, remaining well below any practically meaningful threshold and never exceeding 1.0%. This confirms that the nominal strut diameter $D$ was realised as intended, supporting the morphological results discussed in the previous sections.

### 3.3.2 Gyroid (TPMS)

The parametric space of the sheet-based Gyroid was explored over eight values of unit cell size, $l \in \{1.5, 2.0, 2.5, 3.0, 3.5, 4.0, 5.0, 6.0\}$ mm, and ten values of the level-set constant, $C \in \{0.2, 0.3, 0.4, 0.5, 0.6, 0.7, 0.8, 0.9, 1.0, 1.1\}$, producing a full factorial set of 80 distinct configurations. The upper bound $l = 6.0\,\text{mm}$ was set so that at least two unit cells were accommodated across each specimen dimension, and was chosen with some margin above this strict minimum rather than at the limit itself, so that the parametric study would not be restricted to configurations sitting right at the two-cell boundary. Relative density, specific surface area, average wall thickness and both pore-scale diameters were extracted from the final triangulated mesh of every

configuration, following the procedures set out in Section 3.2. The values reported below come directly from the completed high-resolution study and are treated here as final.

#### 3.3.2.1 Relative Density

Table 3.10 lists the relative density $\rho_r$ (%) obtained for every combination of $l$ and $C$. The 80 configurations span a relative density from 12.7% at $C = 0.2$ to 73.1% at $C = 1.1$, a range that encompasses the trabecular bone window of ∼30–50% identified in Table 2.3 and extends well into the cortical regime, in line with the aim of the parametric study to cover the full morphological space accessible to the architecture.

The data reveal a clear asymmetry between the two governing parameters. Relative density is governed almost exclusively by the level-set constant $C$, which drives it from 12.7% at $C = 0.2$ to 73.1% at $C = 1.1$ in a smooth, monotonic progression. The unit cell size $l$, by contrast, is effectively inert: across the range explored, from 1.5 mm to 6.0 mm, the variation in $\rho_r$ at any fixed $C$ never exceeds 0.83 percentage points, and can be treated as negligible for design purposes.

Table 3.10: Relative density $\rho_r$ (%) of the sheet-based Gyroid across all 80 configurations.

| $l$ (mm) \ $C$ | 0.2 | 0.3 | 0.4 | 0.5 | 0.6 | 0.7 | 0.8 | 0.9 | 1.0 | 1.1 |
|---|---|---|---|---|---|---|---|---|---|---|
| 1.5 | 12.80 | 19.24 | 25.71 | 32.22 | 38.78 | 45.39 | 52.07 | 58.83 | 65.71 | 72.73 |
| 2.0 | 12.81 | 19.24 | 25.69 | 32.19 | 38.73 | 45.32 | 51.99 | 58.75 | 65.62 | 72.63 |
| 2.5 | 12.81 | 19.24 | 25.70 | 32.19 | 38.72 | 45.31 | 51.98 | 58.73 | 65.59 | 72.59 |
| 3.0 | 12.78 | 19.20 | 25.64 | 32.12 | 38.65 | 45.24 | 51.91 | 58.67 | 65.54 | 72.55 |
| 3.5 | 12.84 | 19.27 | 25.71 | 32.20 | 38.72 | 45.29 | 51.93 | 58.65 | 65.49 | 72.48 |
| 4.0 | 12.91 | 19.37 | 25.85 | 32.36 | 38.90 | 45.49 | 52.15 | 58.87 | 65.70 | 72.67 |
| 5.0 | 12.69 | 19.08 | 25.51 | 31.98 | 38.49 | 45.07 | 51.71 | 58.43 | 65.27 | 72.27 |
| 6.0 | 12.89 | 19.36 | 25.87 | 32.41 | 38.98 | 45.62 | 52.35 | 59.15 | 66.07 | 73.10 |

This behaviour follows directly from the level-set rule of Equation 3.9. At $C = 0$ the level set traces the ideal Gyroid surface with zero thickness, and raising $C$ above zero thickens that surface into a solid sheet by retaining every point whose implicit function value falls within the band $[-C, C]$ around it. A larger $C$ simply widens that band, so the sheet grows thicker everywhere in the domain simultaneously, regardless of how many unit cells the surface is divided into. The unit cell size only decides where that extra thickness sits in space, not how much of it there is.

That last point is what makes the decoupling useful rather than a mere curiosity of the geometry. Because $l$ never influences how much solid material exists, only where it sits, the two parameters behave as genuinely independent handles in practice. $C$ can be tuned first to hit a target density, and $l$ can then be chosen on whatever grounds matter most, whether pore-scale requirements, resolvable feature size, or the surface-area considerations discussed in the following subsection, without disturbing the density already fixed.

A quadratic regression on $C$ alone, fitted to all 80 observations, captures this relationship with remarkable fidelity:

$$\rho_r = 0.356 + 61.92C + 3.38C^2 \qquad (R^2 = 0.9999) \tag{3.20}$$

The quadratic term was retained over a simpler linear fit for a concrete reason. A linear regression on $C$ alone already achieves $R^2 = 0.9998$, but the small additional curvature captured by the quadratic term reflects a real trend in the data. Each successive step of $\Delta C = 0.1$ adds slightly more density than the last, rising from 6.44 percentage points between $C = 0.2$ and $C = 0.3$ to 7.02 percentage points between $C = 1.0$ and $C = 1.1$, consistent with the two solid fronts advancing from opposite sides of the sheet beginning to overlap as $C$ grows. The high coefficient of determination leaves almost no residual variance for $l$ to explain, confirming that unit cell size could be dropped from the model altogether without meaningful loss of accuracy. Figure 3.16 provides concrete evidence of this, with the near-total overlap of all eight series onto a single curve in $C$, regardless of unit cell size.

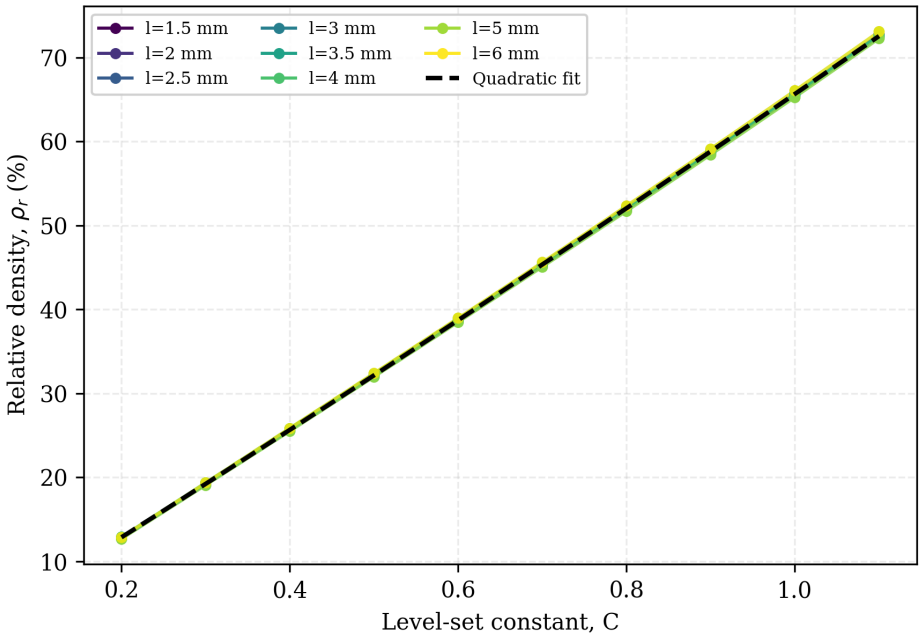



Figure 3.16: Relative density of the sheet-based Gyroid as a function of the level-set constant $C$, for all eight unit cell sizes explored. The dashed line is the quadratic fit of Equation (3.20).

#### 3.3.2.2 Specific Surface Area

Turn to surface area and the roles reverse almost entirely, with Table 3.11 showing that $A$ answers principally to $l$ rather than to $C$, whose influence survives only as a secondary effect whose very sign shifts across the range explored.

Table 3.11: Specific surface area $A$ (cm$^2$) of the sheet-based Gyroid across all 80 configurations.

| $l$ (mm) \ $C$ | 0.2 | 0.3 | 0.4 | 0.5 | 0.6 | 0.7 | 0.8 | 0.9 | 1.0 | 1.1 |
|---|---|---|---|---|---|---|---|---|---|---|
| 1.5 | 49.20 | 49.14 | 48.90 | 48.45 | 47.77 | 46.83 | 45.60 | 44.01 | 42.01 | 39.41 |
| 2.0 | 36.95 | 37.00 | 36.92 | 36.68 | 36.27 | 35.68 | 34.91 | 33.86 | 32.49 | 30.69 |
| 2.5 | 29.63 | 29.72 | 29.69 | 29.55 | 29.27 | 28.88 | 28.32 | 27.55 | 26.57 | 25.28 |
| 3.0 | 24.77 | 24.95 | 25.03 | 25.00 | 24.88 | 24.61 | 24.19 | 23.60 | 22.84 | 21.81 |
| 3.5 | 21.48 | 21.71 | 21.88 | 21.98 | 21.94 | 21.77 | 21.45 | 20.97 | 20.32 | 19.43 |
| 4.0 | 18.98 | 19.18 | 19.30 | 19.34 | 19.29 | 19.15 | 18.90 | 18.55 | 18.07 | 17.41 |
| 5.0 | 15.01 | 15.31 | 15.51 | 15.64 | 15.70 | 15.69 | 15.61 | 15.46 | 15.26 | 14.97 |
| 6.0 | 12.87 | 13.14 | 13.39 | 13.59 | 13.75 | 13.88 | 13.88 | 13.78 | 13.60 | 13.27 |

This dominance of $l$ becomes obvious the moment the two extremes are set side by side. At $l = 1.5$ mm, surface area ranges from roughly 3940 to 4920 mm$^2$ across the ten values of $C$ tested, while at $l = 6.0$ mm the very same sweep collapses to just 1287 to 1388 mm$^2$, amounting to a reduction on the order of 65 to 72% at broadly comparable density. This follows directly from the underlying geometry, since packing a periodic surface into a fixed specimen volume means that halving the cell size roughly doubles the number of Gyroid repeats able to fit inside it, and with them the total solid-to-void interface they generate. Figure 3.17 makes this dominant $1/l$ dependence immediately apparent, as all ten series, one per value of $C$, trace essentially the same steep decay from left to right, separated only by the far more modest spread that $C$ contributes.

The contribution from $C$ is not only smaller in magnitude but also inconsistent in sign across the range explored. In every series except $l = 1.5$ mm, surface area rises slightly as $C$ increases from its lowest value, reaches a peak, and only then declines. The position of this peak shifts progressively with unit cell size, from $C = 0.3$ at $l = 2.0$ mm to $C = 0.8$ at $l = 6.0$ mm, while its amplitude increases correspondingly, from a negligible 0.1% at the smallest cell sizes to a more pronounced 7.9% at the largest, which explains why the peak becomes visually apparent only in the larger series of the figure. At $l = 1.5$ mm alone the rise is entirely absent and the response decreases monotonically throughout the full range of $C$. This behaviour is geometric rather than a product of numerical noise. Truncating the infinite Gyroid at the cylindrical boundary of the specimen exposes new solid faces along the cut itself, corresponding to portions of the lateral wall and the two end caps, and these newly exposed faces add directly to the total surface area. As $C$ increases, more solid material sits close to that boundary, so the cut area initially grows even as the interior surface is already shrinking under the general thickening of the walls, and the data ultimately record the outcome of this competition between the two effects. At small cell sizes the interior surface is so abundant that the boundary contribution barely registers, whereas at large cell sizes, where far fewer periods fit inside the same domain, the two effects become comparable in magnitude and it is precisely that balance which produces the visible peak.

The regression model was built on physical grounds rather than by trial and error. Since a periodic surface packed into a fixed volume must produce a surface area that scales with $1/l$, this

leading term was fixed in advance. Once it accounted for the dominant variation, the remaining residuals depended smoothly on $C$, and a quadratic term sufficed to capture that secondary trend across all eight series:

$$A = \frac{6536.8}{l} + 217.3 + 631.8C - 754.8C^2 \qquad (R^2 = 0.990) \tag{3.21}$$

Equation (3.21) reproduces the trends of Figure 3.17, with the $1/l$ term accounting for the steep decay and the quadratic term in $C$ capturing the secondary spread between curves.

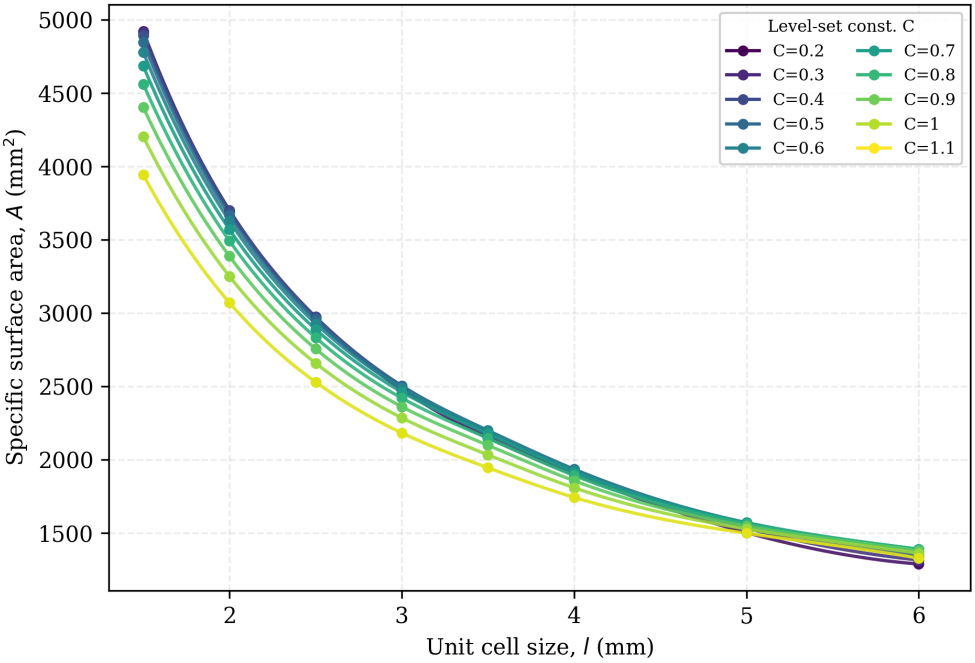



Figure 3.17: Specific surface area of the sheet-based Gyroid as a function of unit cell size $l$, with each curve corresponding to a fixed value of $C$.

The two descriptors are therefore better treated as independently addressable design targets, each governed by its own parameter. $C$ can be set first to fix the relative density, since its residual influence on surface area is comparatively minor, after which $l$ can be tuned freely to reach the desired surface area without disturbing the density already achieved.

#### 3.3.2.3 Average Wall Thickness

Wall thickness $t$ is reported here as the specimen-wide mean of the solid phase dimension, giving a single characteristic length scale for the material across the whole Gyroid structure. This average serves two distinct purposes: it characterises the solid phase geometrically and provides the key reference for the element size adopted in the finite-element models. Values for all 80 configurations are listed in Tables 3.12 and 3.13.

Table 3.12: Average wall thickness $t$ (mm) of the sheet-based Gyroid — lower density range ($C = 0.2$–$0.6$).

| $l$ (mm) \ $C$ | 0.2 | 0.3 | 0.4 | 0.5 | 0.6 |
|---|---|---|---|---|---|
| 1.5 | 0.0613 | 0.0922 | 0.1239 | 0.1567 | 0.1913 |
| 2.0 | 0.0817 | 0.1225 | 0.1640 | 0.2068 | 0.2516 |
| 2.5 | 0.1018 | 0.1525 | 0.2039 | 0.2567 | 0.3116 |
| 3.0 | 0.1216 | 0.1813 | 0.2414 | 0.3027 | 0.3660 |
| 3.5 | 0.1409 | 0.2091 | 0.2768 | 0.3451 | 0.4158 |
| 4.0 | 0.1602 | 0.2380 | 0.3156 | 0.3942 | 0.4752 |
| 5.0 | 0.1992 | 0.2936 | 0.3875 | 0.4818 | 0.5779 |
| 6.0 | 0.2361 | 0.3473 | 0.4550 | 0.5617 | 0.6680 |

Table 3.13: Average wall thickness $t$ (mm) of the sheet-based Gyroid — upper density range ($C = 0.7$–$1.1$).

| $l$ (mm) \ $C$ | 0.7 | 0.8 | 0.9 | 1.0 | 1.1 |
|---|---|---|---|---|---|
| 1.5 | 0.2284 | 0.2691 | 0.3150 | 0.3685 | 0.4348 |
| 2.0 | 0.2992 | 0.3509 | 0.4088 | 0.4758 | 0.5575 |
| 2.5 | 0.3697 | 0.4325 | 0.5024 | 0.5817 | 0.6767 |
| 3.0 | 0.4332 | 0.5057 | 0.5858 | 0.6761 | 0.7838 |
| 3.5 | 0.4903 | 0.5705 | 0.6589 | 0.7595 | 0.8788 |
| 4.0 | 0.5598 | 0.6500 | 0.7480 | 0.8566 | 0.9833 |
| 5.0 | 0.6770 | 0.7806 | 0.8906 | 1.0078 | 1.1377 |
| 6.0 | 0.7747 | 0.8886 | 1.0112 | 1.1445 | 1.2980 |

Wall thickness increases monotonically with both $l$ and $C$, and the trend is well captured by their product alone:

$$t \approx 0.204\, l\, C \qquad (R^2 = 0.978) \tag{3.22}$$

This result is physically intuitive, since unit cell size sets the spatial scale of the periodic structure while the level-set constant determines what fraction of that scale is occupied by solid material, so their product naturally governs the resulting wall dimension. The somewhat lower $R^2$ relative to the fits obtained for density and surface area is consistent with $t$ being a derived quantity that combines both $l$ and $C$ through the ratio $2V_{\text{solid}}/A$, rather than a direct response to a single parameter, and it remains adequate for the secondary role that $t$ plays in this study. Across the full parametric space, $t$ spans from 0.061 mm at ($l = 1.5$ mm, $C = 0.2$) to 1.298 mm at ($l = 6.0$ mm, $C = 1.1$), a range that exceeds one order of magnitude relative to the overall scale of the specimen.

#### 3.3.2.4 Pore-Scale Diameters

As introduced in Section 3.2, two complementary descriptors characterise the void space of the sheet-based Gyroid. The equivalent pore diameter $d_p$ quantifies the static volumetric space available within a unit cell, while the hydraulic diameter $d_h$ reflects the effective diameter of the interconnected channel network and is therefore the more appropriate indicator for comparison

with biological targets, since it is $d_h$ that governs the space through which cells migrate and vascular structures develop. Computed values for both are presented in Tables 3.14 and 3.15.

Table 3.14: Equivalent pore diameter $d_p$ (µm) of the sheet-based Gyroid.

| $l$ (mm) \ $C$ | 0.2 | 0.3 | 0.4 | 0.5 | 0.6 | 0.7 | 0.8 | 0.9 | 1.0 | 1.1 |
|---|---|---|---|---|---|---|---|---|---|---|
| 1.5 | 1778 | 1733 | 1686 | 1635 | 1580 | 1521 | 1456 | 1384 | 1303 | 1207 |
| 2.0 | 2371 | 2311 | 2248 | 2180 | 2108 | 2029 | 1943 | 1847 | 1738 | 1611 |
| 2.5 | 2963 | 2888 | 2809 | 2725 | 2635 | 2536 | 2429 | 2309 | 2174 | 2015 |
| 3.0 | 3556 | 3467 | 3372 | 3271 | 3163 | 3045 | 2916 | 2773 | 2610 | 2419 |
| 3.5 | 4148 | 4043 | 3933 | 3815 | 3688 | 3552 | 3402 | 3235 | 3046 | 2824 |
| 4.0 | 4739 | 4619 | 4492 | 4356 | 4211 | 4054 | 3882 | 3691 | 3474 | 3221 |
| 5.0 | 5929 | 5781 | 5624 | 5456 | 5276 | 5081 | 4867 | 4630 | 4360 | 4045 |
| 6.0 | 7110 | 6929 | 6737 | 6533 | 6314 | 6076 | 5815 | 5523 | 5192 | 4806 |

Table 3.15: Hydraulic diameter $d_h$ (µm) of the sheet-based Gyroid.

| $l$ (mm) \ $C$ | 0.2 | 0.3 | 0.4 | 0.5 | 0.6 | 0.7 | 0.8 | 0.9 | 1.0 | 1.1 |
|---|---|---|---|---|---|---|---|---|---|---|
| 1.5 | 835 | 774 | 716 | 659 | 604 | 550 | 495 | 441 | 385 | 326 |
| 2.0 | 1112 | 1029 | 948 | 871 | 796 | 722 | 648 | 574 | 499 | 420 |
| 2.5 | 1387 | 1280 | 1179 | 1082 | 986 | 892 | 799 | 706 | 610 | 511 |
| 3.0 | 1660 | 1526 | 1400 | 1280 | 1162 | 1049 | 937 | 825 | 711 | 593 |
| 3.5 | 1912 | 1752 | 1600 | 1454 | 1316 | 1184 | 1056 | 929 | 801 | 667 |
| 4.0 | 2162 | 1981 | 1810 | 1648 | 1493 | 1342 | 1193 | 1045 | 894 | 740 |
| 5.0 | 2741 | 2491 | 2263 | 2050 | 1847 | 1650 | 1458 | 1267 | 1072 | 873 |
| 6.0 | 3190 | 2892 | 2608 | 2343 | 2091 | 1846 | 1618 | 1396 | 1176 | 955 |

Both descriptors decrease monotonically with $C$ and increase with $l$, in accordance with the trend established for the primary morphological descriptors, since as the solid fraction grows the void space contracts. The equivalent pore diameter $d_p$ spans from 1207 to 7110 µm across the full parametric space, while $d_h$ ranges from 326 to 3190 µm over the same configurations, systematically smaller, as expected for a descriptor that weights the tortuous, multiply-connected channel geometry rather than the total void volume.

Within the broader 100–600 µm window identified in Section 2.2.3 for porous bone scaffolds in general, TPMS architectures respond to a narrower target. A pore size of 300–600 µm is optimal for osseointegration in TPMS-based scaffolds, since this range best facilitates vascularisation and cell growth [124]. For the sheet-based Gyroid specifically, a combined indicator of normalised specific surface, normalised pressure drop, and cell seeding efficiency places the optimum near 500 µm [125]. This narrower sub-range, roughly 300–600 µm with an optimum near 500 µm, is adopted here as the benchmark for the Gyroid architecture.

Measured against this benchmark, both descriptors lie above the target range throughout the vast majority of the parametric space. For $d_h$, which is the more appropriate comparator, only 10 of the 80 configurations fall within or close to it, all concentrated at $l = 1.5$–$3.0$ mm combined with $C \geq 0.7$. The equivalent pore diameter $d_p$ remains above 1200 µm in all configurations, placing it consistently beyond the range in question.

This outcome is not a consequence of an inadequate architecture but of a geometric constraint inherent to the cell sizes explored. Both $d_p$ and $d_h$ decrease with increasing $C$ at any given $l$, but the dominant effect comes from $l$ itself, and across most of the parametric space the resulting values remain well above the target window. Only at the lowest unit cell sizes, combined with higher $C$ values, does $d_h$ approach the desired range, indicating that further reductions in $l$ would be needed to bring most configurations closer to it.

## 3.4 Additive Manufacturing

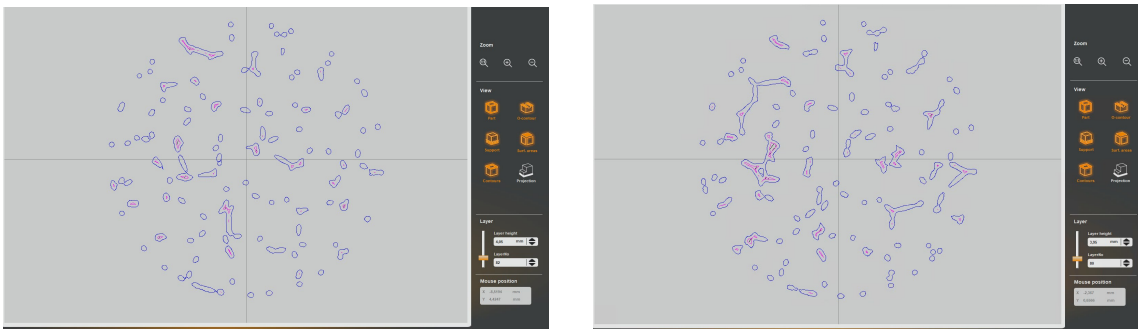
### 3.4.1 Manufacturing Constraints and Design Boundaries

Before committing the full parametric population to manufacture, a preliminary assessment of printability was conducted to establish the minimum feature dimensions that the selected process could reliably resolve. The additive manufacturing process adopted throughout this work is L-PBF, as described previously in Section 2.5.1 applied to a pure iron powder feedstock. In L-PBF, the achievable minimum feature size is governed by the laser spot diameter, the powder particle size distribution, and the layer thickness, which together define a practical floor on the smallest geometric detail that can be reproduced with structural continuity.

#### 3.4.1.1 Minimum Strut Diameter

The minimum manufacturable resolution was assessed after the Voronoi lattice parametric study was established, by examining whether the accessible density range could be extended to lower values by reducing the nominal strut diameter below $D = 0.3\,\text{mm}$. A candidate configuration with $D = 0.2\,\text{mm}$ ($n = 12$) was generated and submitted to the machine preparation software for layer-by-layer analysis prior to any physical build. This analysis compares the nominal part contour, derived directly from the STL geometry, against the effective laser scan path that the machine would actually trace given the spot size and process parameters in use.

For the $D = 0.2\,\text{mm}$ configuration, this comparison revealed that several struts fall below the resolution threshold of the L-PBF system, as shown in Figure 3.18. While the nominal contour (blue) still defines a continuous strut network, the corresponding scan path (pink) is absent over large portions of these thinner regions, meaning the laser would not trace a path there at all. This absence indicates that the intended strut thickness falls below what the current process parameters can reliably melt. The pathology is consistent across the three successive layers shown (heights 3.95, 4.00, and 4.05 mm), confirming that it reflects a systematic resolution limit rather than a localised artefact.



(a) Layer 80 — height 3.95 mm.

(b) Layer 82 — height 4.05 mm.

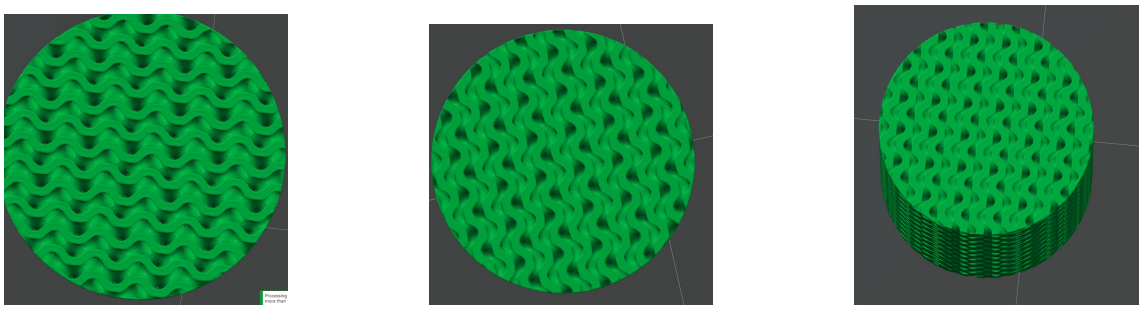
Figure 3.18: Layer-by-layer analysis in the L-PBF machine preparation software of a Voronoi specimen with nominal strut diameter $D = 0.2\,\text{mm}$ ($n = 12$). Blue indicates the nominal contour defined by the STL geometry, while pink indicates the actual laser scan path the machine would trace. Several struts show no corresponding scan path at all, confirming that their thickness falls below what the current process parameters can reproduce, a pattern consistent across the layers shown (heights 3.95 and 4.05 mm).

On the basis of this analysis, the lower bound on strut diameter was set to $D = 0.3\,\text{mm}$ for Voronoi geometry, the smallest value for which a continuous scan path was reproduced across all configurations explored in Section 3.3.1.

#### 3.4.1.2 Upper Bound on the Level-Set Constant

For the sheet-based Gyroid architecture, the wave-crest truncation effect identified during the parametric study (Section 3.3.2) imposed a practical upper bound on the level-set constant $C$ admitted to manufacture. Indeed, as shown in Figure 3.19, increasing $C$ progressively flattens and truncates the wave crests visible on the top face of the specimen. At $C = 0.8$, the wave crests are fully resolved and retain their characteristic curvature, whereas at $C = 0.9$ the crests become noticeably clipped, with the surface beginning to flatten locally. This truncation becomes markedly more pronounced at $C = 1.0$, where it extends across the entire cross-section, such that the crests no longer follow the smooth sinusoidal profile of the underlying level-set surface. Consequently, beyond $C = 0.8$ the geometry departs from the intended Gyroid morphology.

Therefore, an upper limit of $C \leq 0.8$ was imposed on all Gyroid configurations admitted to manufacture. This constraint is not restrictive in practice, however, since the configurations retained within this bound already span relative densities up to approximately 52 %, as shown in Section 3.3.2.1. This range is expected to comfortably cover the scope of densities relevant to the present work.



(a) $C = 0.8$ (b) $C = 0.9$ (c) $C = 1.0$

Figure 3.19: Computational renders of the sheet-based Gyroid for increasing values of $C$, at a fixed unit cell size. Pore openings on the top face progressively close as $C$ increases, from fully resolved at $C = 0.8$ to fully suppressed at $C = 1.0$. On this basis, $C = 0.8$ was adopted as the upper bound for fabrication.

#### 3.4.1.3 Solid Base Addition

A further modification common to both architectures was the addition of a 0.5 mm solid cylindrical pedestal at the base of each specimen. In L-PBF, parts must be anchored to the build platform via support structures, regardless of part geometry. As discussed in Section 2.5.2, the open cellular architecture compromises this attachment, since the voids present in the base do not form a continuous solid surface suitable for reliable support anchoring. A solid base is therefore necessary to guarantee this interface: the pedestal provides the continuous, fully dense surface required for the supports to anchor the part to the build platform. A height of 0.5 mm was adopted for this purpose, remaining negligible relative to the 15 mm specimen height (3.3 % of the total).

The pedestal was incorporated into the STL geometry in Python prior to manufacture, following the same procedure for both the Voronoi and Gyroid architectures. Figure 3.20 shows three Voronoi specimens with the solid base in place, as visualised in the build-preparation software together with the underlying cylindrical support structures used to anchor each part to the build platform.

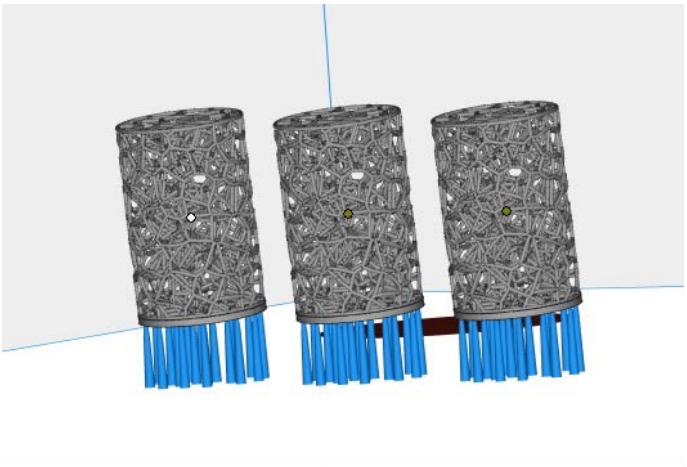


Figure 3.20: Build-preparation software view of three Voronoi specimens with the 0.5 mm base pedestal incorporated into the STL geometry, shown together with the cylindrical support structures generated to anchor each part to the build platform. The same pedestal design was applied to the Gyroid specimens.

### 3.4.2 Selection of Specimens for Manufacture

From each parametric population, nine representative configurations were selected for fabrication, yielding eighteen specimens across both architectures. The selection was guided by two concurrent objectives: achieving broad coverage of the morphological space accessible to each family, so that the fabricated set captures the full range of mechanical and biodegradation behaviour, and ensuring that the selected configurations span a wide spectrum of relative densities, in order to support a statistically meaningful regression of apparent mechanical properties against density.

#### 3.4.2.1 Voronoi

The nine selected Voronoi configurations correspond to a full factorial crossing of the three strut diameters explored, $D \in \{0.3, 0.5, 0.7\}$ mm, with three seed counts spanning the accessible range, $n \in \{10, 14, 18\}$. This choice is effective specifically because, over this range, relative density increases with both $n$ and $D$ in an approximately linear, non-saturating manner, as shown in Section 3.3.1: for instance, at $D = 0.5$ mm, successive increments of $n$ raise $\rho_r$ by 14.81 and 13.72 percentage points in turn, a near-constant step rather than a diminishing one. Because the relationship does not saturate within this interval, an evenly spaced grid in $(n, D)$ maps onto a correspondingly well-spread set of density values, rather than clustering near one extreme as would occur if either parameter's effect flattened out at high values. Indeed, the resulting nine specimens span relative densities from approximately 11 % to 76 % and specific surface areas from 1 500 to 3 350 mm$^2$. The distribution within the $(n, D)$ parametric plane is shown in Figure 3.21.

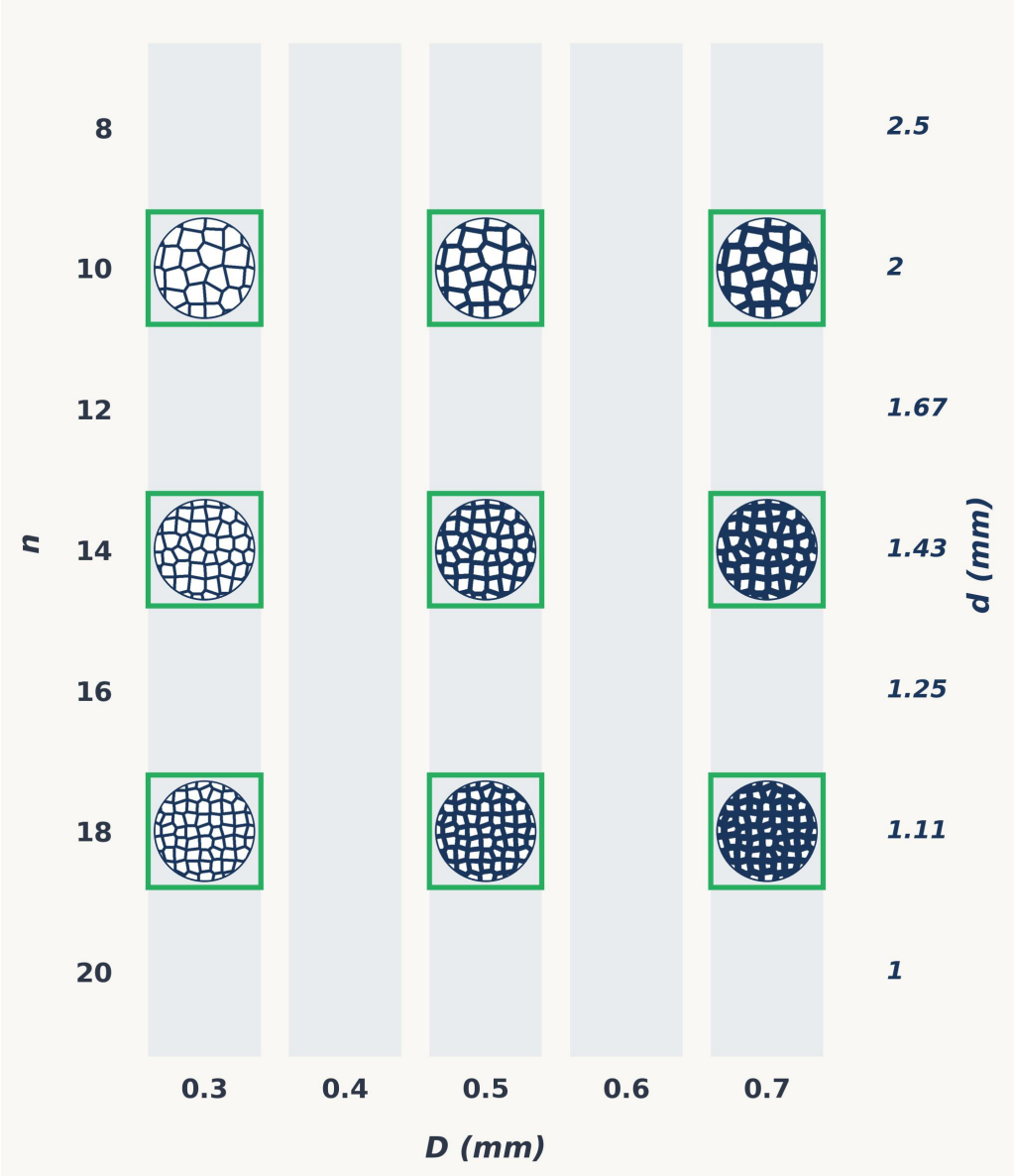



Figure 3.21: Design space of the Voronoi lattice architecture in the $(D, n)$ parametric plane, showing top-surface renderings of all candidate configurations. The nine specimens selected for fabrication (highlighted) span the accessible morphological space across all three strut diameters and a broad range of cell densities, subject to the minimum-feature-size constraint ($D \geq 0.3\,\text{mm}$), established in Section 3.4.1.

#### 3.4.2.2 Gyroid

For the Gyroid, based on the previous analysis in Section 3.3.2.1, relative density is governed almost exclusively by the level-set constant $C$, with unit cell size $l$ having no meaningful effect on this descriptor. Specific surface area follows the opposite pattern, being driven primarily by $l$, as shown in Section 3.3.2.2. Since each parameter controls a different descriptor, the nine

configurations were not chosen from a regular grid, but selected individually across the $(l, C)$ plane so that, taken together, $l$ ranges widely enough to capture variation in surface area, and $C$ ranges widely enough to capture variation in density.

The nine configurations selected in this manner span unit cell sizes $l \in \{1.5, 2.0, 2.5, 3.5, 5.0\}$ mm and level-set constants $C \in \{0.2, 0.3, 0.5, 0.6, 0.7, 0.8\}$. Relative density accordingly ranges from approximately 13 % to 52 %, whereas specific surface area spans roughly 1 500 to 4 500 mm$^2$ across the set. Their distribution within the $(l, C)$ parametric plane is shown in Figure 3.22, where the selected points appear spread across the accessible morphological space without clustering in any particular region, respecting throughout the upper bound $C \leq 0.8$ established in Section 3.4.1.2.

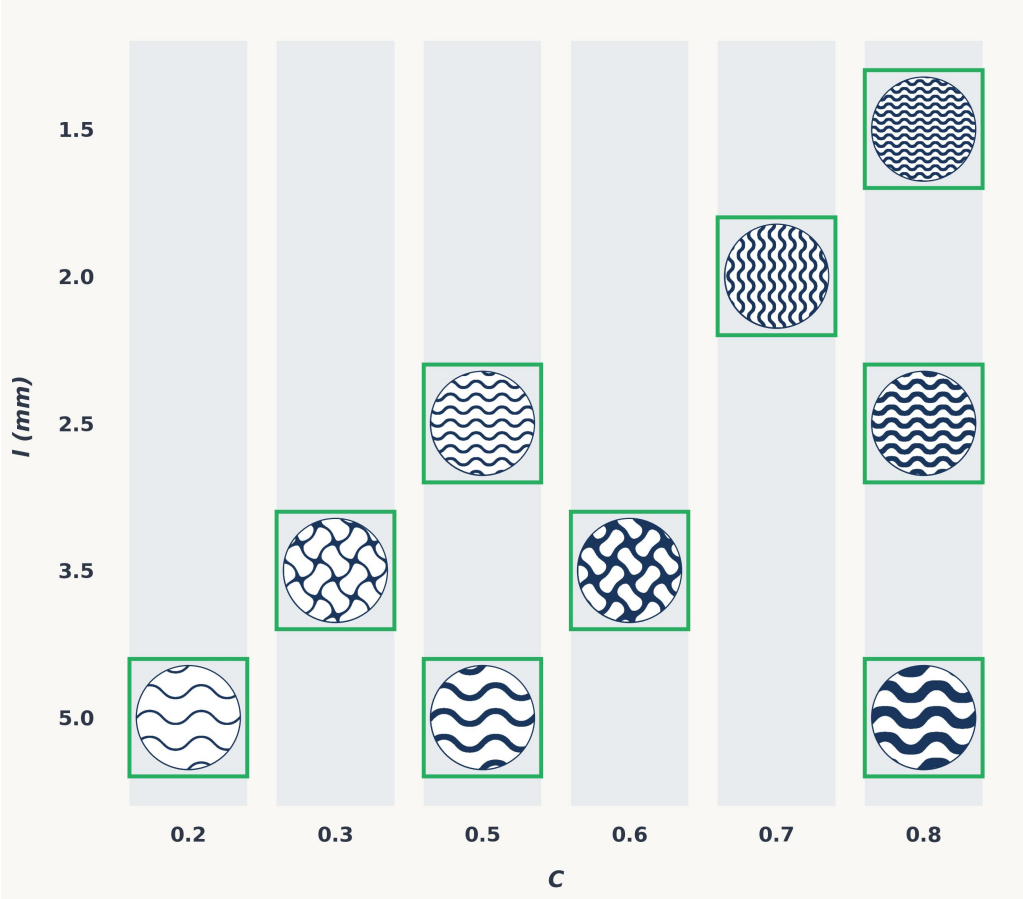



Figure 3.22: Design space of the sheet-based Gyroid architecture in the $(C, l)$ parametric plane, showing top-surface renderings of all candidate configurations. The nine specimens selected for fabrication (highlighted) were chosen to jointly cover the accessible ranges of density and surface area, respecting the upper bound $C \leq 0.8$ established in Section 3.4.1 and the minimum of two unit cells per specimen dimension established in Section 3.3.2.

### 3.4.3 Fabrication

All eighteen specimens were fabricated by L-PBF using a Colibrium Additive M2 Series 5 system, operated with a pure iron powder feedstock under a nitrogen atmosphere to prevent oxidation of the melt pool during consolidation. The bulk region of each specimen was consolidated under the fixed core condition summarised in Table 3.16, while the boundary of each strut and wall was consolidated separately through a contour scanning strategy, summarised in Table 3.17. Nonetheless, all specimens were oriented on the build platform with an inclination of 5 degrees relative to the build direction, in the *Oxz* plane.

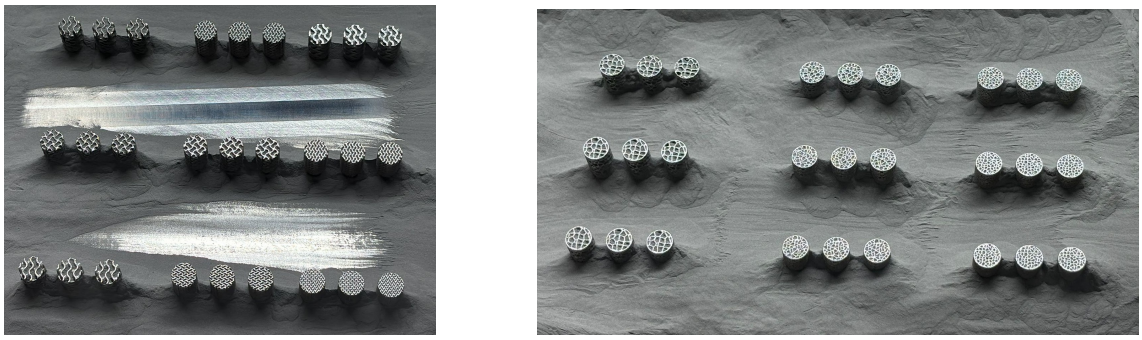
Table 3.16: Fixed bulk L-PBF processing condition adopted throughout fabrication.

| Bulk parameter | Value |
|---|---|
| Laser power, $P$ | 300 W |
| Scanning speed, $v$ | 700 mm s$^{-1}$ |
| Hatch spacing, $h$ | 0.10 mm |
| Laser spot size | 120 µm |
| Layer thickness, $t$ | 50 µm |
| Volumetric energy density, $E_v$ | 85.71 J mm$^{-3}$ |
| Atmosphere | Nitrogen |
| Build plate | Stainless steel |
| Build-plate preheating | None |
| Bulk scan strategy | Bidirectional, 67° layer rotation |

Table 3.17: Contour processing condition adopted for the boundary of each specimen.

| Contour parameter | Value |
|---|---|
| Laser power, $P_c$ | 225 W |
| Scanning speed, $v_c$ | 300 mm s$^{-1}$ |
| Laser spot size | 115 µm |
| Contour offset | 0.09 mm |
| Number of contour passes | 1 |

Figure 3.23 shows the build platform following extraction from the machine, with all specimens still attached to their support structures. The two architectural families occupy distinct rows of the platform, grouped to facilitate post-build identification.

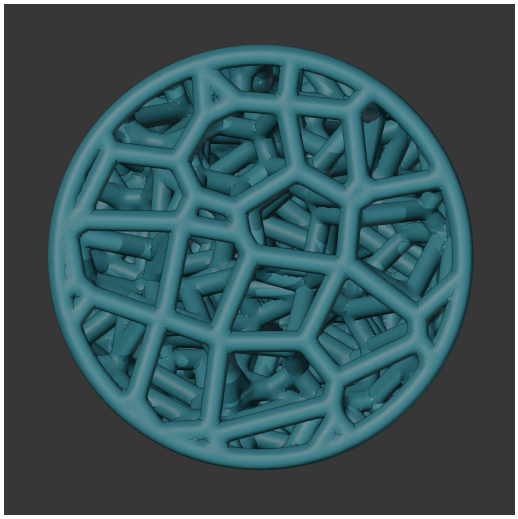


(a) Gyroid batch (b) Voronoi batch

Figure 3.23: Build platforms following extraction from the L-PBF machine, showing both the Gyroid batch (a) and the Voronoi batch (b).

After extraction from the platform, the specimens were stored in an inert cabinet until the biodegradation studies described in Chapter 4, where the subsequent cleaning and treatment procedures are detailed.

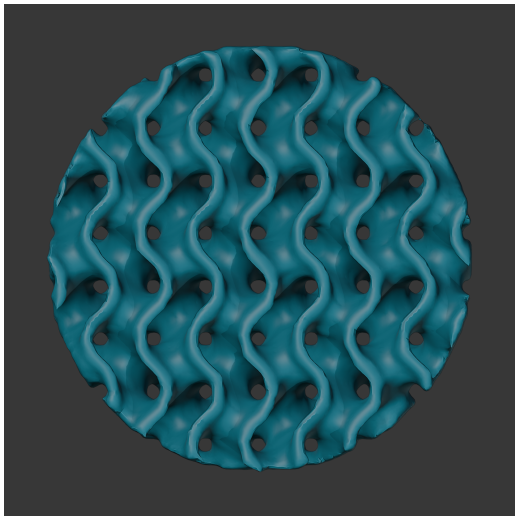
The correspondence between the designed geometry and the as-built specimens is illustrated in Figure 3.24, which present digital stereomicroscope images for representative Voronoi and Gyroid configurations, respectively.



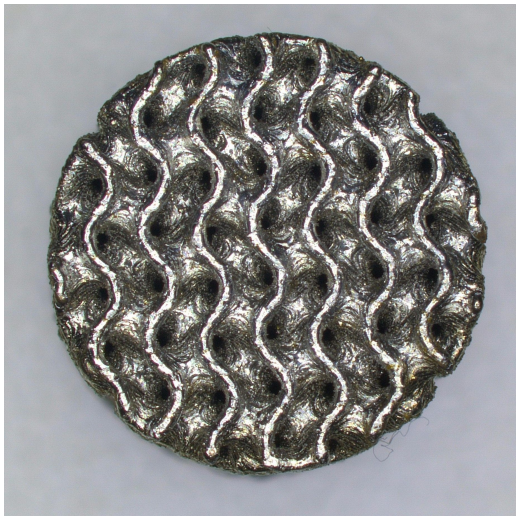
(a) Voronoi (design).



(b) Voronoi (post-fabrication).



(c) Gyroid (design).



(d) Gyroid (post-fabrication).

Figure 3.24: Correspondence between the designed and as-built geometry for representative Voronoi (n=10 D=0.5 mm) and Gyroid (l=2.5 mm c=0.5) specimens, viewed from the top face.

Chapter 4

# Biodegradation Testing

The set of specimens designed and fabricated in Chapter 3 is now carried forward into biodegradation testing. Having already justified why this particular geometric variability was selected, the present chapter turns instead to how it manifests in degradation behaviour once the specimens are exposed to a physiological environment, thereby constituting, alongside the biomechanical simulation of Chapter 5, one of the two experimental pillars on which the work rests. Since no single technique can capture every facet of the corrosion process, the degradation response was instead assessed through three complementary methods: mass loss, quantification of ionic release and surface morphological analysis.

Mass loss immersion testing was employed to assess and compare the in vitro degradation behaviour of the Voronoi and Gyroid porous iron specimens fabricated by L-PBF, providing a quantitative measure of corrosion over time as a function of topology and relative density. The protocol was designed with reference to three normative standards that collectively define best practice for the corrosion assessment of metals and metallic biomaterials: ASTM G31 (*Standard Guide for Laboratory Immersion Corrosion Testing of Metals*), ASTM G1 (*Standard Practice for Preparing, Cleaning, and Evaluating Corrosion Test Specimens*), and ISO 16428:2005 (*Implants for Surgery — Test Solutions and Environmental Conditions for Static and Dynamic Corrosion Tests on Implantable Materials and Medical Devices*). ASTM G31 provides the general methodological framework for laboratory immersion testing, including the formula for calculating the corrosion rate from mass loss, exposed surface area and immersion time (Equation 4.1), together with guidance on solution volume, temperature and specimen support conditions. ASTM G1 establishes the governing principle of post-test cleaning, namely that cleaning procedures must remove corrosion products without causing significant loss of the base metal, thereby enabling an accurate determination of the mass lost to corrosion during exposure. ISO 16428:2005 specifies the reference environmental conditions for corrosion testing of metallic implant materials, controlling the test solution composition, temperature ($37 \pm 1$ °C) and the minimum ratio between solution volume and exposed surface area (10 mL/cm$^2$). These three standards form the normative baseline against which all practical adaptations made in the present protocol were evaluated and justified, as described in the following sections.

However, mass loss only captures the net change in specimen mass and cannot separate iron that dissolved into the surrounding medium from iron that persisted on the surface as solid corrosion products. Chemical analysis of the immersion solutions was therefore carried out in parallel, providing a direct measure of the soluble iron fraction mobilised into the fluid phase at each renewal interval. Inductively Coupled Plasma Optical Emission Spectrometry (ICP-OES) is the technique of choice for this purpose in the in vitro biodegradation literature for iron-based scaffolds produced by additive manufacturing [126–128], and is regarded as one of the more sensitive and precise atomic spectroscopic techniques for elemental analysis of biomedical samples [129]. In the present work, ICP-OES was accordingly the originally intended analytical route, although its application proved incompatible with the sample matrix because the high concentration of dissolved salts inherent to the Simulated Body Fluid (SBF) formulation prevented reliable signal

acquisition with the available instrument. In view of this limitation, Flame Atomic Absorption Spectrometry (FAAS) was adopted as an alternative analytical technique. FAAS operates on a single element basis and provides a direct quantitative measure of dissolved iron, and it is widely applied to biological and environmental samples, remaining suitable for the determination of iron in complex matrices with relatively high dissolved solid loads [129]. Although its detection limit is higher than that of ICP-OES and its sensitivity is therefore reduced at very low ion concentrations [129], it affords a robust and practically useful assessment of iron release under the conditions employed in this study, a constraint that is taken into account in the interpretation of the results presented in Section 4.2.2.

Finally, the morphological and compositional characterisation of the specimen surfaces constitutes an equally necessary dimension of the degradation assessment, offering direct evidence of the nature and spatial distribution of the corrosion products formed upon prolonged immersion in SBF that the previous two techniques are unable to do. Scanning Electron Microscopy (SEM) was employed for this purpose, enabling high-resolution examination of the surface deposits, whilst Energy-Dispersive X-ray Spectroscopy (EDS) provided elemental identification of their principal constituents. Of particular relevance in the context of iron-based biodegradable implants is the potential precipitation of calcium phosphate phases at the specimen surface, since apatite formation upon immersion in SBF constitutes a well-established, though not unanimously accepted, in vitro criterion for predicting the bone-bonding ability of a material and, by extension, its osseointegration potential [130].

## 4.1 Methodology

### 4.1.1 Specimen preparation

Prior to immersion, all specimens underwent a post-fabrication cleaning step to remove unmelted pure iron powder trapped within the porous network during the L-PBF process. Each specimen was placed in an ultrasonic bath with ethanol for 30 min, and its mass was recorded both before and after this treatment. The difference in mass served to confirm that powder removal had taken place and to quantify the contribution of residual powder, thereby ensuring that the reference initial mass ($m_0$) used in subsequent degradation calculations reflected solely the mass of the as-built solid structure. Following cleaning, the specimens were stored in an inert-atmosphere cabinet to minimise surface oxidation prior to the start of the immersion test.

Once the preparatory cleaning was complete, each specimen was weighed on an analytical balance to establish $m_0$, and its identification code, geometry, design parameters, relative density and surface area were recorded. The relative density and surface area values, having been determined during the design phase, are reported in Section 3.3; they are referenced here solely to derive the SBF volumes described in the following section.

### 4.1.2 Immersion conditions and solution volume

All specimens were immersed in SBF at 37.5 °C throughout the entire test duration. The volume of SBF assigned to each specimen was calculated on the basis of a constant ratio of 1 mL/cm$^2$ of exposed surface area, which falls below the minimum of 10 mL/cm$^2$ recommended by ISO 16428:2005. This lower ratio was a direct consequence of the limited availability of reagents for SBF preparation, which, combined with the number of specimens and the frequency of solution changes required over the 30-day period, made a higher ratio impracticable. Despite this constraint, the adaptation was considered acceptable on the basis of three conditions. First, the ratio was maintained strictly constant across all specimens and conditions, ensuring that no group was systematically affected by differences in fluid volume relative to another. Second, the pH of the medium was recorded at every solution change and evaluated against the initial value; deviations exceeding 0.5 units were treated as indicative of excessive ionic saturation, in which case the solution would be renewed regardless of the scheduled interval. Third, the internal validity of the comparative analysis between topologies and density levels is preserved, given that the reduced ratio applies equally and consistently to all groups throughout the test.

Tables 4.1 and 4.2 list, for the Voronoi and gyroid specimens respectively, the relative density, surface area and assigned SBF volume for each sample. In addition to the porous specimens, a fully dense reference sample (100% relative density, Id 57) was included, with a surface area of 6.28 cm$^2$ and a corresponding SBF volume of 6.28 mL, calculated using the same ratio.

Table 4.1: Voronoi specimens: design parameters, relative density, surface area and assigned SBF volume. $n$ denotes the number of cells and $D$ the density parameter.

| **Id** | $n$ | $D$ | **Relative density (%)** | **Surface area (cm$^2$)** | **SBF volume (mL)** |
|---|---|---|---|---|---|
| 1 | 10 | 0.3 | 11.0 | 15.4 | 15.4 |
| 2 | 10 | 0.5 | 25.4 | 19.8 | 19.8 |
| 3 | 10 | 0.7 | 41.3 | 20.7 | 20.7 |
| 4 | 14 | 0.3 | 18.5 | 24.8 | 24.8 |
| 5 | 14 | 0.5 | 40.2 | 28.2 | 28.2 |
| 6 | 14 | 0.7 | 61.1 | 25.7 | 25.7 |
| 7 | 18 | 0.3 | 26.4 | 33.5 | 33.5 |
| 8 | 18 | 0.5 | 53.9 | 33.4 | 33.4 |
| 9 | 18 | 0.7 | 76.4 | 25.5 | 25.5 |

Table 4.2: Gyroid specimens: design parameters, relative density, surface area and assigned SBF volume. $l$ denotes cell size and $C$ the level-set constant.

| Id | $l$ | $C$ | Relative density (%) | Surface area ($cm^2$) | SBF volume (mL) |
|---|---|---|---|---|---|
| 10 | 1.5 | 0.8 | 52.07 | 45.60 | 45.60 |
| 11 | 2.0 | 0.7 | 45.39 | 35.68 | 35.68 |
| 12 | 2.5 | 0.5 | 32.19 | 29.55 | 29.55 |
| 13 | 2.5 | 0.8 | 51.98 | 28.32 | 28.32 |
| 14 | 3.5 | 0.3 | 19.27 | 21.71 | 21.71 |
| 15 | 3.5 | 0.6 | 38.72 | 21.94 | 21.94 |
| 16 | 5.0 | 0.2 | 12.69 | 15.01 | 15.01 |
| 17 | 5.0 | 0.5 | 31.98 | 15.64 | 15.64 |
| 18 | 5.0 | 0.8 | 51.71 | 15.61 | 15.61 |

The test ran for a total of 30 days, with mass readings taken at Days 10, 20 and 30 and the SBF medium renewed every 5 days. This duration is consistent with time frames commonly reported for in vitro biodegradation studies of additively manufactured porous iron [126, 127]. The 5-day renewal interval is shorter than the weekly exchanges typically described in the literature for similar protocols, and was adopted to more actively limit the accumulation of $Fe^{2+}$ and $Fe^{3+}$ ions and prevent pH drift within the same bath, both of which could otherwise alter the corrosivity of the solution and compromise the comparability of measurements across time points.

### 4.1.3 Specimen retrieval and mass measurement

Every five days, the pH of each immersion bath was recorded and the SBF medium was renewed. At the three designated reading points — Days 10, 20 and 30 — specimens were retrieved from the SBF and subjected to the following procedure. Each specimen was briefly immersed in distilled water to remove residual electrolyte and loose surface deposits, without any mechanical friction. It was then placed in an ultrasonic bath with ethanol for 60 min to remove adherent corrosion products from the surface and from within the porous network. Following ultrasonic cleaning, each specimen was dried in an oven at 37.5 °C for 60 min to allow complete evaporation of residual ethanol. Once cooled to room temperature, the specimen was weighed ($m_t$) on an analytical balance, and the measurement was recorded for subsequent mass loss calculation.

Although ASTM G1 identifies controlled acid pickling — such as hydrochloric acid with hexamethylenetetramine — as the normative ideal for removing corrosion products without attacking the base metal, this route was not adopted in the present work. In its place, solvent-based ultrasonic cleaning was employed, an approach that has been reported as the sole post-immersion cleaning method in studies of pure iron and iron-based biodegradable scaffolds of equivalent composition tested under comparable conditions [127, 128]. The consequence of this choice is that partially

adherent corrosion products may remain on specimen surfaces, leading to a slight underestimation of true mass loss. As this effect is systematic and applies identically to all specimens at all time points, it does not affect the validity of comparisons between topologies and density groups, which constitute the primary objective of the analysis. This limitation is revisited in the context of the results in Section 4.2.1.

### 4.1.4 Corrosion rate calculation

The Corrosion Rate (CR) was calculated from the measured mass loss using the expression set out in ASTM G31:

$$\mathrm{CR} = \frac{K \cdot W}{A \cdot t \cdot \rho} \tag{4.1}$$

where $K = 8.76 \times 10^4$ is a unit conversion constant, $W$ is the mass loss (g), $A$ is the exposed surface area ($\mathrm{cm}^2$), $t$ is the immersion time (h), and $\rho$ is the density of pure iron ($\mathrm{g/cm}^3$). The corrosion rate is expressed in mm/year.

### 4.1.5 Iron Ion Release

Iron ion release was monitored throughout the immersion period by collecting the spent SBF at each renewal interval from three selected specimens, namely the fully dense reference, the Voronoi lattice with $n = 14$ and $D = 0.3$, and the Gyroid lattice with $l = 3.5$ and $C = 0.3$. These two porous configurations present comparable relative densities and surface areas, which enables a topology-controlled comparison of ion release under equivalent exposure conditions. The use of a reduced subset was adopted because extending ion-release measurements to every geometry and physical replicate included in the mass loss test was not feasible within the available capacity.

At each of the six renewal intervals, corresponding to days 5, 10, 15, 20, 25 and 30 of the immersion period, the entire volume of SBF removed from each specimen container was transferred to a labelled Falcon tube. To prevent iron precipitation and adsorption onto the tube walls during storage, each collected sample was acidified with concentrated nitric acid (Nitric acid ($HNO_3$)) to a target pH below 2. The acidified samples were subsequently stored at 4 °C until submission for analysis.

A total of nineteen samples were submitted, eighteen immersion solutions and one SBF blank collected at the first renewal interval, included to verify the absence of iron in the uncontaminated medium. Prior to analysis, one immersion sample was lost due to inadequate sealing of the transport container, reducing the dataset to eighteen immersion solutions. Iron concentration in each

sample was determined by FAAS at the Departamento de Engenharia Química e Biológica, Universidade do Porto, through direct analysis of the collected solutions, yielding the concentration of soluble iron present in each renewal volume.

### 4.1.6 Scanning Electron Microscopy and Energy-Dispersive X-ray Spectroscopy

Two specimens were selected for surface characterisation at the end of the 30-day immersion period, namely the Voronoi lattice with $n = 10$ and $D = 0.3$ and the Gyroid lattice with $l = 5.0\,\text{mm}$ and $C = 0.2$, corresponding to the lowest-density conditions of each architecture and to those exhibiting the highest corrosion rates recorded in Section 4.2.1. This selection was made independently of the subset used for ion-release quantification by FAAS, as the morphological analysis was considered most informative for the specimens that had undergone the most extensive degradation throughout the test.

Prior to analysis, each specimen was rinsed with distilled water and subsequently placed in an ultrasonic bath with ethanol for 5 min to remove loosely adherent surface deposits whilst preserving the corrosion product layer bonded to the metal substrate. The specimens were then mounted on conductive adhesive tape to ensure electrical contact with the stage and examined without additional conductive coating of the surface of interest, which was considered acceptable given the inherent electrical conductivity of the iron substrate. All analyses were performed at Centro de Materiais da Universidade do Porto (CEMUP), Universidade do Porto, on a FEI Quanta 400 FEG ESEM operated in high-vacuum mode at an accelerating voltage of 15 kV, using a solid-state backscattered electron detector. Elemental analysis was carried out with an EDAX Pegasus X4M energy-dispersive X-ray spectrometer coupled to the same instrument, with point analyses performed on representative zones selected on the basis of the morphological features identified in the SEM images.

## 4.2 Results

### 4.2.1 Mass loss and corrosion rate analysis

The dataset comprises 27 Gyroid and 27 Voronoi specimens, each geometry spanning nine design conditions with three physical replicates, together with three replicates of a fully dense reference specimen. Mass readings were taken at Days 10, 20 and 30, and SBF pH was recorded at every 5-day renewal interval throughout the 30-day test.

#### 4.2.1.1 pH monitoring

Figure 4.1 shows the mean pH per geometry at each renewal interval, with error bars representing the full range (minimum to maximum) of individual readings across all specimens of that geometry. Across all 228 individual pH readings, no value exceeded the ±0.5-unit deviation threshold from the initial value of 7.4 established as the acceptance criterion in Section 4.1.2. The maximum deviation recorded was 0.44 units, observed at Day 5. The reduced solution-to-area ratio therefore did not result in excessive ionic saturation over the 30-day period, and the scheduled 5-day renewal interval was sufficient to maintain physiologically representative solution chemistry throughout the test.

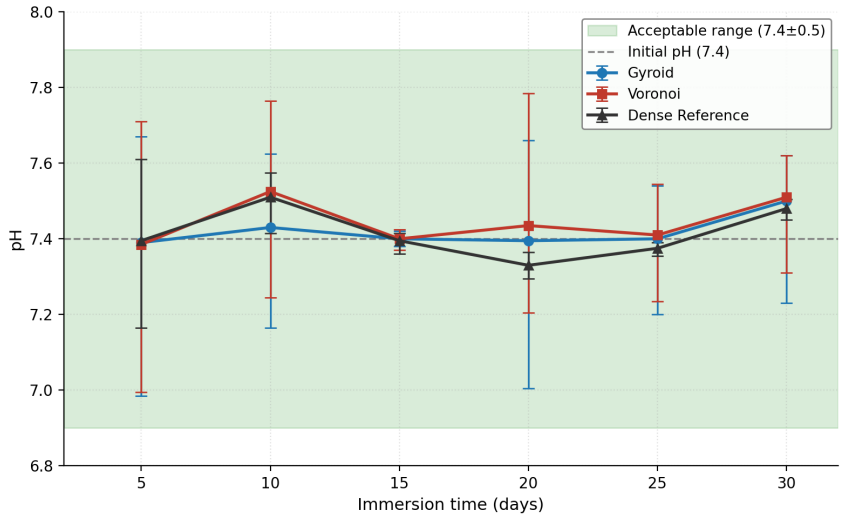



Figure 4.1: Mean pH at each SBF renewal interval for Gyroid, Voronoi and dense reference specimens. Error bars show the full range (min–max) of individual readings. The dashed line marks the initial pH (7.4); the green band marks the ±0.5-unit acceptance range.

#### 4.2.1.2 Mass loss

Figure 4.2 presents the time evolution of mass loss for all nine conditions of each geometry, and Tables 4.3 and 4.4 report the corresponding numerical data. Across both geometries, every condition exhibits a monotonically increasing mass loss with immersion time, and in both cases lower relative density consistently yields higher mass loss throughout the test. Gyroid Day-30 values range from $5.39 \pm 0.15\,\%$ at the lowest-density condition ($l = 5.0$, $C = 0.2$, $\rho_r = 12.7\,\%$) to $1.79 \pm 0.58\,\%$ at the highest resolved condition ($l = 5.0$, $C = 0.8$, $\rho_r = 51.7\,\%$); Voronoi from $6.09 \pm 0.54\,\%$ ($n = 10$, $D = 0.3$, $\rho_r = 11.0\,\%$) to $0.41 \pm 0.09\,\%$ ($n = 18$, $D = 0.7$, $\rho_r = 76.4\,\%$). The dense reference specimens lost $0.44 \pm 0.38\,\%$ by Day 30, closely matching the highest-density porous conditions of both geometries.

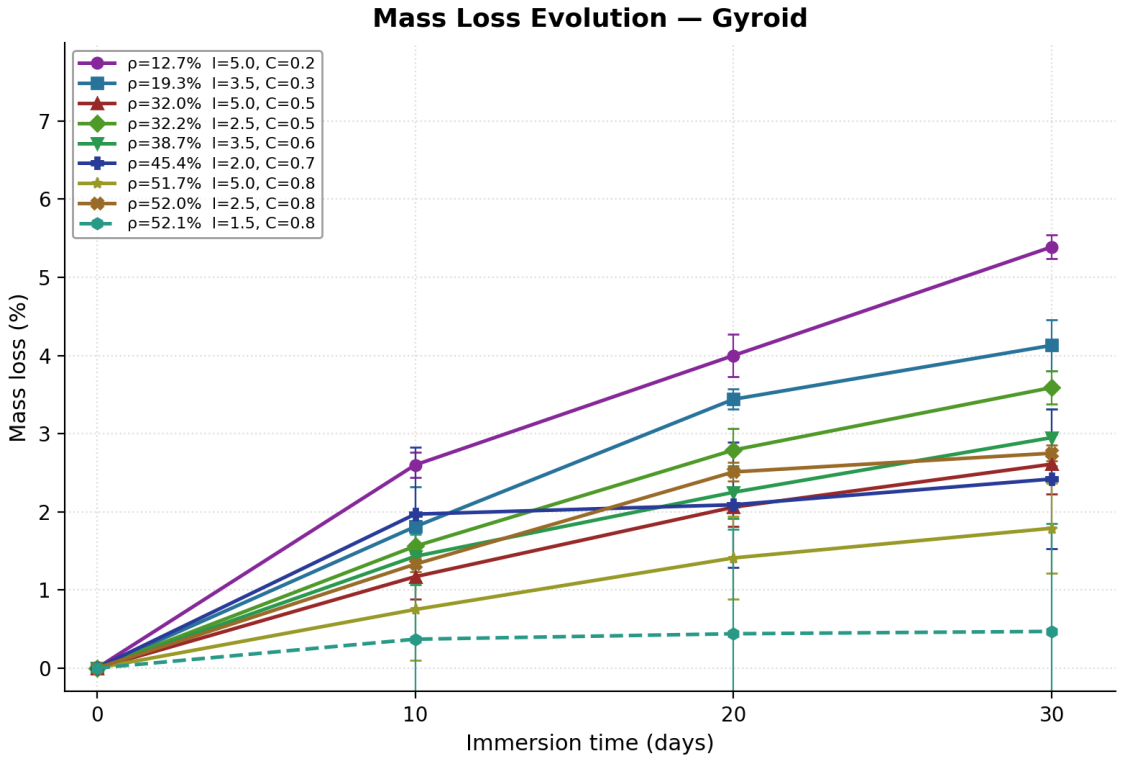
Table 4.3: Gyroid specimens: mean mass loss ($\pm$ SD, %) at Days 10, 20 and 30, ordered by relative density. Values of $\rho_r$ and $A$ are from the parametric study (Section 3.3.2).

| Condition | $\rho_r$ (%) | $A$ (cm$^2$) | Loss D10 (%) | Loss D20 (%) | Loss D30 (%) |
|---|---|---|---|---|---|
| $l = 5.0$, $C = 0.2$ | 12.7 | 15.0 | $2.60 \pm 0.16$ | $4.00 \pm 0.27$ | $5.39 \pm 0.15$ |
| $l = 3.5$, $C = 0.3$ | 19.3 | 21.6 | $1.81 \pm 0.51$ | $3.44 \pm 0.13$ | $4.13 \pm 0.33$ |
| $l = 5.0$, $C = 0.5$ | 32.0 | 15.6 | $1.17 \pm 0.29$ | $2.06 \pm 0.25$ | $2.61 \pm 0.38$ |
| $l = 2.5$, $C = 0.5$ | 32.2 | 29.4 | $1.56 \pm 0.17$ | $2.79 \pm 0.28$ | $3.59 \pm 0.21$ |
| $l = 3.5$, $C = 0.6$ | 38.7 | 21.9 | $1.43 \pm 0.36$ | $2.25 \pm 0.34$ | $2.95 \pm 0.36$ |
| $l = 2.0$, $C = 0.7$ | 45.4 | 35.5 | $1.97 \pm 0.86$ | $2.09 \pm 0.80$ | $2.42 \pm 0.89$ |
| $l = 5.0$, $C = 0.8$ | 51.7 | 15.6 | $0.75 \pm 0.65$ | $1.41 \pm 0.53$ | $1.79 \pm 0.58$ |
| $l = 2.5$, $C = 0.8$ | 52.0 | 28.2 | $1.33 \pm 0.10$ | $2.51 \pm 0.12$ | $2.75 \pm 0.10$ |
| $l = 1.5$, $C = 0.8$ [†] | 52.1 | 45.1 | $0.37 \pm 1.34$ | $0.44 \pm 1.34$ | $0.47 \pm 1.38$ |
| Dense (ref.) | 100 | 6.3 | — | — | $0.44 \pm 0.38$ |

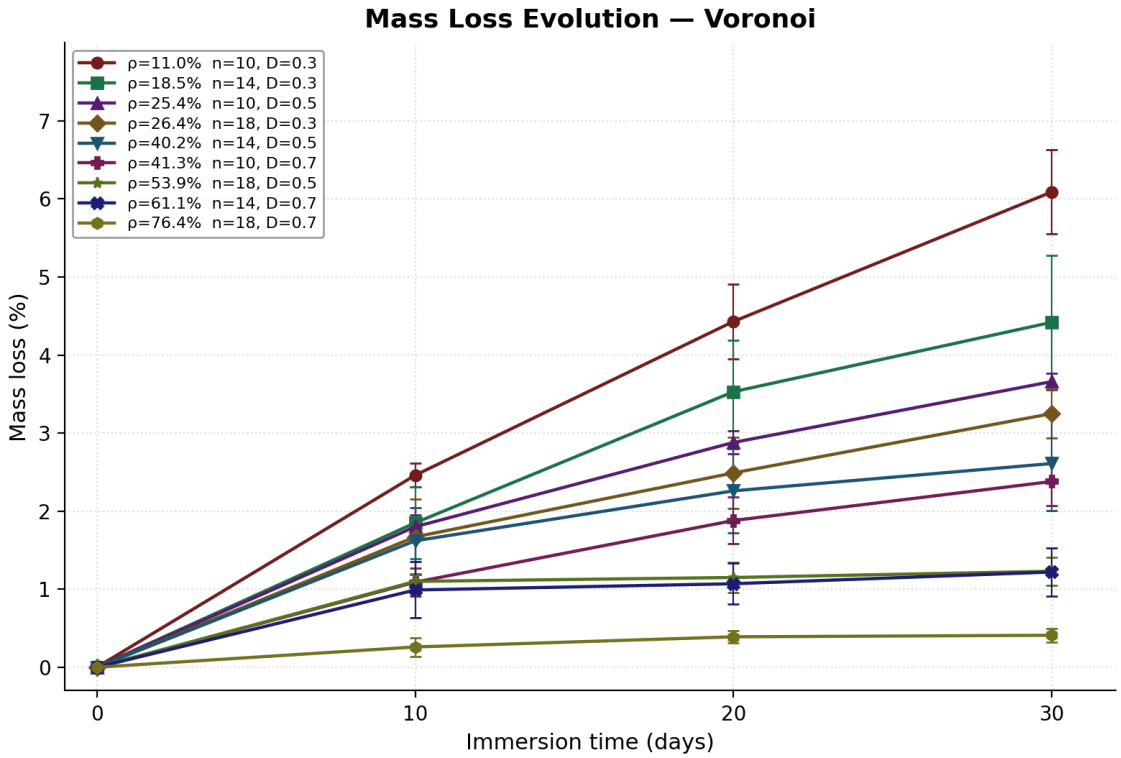
[†] $n = 2$; one replicate excluded due to net mass gain throughout the test (see text).

Table 4.4: Voronoi specimens: mean mass loss ($\pm$ SD, %) at Days 10, 20 and 30, ordered by relative density. Values of $\rho_r$ and $A$ are from the parametric study (Section 3.3.1).

| Condition | $\rho_r$ (%) | $A$ (cm$^2$) | Loss D10 (%) | Loss D20 (%) | Loss D30 (%) |
|---|---|---|---|---|---|
| $n = 10$, $D = 0.3$ | 11.0 | 15.4 | $2.46 \pm 0.15$ | $4.43 \pm 0.48$ | $6.09 \pm 0.54$ |
| $n = 14$, $D = 0.3$ | 18.5 | 24.8 | $1.85 \pm 0.46$ | $3.53 \pm 0.66$ | $4.42 \pm 0.86$ |
| $n = 10$, $D = 0.5$ | 25.4 | 19.8 | $1.80 \pm 0.15$ | $2.88 \pm 0.15$ | $3.66 \pm 0.11$ |
| $n = 18$, $D = 0.3$ | 26.4 | 33.5 | $1.67 \pm 0.48$ | $2.49 \pm 0.46$ | $3.25 \pm 0.31$ |
| $n = 14$, $D = 0.5$ | 40.2 | 28.2 | $1.62 \pm 0.42$ | $2.26 \pm 0.54$ | $2.61 \pm 0.60$ |
| $n = 10$, $D = 0.7$ | 41.3 | 20.7 | $1.09 \pm 0.18$ | $1.88 \pm 0.30$ | $2.38 \pm 0.31$ |
| $n = 18$, $D = 0.5$ | 53.9 | 33.4 | $1.10 \pm 0.09$ | $1.15 \pm 0.19$ | $1.23 \pm 0.18$ |
| $n = 14$, $D = 0.7$ | 61.1 | 25.7 | $0.99 \pm 0.36$ | $1.07 \pm 0.26$ | $1.22 \pm 0.31$ |
| $n = 18$, $D = 0.7$ | 76.4 | 25.4 | $0.26 \pm 0.12$ | $0.39 \pm 0.08$ | $0.41 \pm 0.09$ |
| Dense (ref.) | 100 | 6.3 | — | — | $0.44 \pm 0.38$ |




(a) Gyroid conditions, ordered in the legend from lowest to highest relative density. Dashed line and triangle markers: $l = 1.5$, $C = 0.8$ ($n = 2$; one replicate excluded — see text). Error bars: $\pm 1$ SD.




(b) Voronoi conditions, ordered in the legend from lowest to highest relative density. Error bars: $\pm 1$ SD.

Figure 4.2: Mass loss (%, mean $\pm$ SD) over 30 days of immersion for all nine Gyroid (a) and Voronoi (b) conditions. Colour encodes $\rho_r$ within each architecture.

The ranking of conditions by mass loss is broadly stable over time in both geometries, although not entirely rigid, since the Voronoi preserves it almost perfectly throughout the 30 days while the Gyroid shows two conditions that depart from this pattern in a similar way. The condition $l = 2.0$, $C = 0.7$ records the second-highest mass loss of all nine conditions at Day 10 ($1.97 \pm 0.86\,\%$), yet it accumulates only 0.12 percentage points (pp) between Days 10 and 20 — against 0.66–1.63 pp for most other conditions — and is overtaken by several others by Day 30, finishing with $2.42 \pm 0.89\,\%$. A comparable plateau is observed for $l = 1.5$, $C = 0.8$, which accumulates almost no further mass loss beyond Day 10, going from $0.37 \pm 1.34\,\%$ to only $0.47 \pm 1.38\,\%$ between Days 10 and 30. Since both plateaus are consistent across replicates rather than driven by a single divergent specimen, a measurement artefact appears unlikely, pointing instead to a reproducible feature of these two specific configurations. Notably, both conditions combine intermediate to high density with the second-highest and highest surface areas of the Gyroid set ($\rho_r = 45.4\,\%$, $A = 35.5\,\mathrm{cm}^2$ and $\rho_r = 52.1\,\%$, $A = 45.1\,\mathrm{cm}^2$ respectively).

The dominant role of relative density is evident across the full range of Figure 4.2, since mass loss decreases monotonically with $\rho_r$ in the Voronoi and near-monotonically in the Gyroid, with the exception of the two plateauing conditions ($l = 2.0$, $C = 0.7$ and $l = 1.5$, $C = 0.8$) already noted for their temporal behaviour. This relationship can be quantified through the Pearson correlation coefficient $r$, which measures the strength of a linear association between two variables, with the associated $p$-value testing whether the observed correlation could plausibly arise by chance. When applied to the present data, the correlation between $\rho_r$ and Day-30 mass loss reaches $r = -0.96$ ($p < 0.001$) for the Voronoi and $r = -0.88$ ($p = 0.002$) for the Gyroid, confirming a strong and statistically robust inverse relationship in both geometries.

Since corrosion is fundamentally a surface-mediated process, surface area would be expected, all else being equal, to promote a greater total mass loss, and the Gyroid parametrisation makes it possible to test this directly, since fixing $C$ isolates the density while varying $l$ changes $A$, as established in Section 3.3.2. The three conditions at $C = 0.8$ ($\rho_r \approx 52\,\%$) provide a direct test at constant density, spanning $A = 15.6$, 28.2 and $45.1\,\mathrm{cm}^2$ for $l = 5.0$, 2.5 and 1.5 mm respectively. Contrary to expectation, Day-30 mass loss does not increase monotonically with $A$, since $l = 2.5$ records the highest loss (2.75 %), followed by $l = 5.0$ (1.79 %), while $l = 1.5$, despite having the largest surface area of the entire Gyroid set, records the lowest value of the three (0.47 %, $n = 2$), as shown in Figure 4.3. This inversion cannot be treated as conclusive, however, given the considerable uncertainty carried by the $l = 1.5$ result ($n = 2$, SD = 1.38 %), so it is reported here as an observation whose interpretation is developed further in Section 4.2.1.3, where the corrosion rate offers a complementary and more discriminating perspective on the same data.

In the Voronoi, by contrast, $d$ and $D$ jointly govern both $\rho_r$ and $A$ without an equivalent parametric decoupling, so that the contribution of surface area to mass loss cannot be isolated in the same way. Relative density remains the dominant predictor of mass loss ($r = -0.96$, $p < 0.001$), while surface area adds comparatively little independent predictive value ($r = -0.54$, $p = 0.13$).

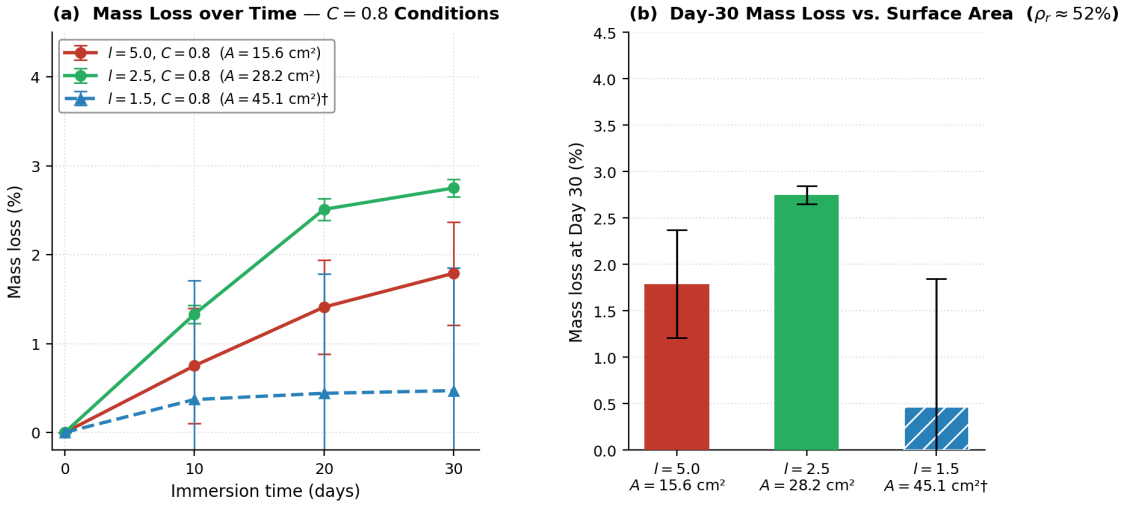


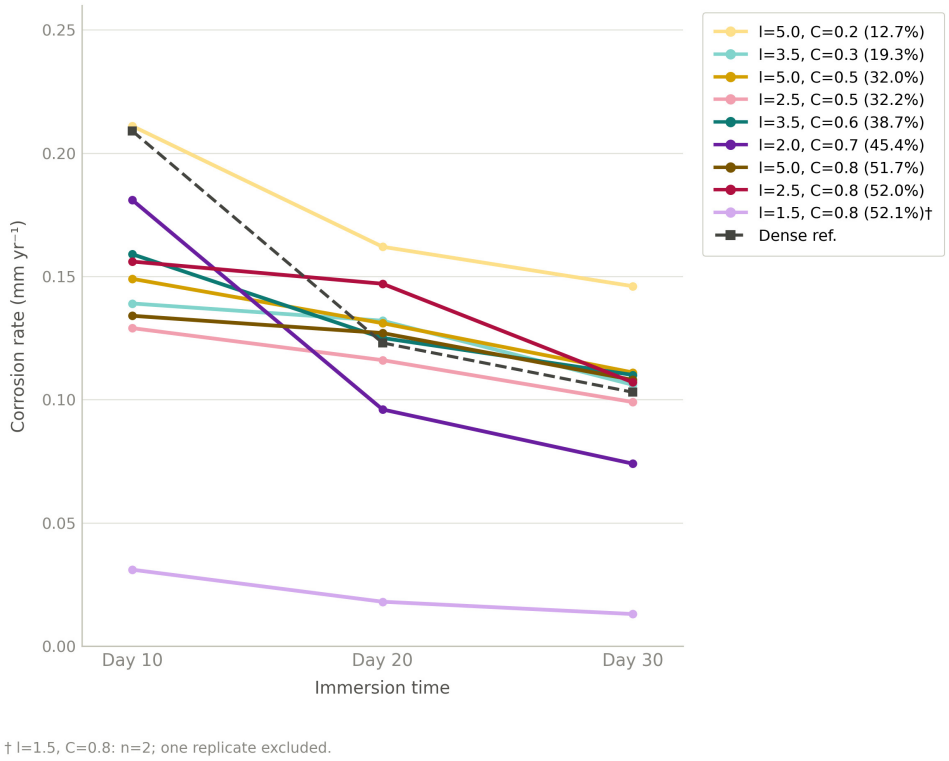

Figure 4.3: The three Gyroid conditions at $C = 0.8$ ($\rho_r \approx 52\%$), isolating the contribution of surface area at constant density. (a) Mass loss evolution over 30 days for the three configurations, with the $l = 1.5$ mm condition ($A = 45.1$ cm$^2$) plotted with a dashed line and triangular markers, denoting the exclusion of one replicate. (b) Day-30 mass loss plotted against surface area $A$ for the same three configurations. Error bars represent $\pm 1$ SD.

This reflects the parametric architecture of the Voronoi lattice rather than a material difference, since the contrast with the Gyroid shows that the relationship between design parameters and degradation depends on the nature of the generative model rather than on the material or process alone.

#### 4.2.1.3 Corrosion rate

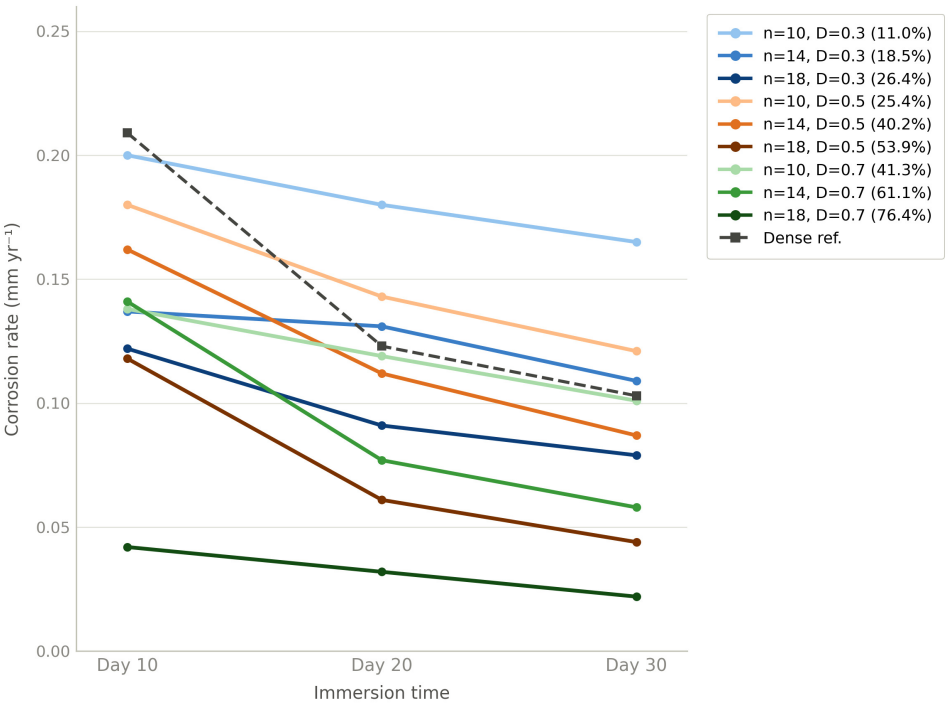
The CR (mm yr$^{-1}$) converts cumulative mass loss into an area-specific reaction intensity by normalising the measured weight loss by the nominal exposed area and immersion time according to Equation 4.1, and constitutes the appropriate metric for comparing conditions whose surface areas span significantly, from 6.3 cm$^2$ for the dense reference to 45.1 cm$^2$ for $l = 1.5$, $C = 0.8$. Figure 4.4 presents its temporal evolution for all conditions of both architectures and the dense reference, and Tables 4.5 and 4.2.1.3 report the corresponding numerical values.

A monotonic decrease in CR from Day 10 to Day 30 is observed across every condition of both architectures without exception, and the dense reference follows the same trajectory, falling from 0.209 mm yr$^{-1}$ at Day 10 to 0.103 mm yr$^{-1}$ at Day 30, confirming that this progressive attenuation belongs to the iron–SBF electrochemical system as a whole rather than being induced by the porous architecture. The behaviour is consistent with the surface passivation mechanism, whereby the gradual accumulation of iron oxyhydroxides, carbonates and phosphate precipitates reduces the effective reactive interface and decelerates dissolution over time [126]. The spread of CR values across conditions is markedly wider at Day 10 than at Day 30, which suggests that




† l=1.5, C=0.8: n=2; one replicate excluded.

(a) Gyroid




(b) Voronoi

Figure 4.4: CR ($\mathrm{mm\,yr^{-1}}$), mean, as a function of immersion time for all nine Gyroid (a) and Voronoi (b) conditions and the dense reference (dashed line with square markers). The legend orders conditions from lowest to highest relative density, with colour encoding $\rho_r$ (lighter shades correspond to lower density). ($l = 1.5$, $C = 0.8$: $n = 2$, one replicate excluded.)

early-stage reaction intensity may be more sensitive to channel geometry, whereas at later stages the accumulating corrosion product layer appears to increasingly affect dissolution across all conditions, tending to attenuate the influence of scaffold topology as it progressively affects every geometry in a similar manner.

Table 4.5: Gyroid specimens: mean CR ($\pm$ SD, mm yr$^{-1}$) at Days 10, 20 and 30, ordered by relative density. $\rho_r$ and $A$ values are from Section 3.3.2.

| Condition | $\rho_r$ (%) | $A$ (cm$^2$) | CR D10 | CR D20 | CR D30 |
|---|---|---|---|---|---|
| $l = 5.0$, $C = 0.2$ | 12.7 | 15.0 | $0.211 \pm 0.013$ | $0.162 \pm 0.011$ | $0.146 \pm 0.004$ |
| $l = 3.5$, $C = 0.3$ | 19.3 | 21.6 | $0.139 \pm 0.040$ | $0.132 \pm 0.004$ | $0.106 \pm 0.008$ |
| $l = 5.0$, $C = 0.5$ | 32.0 | 15.6 | $0.149 \pm 0.036$ | $0.131 \pm 0.016$ | $0.111 \pm 0.016$ |
| $l = 2.5$, $C = 0.5$ | 32.2 | 29.4 | $0.129 \pm 0.017$ | $0.116 \pm 0.014$ | $0.099 \pm 0.008$ |
| $l = 3.5$, $C = 0.6$ | 38.7 | 21.9 | $0.159 \pm 0.040$ | $0.125 \pm 0.019$ | $0.110 \pm 0.013$ |
| $l = 2.0$, $C = 0.7$ | 45.4 | 35.5 | $0.181 \pm 0.080$ | $0.096 \pm 0.037$ | $0.074 \pm 0.028$ |
| $l = 5.0$, $C = 0.8$ | 51.7 | 15.6 | $0.134 \pm 0.117$ | $0.127 \pm 0.048$ | $0.108 \pm 0.035$ |
| $l = 2.5$, $C = 0.8$ | 52.0 | 28.2 | $0.156 \pm 0.176$ | $0.147 \pm 0.009$ | $0.107 \pm 0.004$ |
| $l = 1.5$, $C = 0.8$ [†] | 52.1 | 45.1 | $0.031 \pm 0.109$ | $0.018 \pm 0.054$ | $0.013 \pm 0.038$ |
| Dense (ref.) | 100 | 6.3 | $0.209 \pm 0.247$ | $0.123 \pm 0.144$ | $0.103 \pm 0.089$ |

[†] $n = 2$; one replicate excluded due to net mass gain throughout the test.

Table 4.6: Voronoi specimens: mean CR ($\pm$ SD, mm yr$^{-1}$) at Days 10, 20 and 30, ordered by relative density. $\rho_r$ and $A$ values are from Section 3.3.1.

| Condition | $\rho_r$ (%) | $A$ (cm$^2$) | CR D10 | CR D20 | CR D30 |
|---|---|---|---|---|---|
| $n = 10$, $D = 0.3$ | 11.0 | 15.4 | $0.200 \pm 0.012$ | $0.180 \pm 0.018$ | $0.165 \pm 0.014$ |
| $n = 14$, $D = 0.3$ | 18.5 | 24.8 | $0.137 \pm 0.033$ | $0.131 \pm 0.024$ | $0.109 \pm 0.020$ |
| $n = 10$, $D = 0.5$ | 25.4 | 19.8 | $0.180 \pm 0.216$ | $0.143 \pm 0.010$ | $0.121 \pm 0.006$ |
| $n = 18$, $D = 0.3$ | 26.4 | 33.5 | $0.122 \pm 0.040$ | $0.091 \pm 0.020$ | $0.079 \pm 0.010$ |
| $n = 14$, $D = 0.5$ | 40.2 | 28.2 | $0.162 \pm 0.041$ | $0.112 \pm 0.026$ | $0.087 \pm 0.020$ |
| $n = 10$, $D = 0.7$ | 41.3 | 20.7 | $0.138 \pm 0.024$ | $0.119 \pm 0.020$ | $0.101 \pm 0.014$ |
| $n = 18$, $D = 0.5$ | 53.9 | 33.4 | $0.118 \pm 0.010$ | $0.061 \pm 0.010$ | $0.044 \pm 0.007$ |
| $n = 14$, $D = 0.7$ | 61.1 | 25.7 | $0.141 \pm 0.052$ | $0.077 \pm 0.019$ | $0.058 \pm 0.015$ |
| $n = 18$, $D = 0.7$ | 76.4 | 25.4 | $0.042 \pm 0.020$ | $0.032 \pm 0.006$ | $0.022 \pm 0.005$ |
| Dense (ref.) | 100 | 6.3 | $0.209 \pm 0.247$ | $0.123 \pm 0.144$ | $0.103 \pm 0.089$ |

Given that the CR normalises mass loss by the nominal exposed area, it would be approximately constant across all specimens of the same material if every surface element were equally accessible to the surrounding fluid, and deviations from this expectation therefore reveal the degree to which the nominal geometric area faithfully represents the effective reactive interface. Figure 4.5 revisits the three Gyroid conditions at $C = 0.8$, already examined in Section 4.2.1.2 for their anomalous mass loss behaviour, and shows that the two larger cell sizes, $l = 5.0$ and $l = 2.5$, reach Day-30 CR values of 0.108 and 0.107 mm yr$^{-1}$ respectively, indistinguishable despite an

81 % increase in nominal surface area from 15.6 to 28.2 $cm^2$, confirming that area normalisation adequately captures per-unit-area reaction intensity when the channel network is open enough to sustain diffusion-driven exchange with the surrounding SBF. The $l = 1.5$ mm condition, by contrast, shows a substantially weaker reaction intensity despite having the largest nominal surface area of the entire dataset, and since the CR already accounts for area this result implies that a considerable fraction of that surface is not effectively reactive under static immersion, most plausibly because the narrowest channel network of the entire set progressively restricts internal fluid renewal whilst corrosion precipitates accumulate within it. An analogous comparison in the Voronoi architecture, contrasting $n = 14$, $D = 0.5$ ($\rho_r = 40.2\,\%$, $A = 28.2\,cm^2$) against $n = 10$, $D = 0.7$ ($\rho_r = 41.3\,\%$, $A = 20.7\,cm^2$) at closely matched density, yields Day-30 CR values of 0.087 and 0.101 mm $yr^{-1}$, broadly consistent with the expectation that area normalisation holds when the pore network is adequately interconnected.

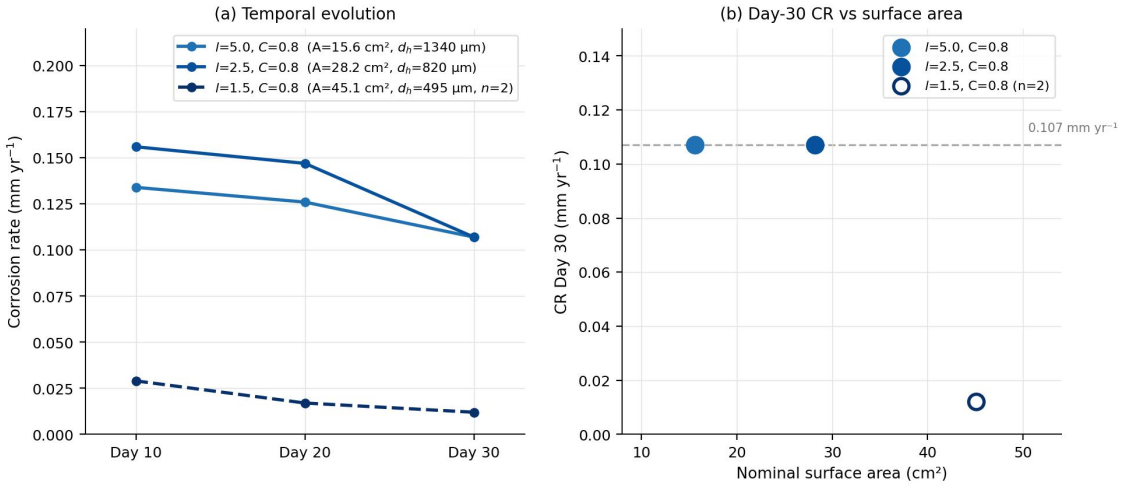



Figure 4.5: The three Gyroid conditions at $C = 0.8$ ($\rho_r \approx 52\,\%$): (a) Temporal evolution of CR over 30 days. (b) Day-30 CR against nominal surface area $A$; the dashed reference marks the common value of 0.107 mm $yr^{-1}$ reached by $l = 5.0$ and $l = 2.5$.

The slow degradation rate of bulk iron, identified in Section 2.5.3 as the principal limitation preventing its clinical use as a biodegradable material, motivates the introduction of porosity as a strategy for accelerating corrosion kinetics through increased surface area exposure. Figure 4.6 tests this expectation directly by ranking the Day-30 CR of all eighteen porous conditions against the dense reference, which serves here as the empirical benchmark for bulk iron behaviour under identical test conditions.

The dense reference falls almost exactly midway across the full distribution, with nine porous conditions recording a higher Day-30 CR and nine recording a lower one. Only half of the fabricated porous conditions, therefore, achieve the accelerated degradation that porosity is expected to confer, indicating that increased surface area alone does not guarantee a faster reaction intensity per unit area, and that the outcome instead depends jointly on relative density and on whether the channel network remains open enough to sustain electrolyte renewal. Among the conditions

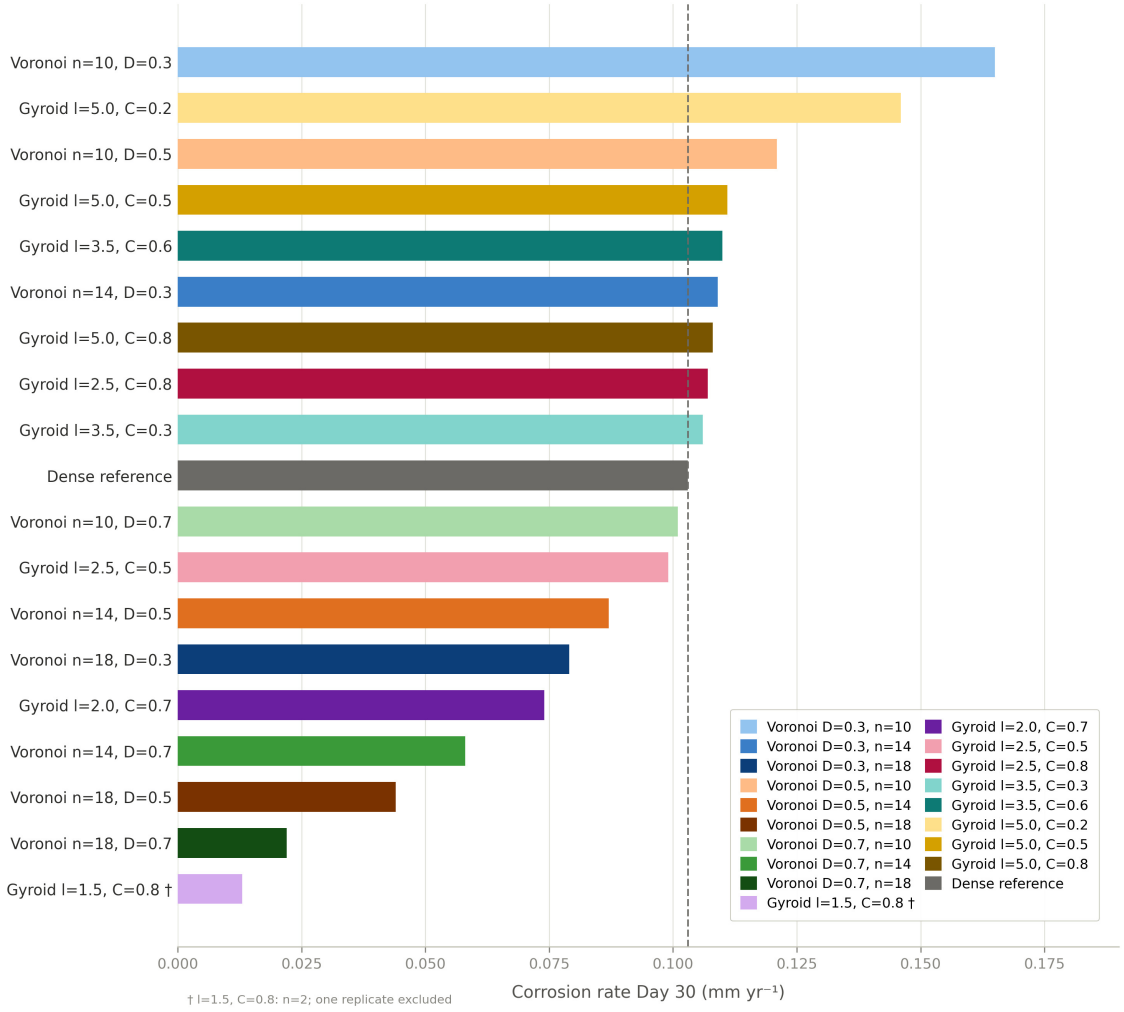



Figure 4.6: Day-30 corrosion rate (mm $\mathrm{yr}^{-1}$, mean) for all conditions of both architectures and the dense reference, ranked in descending order. The vertical dashed line marks the dense reference value (0.103 mm $\mathrm{yr}^{-1}$). $^{\dagger}l = 1.5, C = 0.8$: $n = 2$; one replicate excluded.

that surpass the dense reference, relative density is consistently low to intermediate, consistent with the abundant, freely accessible reactive surface expected at this end of the porosity range. Nevertheless, most conditions falling below the dense reference correspond to higher relative density, where the reduced pore volume per unit of specimen limits the total reactive surface area available, in line with the mechanism established in Section 4.2.1.2 for mass loss. The clearest exception to this density-based pattern is $l = 1.5$, $C = 0.8$, which records the lowest CR of the entire dataset despite a relative density ($\rho_r \approx 52\,\%$) comparable to several conditions positioned well above the dense reference, confirming that channel confinement, rather than density alone, can independently suppress the accelerating effect that porosity is otherwise expected to provide.

The relationship between nominal area and effective reactivity underlying this ranking is further clarified by Figure 4.8, which offers a direct illustration using the highest-density Voronoi condition ($n = 18$, $D = 0.7$, $\rho_r = 76.4\,\%$), one of the conditions falling below the dense reference. The two specimens present virtually identical Day-30 mass losses of 0.44 and 0.41 %, indicating that, over the 30-day window captured here, both specimens exhibit essentially the same degradation behaviour in absolute terms, yet they differ substantially in CR (0.103 against 0.022 mm $\mathrm{yr}^{-1}$) owing solely to the considerable difference in their exposed areas (6.3 against 25.4 $\mathrm{cm}^2$). This difference in CR does not, therefore, reflect a genuine difference in how much material has actually degraded, but rather shows that the accelerating potential porosity is expected to confer has not materialised at this relative density: the additional surface area, while still considerably larger than that of the solid reference, belongs to a specimen dense enough that fluid circulation through the pore network is restricted, an effect that may be further compounded by residual powder retained within the narrowest channels despite the post-fabrication cleaning step described in Section 4.1.1, preventing that larger area from translating into a matching increase in mass loss and instead diluting the resulting CR across a wider surface rather than signalling a genuinely more intense or more favourable degradation process, a pattern that extends to every other condition positioned below the dense reference in Figure 4.6, all of which combine this same elevated relative density with a correspondingly restricted fluid access. This contrast demonstrates concretely why CR, expressed in mm $\mathrm{yr}^{-1}$ under the assumption of uniform mass loss across the nominal surface, measures reaction intensity per unit area rather than a literal penetration rate, and why it should therefore be read alongside mass loss rather than in its place, since an architecturally dissimilar specimen may lose a comparable amount of mass while reacting at a markedly different intensity per unit area.

The inverse pattern holds among the conditions above the dense reference. At low to intermediate relative density, the more open pore network no longer restricts fluid circulation, so the additional surface area translates directly into a faster reaction, bringing the specimen closer to the accelerated degradation that porosity is intended to provide.

This restriction in fluid access is, in fact, a direct consequence of the partial fusion of powder particles already identified in Section 4.2.3. Since this mechanism deposits solid material beyond what was computationally designed, it causes the specimen to depart from its nominal geometry

in a manner that progressively encloses its pores. Consequently, in configurations where the nominal pore size is already small, this excess material is sufficient to nearly close the pore network, bringing the specimen's real morphological characteristics closer to those of the solid reference than its nominal relative density would suggest.

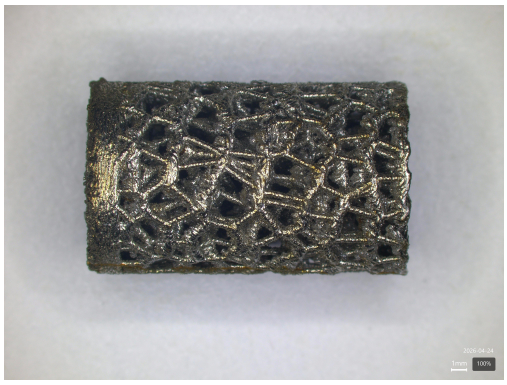
Figure 4.7 illustrates this contrast directly in the as-built condition, prior to any immersion in SBF. The $n = 18$, $D = 0.5$ mm configuration, whose narrower nominal pores already leave comparatively little margin, appears almost entirely closed (Figure 4.7c), whereas the $n = 10$, $D = 0.3$ mm condition, the same low-density specimen examined further in Section 4.2.3, retains a clearly open channel network (Figure 4.7a). A magnified detail of this latter specimen (Figure 4.7b) makes the underlying mechanism directly visible, showing rounded, semi-spherical protrusions along several strut edges, consistent with powder particles adjacent to the melt track that were partially, rather than fully, fused during fabrication. This macroscopic observation is consistent with, and is further corroborated at higher magnification by, the SEM micrographs presented in Section 4.2.3, confirming that the same partial-fusion phenomenon is verifiable across distinct observation scales. This approximation to the solid reference, combined with the density-driven restriction already discussed for the $n = 18$, $D = 0.7$,mm condition above, offers a further explanation for why several nominally porous configurations exhibit a CR at or below that of the fully dense reference.

This finding carries a direct implication for the pore-size discussion in Section 3.3, where pore size was treated as a secondary design metric and most fabricated configurations were found to fall outside the 100–600 µm range, presented in Section 2.2.3 as ideal values for osteointegration, with only the highest-density configurations approaching that benchmark. The present analysis indicates that this shortfall cannot be corrected by simply favouring denser configurations to bring pore size closer to the ideal range, since it is precisely at these higher densities that fluid circulation becomes restricted and the accelerating effect of porosity on iron degradation fails to be accomplished.

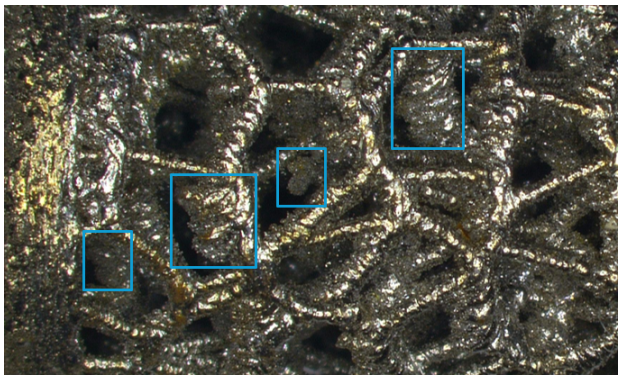
Table 4.7 places the Day-30 values obtained in this study alongside those reported for AM pure iron scaffolds immersed in physiological solutions, the study closest in method and material to the present work [126].

Table 4.7: Day-28/30 corrosion rates from static immersion tests for AM pure iron scaffolds in physiological solutions. All CR values are mass-loss-based and normalised by the nominal geometric surface area according to ASTM G31. $\rho_r$: relative density.

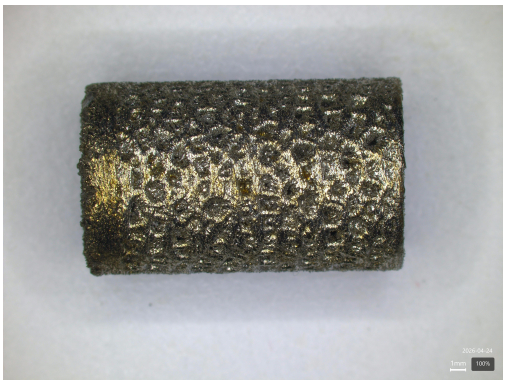
| Reference | Architecture | Fab. | $\rho_r$ (%) | Pore ($\mu$m) | Fluid | Conditions | CR (mm yr$^{-1}$) |
|---|---|---|---|---|---|---|---|
| Li et al. (2018) [126] | Diamond (TPMS) | DMP | 22–27 | ~750 | r-SBF | Static, no renewal, 37°C | 0.030 |
| Present study | Gyroid (TPMS) | L-PBF | 13–52 | 495–2741 | SBF | Static, 5-day renewal, 37°C | 0.013–0.146 |
| Present study | Voronoi | L-PBF | 11–76 | 685–1665 | SBF | Static, 5-day renewal, 37°C | 0.022–0.165 |
| Present study | Dense | L-PBF | 100 | — | SBF | Static, 5-day renewal, 37°C | 0.103 |



(a) $n = 10$, $D = 0.3$ mm



(b) Detail of strut surface



(c) $n = 18$, $D = 0.5$ mm

Figure 4.7: As-built digital stereomicroscope images of two Voronoi configurations prior to immersion in SBF. (a) The $n = 10$, $D = 0.3$ mm condition retains a clearly open, well-resolved channel network. (b) Magnified detail of the strut surface in (a), where rounded protrusions along the strut edges (blue boxes), consistent with partially fused powder particles, are directly visible. (c) The narrower nominal pore size of the $n = 18$, $D = 0.5$ mm condition results in near-complete pore closure.

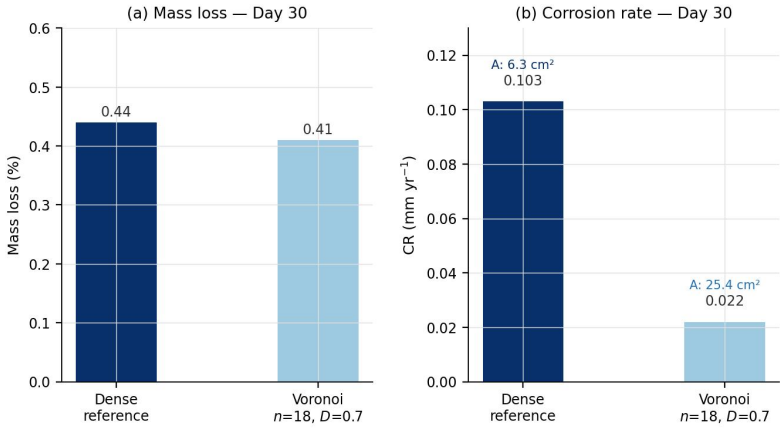



Figure 4.8: Comparison of the dense reference and the highest-density Voronoi condition ($n = 18$, $D = 0.7$, $\rho_r = 76.4\,\%$) at Day 30. (a) Mass loss (%): both specimens record virtually identical values (0.44 and 0.41 %). (b) Corrosion rate (mm $\mathrm{yr}^{-1}$): despite the equivalent mass loss, the CR differs by nearly a factor of five.

Table 4.8 isolates the conditions of the present study whose relative density falls within, or closest to, the 22–27 % range reported by Li et al. (2018), enabling a comparison at matched density rather than across the full explored range.

Table 4.8: Corrosion rate comparison at matched relative density between the present study and Li et al. (2018) [126], the latter reporting $\rho_r = 22$–$27\,\%$. No Gyroid condition falls exactly within this window, so the two closest configurations are included for reference.

| Reference | Architecture | $\rho_r$ (%) | CR (mm yr$^{-1}$) | Comparison Ratio |
|---|---|---|---|---|
| Li et al. (2018) | Diamond (TPMS) | 22–27 | 0.030 | 1.0× |
| Present study | Voronoi ($n = 10$, $D = 0.5$) | 25.4 | 0.121 | 4.0× |
| Present study | Voronoi ($n = 18$, $D = 0.3$) | 26.4 | 0.079 | 2.6× |
| Present study | Gyroid ($l = 3.5$, $C = 0.3$) | 19.3 | 0.106 | 3.5× |
| Present study | Gyroid ($l = 5.0$, $C = 0.5$) | 32.0 | 0.111 | 3.7× |
| Present study | Gyroid ($l = 2.5$, $C = 0.5$) | 32.2 | 0.099 | 3.3× |

At matched density, the CR values obtained here are consistently 2.6 to 4.0 times higher than the 0.030 mm yr$^{-1}$ reported by Li et al. (2018), across both architectures. Both protocols are otherwise very similar, but differ in the presence of a scheduled renewal of the immersion fluid. Li et al. (2018) report no renewal of the r-SBF over their 28-day test, whereas the present protocol renewed the medium every 5 days. This difference in renewal regime, which at the same time approximates to physiological conditions, may itself be an explanation for the gap observed, since a medium left unrenewed for longer periods can approach local ionic saturation and slow the anodic reaction over time.

### 4.2.2 Iron ion release

The SBF blank collected at the first renewal interval returned a soluble iron concentration below the detection limit of the technique ($< 0.6\,\mathrm{g\,L^{-1}}$), confirming that the iron quantified in the immersion solutions originated exclusively from the corrosion of the specimens and not from the surrounding medium.

The monitoring of soluble iron release throughout the immersion period was intended to provide a profile of corrosion activity across the three specimen types. By tracking the concentration of iron mobilised into solution at each five-day renewal interval, it was expected to be possible to characterise how the intensity of the corrosion process evolved over time and whether meaningful differences could be identified between the dense reference and the two porous architectures. Table 4.9 presents the concentrations determined by FAAS at each of the six renewal intervals.

The temporal profiles depicted in Figure 4.9 reveal, however, that achieving this objective is not straightforward given the character of the data obtained. Rather than exhibiting a coherent and

Table 4.9: Soluble iron concentration ($\mathrm{mg\,L^{-1}}$, mean $\pm$ measurement uncertainty) determined by FAAS in the spent SBF collected at each renewal interval for the three specimens selected for chemical analysis. The SBF blank returned a concentration below the detection limit of the technique ($<0.6\,\mathrm{g\,L^{-1}}$). The Day 10 value for the dense reference is unavailable owing to loss of the sample during transit.

| **Renewal interval (day)** | **Dense reference** | **Voronoi** ($n$=14, $D$=0.3) | **Gyroid** ($l$=3.5 **mm**, $C$=0.3) |
|---|---|---|---|
| 5 | $322.7 \pm 0.6$ | $693.6 \pm 2.7$ | $333.4 \pm 0.6$ |
| 10 | — | $880.6 \pm 2.7$ | $648.6 \pm 1.7$ |
| 15 | $464.4 \pm 3.5$ | $528.4 \pm 1.3$ | $720.3 \pm 1.7$ |
| 20 | $680.1 \pm 0.8$ | $644.0 \pm 2.3$ | $948.6 \pm 1.7$ |
| 25 | $565.6 \pm 2.7$ | $533.1 \pm 2.9$ | $533.1 \pm 0.8$ |
| 30 | $484.5 \pm 1.6$ | $426.7 \pm 0.6$ | $369.9 \pm 1.9$ |

interpretable evolution, the concentration profiles of all three specimens are considerably irregular, with values fluctuating between successive intervals in a manner that does not conform to a consistent pattern. This inconsistency is further supported by differences between the profiles of the two porous specimens: the Voronoi architecture presents high concentrations from the outset, reaching a peak at Day 10 before declining, whereas the Gyroid begins at a considerably lower level and rises progressively to its maximum at Day 20, after which it too decreases.

Nevertheless, the loss of the sample carrying the dense reference specimen further undermines the assessment, since it results in the absence of the Day 10 measurement for the dense reference specimen, introducing an additional layer of uncertainty. As a result, the reference profile cannot be traced at this specific point, which corresponds precisely to the interval at which the two porous profiles diverge most markedly, thereby weakening the precision with which this divergence can be interpreted. Equally, the analytical dataset as a whole is limited to a single specimen per group, a constraint that precludes any statistical treatment of the results and substantially reduces the confidence with which differences between specimens can be attributed to differences in corrosion behaviour rather than to individual variability. In view of these constraints, determining whether topology genuinely plays a role in shaping the temporal dynamics of dissolution becomes an even more pressing question, precisely because the resulting inability to draw firm conclusions leaves open the possibility that this factor is in fact relevant.

Notwithstanding these limitations, one observation emerges consistently across all three specimens. Soluble iron concentration decreases from Day 20 onward in each case, a trend that is visible regardless of the differences in profile shape that precede it. Therefore, the convergence of this behaviour across topologically distinct specimens suggests that the corrosion process undergoes a genuine deceleration during the final phase of the immersion period.

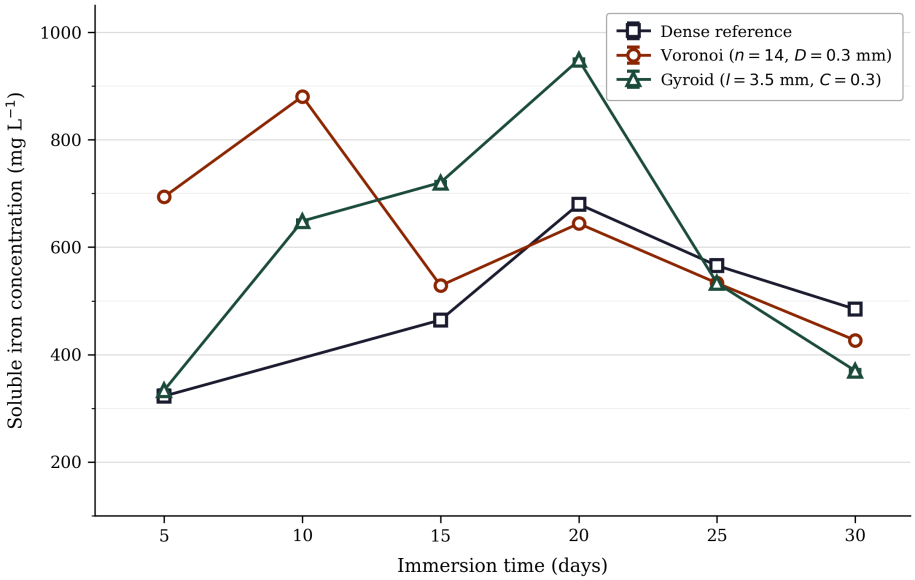
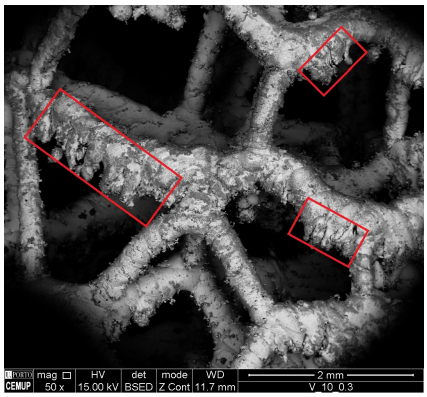



Figure 4.9: Soluble iron concentration (mg L$^{-1}$, mean $\pm$ measurement uncertainty) measured by FAAS in the spent SBF collected at each of the six renewal intervals (Days 5, 10, 15, 20, 25 and 30) for the dense reference, the Voronoi specimen ($n = 14$, $D = 0.3$ mm) and the Gyroid specimen ($l = 3.5$ mm, $C = 0.3$).

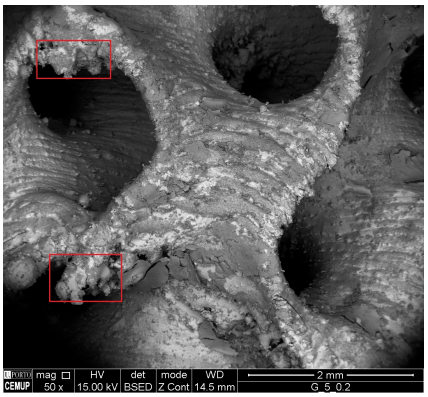
### 4.2.3 Surface morphology and corrosion product characterisation

SEM imaging of both specimens at low magnification revealed extensive corrosion product coverage across the entirety of the porous network following the 30-day immersion period, with no region of either architecture remaining unaffected by surface degradation, which is an observation consistent with the corrosion rates recorded for both conditions throughout the test (Section 4.2.1). In addition to this corrosion product layer, both micrographs also reveal a generalised surface roughness along the strut and wall surfaces, attributed to partial fusion of powder particles adjacent to the melt track during fabrication, whereby heat conducted from the melt pool into the surrounding powder bed is sufficient to bond neighbouring particles. This mechanism is directly visible in the regions highlighted in Figure 4.10, where rounded, semi-spherical protrusions extend from the strut and wall surfaces of both specimens, corroborating at higher magnification the same partially fused powder particles already observed at the as-built stage in the stereomicroscope images of Section 4.2.1.3.

On one hand, the Voronoi specimen (Figure 4.10a) shows its stochastic arrangement of struts, varying in diameter and orientation, uniformly enveloped by a heterogeneous deposit layer, with the original strut geometry still discernible beneath this surface coverage. On the other hand, the Gyroid specimen (Figure 4.10b) likewise displays generalised surface coverage, yet here the characteristic curvature of the triply periodic minimal surface architecture remains visible beneath the corrosion product layer along the continuous curved struts.




(a) Voronoi ($n = 10$, $D = 0.3$)

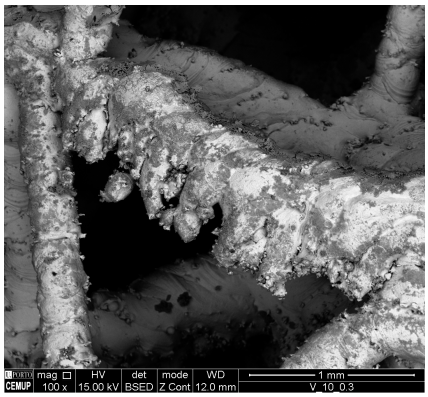



(b) Gyroid ($l = 5.0\,\text{mm}$, $C = 0.2$)

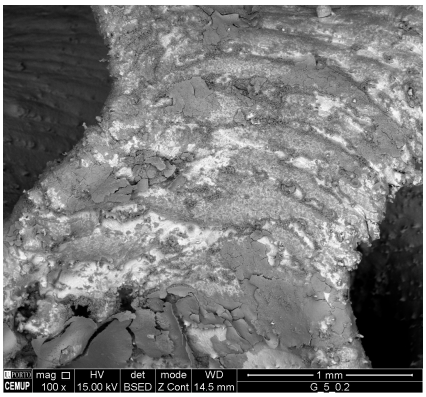
Figure 4.10: SEM micrographs (50×) of corrosion product distribution after 30 days of immersion in SBF. (a) HV = 15 kV, WD = 11.7 mm. (b) HV = 15 kV, WD = 14.5 mm. Red boxes indicate representative regions of rounded, semi-spherical protrusions consistent with partially fused powder particles.

To examine this surface coverage in greater detail, additional micrographs were acquired at higher magnification, as presented in Figure 4.11. As evidenced there, the SEM images reveal a clear contrast between distinct surface regions in both specimens, exposing a heterogeneous surface in which zones of markedly different brightness coexist across the strut surfaces. The brightest regions correspond to areas where the metallic iron substrate is directly exposed, iron being the heaviest element present and therefore producing the strongest backscattered electron signal under compositional contrast imaging. The darker regions, by contrast, are attributed to corrosion product phases in which iron is associated with lighter elements such as oxygen, reducing the mean atomic number of the layer relative to the underlying metal and thereby lowering the backscattered signal intensity. The spatial alternation of these contrasting zones across both specimens provides direct morphological evidence of active surface degradation, demonstrating the capacity of SEM imaging to spatially resolve the corrosion front at the strut scale and distinguish regions of intact metal from those transformed by the degradation process.

The corrosion product layer exhibits additional morphological detail when examined at closer range in both specimens, as depicted in Figure 4.12. The metallic regions identified by their elevated brightness exhibit localised surface depressions and topographical irregularities that are consistent with areas from which partially adherent corrosion products were detached during the ultrasonic cleaning step, leaving behind impressions of the former deposit on the metal surface. This observation suggests that the corrosion product layer had developed with spatially variable adhesion to the substrate, with more weakly bonded regions preferentially removed during cleaning whilst more adherent zones remained intact. In the areas where the layer is preserved, its finite thickness becomes visible at the edges of cracks and spalled regions, where the cross-sectional relief of the deposit above the underlying metal is visible, providing direct evidence that the degradation process resulted in the formation of a three-dimensional product layer rather than a mere



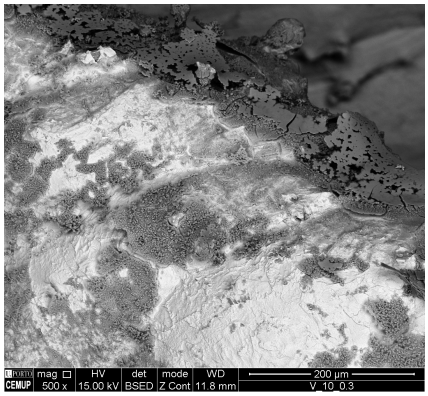

(a) Voronoi ($n = 10$, $D = 0.3$)



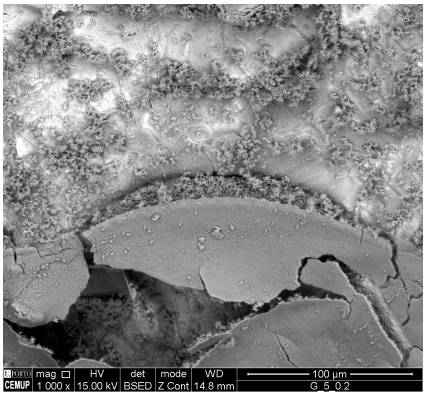

(b) Gyroid ($l = 5.0\,\text{mm}$, $C = 0.2$)

Figure 4.11: SEM micrographs (100×) showing the contrast between exposed metallic iron regions and corrosion product zones after 30 days of immersion in SBF. (a) HV = 15 kV, WD = 12.0 mm. (b) HV = 15 kV, WD = 14.5 mm.

surface discolouration.




(a) Voronoi ($n = 10$, $D = 0.3$)




(b) Gyroid ($l = 5.0\,\text{mm}$, $C = 0.2$)

Figure 4.12: SEM micrographs (500–1000×) showing surface depressions on exposed metallic regions and the thickness of the corrosion product layer at crack edges after 30 days of immersion in SBF. (a) HV = 15 kV, WD = 11.8 mm. (b) HV = 15 kV, WD = 14.8 mm.

EDS point analysis was performed on selected zones identified in the SEM images of both specimens (Figure 4.13), with the aim of determining the elemental composition of the morphologically distinct regions observed at the surface. In the zones corresponding to the bright metallic regions, namely Z3 in the Voronoi specimen and Z6 in the Gyroid specimen, iron constitutes virtually the entirety of the detected signal, with no oxygen contribution above the noise level, which confirms that these areas represent the unoxidised metallic substrate exposed at the surface.

Beyond these principal constituents, the spectra of the corrosion product zones also reveal the presence of chlorine, sodium and sulphur, elements characteristic of the ionic composition of the SBF, whose incorporation into the surface layer reflects the chemical interaction between the corroding substrate and the immersion medium throughout the test period. Notably absent from all

analysed zones across both specimens are calcium and phosphorus, whose detection would constitute the primary compositional evidence for the formation of hydroxyapatite, and no crystalline morphology consistent with such a phase is observed in the preceding images. Consequently, these observations lead to the conclusion that hydroxyapatite formation was not detected at the surface of either specimen, and that the combined SEM/EDS evidence does not support the occurrence of a bioactive response under the conditions employed.

Finally, aluminium is consistently detected in the corrosion product zones of both specimens but is absent from the metallic substrate regions. Although an artefact originating from the aluminium stub would account for this pattern, this hypothesis was experimentally discarded by acquiring a spectrum under equivalent beam conditions on a redundant metallic zone, which returned no detectable aluminium signal. The source of this element could therefore not be conclusively established within the scope of the present analysis.

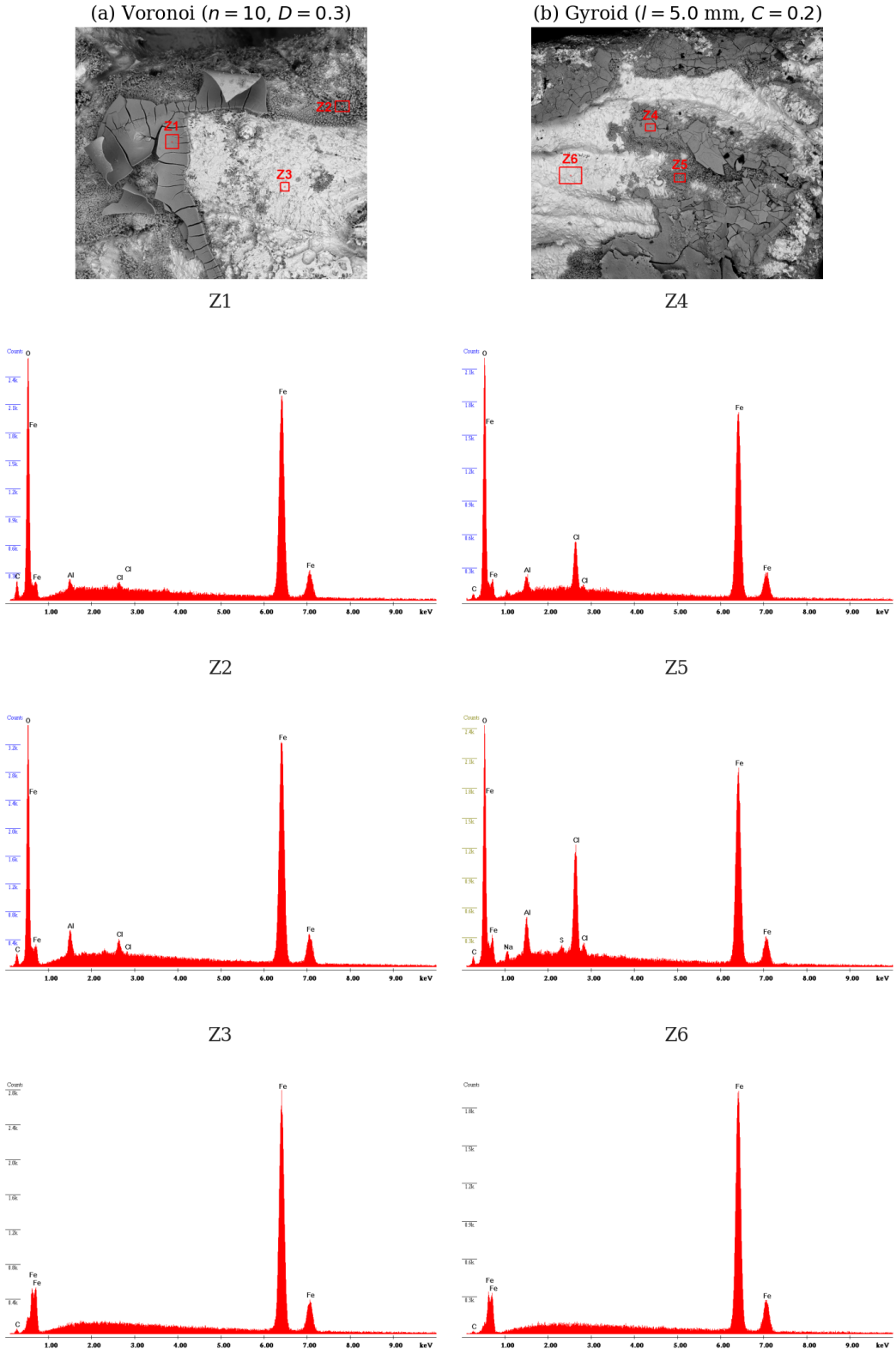



Figure 4.13: SEM micrographs with identified EDS analysis zones and corresponding point spectra acquired at 15 kV following 30 days of immersion in SBF. (a) Voronoi ($n = 10$, $D = 0.3$). (b) Gyroid ($l = 5.0$ mm, $C = 0.2$).

Chapter 5

# Numerical Finite Element Simulation

The two previous chapters addressed the morphological definition of the Voronoi and Gyroid architectures and their degradation response under simulated physiological conditions. However, neither characterisation speaks directly to the property that ultimately justifies the use of a porous architecture in the first place. The rationale behind introducing porosity into a metallic implant, as established in Chapter 2, is to bring its stiffness closer to that of the surrounding bone, mitigating stress shielding and preserving the mechanical stimulus that healthy tissue requires to remain functional. Whether a given configuration actually delivers this reduction, cannot be exclusively inferred from relative density or surface area alone, since neither descriptor translates directly into a stiffness or strength value.

Therefore, that is the mission this chapter intends to accomplish, reporting the finite element analysis carried out on the eighteen specimens, nine Voronoi and nine Gyroid, with the aim of extracting their compressive stress strain response and thereby quantifying the apparent stiffness and strength associated with each architecture and relative density. The specimens were dimensioned as right circular cylinders of 10 mm in diameter and 15 mm in height, with a height to diameter ratio of 1.5 consistent with the recommendations for compression testing of porous and cellular metals, so that the numerical model reproduces, in idealised form, the uniaxial compression conditions prescribed for this class of materials. Within this framework, the simulations were performed in Abaqus following a single procedure applied consistently throughout, so that the mechanical behaviour of the two architectures could be compared on equal terms and traced back to the parameters that generated each geometry.

## 5.1 Surface mesh pre-processing

The triangulated geometries generated in Chapter 3 were produced by marching cubes extraction from the implicit Voronoi and Gyroid fields, followed by immediate post-processing within the design framework. Although this procedure delivered meshes that were suitable for morphological characterisation, the necessary mesh quality for volumetric discretisation and finite element analysis was not verified. In particular, the resulting STL files could still present non manifold edges, residual holes, small disconnected components and irregular triangle size. Such defects undermine the generation of a stable solid mesh, with direct consequences for the reliability of the subsequent simulation.

### 5.1.1 Open-source processing attempt

An open-source pipeline was implemented in Python, combining established libraries for polygonal mesh handling, automatic defect correction and isotropic remeshing. Beyond the basic manifold correction applied during geometry generation, this approach additionally targeted mesh

size reduction and triangle homogenisation through remeshing, aiming to obtain geometries that were both topologically valid and better conditioned for volumetric discretisation.

Table 5.1 illustrates the outcome for a representative Voronoi specimen. The first repair stage successfully resolved the non-manifold edges and restored the watertight condition without any measurable change in volume, confirming that the correction was geometrically conservative. The subsequent remeshing operation, however, reintroduced a substantial number of non-manifold edges and left the surface open, despite having operated on an already valid geometry. Although a final sealing stage recovered a watertight and manifold mesh, the recurrence of these defects after remeshing suggested that this approach lacked the robustness required to handle the geometric complexity of the architecture.

Table 5.1: Mesh integrity metrics across the stages of the open-source repair pipeline, for a representative Voronoi specimen.

| Stage | Faces | Watertight | Non-manifold edges | Self-intersections | Volume ($mm^3$) |
|---|---|---|---|---|---|
| Original (Post-generation) | 6,347,332 | No | 26 | None | 809.049 |
| After first repair | 6,347,320 | Yes | 0 | None | 809.049 |
| After remeshing | 393,370 | No | 12 | None | 810.429 |
| After final sealing | 392,884 | Yes | 0 | None | 810.437 |

Even when the final surface passed all integrity checks, the generation of a solid volumetric mesh in the downstream software still failed. The precise causes could not be conclusively determined, though they are likely rooted in residual local irregularities that global metrics do not capture, namely non-uniform triangle size distribution and surface curvature discontinuities, which volumetric discretisation algorithms are known to be sensitive to.

### 5.1.2 Global repair and remeshing in Geomagic

Given the inability of the open-source approach to consistently produce surfaces suitable for volumetric discretisation, the pre-processing workflow was migrated to Geomagic, a commercial environment offering more robust and controllable mesh editing tools. Each specimen was processed following a fixed sequence of operations applied consistently across the specimen set, in order to obtain a standardised processing procedure, summarised in Figure 5.1.

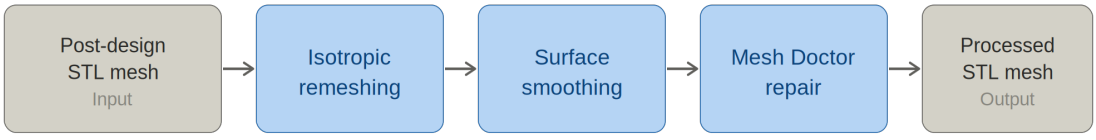
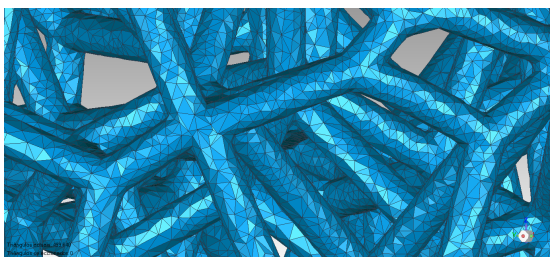
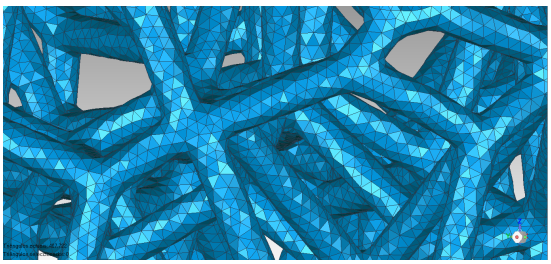



Figure 5.1: Overview of the Geomagic processing workflow, from the post-design STL mesh to the final processed output.

The first operation was isotropic remeshing, with a target edge length defined relative to the volumetric element size intended for Abaqus. This produced a surface density suited to solid discretisation, while also reducing the overall triangle count and making the element distribution more uniform. In doing so, it mitigated the size disparities and elongated triangles inherited from the decimated post-designed mesh, as illustrated in Figure 5.2. A smoothing pass followed, attenuating surface noise while preserving the curvature features of each architecture. Lastly, the Mesh Doctor utility was then applied to detect and correct the residual topological defects that remained after remeshing, including non-manifold edges, open boundaries, small components and self-intersections, bringing each surface to a watertight and manifold condition.



(a) Surface prior to remeshing, showing irregular triangle size and elongated elements.

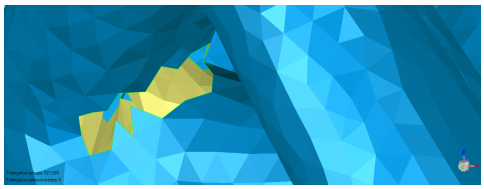


(b) Same region after processing workflow, with a more uniform triangle size and distribution.

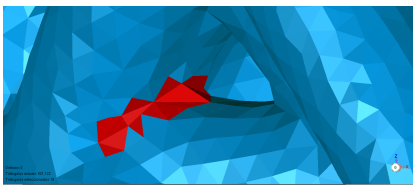
Figure 5.2: Comparison of surface triangulation before and after isotropic remeshing.

Even so, some localised regions still required manual correction that the automated tools could not fully resolve. Two distinct situations were encountered in this respect and are illustrated in Figures 5.3 and 5.4.

The first situation was not exclusive to a single architecture, and inspection of the repaired surfaces occasionally revealed localised anomalies pointing to potential sources of defects or artefacts in the volumetric mesh generation. Therefore, they were corrected by removing the affected elements, as shown in Figure 5.3a for a representative Voronoi specimen, and reconstructing the local surface as a smooth patch tangent to the surrounding faces, conserving the original curvature, as shown in Figure 5.3b. This procedure was repeated wherever such anomalies appeared across the specimen set, functioning essentially as a precautionary measure to minimise the risk of compromising the subsequent meshing stage.



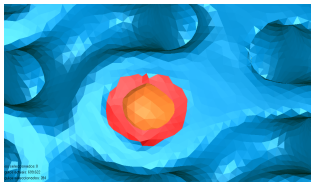
(a) Critical zone triangles removed, exposing the underlying void prior to surface reconstruction.



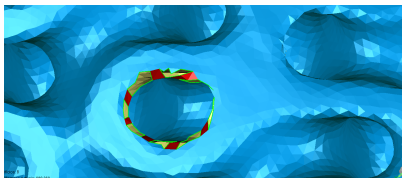
(b) Local surface reconstructed tangentially to the surrounding geometry, restoring continuity.

Figure 5.3: Manual correction sequence applied to localised boundary anomalies in a Voronoi specimen.

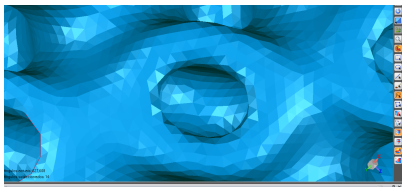
The second situation arose whenever reconstructing a defective region would compromise the original architecture, due to the excessive removal of triangles it required, calling for a different approach. This was the case for the sheet-based Gyroid architecture, where the automated hole-filling routine could not distinguish an intentional aperture from a genuine hole, and sealed both indiscriminately, as shown in Figure 5.4a. To preserve the intended topology, a bridge-based strategy was used instead. Thin polygonal bridges were built manually to guide the reconstruction, constraining the fill to the defective region without closing the intended void, as shown in Figure 5.4b. These bridges allowed the surface to be reconstructed with a tangent fill that restored the original architecture, as shown in Figure 5.4c.



(a) Incorrect closure produced by the standard hole-filling routine.



(b) Bridges constructed manually to guide the reconstruction.



(c) Final surface with the local topology restored.

Figure 5.4: Bridge-guided reconstruction strategy applied to residual open boundaries in a Gyroid specimen.

## 5.2 Simulation setup

The surface geometries produced by the processing workflow described in Section 5.1.2 were imported into Abaqus as STL files, where they served as the basis for volumetric discretisation. Each specimen was meshed independently using four-node linear tetrahedral elements (C3D4). The element type and target element size adopted across the specimen set were determined by a mesh convergence study, described in Section 5.2.4, and applied uniformly to all eighteen specimens to ensure consistency throughout the simulation study. The following subsections describe

the complete simulation setup adopted for every specimen, from material definition through to the output requests extracted from each analysis.

### 5.2.1 Material Definition

The material considered throughout all simulations is pure iron produced by L-PBF, whose selection and general characterisation were presented in Chapter 2. Given that the applied displacement of 1 mm corresponds to a nominal compressive strain of approximately 6.7 % on a 15 mm gauge length, the mechanical response of the material is expected to extend beyond the elastic regime. Accordingly, an elasto-plastic constitutive model was adopted, requiring the independent definition of both elastic and plastic components.

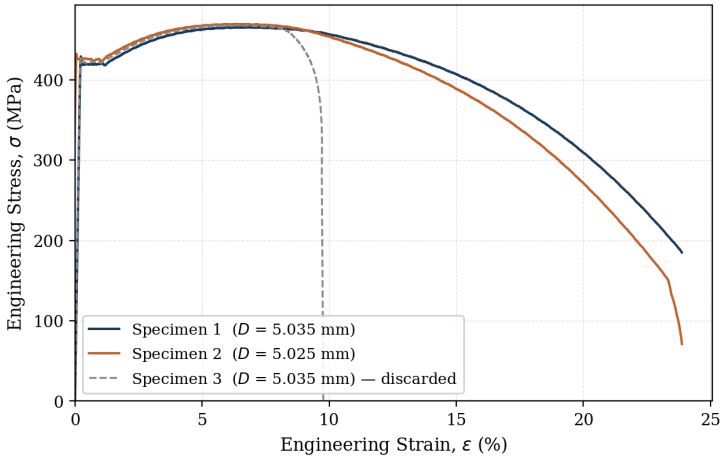
The elastic properties adopted in the simulations are summarised in Table 5.2. The Young's modulus was determined from uniaxial tensile tests performed on L-PBF fabricated pure iron specimens produced within the scope of this project, while the Poisson's ratio was set to a value consistent with prior simulation studies carried out by the same research group on the same material system [67, 68, 97].

Table 5.2: Elastic properties of pure iron adopted in the finite element simulations.

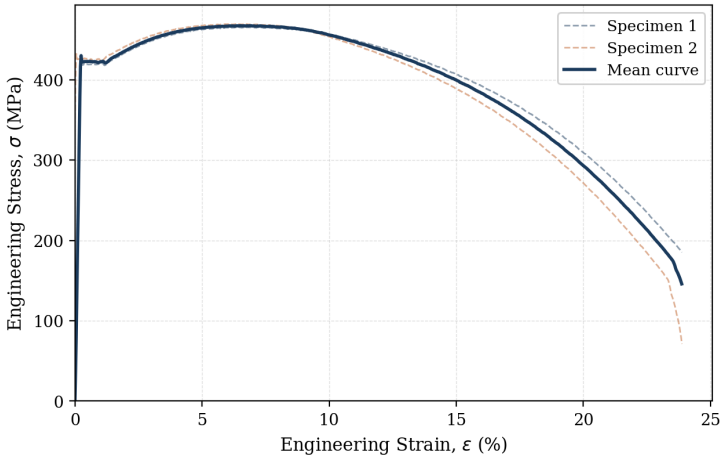
| **Property** | **Value** |
|---|---|
| Young's modulus, $E$ | 207.3 GPa |
| Poisson's ratio, $\nu$ | 0.29 |

The plastic behaviour was characterised from a set of three uniaxial tensile tests performed on L-PBF-fabricated pure iron specimens of the same material and processing condition, with the resulting engineering stress-strain curves presented in Figure 5.5a. Inspection of the three responses reveals that Specimen 3 fractured at approximately 9.8 %, well below the elongations reached by the other two specimens, a premature failure more consistent with a localised defect in the specimen than with the intrinsic material response. Specimen 3 was therefore identified as an outlier and excluded from further processing, leaving Specimens 1 and 2 as the basis for the mean curve. Since only a single test remained beyond the fracture point of Specimen 2, at approximately 23.9 %, the mean would no longer be statistically representative past that strain, and the two curves were accordingly compared only up to this common limit. The resulting mean engineering stress-strain curve, computed from Specimens 1 and 2 over their common strain range, is shown in Figure 5.5b, overlaid with the two contributing curves for reference.

The mean engineering curve, however, cannot be introduced directly into Abaqus as the material plasticity input. As stated in the Abaqus documentation, plasticity data must be defined in terms of true stress and true strain, since the solver operates internally with Cauchy stress and with strain measures referenced to the current deformed configuration rather than to the original




(a) Engineering stress-strain curves obtained from the three tensile specimens. Specimen 3 was excluded as an outlier owing to premature fracture at approximately 9.8 % strain.




(b) Mean engineering stress-strain curve computed from the two retained specimens, overlaid with the individual contributing curves.

Figure 5.5: Tensile test results used to characterise the plastic behaviour of pure iron: (a) curves of all three specimens, and (b) mean curve computed from the two retained specimens.

geometry [131]. Providing engineering quantities instead would therefore cause the solver to misinterpret the material response as strains grow beyond the small-strain regime [131]. The mean curve was accordingly converted to true stress, which accounts for the actual, instantaneous cross-sectional area of the specimen, and true strain, which accumulates incrementally with respect to the current gauge length, both describing the actual deformed state of the material at each loading instant and thus consistent with the finite-deformation framework adopted by the solver. This conversion follows the standard relations

$$\sigma_{\text{true}} = \sigma_{\text{eng}}\,(1+\varepsilon_{\text{eng}}), \qquad \varepsilon_{\text{true}} = \ln(1+\varepsilon_{\text{eng}}). \tag{5.1}$$

Applying Equation 5.1 to the mean engineering curve yields the true stress-strain response shown in Figure 5.6.

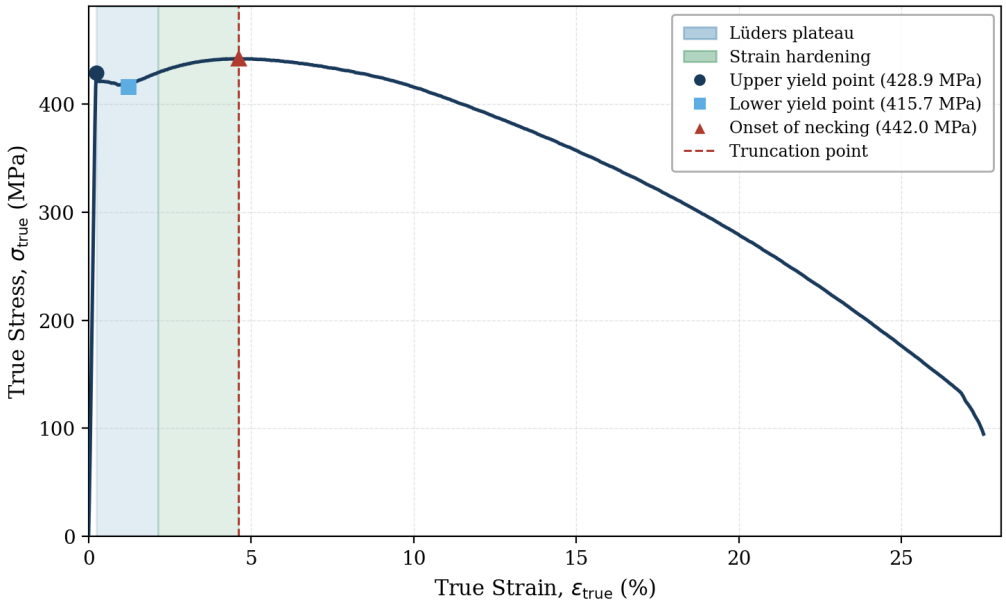



Figure 5.6: True stress-strain curve obtained from the mean engineering curve via Equation 5.1, with identification of the main deformation regimes. The dashed vertical line marks the onset of necking, beyond which the conversion is no longer physically valid.

The resulting curve exhibits a sequence of responses characteristic of L-PBF-fabricated pure iron [132]. After the elastic regime, the stress reaches an upper yield point at approximately 429 MPa and drops to a lower yield point of around 416 MPa, a behaviour associated with the Lüders phenomenon, in which dislocations pinned by interstitial solute atoms are collectively released upon reaching the critical stress and a localised plastic band propagates through the specimen at near-constant stress [133, 134].

The material then enters strain hardening, in which dislocation multiplication progressively increases resistance to further plastic flow, raising the true stress steadily to a peak of approxi-

mately 442 MPa at 4.6 % true strain. This peak corresponds to the point at which the rate of strain hardening can no longer compensate for the reduction in cross-sectional area, so that deformation ceases to be stable and uniform along the gauge length [135]. Beyond this point, plastic flow concentrates locally in a single region, the neck, where the area decreases far faster than in the remainder of the specimen, causing the load the specimen can sustain to fall and producing the characteristic decline of the engineering curve seen in Figure 5.5b. The conversion expressed in Equation 5.1, however, is derived under the assumption of homogeneous and uniform deformation along the gauge length, an assumption that is fundamentally violated once necking begins, such that applying it beyond the peak would give true stress values that systematically underestimate the actual stress state within the neck.

Since the conversion is no longer physically valid beyond the peak, the data past this point were discarded and the true stress-strain curve was retained only up to the point of maximum stress. The plastic component of the material definition was then derived by subtracting the elastic strain from the total true strain at each point, giving true stress as a function of true plastic strain as required by the **PLASTIC* option in Abaqus

$$\varepsilon_p = \varepsilon_{\text{true}} - \frac{\sigma_{\text{true}}}{E}, \tag{5.2}$$

where the first point corresponds to the initial yield stress at zero plastic strain [131]. The tabulated plasticity input in Abaqus further requires the stress to be a monotonically non-decreasing function of plastic strain [131]. The derived curve violates this condition immediately after yielding, where the stress drops from the upper yield point of approximately 429 MPa to the lower yield point of around 416 MPa, corresponding to the Lüders plateau described previously [133]. This region was therefore smoothed by holding the stress constant at the upper yield value throughout the plateau, a simplification whose effect is limited to approximately 9 MPa, under 2 % of the local flow stress, and is considered negligible.

Beyond the last defined data point, Abaqus automatically holds the flow stress constant at the peak value of 442 MPa, effectively extending the response as perfect plasticity [131]. Although the maximum plastic strain developed locally in the simulation may exceed the truncation point of approximately 4.4 %, the discrepancy introduced by the perfect plasticity assumption is expected to be small, given that the true stress-strain curve had only just reached its peak at the truncation point and had not yet begun to descend appreciably. The stress adopted by the solver beyond this limit therefore is expected to remain a close approximation to the actual material response in that range.

The plastic flow curve supplied to Abaqus is shown in Figure 5.7, overlaid with the full true stress-strain curve for comparison.

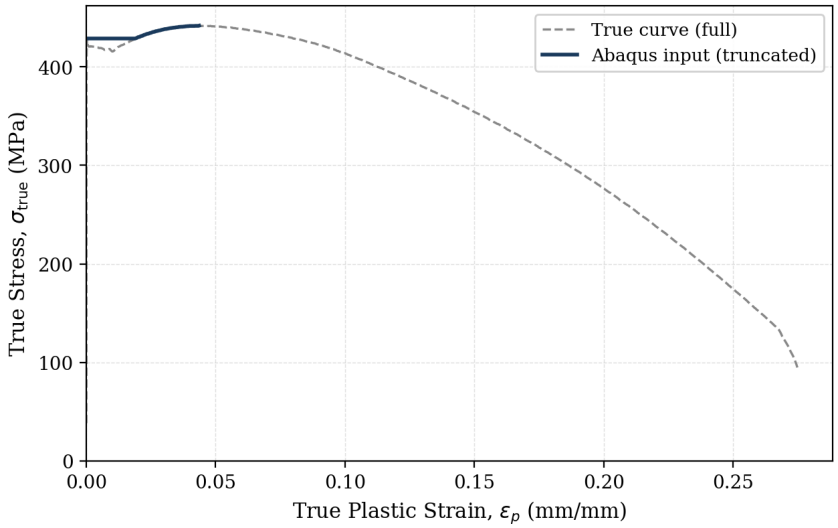



Figure 5.7: Plastic flow curve supplied to Abaqus as a function of true plastic strain, overlaid with the full true stress-strain curve. The input data are limited to the region of valid engineering-to-true conversion and monotonically non-decreasing flow stress, beyond which perfect plasticity is assumed by the solver.

### 5.2.2 Boundary conditions

Firstly, two node sets were defined to apply the boundary conditions, as depicted in Figure 5.8. `SET_BASE` comprised all nodes within 0.25 mm of the bottom face of the specimen, and `SET_TOP` comprised all nodes within 0.25 mm of the top face. This thickness was chosen to ensure that a sufficient number of nodes was captured across all specimen geometries, while remaining small enough to avoid including nodes belonging to the interior of the structure.

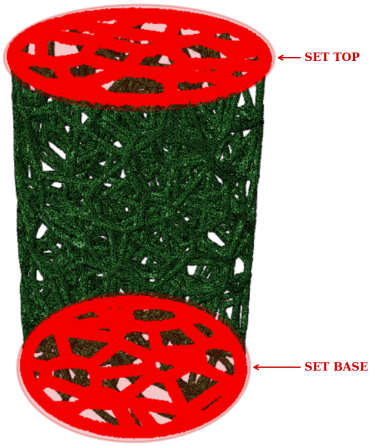
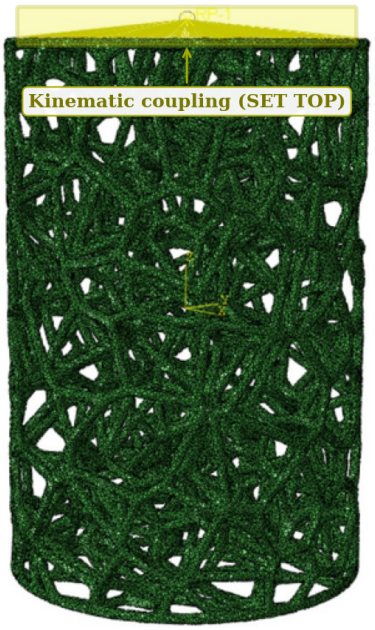


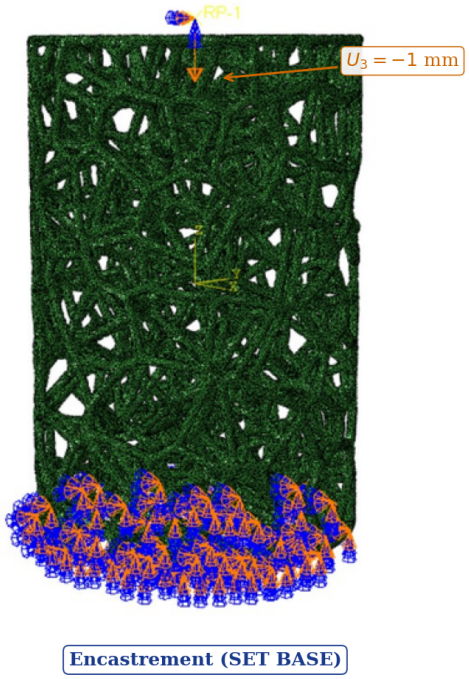

Figure 5.8: Node sets defined for the application of boundary conditions, shown for a representative Voronoi specimen.

The base of each specimen was fully fixed by constraining all translational and rotational degrees of freedom of `SET_BASE` directly, replicating the condition of a rigid support in a compression test. At the top, a Reference Point (RP) was created 1 mm above the centroid of the top face and connected to `SET_TOPO` through a kinematic coupling constraint with all six degrees of freedom active, as illustrated in Figure 5.9a. This constraint forces the nodes of `SET_TOPO` to follow the rigid-body motion defined by the RP, reproducing the effect of a rigid loading platen in contact with the top surface without explicitly modelling contact. A pair of rigid surfaces interacting through a frictional contact formulation would represent the experimental boundary condition most closely, as it allows for the platen-specimen interface to develop non-uniform pressure and relative sliding. However, for a flat top surface loaded in pure compression, a kinematic coupling constraint enforces the same rigid, uniformly distributed displacement boundary that a fully bonded rigid platen would impose, since, by definition, this constraint restricts the motion of the coupled nodes to the rigid-body motion defined by the reference point [136]. It is therefore considered an adequate and computationally efficient representation of a rigid loading platen for capturing the global load-displacement response of the specimen. To ensure that the coupled surface displaces strictly along the loading axis, all displacement and rotation components of the RP other than the axial one were constrained to zero, and the compressive displacement of 1 mm was applied to the remaining active degree of freedom ($U_3 = -1\,\text{mm}$), as depicted in Figure 5.9b. This guarantees that `SET_TOPO` moves as a rigid body purely in the axial direction, without residual in-plane translation or rotation that would otherwise remain unconstrained under the kinematic coupling alone.

For the Gyroid specimens, the periodic nature of the TPMS geometry allows the cylindrical domain to be reduced to one quarter of its full cross-section, as illustrated in Figure 5.10. This reduction was performed in Geomagic prior to meshing and yields a mechanical response identical to that of the full model, under the assumption of geometric and loading symmetry. Two additional boundary conditions were applied on the planar cut faces to enforce this symmetry. `XSYMM` ($U_1 = UR_2 = UR_3 = 0$) was applied on the face normal to the $x$-axis and `YSYMM` ($U_2 = UR_1 = UR_3 = 0$) on the face normal to the $y$-axis, as depicted in Figure 5.10b. The reaction force extracted at the RP was accordingly multiplied by four in post-processing to recover the total force acting on the full cross-section. In contraste, the Voronoi specimens,lacking geometric periodicity, were simulated as full cylinders without symmetry reduction.

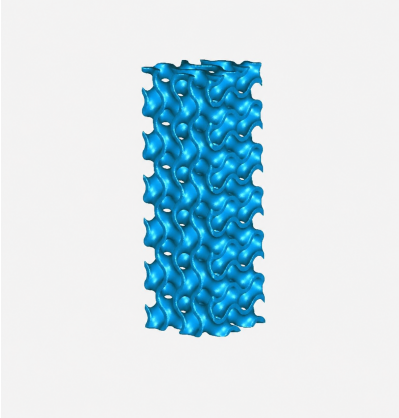



(a) Kinematic coupling constraint between RP and SET_TOP.

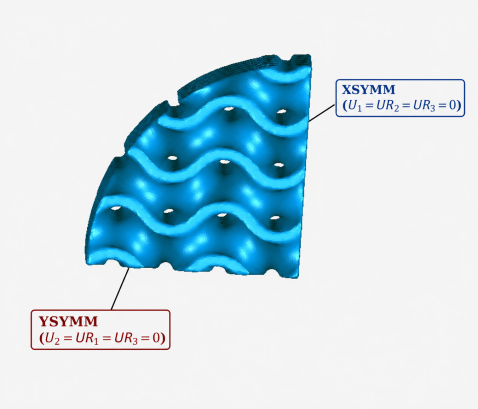



(b) Boundary condition setup showing $U_3 = -1\,\text{mm}$ at the RP and encastrement of SET_BASE.

Figure 5.9: Boundary conditions applied to each specimen.



(a) Quarter-symmetry model (lateral view).




(b) Quarter-symmetry model (top view) with `XSYMM` and `YSYMM` boundary conditions applied on the planar cut faces.

Figure 5.10: Symmetry reduction applied to the Gyroid specimens: (a) lateral view of the full cylindrical domain, and (b) top view of the one-quarter model with the symmetry boundary conditions used to reproduce the response of the full geometry.

### 5.2.3 Analysis procedure and output requests

All simulations were performed using a Static General step, which solves the equilibrium equations quasi-statically through an implicit integration scheme. This procedure was selected as the loading is applied monotonically and inertia effects are considered negligible, making a dynamic formulation unnecessary [131]. Furthermore, geometric nonlinearity was activated (`NLGEOM=ON`), meaning that equilibrium is enforced on the deformed configuration and strain measures account for finite deformations. This was considered appropriate given that the applied displacement of 1 mm over a cylindrical specimen of 15 mm height corresponds to a nominal compressive strain of approximately 6.7 %, a level at which the small-deformation assumption becomes questionable [131].

The output requested from each simulation was limited to the quantities necessary to reconstruct the compressive stress-strain curve of each specimen. The reaction force in the loading direction (`RF3`) and the displacement along the same axis (`U3`) were both extracted at the reference point of the top coupling constraint. These quantities were subsequently used to compute the apparent stress and strain according to

$$\sigma = \frac{F}{A_0}, \qquad \varepsilon = \frac{U}{L_0}, \tag{5.3}$$

where $F$ is the reaction force, $U$ the displacement of the reference point, $A_0 = \pi(D/2)^2$ the nominal cross-sectional area of the cylindrical specimen with diameter $D = 10\,\text{mm}$, and $L_0 = 15\,\text{mm}$ the nominal height. Because the quarter model was adopted to exploit the symmetry of the

Gyroid architecture, however, the reaction force $F$ used in this case had already been multiplied by four, as described in Section 5.2.2, so that it would reflect the load acting on the full cross-section rather than on the reduced domain alone. The displacement $U$ did not require an equivalent adjustment, given that the symmetry cut only affected the cross-sectional planes and left the axial dimension of the specimen unchanged. Consequently, $A_0$ and $L_0$ in Equation 5.3 could always be taken as the nominal dimensions of the full cylindrical specimen, independently of whether the underlying simulation had been performed on the full geometry or on the one-quarter model.

The resulting stress-strain curve was then used to extract two mechanical properties for each specimen. The apparent elastic modulus was determined by fitting a linear regression to the initial elastic region of the curve, identified as the range over which the local tangent stiffness remained consistent with the initial slope. The apparent yield strength was subsequently identified using the 0.2 % offset method, in accordance with ISO 13314:2011, the standard governing compression testing of porous and cellular metallic materials, in which a line parallel to the initial elastic slope is offset by a strain of 0.002, and its intersection with the stress-strain curve defines the yield point.

Table 5.3 summarises the key modelling choices adopted throughout the simulation campaign, consolidating the decisions described across the preceding subsections into a single reference for the finite element setup common to all eighteen specimens.

Table 5.3: Summary of the finite element simulation setup adopted for all specimens.

| **Aspect** | **Adopted setting** |
|---|---|
| Element type | Four-node linear tetrahedral element (`C3D4`) |
| Element size | Determined by mesh convergence study (Section 5.2.4), applied uniformly to all specimens |
| Elastic properties | $E = 207.3$ GPa, $\nu = 0.29$ |
| Plastic behaviour | True stress–true plastic strain curve derived from the mean tensile response |
| Base boundary condition | Rigid support, achieved by fully encastring the base node set (`SET_BASE`) |
| Top boundary condition | Rigid loading platen, achieved by coupling the top node set (`SET_TOP`) kinematically to a reference point (RP) and applying an axial displacement of 1 mm ($U_3 = -1$ mm), with the remaining RP degrees of freedom fixed |
| Symmetry reduction | One-quarter model with planar symmetry boundary conditions (`XSYMM`/`YSYMM`) for Gyroid specimens; full cylinder for Voronoi specimens |
| Analysis step | Static General step with geometric nonlinearity enabled (`NLGEOM=ON`) |
| Output requested | Axial reaction force and displacement at the reference point (`RF3`, `U3`) |

### 5.2.4 Mesh Convergence Study

Before conducting the main set of simulations, a mesh convergence study was conducted to ensure that the discretisation was sufficiently fine for the mechanical response to be independent of the mesh. A convergence criterion of 5 % was adopted, consistent with the threshold applied in comparable finite element studies of porous scaffolds [17]. To guard against false convergence, in which two refinement levels that are both inadequate produce similar results and thus satisfy the criterion without the solution being mesh-independent, a minimum of three refinement levels was required before any conclusion could be drawn. This requirement ensures that at least two consecutive pairs are available for evaluation, allowing the trend of the solution with increasing refinement to be characterised rather than inferred from a single comparison.

The element size was not defined as an absolute dimension common to all specimens. The present study encompasses eighteen geometries whose strut or wall thickness varies substantially across both architectures and relative density levels, and imposing a fixed absolute element size would produce discretisations of inconsistent resolution relative to the governing geometric feature. To avoid this, the target edge length supplied to the isotropic remeshing step in Geomagic was defined in proportion to the characteristic thickness of the solid phase of each specimen, so that a comparable number of elements was maintained across the solid phase cross-section irrespective of the absolute dimensions involved. This criterion mirrors the approach adopted in finite element studies of trabecular bone, where element size is prescribed relative to trabecular thickness, and is particularly well suited to the present context given that the Voronoi struts and Gyroid walls constitute the structural analogue of individual trabeculae [137].

Since it was not computationally feasible to conduct independent convergence studies for all eighteen specimens, the study was instead carried out on the most critical geometry of each architecture, defined as the one with the thinnest solid phase, and the resulting elements-per-thickness ratio was then applied uniformly across the remaining specimens of the same architecture.

#### 5.2.4.1 Voronoi Architecture

For the Voronoi architecture, the smallest nominal strut diameter, $D = 0.3$ mm, is shared by the $n = 10$, $n = 14$, and $n = 18$ configurations, of which the $n = 10$ specimen was selected as the critical case. Its realised strut diameter was confirmed to be 0.301 mm, as reported in Section 3.3.1.4. The convergence study was therefore conducted on this specimen, and it was on this architecture that the mesh sensitivity analysis was first carried out, establishing the discretisation criterion later extended to the Gyroid architecture (Section 5.2.4.2).

The study was initiated using quadratic tetrahedral elements (C3D10), illustrated alongside the linear formulation in Figure 5.11. The ten-node quadratic tetrahedron places additional nodes at the midpoint of each edge, thereby enabling a quadratic displacement field within each element.

This formulation offers two complementary advantages over its linear counterpart. On one hand, stress and strain gradients are captured more accurately within a single element, a feature particularly relevant in geometries with pronounced curvature such as the Voronoi strut junctions and the Gyroid sheet surfaces. On the other hand, fewer elements are required to achieve a given level of accuracy, which in turn reduces the computational cost relative to a linear mesh of equivalent precision [14, 17].

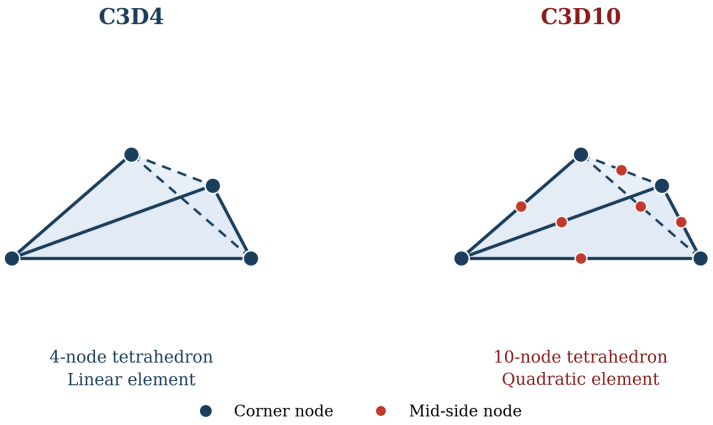



Figure 5.11: Comparison between the linear tetrahedral element (C3D4, 4 nodes) and the quadratic tetrahedral element (C3D10, 10 nodes).

Two element sizes were evaluated, namely $e = 0.15$ mm, corresponding to two elements across the strut diameter, and $e = 0.10$ mm, corresponding to three elements across the strut diameter. The peak apparent stress obtained at each level, together with the associated node counts, is summarised in Table 5.4, and the corresponding convergence behaviour and stress-strain curves are presented in Figure 5.12.

Table 5.4: Mesh convergence study for the Voronoi $n$=10, $D$=0.3 mm specimen using quadratic tetrahedral elements (C3D10). Peak apparent stress is taken as the convergence indicator. The third refinement level ($e = 0.075$ mm) could not be completed owing to computational resource constraints.

| Element size (mm) | Elem./thickness | Nodes | Peak stress (MPa) | Δ (%) |
|---|---|---|---|---|
| 0.15 | 2 | 651,681 | 6.806 | — |
| 0.10 | 3 | 1,316,559 | 7.651 | 11.0 |
| 0.075 | 4 | 4,985,171 | *simulation did not complete* | |

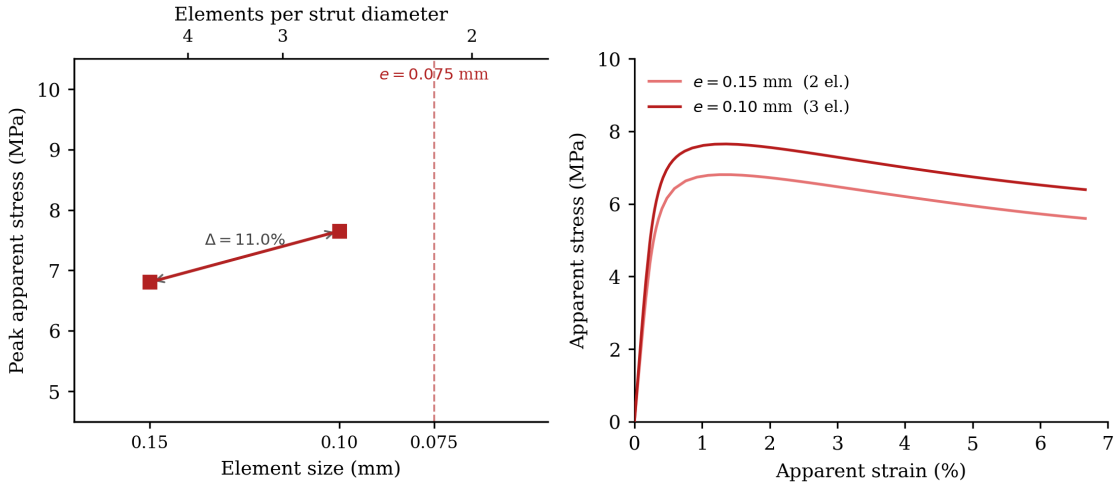



Figure 5.12: Mesh convergence study for the Voronoi $n$=10, $D$=0.3 mm specimen using C3D10 elements. Left: peak apparent stress as a function of element size; the dashed vertical line at $e = 0.075$ mm marks the refinement level at which the simulation could not be completed due to computational resource constraints. Right: apparent stress-strain curves for the two simulated refinement levels.

The difference between the two simulated levels exceeded the 5 % convergence criterion, confirming that a mesh-independent solution had not yet been achieved at three elements per strut diameter. Progression to the subsequent refinement level of four elements per strut diameter ($e = 0.075$ mm, 4,985,171 nodes) reached the limit of the available computational resources and could not be completed. Given this constraint, the use of C3D10 elements was abandoned and the convergence study was restarted using four-node linear tetrahedral elements (C3D4).

Five refinement levels were evaluated with the C3D4 formulation, ranging from $e = 0.15$ mm to $e = 0.05$ mm, and the corresponding results are presented in Table 5.5 and Figure 5.13.

Table 5.5: Mesh convergence study for the Voronoi $n$=10, $D$=0.3 mm specimen using linear tetrahedral elements (C3D4). Peak apparent stress is taken as the convergence indicator.

| Element size (mm) | Elem./thickness | Nodes | Peak stress (MPa) | Δ (%) |
|---|---|---|---|---|
| 0.15 | 2 | 107,683 | 11.873 | — |
| 0.10 | 3 | 326,329 | 11.516 | 3.1 |
| 0.075 | 4 | 719,347 | 10.828 | 6.4 |
| 0.06 | 5 | 1,234,249 | 9.661 | 12.1 |
| 0.05 | 6 | 2,034,519 | 9.302 | 3.9 |

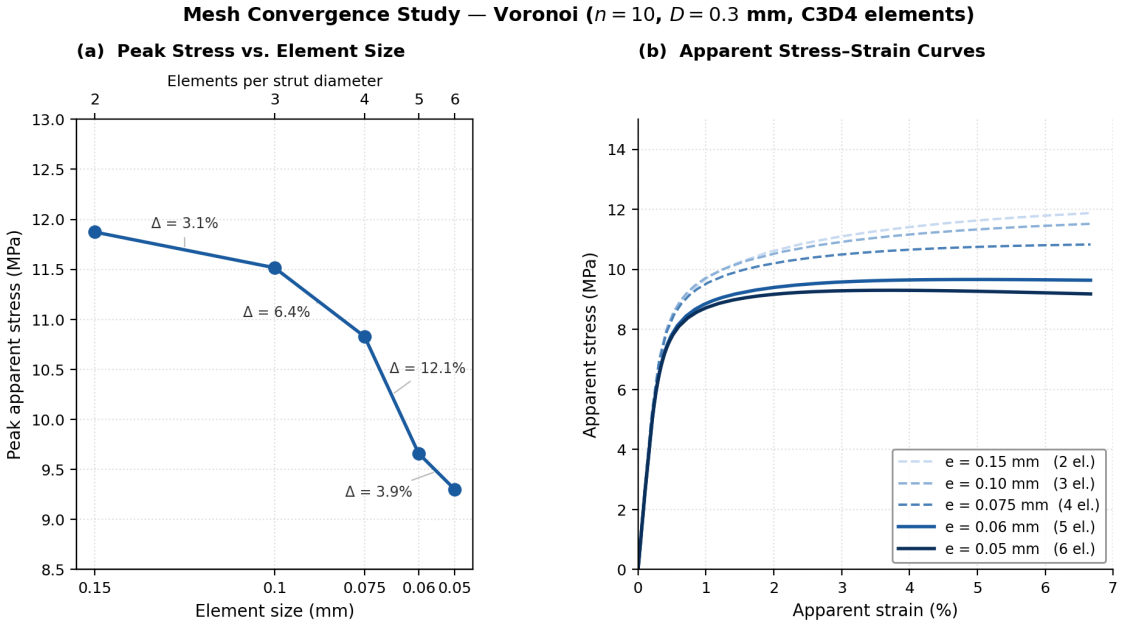



Figure 5.13: Mesh convergence study for the Voronoi $n$=10, $D$=0.3 mm specimen using C3D4 elements. Left: peak apparent stress as a function of element size, with the difference between each pair of consecutive refinement levels indicated. Right: apparent stress-strain curves for all five refinement levels, with the two finest levels shown as solid lines.

The results reveal a non-monotonic variation in the consecutive differences, with the initial pair ($e = 0.15$ mm to $e = 0.10$ mm) yielding a difference of only 3.1 %, followed by a progressive increase to 6.4 % and 12.1 % at the subsequent levels, before falling to 3.9 % between $e = 0.06$ mm and $e = 0.05$ mm. This behaviour is consistent with the transition from a zone of false stability, in which the coarser meshes are similarly inadequate and therefore produce comparable results, to the region where the mesh begins to resolve the stress gradients at the strut junctions, after which the solution stabilises. Had the minimum three-refinement requirement not been imposed, the 3.1 % difference obtained at the second level would have satisfied the criterion prematurely, leading to an incorrect conclusion regarding mesh independence. The enforced continuation of the study to five levels was therefore essential to correctly identify the onset of genuine convergence, which occurs between the five- and six-element levels with $\Delta = 3.9\,\%$. Accordingly, the element size of $e = 0.06$ mm was selected as the discretisation standard for all Voronoi specimens. For each configuration, the target edge length supplied to Geomagic was set to $D_i/5$, where $D_i$ denotes the nominal strut diameter, thereby preserving the converged ratio throughout the full specimen set.

As an additional verification of the adopted discretisation criterion, a cross-validation was carried out on the remaining strut diameters, $D = 0.5$ mm and $D = 0.7$ mm, to confirm that the observed variation in peak stress remained within the 5 % criterion at the two refinement levels bracketing convergence in the primary study. The peak apparent stress obtained at each level and the corresponding difference are reported in Table 5.6, and the stress-strain curves are shown in

Figure 5.14.

Table 5.6: Cross-validation of the discretisation criterion for the Voronoi $n$=10 specimen at strut diameters $D$=0.5 mm and $D$=0.7 mm. Peak apparent stress is taken as the convergence indicator.

| $D$ (mm) | Element size (mm) | Elem./thickness | Peak stress (MPa) | Δ (%) |
|---|---|---|---|---|
| 0.5 | 0.100 | 5 | 41.761 | — |
| | 0.083 | 6 | 43.812 | 4.7 |
| 0.7 | 0.140 | 5 | 79.723 | — |
| | 0.117 | 6 | 75.922 | 5.0 |

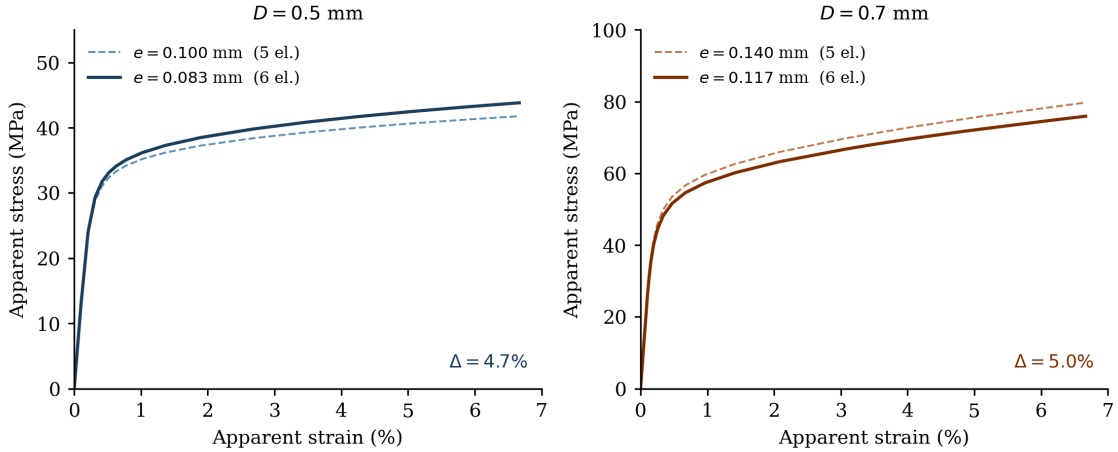



Figure 5.14: Cross-validation of the discretisation criterion for the Voronoi $n$=10 specimens with $D = 0.5$ mm (left) and $D = 0.7$ mm (right). In each panel, the dashed line corresponds to five elements per strut diameter and the solid line to six elements per strut diameter. The percentage difference between the two levels is indicated in the lower right corner of each panel.

In both cases the difference between the two refinement levels remained within the 5 % criterion, with values of 4.7 % for $D = 0.5$ mm and 5.0 % for $D = 0.7$ mm. The consistency of the convergence behaviour across the three strut diameters evaluated supports the extension of the ratio of five elements per strut diameter to the remaining Voronoi specimens, for which the element size was accordingly set to $D_i/5$ throughout the simulation campaign.

#### 5.2.4.2 Gyroid Architecture

The mesh convergence study for the Gyroid architecture was conducted on the specimen with the thinnest wall, corresponding to $l = 5.0$ mm and $C = 0.2$, whose average wall thickness is $t = 0.199$ mm, as reported in Table 3.12. To maintain methodological consistency with the Voronoi study, and given that quadratic elements had already been shown to be computationally infeasible,

the same element type (C3D4) and convergence criterion (5 %) were adopted directly, and the minimum of three refinement levels was equally enforced.

Three refinement levels were evaluated, ranging from three to five elements across the wall thickness, as summarised in Table 5.7 and illustrated in Figure 5.15.

Table 5.7: Mesh convergence study for the Gyroid $l$=5.0 mm, $C$=0.2 specimen using linear tetrahedral elements (C3D4). Peak apparent stress is taken as the convergence indicator.

| Element size (mm) | Elem./thickness | Nodes | Peak stress (MPa) | Δ (%) |
|---|---|---|---|---|
| 0.0667 | 3 | 249,312 | 4.428 | — |
| 0.050 | 4 | 495,541 | 4.202 | 5.4 |
| 0.040 | 5 | 974,048 | 4.069 | 3.3 |

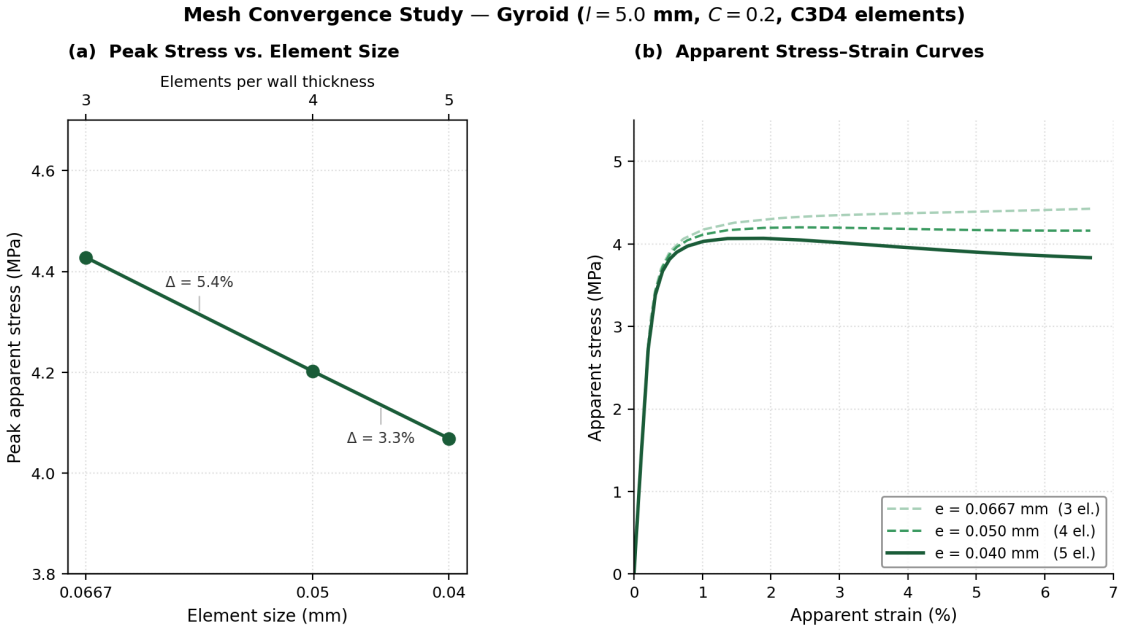



Figure 5.15: Mesh convergence study for the Gyroid $l$=5.0 mm, $C$=0.2 specimen using C3D4 elements. Left: peak apparent stress as a function of element size, with the difference between each pair of consecutive refinement levels indicated. Right: apparent stress-strain curves for all three refinement levels, with the two finest levels shown as solid lines.

The difference between three and four elements per wall thickness is 5.4 %, marginally exceeding the convergence criterion. Refinement to five elements per wall thickness reduces this difference to 3.3 %, confirming that the criterion is satisfied between the four- and five-element levels. The element size of $e = 0.050$ mm, corresponding to four elements per wall thickness, was therefore selected as the discretisation standard for all Gyroid specimens, with the target edge length set to $t_i/4$ for each configuration, where $t_i$ denotes the average wall thickness reported in Tables 3.12 and 3.13.

Although the same criterion and methodology were applied to both architectures, the converged ratio differed between them: five elements per characteristic thickness for the Voronoi and four for the Gyroid, as summarised in Table 5.8. This difference reflects the distinct geometric character of each architecture and confirms the relevance of conducting an independent convergence study for each rather than assuming a common ratio.

Table 5.8: Summary of the converged discretisation criteria adopted for each architecture.

| Architecture | Studied specimen | Element type | Converged ratio | Element size |
|---|---|---|---|---|
| Voronoi | $n$=10, $D$=0.3 mm | C3D4 | 5 elem./strut diam. | $e = D_i/5$ |
| Gyroid | $l$=5.0 mm, $C$=0.2 | C3D4 | 4 elem./wall thick. | $e = t_i/4$ |

### 5.2.5 Mesh Quality Assessment

Following the determination of the element size through the convergence study, the quality of the eighteen final simulation meshes was assessed using two standard metrics evaluated in Abaqus: the scaled Jacobian and the aspect ratio. The scaled Jacobian measures the deviation of each element from an ideal regular tetrahedron, with a value of unity corresponding to a perfect element, values below 0.2 indicative of poor element quality and negative values denoting geometrically invalid elements [136]. The aspect ratio quantifies element elongation, with values close to unity corresponding to well-shaped elements. The resulting metrics are reported in Tables 5.9 and 5.10.

Table 5.9: Mesh quality metrics for the nine Voronoi simulation meshes. Jac. mean: mean scaled Jacobian; Jac. $< 0.2$: fraction of elements with scaled Jacobian below 0.2 (%); AR mean: mean aspect ratio; AR $> 10$: fraction of elements with aspect ratio above 10 (%).

| Specimen | Nodes | Elements | Jac. mean | Jac. <0.2 (%) | AR mean | AR >10 (%) |
|---|---|---|---|---|---|---|
| $n$=10, $D$=0.3 | 1,234,249 | 5,725,621 | 0.809 | 0.000 | 1.596 | 0.000 |
| $n$=10, $D$=0.5 | 658,502 | 3,165,175 | 0.805 | 0.008 | 1.601 | 0.001 |
| $n$=10, $D$=0.7 | 315,555 | 1,545,430 | 0.809 | 0.017 | 1.593 | 0.003 |
| $n$=14, $D$=0.3 | 2,219,662 | 10,520,429 | 0.807 | 0.000 | 1.601 | 0.000 |
| $n$=14, $D$=0.5 | 865,300 | 4,262,837 | 0.811 | 0.004 | 1.585 | 0.001 |
| $n$=14, $D$=0.7 | 552,708 | 2,870,167 | 0.808 | 0.001 | 1.594 | 0.001 |
| $n$=18, $D$=0.3 | 3,244,056 | 15,622,829 | 0.800 | 0.001 | 1.613 | 0.000 |
| $n$=18, $D$=0.5 | 839,000 | 4,217,815 | 0.796 | 0.016 | 1.625 | 0.000 |
| $n$=18, $D$=0.7 | 493,179 | 26,668,431 | 0.798 | 0.002 | 1.613 | 0.000 |

Table 5.10: Mesh quality metrics for the nine Gyroid simulation meshes. Column definitions as in Table 5.9.

| Specimen | Nodes | Elements | Jac. mean | Jac. <0.2 (%) | AR mean | AR >10 (%) |
|---|---|---|---|---|---|---|
| $l$=5.0, $C$=0.2 | 495,541 | 2,395,409 | 0.741 | 0.001 | 1.774 | 0.002 |
| $l$=1.5, $C$=0.8 | 1,063,539 | 5,412,292 | 0.794 | 0.000 | 1.631 | 0.000 |
| $l$=2.0, $C$=0.7 | 664,859 | 3,391,074 | 0.792 | 0.001 | 1.633 | 0.001 |
| $l$=2.5, $C$=0.8 | 233,873 | 1,175,505 | 0.801 | 0.000 | 1.614 | 0.000 |
| $l$=2.5, $C$=0.5 | 745,545 | 3,755,095 | 0.792 | 0.002 | 1.634 | 0.001 |
| $l$=3.5, $C$=0.3 | 730,480 | 3,644,407 | 0.794 | 0.000 | 1.634 | 0.000 |
| $l$=3.5, $C$=0.6 | 137,386 | 683,667 | 0.795 | 0.002 | 1.626 | 0.002 |
| $l$=5.0, $C$=0.5 | 106,832 | 535,435 | 0.796 | 0.006 | 1.627 | 0.004 |
| $l$=5.0, $C$=0.8 | 46,852 | 231,158 | 0.796 | 0.013 | 1.626 | 0.002 |

Mean scaled Jacobian values range from 0.796 to 0.811 across the nine Voronoi meshes and from 0.741 to 0.801 across the Gyroid meshes, remaining well above the 0.2 threshold in all cases. Although higher mean values would be desirable, these results are acceptable given the geometric complexity of the parts. In addition, the fraction of elements below this threshold does not exceed 0.017% in any specimen. Isolated elements with slightly negative Jacobian values were detected in some meshes, but they are associated with the complex geometry of the strut junctions and Gyroid sheet surfaces and represent a negligible fraction of the total element count.

Within the Gyroid set, the $l = 5.0$,mm, $C = 0.2$ specimen shows the lowest mean Jacobian value, 0.741, which reflects the difficulty of discretising the thinnest wall configuration. Even so, the fraction of elements below 0.2 remains at only 0.001% for this specimen. Moreover, mean aspect ratios range from 1.585 to 1.774, and the fraction of elements with an aspect ratio above 10 stays below 0.004% in all cases. Overall, although the mesh quality is not optimal, all eighteen meshes achieve a level that is acceptable for finite element analysis in view of the complexity of the geometries.

## 5.3 Results and Discussion

### 5.3.1 Apparent Stress–Strain Response

The apparent stress–strain curves obtained from the finite element simulations across all eighteen specimens are shown in Figures 5.16 and 5.17, corresponding to the Voronoi and Gyroid architectures respectively. In both cases, the curves share a common qualitative structure, beginning with a brief linear elastic regime that transitions into yielding at a small apparent strain and continuing thereafter through a progressively hardening plateau, which extends across the remainder of the applied deformation.

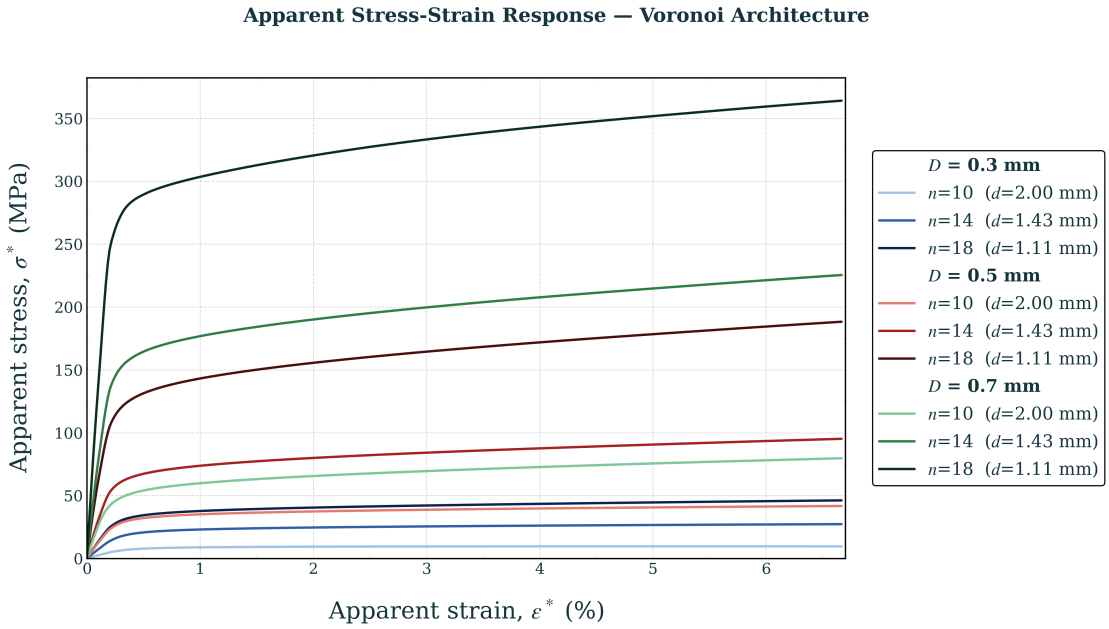



Figure 5.16: Apparent stress–strain curves for the nine Voronoi specimens.

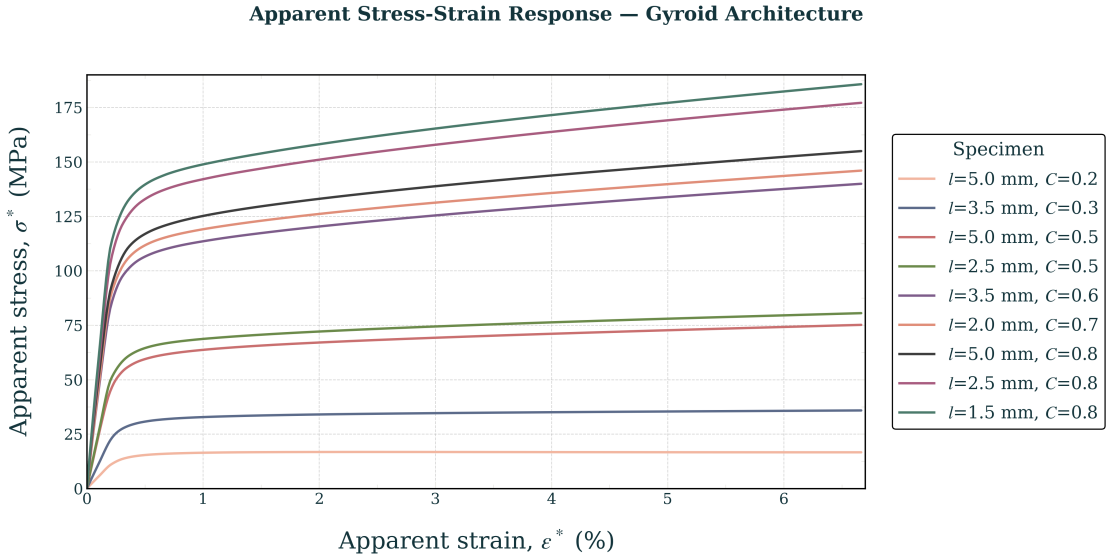



Figure 5.17: Apparent stress–strain curves for the nine Gyroid specimens.

Across all eighteen specimens, yielding consistently begins between 0.23 % and 0.33 % of apparent strain, a narrow range observed across both architectures and the full span of relative densities evaluated. This range lies in close proximity to the yield strain of the constituent material, $\varepsilon_{y,s} = \sigma_{ys}/E_s = 0.207\,\%$, as characterised in Section 5.2.1, a result that is not unexpected, given that the intrinsic properties of the constituent material are expected to have influence on the onset of plastic deformation irrespective of topology.

Beyond the yield point, all eighteen specimens exhibit continued post-yield hardening throughout the full applied deformation of 6.7 %, as expected from the strain-hardening character of the iron base material demonstrated in Section 5.2.1. The extent of this hardening differs markedly with relative density, with denser specimens exhibiting a pronounced and sustained increase in stress whereas less dense specimens present a response that, while still hardening, is considerably more gradual and approaches a near plateau visually.

Within the Voronoi results (Figure 5.16), the curves do not separate into neat families by either $d$ or $D$ alone, but instead follow the combined effect of both parameters through their influence on relative density. Specimens with similar $\rho$ but different combinations of $d$ and $D$ produce closely overlapping responses, while those within the same $D$ family but with different $d$ spread across a wide stress range. This mixing reflects the dual parametric control of $\rho$ established in Chapter 3, since as $\rho^*$ increases, whether through a larger $D$, a smaller $d$, or both combined, apparent stiffness and strength increase consistently, given that a denser structure carries more load.

In the Gyroid results (Figure 5.17), the progression is considerably more ordered. The curves shift upward in a near-monotonic pattern with increasing $C$, and specimens sharing the same $C$ cluster tightly together regardless of $l$. This reflects the exclusive role of $C$ in controlling $\rho$ within the Gyroid architecture, as established in Chapter 3, where $C$ alone, rather than any combination with $l$, determines the relative density of the structure. A higher $C$ produces denser structure, which translates directly into higher apparent stiffness and strength, while $l$ has no influence on $\rho$ and therefore introduces only minor secondary shifts within each group, in clear contrast to the dual dependence on $D$ and $d$ observed in the Voronoi architecture.

### 5.3.2 Mechanical Properties Evaluation

The apparent elastic modulus $E^*$ and yield strength $\sigma_y^*$ extracted from each simulation are compiled in Tables 5.11 and 5.12.

Table 5.11: Apparent elastic modulus and yield strength for the nine Voronoi specimens. The cell size $d = L/n$, with $L = 20$ mm.

| $n$ | $d$ (mm) | $D$ (mm) | $\rho^*$ (%) | $E^*$ (GPa) | $\sigma_y^*$ (MPa) |
|---|---|---|---|---|---|
| 10 | 2.00 | 0.3 | 10.95 | 2.38 | 7.96 |
| 14 | 1.43 | 0.3 | 18.49 | 6.89 | 20.72 |
| 10 | 2.00 | 0.5 | 25.37 | 11.57 | 31.80 |
| 18 | 1.11 | 0.3 | 26.39 | 12.37 | 34.01 |
| 10 | 2.00 | 0.7 | 41.30 | 23.09 | 52.28 |
| 14 | 1.43 | 0.5 | 40.18 | 26.64 | 66.06 |
| 18 | 1.11 | 0.5 | 53.90 | 53.27 | 128.82 |
| 14 | 1.43 | 0.7 | 61.07 | 67.79 | 161.64 |
| 18 | 1.11 | 0.7 | 76.41 | 123.02 | 285.16 |

Table 5.12: Apparent elastic modulus and yield strength for the nine Gyroid specimens.

| $l$ (mm) | $C$ | $\rho^*$ (%) | $E^*$ (GPa) | $\sigma_y^*$ (MPa) |
|---|---|---|---|---|
| 5.0 | 0.2 | 12.69 | 5.35 | 15.29 |
| 3.5 | 0.3 | 19.27 | 10.56 | 30.61 |
| 5.0 | 0.5 | 31.98 | 23.23 | 58.39 |
| 2.5 | 0.5 | 32.19 | 24.43 | 63.37 |
| 3.5 | 0.6 | 38.72 | 41.24 | 104.92 |
| 2.0 | 0.7 | 45.32 | 43.42 | 109.63 |
| 5.0 | 0.8 | 51.71 | 45.45 | 114.73 |
| 2.5 | 0.8 | 51.98 | 51.35 | 130.85 |
| 1.5 | 0.8 | 52.07 | 54.88 | 136.89 |

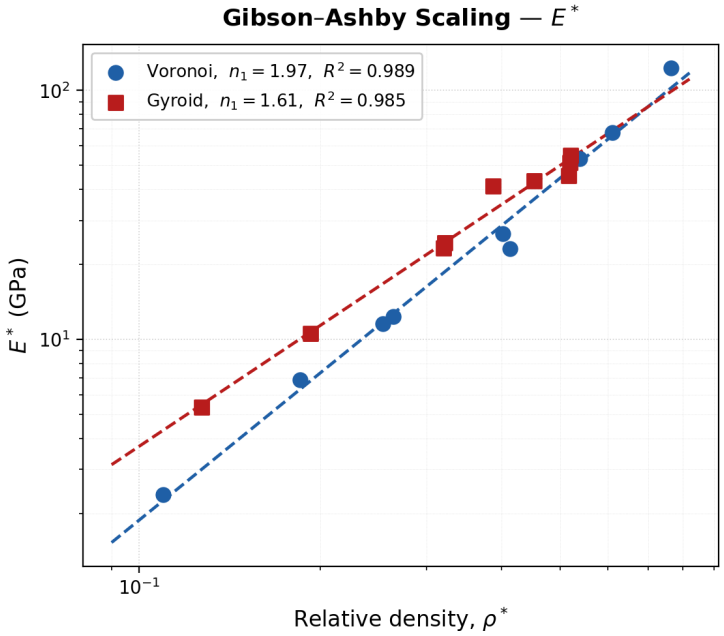
The same parametric influence on relative density established in Chapter 3 and confirmed in the stress–strain curves of Section 5.3.1 is reflected directly in the extracted mechanical properties, since as $\rho^*$ increases, both $E^*$ and $\sigma_y^*$ increase consistently across both architectures and across all parameter combinations, ranging from $E^* = 2.38$ GPa to $E^* = 123$ GPa. The generation parameters $d$ and $D$ in the Voronoi and $C$ in the Gyroid influence $E^*$ and $\sigma_y^*$ in the same hierarchical manner already established for $\rho^*$ in Section 5.3.1, with $l$ again producing a secondary residual variation of approximately 5–21 % in $E^*$ at constant $\rho^*$ within the Gyroid architecture.

This behaviour is formally captured by the Gibson–Ashby power law introduced in Section 2.2.3 (Equation 2.1), whose fits to the present data are shown in Figure 5.18 and summarised in Table 5.13. Both architectures follow this scaling with $R^2 > 0.976$, confirming $\rho^*$ as the primary predictor of apparent mechanical properties and quantifying the topological difference between them through the scaling exponents. The Voronoi yields $n_1 = 1.97$, close to the theoretical value of 2 characteristic of bending-dominated cellular solids [61], while the Gyroid yields $n_1 = 1.61$, intermediate between the bending and stretching limits, consistent with the smooth and continuous sheet topology of TPMS structures discussed in Section 2.2.3. As a direct consequence, the Gyroid delivers higher stiffness and strength than the Voronoi at any given density, with an advantage of approximately 46 % in $E^*$ at $\rho^* = 20\,\%$.

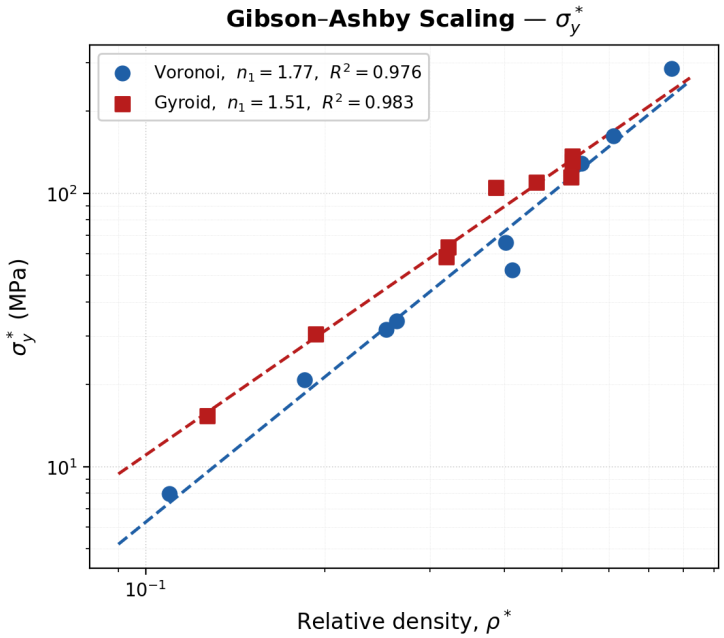
Table 5.13: Gibson–Ashby power-law parameters for both architectures. $P^*/P_s = C_1 \cdot (\rho^*)^{n_1}$.

| Architecture | Property | $C_1$ | $n_1$ | $R^2$ |
|---|---|---|---|---|
| Voronoi | $E^*/E_s$ | 173.7 | 1.97 | 0.989 |
| | $\sigma_y^*/\sigma_{ys}$ | 365.5 | 1.77 | 0.976 |
| Gyroid | $E^*/E_s$ | 153.0 | 1.61 | 0.985 |
| | $\sigma_y^*/\sigma_{ys}$ | 356.4 | 1.51 | 0.984 |

The scaling exponents confirm that both architectures operate within the bending-dominated regime anticipated in Section 2.2.3 as the more appropriate deformation regime for biodegradable bone implants.




(a) Apparent elastic modulus scaling as a function of relative density.




(b) Apparent yield strength scaling as a function of relative density.

Figure 5.18: Gibson–Ashby scaling of apparent elastic modulus (a) and apparent yield strength (b) as a function of relative density for both architectures in log–log scale. Dashed lines represent the power-law regressions; exponents and $R^2$ values are indicated in the legend.

Considering the high fidelity of the Gibson–Ashby fits ($R^2 > 0.976$), the validated scaling laws can further be used to compare both architectures at equivalent relative densities through interpolation within the fitted range. Figure 5.19 presents this comparison at four representative density levels.

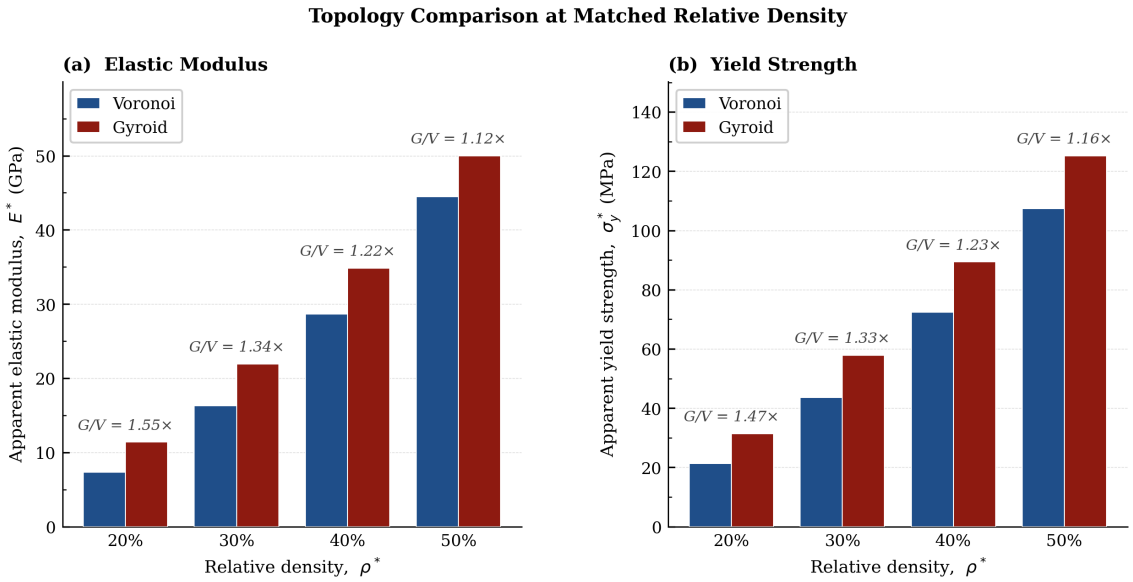



Figure 5.19: Apparent elastic modulus (a) and yield strength (b) of both architectures at matched relative densities, obtained by interpolation from the fitted Gibson–Ashby scaling laws. Ratios indicate the Gyroid-to-Voronoi values at each density level.

Figure 5.19 shows that the difference between the Gyroid and Voronoi values decreases monotonically with increasing relative density, from approximately 1.55× in $E^*$ (1.47× in $\sigma_y^*$) at $\rho^* = 20\,\%$ to 1.12× (1.16×) at $\rho^* = 50\,\%$, a trend that follows directly from the difference in the fitted exponents $n_1$. The Voronoi's exponent, at 1.97, sits almost exactly at the theoretical bending-dominated limit of 2, since only a small fraction of struts happen to be perfectly aligned with the loading direction, leaving bending as the prevailing deformation mechanism. The Gyroid's curved wall is less subject to this transverse loading condition, shifting its response slightly toward a more stretching-like behaviour and accounting for its lower exponent of 1.62, keeping nonetheless the macroscopic behaviour predominantly bending-dominated.

This gap in $E^*$ and $\sigma_y^*$ is most pronounced at lower densities precisely because the Gyroid deviates further from the bending-dominated limit, giving it a comparatively higher stiffness and strength than the Voronoi at the same $\rho^*$. As density increases, both architectures approach the solid material response at $\rho^* = 1$, where the lattice structure itself effectively disappears and the material becomes fully dense, so the two architectures must converge to the same value regardless of their differing exponents, which explains why the gap between them progressively vanishes at higher densities. This behaviour becomes particularly relevant at low densities, since the intended application range for biodegradable implants culminates precisely within these density

levels, making this stiffness difference an important factor to consider for design adjustments and property matching.

### 5.3.3 Comparison with Bone Mechanical Properties

The apparent mechanical properties of all eighteen specimens are compared against the property ranges of cortical and trabecular bone established in Table 2.1 of Chapter 2, namely $E^* = 18$–$30\,\text{GPa}$ and $\sigma_y^* = 100$–$200\,\text{MPa}$ for cortical bone, and $E^* = 0.1$–$3\,\text{GPa}$ and $\sigma_y^* = 2$–$20\,\text{MPa}$ for trabecular bone [28, 29]. This comparison is presented in Figure 5.20, where the iso-yield-strain line $\varepsilon_y = \sigma_y^*/E^*$ of the iron lattice specimens (0.26 %) is also shown.

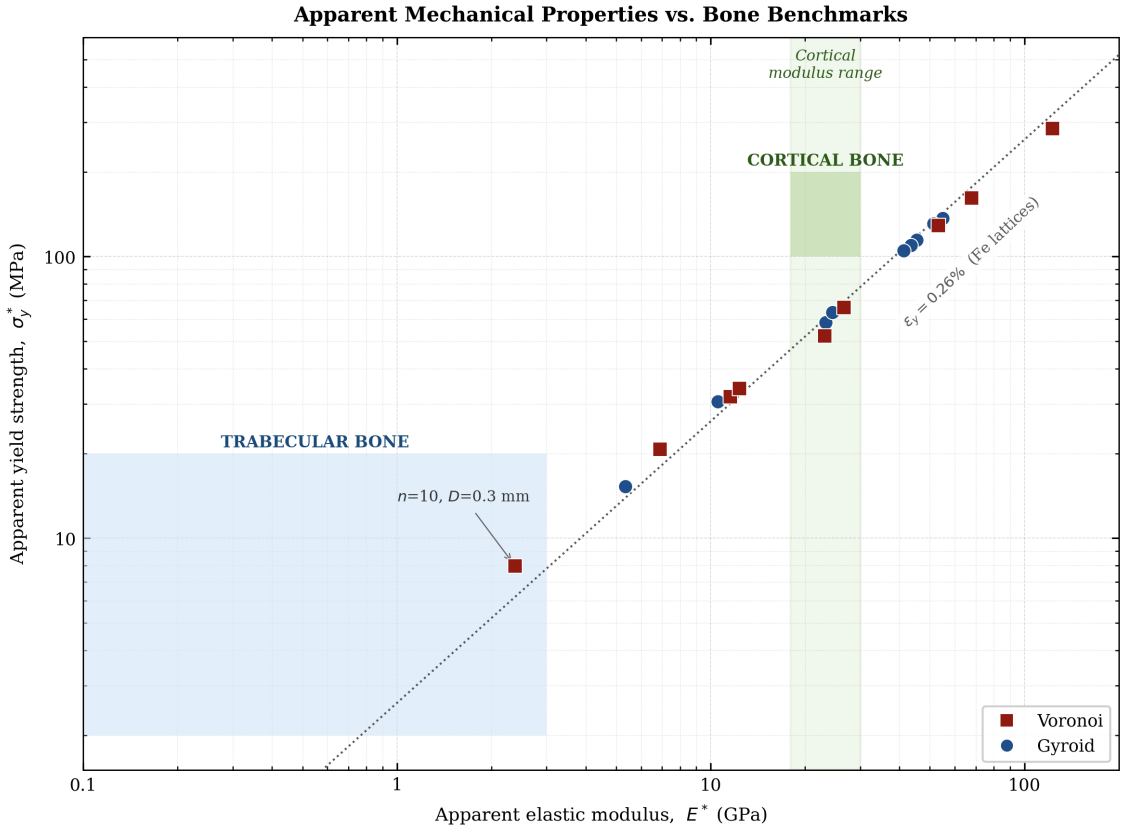



Figure 5.20: Apparent elastic modulus and yield strength of all eighteen specimens plotted against the mechanical property windows of trabecular and cortical bone. The shaded vertical band identifies the cortical modulus range (18–30 GPa) independently of strength. The dotted line indicates the constant yield strain shared by all iron lattice specimens ($\varepsilon_y = 0.26\,\%$). Voronoi specimens are shown as squares and Gyroid specimens as circles.

Of the eighteen configurations, only the Voronoi $n = 10$, $D = 0.3\,\text{mm}$ specimen simultaneously satisfies both mechanical criteria for trabecular bone, presenting $E^* = 2.38\,\text{GPa}$ and $\sigma_y^* = 7.96\,\text{MPa}$. No other specimen reaches even the elastic modulus range of trabecular bone,

so that this configuration stands as the sole candidate for full trabecular matching among those evaluated.

Regarding cortical bone, no specimen falls within both the modulus and strength windows simultaneously. This is made evident by the iso-yield-strain line of the iron lattice specimens included in Figure 5.20, since none of the eighteen data points crosses into the cortical yield strength window of 100–200 MPa. The line illustrates directly the proximity to the material's own yield strain noted earlier in Section 5.3.1, and shows that this constraint on $\sigma_y^*$ will remain difficult to overcome through architecture alone, since raising $E^*$ into the cortical range under a fixed $\varepsilon_y$ simply carries $\sigma_y^*$ along the same line rather than into the target window.

However, as established in Section 2.2.2, the primary mechanical criterion for a porous biodegradable implant is compatibility of elastic modulus with the host bone, given that it is the stiffness mismatch that drives stress shielding and the consequent periprosthetic bone resorption [3, 6]. Evaluated on this basis, four specimens fall within the cortical modulus range of 18–30 GPa: two Gyroid configurations ($l = 5.0$ mm, $C = 0.5$ and $l = 2.5$ mm, $C = 0.5$, with $E^* = 23.2$ and 24.4 GPa respectively) and two Voronoi configurations ($n = 10$, $D = 0.7$ mm and $n = 14$, $D = 0.5$ mm, with $E^* = 23.1$ and 26.6 GPa), as highlighted by the vertical shaded band in Figure 5.20. These configurations therefore address the dominant clinical concern of stress shielding through stiffness matching, even though their yield strengths of 52–66 MPa remain below the cortical bone range, consistent with the constant yield-strain limitation described above.

Beyond these configurations, a further five specimens present elastic moduli in the intermediate range of 3–18 GPa, between the two bone property windows. While not matching either tissue exactly, these designs represent a substantial reduction in stiffness relative to the conventional dense metallic implants currently in clinical use, whose elastic moduli typically exceed 100 GPa for Ti-6Al-4V [88], thereby partially mitigating the severe impact of stress shielding. The least stiff specimen among those in the cortical modulus range achieves a 4 to 5 times reduction relative to that benchmark, while the trabecular candidate ($n = 10$, $D = 0.3$ mm) represents a reduction of approximately 46×, demonstrating the broad span of stiffness values accessible through geometric design alone and the consequent potential to substantially mitigate stress shielding across a wide range of clinical scenarios.

In conclusion, Table 5.14 condenses the classification introduced throughout this section, grouping the specimens by the bone property window each one satisfies, together with their generation parameters and apparent mechanical properties.

Table 5.14: Configurations satisfying the trabecular and cortical elastic modulus windows, together with the intermediate configurations lying between them, and the corresponding generation parameters and apparent mechanical properties.

| **Architecture** | **Parameters** | $E^*$ **(GPa)** | $\sigma_y^*$ **(MPa)** |
|---|---|---|---|
| | *Trabecular match* | | |
| Voronoi | $n = 10$, $d = 2.00\,\text{mm}$, $D = 0.3\,\text{mm}$ | 2.38 | 7.96 |
| | *Cortical $E^*$ match* | | |
| Voronoi | $n = 10$, $d = 2.00\,\text{mm}$, $D = 0.7\,\text{mm}$ | 23.09 | 52.28 |
| Gyroid | $l = 5.0\,\text{mm}$, $C = 0.5$ | 23.23 | 58.39 |
| Gyroid | $l = 2.5\,\text{mm}$, $C = 0.5$ | 24.43 | 63.37 |
| Voronoi | $n = 14$, $d = 1.43\,\text{mm}$, $D = 0.5\,\text{mm}$ | 26.64 | 66.06 |
| | *Intermediate Trabecular - Cortical window* | | |
| Gyroid | $l = 5.0\,\text{mm}$, $C = 0.2$ | 5.35 | 15.29 |
| Voronoi | $n = 14$, $d = 1.43\,\text{mm}$, $D = 0.3\,\text{mm}$ | 6.89 | 20.72 |
| Gyroid | $l = 3.5\,\text{mm}$, $C = 0.3$ | 10.56 | 30.61 |
| Voronoi | $n = 10$, $d = 2.00\,\text{mm}$, $D = 0.5\,\text{mm}$ | 11.57 | 31.80 |
| Voronoi | $n = 18$, $d = 1.11\,\text{mm}$, $D = 0.3\,\text{mm}$ | 12.37 | 34.01 |

The remaining eight specimens exceed the cortical range, with $E^* = 41$–$123\,\text{GPa}$.

Chapter 6

# Conclusions and Future Work

## 6.1 Conclusions

The mechanical incompatibility between conventional dense metallic implants and the surrounding bone tissue, and the characteristically slow degradation of iron in its bulk form, constituted the two clinical limitations that motivated the present work. Addressing both simultaneously through the introduction of a controlled porous architecture was the central hypothesis under investigation, evaluated across Voronoi and Gyroid geometries fabricated by L-PBF.

The development of an open-source computational pipeline showed that both architectures can be produced across a wide morphological space in a fully transparent and reproducible way. This pipeline supported a systematic parametric study, which established empirical formulations linking the generation parameters to the two descriptors that matter most, relative density and surface area, with coefficients of determination high enough to support their use in reverse engineering. These formulations also revealed that the resulting morphology does not respond equally to every parameter. In the Gyroid architecture, relative density is governed almost exclusively by the level-set constant, leaving the unit cell size free to be tuned toward secondary design goals without disturbing the intended density. On the other hand, in the Voronoi lattice, density emerges from the combined action of both parameters, so that reaching a specific morphology requires optimising them jointly rather than independently.

The biodegradation results confirmed that introducing porosity can effectively accelerate the corrosion of iron, though the governing mechanism turned out to be fluid accessibility rather than nominal surface area alone. Specimens whose pore networks stayed open enough to sustain fluid circulation rather than low relative density alone, exhibited corrosion rates consistently above those of the dense reference, confirming porosity can be viable strategy to overcome the slow degradation of iron in its bulk form. When reduced pore dimensions restricted fluid ingress, a limitation driven by channel confinement and by the partial fusion of powder particles, the effective reactive interface was severely reduced, and the corrosion rate dropped to levels below the dense reference regardless of the larger nominal surface area. Moreover, surface characterisation also revealed the formation of corrosion product layer, while the absence of hydroxyapatite precipitation under these conditions indicated that neither architecture triggered a bioactive response in the analyzed areas.

The finite element simulations established that relative density is the primary predictor of the apparent elastic modulus, with the Gibson–Ashby scaling law verified with high fidelity for both architectures. The derived scaling exponents confirmed that both geometries operate predominantly within a bending-dominated deformation regime, though the Gyroid presented a lower exponent than the Voronoi, meaning that at any equivalent relative density it consistently delivers superior stiffness and strength, an advantage most pronounced at the low densities, the most relevant interval for clinical applications. Moreover, the mechanical evaluation demonstrated that the apparent elastic modulus of these structures can be tailored to match the reference property ranges

of human bone tissue reported in the literature, bringing implant stiffness down to physiological levels and directly addressing the stiffness mismatch that drives stress shielding, the primary biomechanical limitation of conventional dense implants. One Voronoi configuration achieved full mechanical compatibility with trabecular bone, whilst four configurations across both architectures fell within the cortical bone modulus window.

Combined with the corrosion acceleration, these findings suggest that architected cellular materials open a possible pathway towards biodegradable metallic implants. While the proposed geometries reduced apparent stiffness to values within or close to the bone property windows, offering a means to mitigate stress shielding, the degradation behaviour confirmed that corrosion could indeed be accelerated.

## 6.2 Future Work

Despite these promising findings, several directions for future research still need to be pursued before this approach can progress towards its intended clinical application.

1. **Experimental Mechanical Validation:** The most immediate work to proceed is the physical uniaxial compression testing of the 3D-printed iron specimens in order to experimentally validate the finite element simulations and assess the broader applicability of the derived Gibson–Ashby scaling laws.

2. **Dynamic Biodegradation Testing:** Future work should move from static immersion towards dynamic testing environments based on bioreactor systems, applied specifically to the configurations that performed best in the present study, to assess their degradation behaviour under conditions that more closely resemble the physiological fluid flow experienced in vivo. Moreover, since the present findings highlighted fluid accessibility and channel confinement as dominant degradation factors, such testing would also make it possible to determine whether continuous perfusion further increases the corrosion rate relative to the static conditions evaluated here.

3. **Coupled Degradation and Mechanical Integrity Over Time:** The long-term structural evolution of the implants should be investigated by linking mass-loss kinetics with mechanical testing. The ultimate goal is a degradation profile that remains concordant with the pace of bone regeneration, since a biodegradable implant must gradually transfer load to the healing bone while preserving sufficient structural integrity to prevent premature failure. Studying how apparent stiffness and strength decay as corrosion advances is therefore an important step towards that balance, and towards clinical translation.

4. **Bioactivity Assessment:** Bioactivity is a key requirement for this application, since successful bone regeneration depends on the ability of the implant surface to form a stable

bond with the surrounding tissue. As this response was not observed in the present tests, it should be examined more specifically in future work. A natural next step is to complement the current degradation assays with basic biocompatibility tests, such as cytotoxicity and cell viability measurements, in order to assess whether these porous iron architectures can support a favourable cellular response and early-stage bone bonding.

5. **Design and Fabrication of Functionally Graded Structures:** The adaptable open-source computational design pipeline developed in this work can be extended to generate functionally graded architectures. Building on this framework, future developments can vary the relative density and internal topology across the implant domain so that different regions are assigned distinct structural roles. Depending on the target anatomical site and application, this graded design would allow a more refined local mechanical match and improved mass transport.

# References


[1] Abdulla All Noman et al. “Recent advancements in additively manufactured hip implant design using topology optimization technique”. In: *Results in Engineering* 25 (2025), p. 103932. ISSN: 2590-1230. DOI: https://doi.org/10.1016/j.rineng.2025.103932. URL: https://www.sciencedirect.com/science/article/pii/S2590123025000209.

[2] Samuel Polo et al. “Lattice structures in additive manufacturing for biomedical applications: a systematic review”. In: *Polymers* 17.17 (2025), p. 2285.

[3] Roberto Ramaglia Amadasi et al. “An integrated experimental and analytical approach for the analysis of the mechanical interaction between metal porous scaffolds and bone: implications for stress shielding in orthopedic implants”. In: *Frontiers in Bioengineering and Biotechnology* Volume 13 - 2025 (2025). ISSN: 2296-4185. DOI: 10.3389/fbioe.2025.1562367. URL: https://www.frontiersin.org/journals/bioengineering-and-biotechnology/articles/10.3389/fbioe.2025.1562367.

[4] Naichao Wu et al. “The advances of topology optimization techniques in orthopedic implants: A review”. In: *Medical Biological Engineering Computing* 59 (Aug. 2021), pp. 1–17. DOI: 10.1007/s11517-021-02361-7.

[5] Nik Nur Ain Azrin Abdullah, Abdul Halim Abdullah, and Muhammad Hanif Ramlee. “Current trend of lattice structures designed and analysis for porous hip implants: A short review”. In: *Materials Today: Proceedings* 110 (2024). Sustainable Integrated Engineering International Conference (SIE 2022), pp. 96–100. ISSN: 2214-7853. DOI: https://doi.org/10.1016/j.matpr.2023.09.199. URL: https://www.sciencedirect.com/science/article/pii/S2214785323048800.

[6] Kazuyoshi Baba et al. “Effectiveness of Stress Shielding Prevention Using a Low Young’s Modulus Ti-33.6Nb-4Sn Stem: A 7-Year Follow-Up Study”. In: *Medical Sciences* 13.2 (2025). ISSN: 2076-3271. DOI: 10.3390/medsci13020051. URL: https://www.mdpi.com/2076-3271/13/2/51.

[7] Xiaojian Wang et al. “Topological design and additive manufacturing of porous metals for bone scaffolds and orthopaedic implants: A review”. In: *Biomaterials* 83 (2016), pp. 127–141. ISSN: 0142-9612. DOI: https://doi.org/10.1016/j.biomaterials.2016.01.012. URL: https://www.sciencedirect.com/science/article/pii/S0142961216000144.

[8] Gabriela Gąsior, Jonasz Szczepański, and Aleksandra Radtke. “Biodegradable Iron-Based Materials—What Was Done and What More Can Be Done?” In: *Materials* 14.12 (2021).

ISSN: 1996-1944. DOI: 10.3390/ma14123381. URL: https://www.mdpi.com/1996-1944/14/12/3381.

[9] Irene Limón et al. "A Review of Additive Manufacturing of Biodegradable Fe and Zn Alloys for Medical Implants Using Laser Powder Bed Fusion (LPBF)". In: *Materials* 17.24 (2024). ISSN: 1996-1944. DOI: 10.3390/ma17246220. URL: https://www.mdpi.com/1996-1944/17/24/6220.

[10] Michael Heiden, Eric Nauman, and Lia Stanciu. "Bioresorbable Fe–Mn and Fe–Mn–HA Materials for Orthopedic Implantation: Enhancing Degradation through Porosity Control". In: *Advanced Healthcare Materials* 6.13 (2017), p. 1700120. DOI: https://doi.org/10.1002/adhm.201700120. eprint: https://advanced.onlinelibrary.wiley.com/doi/pdf/10.1002/adhm.201700120. URL: https://advanced.onlinelibrary.wiley.com/doi/abs/10.1002/adhm.201700120.

[11] N.E. Putra et al. "Extrusion-based 3D printed biodegradable porous iron". In: *Acta Biomaterialia* 121 (2021), pp. 741–756. ISSN: 1742-7061. DOI: https://doi.org/10.1016/j.actbio.2020.11.022. URL: https://www.sciencedirect.com/science/article/pii/S1742706120306759.

[12] Shriniketan Kumawat, Sachin R Deshmukh, and RR Ghorpade. "Fabrication of Ti-6Al-4v cellular lattice structure using selective laser melting for orthopedic use: a review". In: *Materials Today: Proceedings* 113 (2024), pp. 166–172.

[13] Leonie Wallat et al. "Computational design and characterisation of gyroid structures with different gradient functions for porosity adjustment". In: *Materials* 15.10 (2022), p. 3730. DOI: 10.3390/ma15103730.

[14] Dawit Bogale Alemayehu, Masahiro Todoh, and Song-Jeng Huang. "Advancing 3D Dental Implant Finite Element Analysis: Incorporating Biomimetic Trabecular Bone with Varied Pore Sizes in Voronoi Lattices". In: *Journal of Functional Biomaterials* 15.4 (2024). ISSN: 2079-4983. DOI: 10.3390/jfb15040094. URL: https://www.mdpi.com/2079-4983/15/4/94.

[15] Yijun Zhou, Per Isaksson, and Cecilia Persson. "An improved trabecular bone model based on Voronoi tessellation". In: *Journal of the Mechanical Behavior of Biomedical Materials* 148 (2023), p. 106172. ISSN: 1751-6161. DOI: https://doi.org/10.1016/j.jmbbm.2023.106172. URL: https://www.sciencedirect.com/science/article/pii/S1751616123005258.

[16] Ekaterina Maevskaia et al. "Triply periodic minimal surface-based scaffolds for bone tissue engineering: a mechanical, in vitro and in vivo study". In: *Tissue Engineering Part A* 29.19-20 (2023), pp. 507–517.

[17] Seyed Ataollah Naghavi et al. "Mechanical characterisation and numerical modelling of TPMS-based gyroid and diamond Ti6Al4V scaffolds for bone implants: an integrated approach for translational consideration". In: *Bioengineering* 9.10 (2022), p. 504.

[18] Adrian Rodriguez-Palomo, Maja Østergaard, and Henrik Birkedal. "Bone Hierarchical Structure: Heterogeneity and Uniformity". In: *Advanced Functional Materials* 34.35 (2024), p. 2307026. DOI: https://doi.org/10.1002/adfm.202307026. URL: https://advanced.onlinelibrary.wiley.com/doi/abs/10.1002/adfm.202307026.

[19] Holly D. Barth et al. “Characterization of the effects of x-ray irradiation on the hierarchical structure and mechanical properties of human cortical bone”. In: *Biomaterials* 32.34 (2011), pp. 8892–8904. ISSN: 0142-9612. DOI: https://doi.org/10.1016/j.biomaterials.2011.08.013. URL: https://www.sciencedirect.com/science/article/pii/S0142961211009185.

[20] C.J. Hernandez and T.M. Keaveny. “A biomechanical perspective on bone quality”. In: *Bone* 39.6 (2006), pp. 1173–1181. ISSN: 8756-3282. DOI: https://doi.org/10.1016/j.bone.2006.06.001. URL: https://www.sciencedirect.com/science/article/pii/S8756328206005552.

[21] Nail Beisekenov et al. “Analysis of Biomechanical Characteristics of Bone Tissues Using a Bayesian Neural Network: A Narrative Review”. In: *Journal of Functional Biomaterials* 16.5 (2025). ISSN: 2079-4983. DOI: 10.3390/jfb16050168. URL: https://www.mdpi.com/2079-4983/16/5/168.

[22] Ramin Oftadeh et al. “Hierarchical analysis and multi-scale modelling of rat cortical and trabecular bone”. In: *Journal of The Royal Society Interface* 12.106 (May 2015), p. 20150070. ISSN: 1742-5689. DOI: 10.1098/rsif.2015.0070. eprint: https://royalsocietypublishing.org/rsif/article-pdf/doi/10.1098/rsif.2015.0070/203739/rsif.2015.0070.pdf. URL: https://doi.org/10.1098/rsif.2015.0070.

[23] M-Ali H. Al-Akhras et al. “Investigation of composition and structure of spongy and hard bone tissue using FTIR spectroscopy, XRD and SEM”. In: *IOP Conference Series: Materials Science and Engineering* 305.1 (Feb. 2018), p. 012010. DOI: 10.1088/1757-899X/305/1/012010. URL: https://doi.org/10.1088/1757-899X/305/1/012010.

[24] Gurjit S Mandair and Michael D Morris. “Contributions of Raman spectroscopy to the understanding of bone strength”. In: *BoneKEy reports* 4 (2015), p. 620.

[25] Parinaz Tabrizian, Sean Davis, and Bo Su. “From bone to nacre–development of biomimetic materials for bone implants: a review”. In: *Biomaterials Science* 12.22 (2024), pp. 5680–5703.

[26] Stacyann Bailey and Deepak Vashishth. “Mechanical characterization of bone: state of the art in experimental approaches—what types of experiments do people do and how does one interpret the results?” In: *Current osteoporosis reports* 16.4 (2018), pp. 423–433.

[27] Jingzhi Fan et al. “A Review of Recent Advances in Natural Polymer-Based Scaffolds for Musculoskeletal Tissue Engineering”. In: *Polymers* 14 (May 2022). DOI: 10.3390/polym14102097.

[28] Elise F Morgan, Ginu U Unnikrisnan, and Amira I Hussein. “Bone mechanical properties in healthy and diseased states”. In: *Annual review of biomedical engineering* 20.1 (2018), pp. 119–143.

[29] Nicolas H Hart et al. “Mechanical basis of bone strength: influence of bone material, bone structure and muscle action”. In: *Journal of musculoskeletal & neuronal interactions* 17.3 (2017), p. 114.

[30] Daniele Casari et al. “Microtensile properties and failure mechanisms of cortical bone at the lamellar level”. In: *Acta Biomaterialia* 120 (2021). Biomineralization: From Cells to Biomaterials, pp. 135–145. ISSN: 1742-7061. DOI: https://doi.org/10.1016/j.actbio.2020.04.030. URL: https://www.sciencedirect.com/science/article/pii/S1742706120302270.

[31] Qianli Ma et al. “Significance of mechanical loading in bone fracture healing, bone regeneration, and vascularization”. In: *Journal of Tissue Engineering* 14 (2023), p. 20417314231172573.

[32] Encyclopaedia Britannica. *Bone: Remodeling, Growth, and Development*. Accessed: 2026-04-27. 2026. URL: https://www.britannica.com/science/bone/Bone-remodeling-growth-and-development.

[33] Frédéric Deschaseaux, Luc Sensébé, and Dominique Heymann. “Mechanisms of bone repair and regeneration”. In: *Trends in molecular medicine* 15.9 (2009), pp. 417–429.

[34] Mojtaba Ansari. “Bone tissue regeneration: biology, strategies and interface studies”. In: *Progress in Biomaterials* 8 (Nov. 2019). DOI: 10.1007/s40204-019-00125-z.

[35] Agnieszka Chmielewska and David Dean. “The role of stiffness-matching in avoiding stress shielding-induced bone loss and stress concentration-induced skeletal reconstruction device failure”. In: *Acta Biomaterialia* 173 (2024), pp. 51–65. ISSN: 1742-7061. DOI: https://doi.org/10.1016/j.actbio.2023.11.011. URL: https://www.sciencedirect.com/science/article/pii/S174270612300658X.

[36] Marinela Peto et al. “Review on structural optimization techniques for additively manufactured implantable medical devices”. In: *Frontiers in Mechanical Engineering* Volume 10 - 2024 (2024). ISSN: 2297-3079. DOI: 10.3389/fmech.2024.1353108. URL: https://www.frontiersin.org/journals/mechanical-engineering/articles/10.3389/fmech.2024.1353108.

[37] Elijah Ejun Huang et al. “Novel Techniques and Future Perspective for Investigating Critical-Size Bone Defects”. In: *Bioengineering* 9.4 (2022). ISSN: 2306-5354. DOI: 10.3390/bioengineering9040171. URL: https://www.mdpi.com/2306-5354/9/4/171.

[38] Erika Roddy et al. “Treatment of critical-sized bone defects: clinical and tissue engineering perspectives”. In: *European Journal of Orthopaedic Surgery & Traumatology* 28.3 (2018), pp. 351–362.

[39] T. J. de Villiers and S. R. Goldstein. “Bone health 2022: an update”. In: *Climacteric* 25.1 (2022), pp. 1–3. DOI: 10.1080/13697137.2021.1965408.

[40] Jasvinder A. Singh et al. “Rates of Total Joint Replacement in the United States: Future Projections to 2020–2040 Using the National Inpatient Sample”. In: *The Journal of Rheumatology* 46.9 (2019), pp. 1134–1140. ISSN: 0315-162X. DOI: 10.3899/jrheum.170990. eprint: https://www.jrheum.org/content/46/9/1134.full.pdf. URL: https://www.jrheum.org/content/46/9/1134.

[41] Steven Kurtz et al. “Projections of primary and revision hip and knee arthroplasty in the United States from 2005 to 2030”. In: *Jbjs* 89.4 (2007), pp. 780–785.

[42] Yuyan Shen et al. “The Global Burden of Osteoporosis, Low Bone Mass, and Its Related Fracture in 204 Countries and Territories, 1990-2019”. In: *Frontiers in Endocrinology* Volume 13 - 2022 (2022). ISSN: 1664-2392. DOI: 10.3389/fendo.2022.882241. URL: https://www.frontiersin.org/journals/endocrinology/articles/10.3389/fendo.2022.882241.

[43] Davide Savio and Andrea Bagno. “When the Total Hip Replacement Fails: A Review on the Stress-Shielding Effect”. In: *Processes* 10.3 (2022). ISSN: 2227-9717. DOI: 10.3390/pr10030612. URL: https://www.mdpi.com/2227-9717/10/3/612.

[44] Felix Werneburg et al. “Clinically relevant differences in stress shielding between two short-stemmed femoral prostheses”. In: *Archives of Orthopaedic and Trauma Surgery* 145.1 (2025), p. 365.

[45] Dongdong Li et al. “Mechanical properties, degradation behavior, and biocompatibility of porous iron scaffold fabricated by laser powder bed fusion”. In: *Smart Materials in Manufacturing* 3 (2025), p. 100089. ISSN: 2772-8102. DOI: https://doi.org/10.1016/j.smmf.2025.100089. URL: https://www.sciencedirect.com/science/article/pii/S2772810225000194.

[46] Lingyun Kong et al. “A Comprehensive Review of the Current Research Status of Biodegradable Zinc Alloys and Composites for Biomedical Applications”. In: *Materials* 16.13 (2023). ISSN: 1996-1944. DOI: 10.3390/ma16134797. URL: https://www.mdpi.com/1996-1944/16/13/4797.

[47] Víctor Tuninetti et al. “Biomimetic Lattice Structures Design and Manufacturing for High Stress, Deformation, and Energy Absorption Performance”. In: *Biomimetics* 10.7 (2025). ISSN: 2313-7673. DOI: 10.3390/biomimetics10070458. URL: https://www.mdpi.com/2313-7673/10/7/458.

[48] Haozhang Zhong et al. “The Gibson-Ashby model for additively manufactured metal lattice materials: Its theoretical basis, limitations and new insights from remedies”. In: *Current Opinion in Solid State and Materials Science* 27.3 (2023), p. 101081. ISSN: 1359-0286. DOI: https://doi.org/10.1016/j.cossms.2023.101081. URL: https://www.sciencedirect.com/science/article/pii/S1359028623000268.

[49] Hao Chen et al. “Porous Scaffold Design for Additive Manufacturing in Orthopedics: A Review”. In: *Frontiers in Bioengineering and Biotechnology* Volume 8 - 2020 (2020). ISSN: 2296-4185. DOI: 10.3389/fbioe.2020.00609. URL: https://www.frontiersin.org/journals/bioengineering-and-biotechnology/articles/10.3389/fbioe.2020.00609.

[50] Rana Dabaja et al. “Spatially distributed and interconnected porous architectures for dental implants”. In: *International Journal of Implant Dentistry* 11.1 (2025), p. 30.

[51] Lamiae Jaouher et al. “Biomimetic and personalized optimization of additively manufactured metallic bone implants: Design, simulation, and clinical outcomes”. In: *International Journal of Bioprinting* 11.6 (2025), pp. 51–82. ISSN: 2424-7723. DOI: https://doi.org/10.36922/IJB025270261. URL: https://accscience.com/journal/IJB/11/6/10.36922/IJB025270261.

[52] Dalia Mahmoud and Mohamed A. Elbestawi. “Lattice Structures and Functionally Graded Materials Applications in Additive Manufacturing of Orthopedic Implants: A Review”. In: *Journal of Manufacturing and Materials Processing* 1.2 (2017). ISSN: 2504-4494. DOI: 10.3390/jmmp1020013. URL: https://www.mdpi.com/2504-4494/1/2/13.

[53] Tobias A Schaedler and William B Carter. “Architected cellular materials”. In: *Annual Review of Materials Research* 46.1 (2016), pp. 187–210.

[54] Karel Ráž, Zdeněk Chval, and Mathis Pereira. “Lattice Structures—Mechanical Description with Respect to Additive Manufacturing”. In: *Materials* 17.21 (2024). ISSN: 1996-1944. DOI: 10.3390/ma17215298. URL: https://www.mdpi.com/1996-1944/17/21/5298.

[55] Reshma McMullan et al. “Review of 3D Printing of Polyaryletherketone/Apatite Composites for Lattice Structures for Orthopedic Implants”. In: *Applied Sciences* 15.4 (2025). ISSN: 2076-3417. DOI: 10.3390/app15041804. URL: https://www.mdpi.com/2076-3417/15/4/1804.

[56] Rashwan Alkentar, File Mate, and Tamás Mankovits. “Investigation of the performance of Ti6Al4V lattice structures designed for biomedical implants using the finite element method”. In: *Materials* 15.18 (2022), p. 6335.

[57] P Parameswaran et al. “Compression Behavior and Fatigue Strength of Additively Manufactured Ti6Al4V Strut-Based Lattice Structures: A Review”. In: *Journal of Materials Engineering and Performance* 35.9 (2026), pp. 8131–8156.

[58] Seyed Mohammad Ahmadi et al. “Additively manufactured open-cell porous biomaterials made from six different space-filling unit cells: The mechanical and morphological properties”. In: *Materials* 8.4 (2015), pp. 1871–1896.

[59] J Kadkhodapour et al. “Failure mechanisms of additively manufactured porous biomaterials: Effects of porosity and type of unit cell”. In: *Journal of the mechanical behavior of biomedical materials* 50 (2015), pp. 180–191.

[60] VS Deshpande, MF Ashby, and NA Fleck. “Foam topology: bending versus stretching dominated architectures”. In: *Acta materialia* 49.6 (2001), pp. 1035–1040.

[61] Lorna J. Gibson and Michael F. Ashby. *Cellular Solids: Structure and Properties*. 2nd ed. Cambridge Solid State Science Series. Cambridge University Press, 1997. ISBN: 9780521499118. DOI: 10.1017/CBO9781139878326.

[62] Behzad Bahrami Babamiri, Hesam Askari, and Kavan Hazeli. “Deformation mechanisms and post-yielding behavior of additively manufactured lattice structures”. In: *Materials & Design* 188 (2020), p. 108443.

[63] Amir A Zadpoor. “Mechanical performance of additively manufactured meta-biomaterials”. In: *Acta biomaterialia* 85 (2019), pp. 41–59.

[64] Amir A Zadpoor. “Additively manufactured porous metallic biomaterials”. In: *Journal of Materials Chemistry B* 7.26 (2019), pp. 4088–4117.

[65] M Gundry, S Hopkins, and K Knapp. “A review on bone mineral density loss in total knee replacements leading to increased fracture risk”. In: *Clinical Reviews in Bone and Mineral Metabolism* 15.4 (2017), pp. 162–174.

[66] Mariana Salama et al. “Biodegradable iron and porous iron: mechanical properties, degradation behaviour, manufacturing routes and biomedical applications”. In: *Journal of functional biomaterials* 13.2 (2022), p. 72.

[67] Pedro Nogueira et al. “Evaluation of lattice structures for medical implants: a study on the mechanical properties of various unit cell types”. In: *Metals* 14.7 (2024), p. 780.

[68] Pedro Nogueira et al. “Computational evaluation of the compressive properties of different lattice geometries to be used as temporary implants”. In: *Procedia Computer Science* 217 (2023), pp. 928–937.

[69] Michele Dallago et al. “On the effect of geometrical imperfections and defects on the fatigue strength of cellular lattice structures additively manufactured via Selective Laser Melting”. In: *International Journal of Fatigue* 124 (2019), pp. 348–360.

[70] Lu Liu et al. “Elastic and failure response of imperfect three-dimensional metallic lattices: the role of geometric defects induced by Selective Laser Melting”. In: *Journal of the Mechanics and Physics of Solids* 107 (2017), pp. 160–184.

[71] Esa Dube Kerme et al. “Experimental investigation of porous gyroid structure: Effect of cell size and porosity on performance”. In: *Thermal Science and Engineering Progress* 53 (2024), p. 102728.

[72] FSL Bobbert et al. “Additively manufactured metallic porous biomaterials based on minimal surfaces: A unique combination of topological, mechanical, and mass transport properties”. In: *Acta biomaterialia* 53 (2017), pp. 572–584.

[73] Rati Verma et al. “Design and analysis of biomedical scaffolds using TPMS-based porous structures inspired from additive manufacturing”. In: *Coatings* 12.6 (2022), p. 839.

[74] Zhilong Cheng et al. “Investigations on porous media customized by triply periodic minimal surface: Heat transfer correlations and strength performance”. In: *International Communications in Heat and Mass Transfer* 129 (2021), p. 105713.

[75] Chrysoula Chatzigeorgiou et al. “Numerical investigation of the effective mechanical properties and local stress distributions of TPMS-based and strut-based lattices for biomedical applications”. In: *Journal of the mechanical behavior of biomedical materials* 126 (2022), p. 105025.

[76] Oraib Al-Ketan and Rashid K Abu Al-Rub. “Multifunctional mechanical metamaterials based on triply periodic minimal surface lattices”. In: *Advanced Engineering Materials* 21.10 (2019), p. 1900524.

[77] Tobias Maconachie et al. “SLM lattice structures: Properties, performance, applications and challenges”. In: *Materials & Design* 183 (2019), p. 108137.

[78] M Benedetti et al. “Architected cellular materials: A review on their mechanical properties towards fatigue-tolerant design and fabrication”. In: *Materials Science and Engineering: R: Reports* 144 (2021), p. 100606.

[79] Elham Davoodi et al. “Additively manufactured metallic biomaterials”. In: *Bioactive Materials* 15 (2022), pp. 214–249.

[80] Khaoula Amara, Mohamad Ziad Saghir, and Ridha Abdeljabar. “Review of Triply Periodic Minimal Surface (TPMS) Structures for Cooling Heat Sinks”. In: *Energies* 18.18 (2025), p. 4920.

[81] Ian Ashcroft et al. “A multiscale optimisation method for bone growth scaffolds based on triply periodic minimal surfaces”. In: *Biomechanics and Modeling in Mechanobiology* 20 (Dec. 2021). DOI: 10.1007/s10237-021-01496-8.

[82] Raffaele Pugliese and Serena Graziosi. “Biomimetic scaffolds using triply periodic minimal surface-based porous structures for biomedical applications”. In: *SLAS technology* 28.3 (2023), pp. 165–182.

[83] Diab W Abueidda et al. “Mechanical properties of 3D printed polymeric Gyroid cellular structures: Experimental and finite element study”. In: *Materials & Design* 165 (2019), p. 107597.

[84] Xiaofeng Guo et al. “Mechanical behavior of TPMS-based scaffolds: a comparison between minimal surfaces and their lattice structures”. In: *SN Applied Sciences* 1.10 (2019), p. 1145.

[85] Chen Pan, Yafeng Han, and Jiping Lu. “Design and optimization of lattice structures: A review”. In: *Applied Sciences* 10.18 (2020), p. 6374.

[86] Ana Karilú Arvizu Alonso et al. “Control of the Properties of the Voronoi Tessellation Technique and Biomimetic Patterns: A Review”. In: *Designs* 8.5 (2024). ISSN: 2411-9660. DOI: 10.3390/designs8050093. URL: https://www.mdpi.com/2411-9660/8/5/93.

[87] Qingyu Xu et al. “Mechanical and Permeability Properties of Radial-Gradient Bone Scaffolds Developed by Voronoi Tessellation for Bone Tissue Engineering”. In: *Journal of Shanghai Jiaotong University (Science)* 30.3 (2025), pp. 433–445. DOI: 10.1007/s12204-024-2770-8. URL: https://doi.org/10.1007/s12204-024-2770-8.

[88] Michael Thompson et al. “Machine learning-optimized stochastic Voronoi lattices for enhanced mechanical performance”. In: *Engineering Applications of Artificial Intelligence* 160 (2025), p. 111937. ISSN: 0952-1976. DOI: https://doi.org/10.1016/j.engappai.2025.111937. URL: https://www.sciencedirect.com/science/article/pii/S0952197625019396.

[89] Gabriel de Souza Vieira Bié et al. “Development of Parametric Voronoi-Based Scaffolds for Trabecular Bone Tissue Replacement Using Additive Manufacturing”. In: *Recent Progress in Materials* 7.2 (2025), p. 010. DOI: 10.21926/rpm.2502010. URL: https://www.lidsen.com/journals/rpm/rpm-07-02-010.

[90] İ. Ekinci, M. M. Karaca, and D. Ali. “Mechanical performance of Schwarz and lattice diamond regular architecture versus stochastic Voronoi structure for bone scaffolds: Design, Manufacturing, and FEM analysis”. In: *The International Journal of Advanced Manufacturing Technology* 142 (2026), pp. 1735–1747. DOI: 10.1007/s00170-025-17190-3. URL: https://doi.org/10.1007/s00170-025-17190-3.

[91] Jialiang Li et al. “Integrated evaluation of biomechanical and biological properties of the biomimetic structural bone scaffold: Biomechanics, simulation analysis, and osteogenesis”. In: *Materials Today Bio* 24 (2024), p. 100934. ISSN: 2590-0064. DOI: https://doi.org/10.1016/j.mtbio.2023.100934. URL: https://www.sciencedirect.com/science/article/pii/S2590006423003940.

[92] Chiara Bregoli et al. “Mechanical response of LPBFed TI64 thickness graded Voronoi lattice structures”. In: *Materialia* 38 (2024), p. 102234. ISSN: 2589-1529. DOI: https://doi.org/10.1016/j.mtla.2024.102234. URL: https://www.sciencedirect.com/science/article/pii/S258915292400231X.

[93] Miguel Araya et al. “Assessing the compressive and tensile properties of TPMS-Gyroid and stochastic Ti64 lattice structures: A study on laser powder bed fusion manufacturing for biomedical implants”. In: *Journal of Science: Advanced Materials and Devices* 9 (Dec. 2023), p. 100663. DOI: 10.1016/j.jsamd.2023.100663.

[94] Long Chao et al. “Design of porous structure based on the Voronoi diagram and stress line for better stress shielding relief and permeability”. In: *Journal of Materials Research and Technology* 25 (2023), pp. 1719–1734. ISSN: 2238-7854. DOI: https://doi.org/10.1016/j.jmrt.2023.05.282. URL: https://www.sciencedirect.com/science/article/pii/S2238785423012486.

[95] Fei Liu et al. "Functionally graded porous scaffolds in multiple patterns: New design method, physical and mechanical properties". In: *Materials Design* 160 (2018), pp. 849–860. ISSN: 0264-1275. DOI: https://doi.org/10.1016/j.matdes.2018.09.053. URL: https://www.sciencedirect.com/science/article/pii/S026412751830755X.

[96] Bradley Hanks et al. "Mechanical properties of additively manufactured metal lattice structures: Data review and design interface". In: *Additive Manufacturing* 35 (2020), p. 101301. ISSN: 2214-8604. DOI: https://doi.org/10.1016/j.addma.2020.101301. URL: https://www.sciencedirect.com/science/article/pii/S2214860420306734.

[97] Pedro Nogueira et al. "Graded Lattice Structures for Biodegradable Temporary Implants: Computational Evaluation with Two Unit Cell Types". In: *Towards a Smart, Resilient and Sustainable Industry*. Ed. by Yuri Borgianni et al. Cham: Springer Nature Switzerland, 2023, pp. 534–543. ISBN: 978-3-031-38274-1.

[98] Sakkadech Limmahakhun et al. "Stiffness and strength tailoring of cobalt chromium graded cellular structures for stress-shielding reduction". In: *Materials Design* 114 (2017), pp. 633–641. ISSN: 0264-1275. DOI: https://doi.org/10.1016/j.matdes.2016.11.090. URL: https://www.sciencedirect.com/science/article/pii/S0264127516314915.

[99] Erica Liverani and Alessandro Fortunato. "Stiffness prediction and deformation analysis of Cobalt-Chromium lattice structures: From periodic to functionally graded structures produced by additive manufacturing". In: *Journal of Manufacturing Processes* 68 (2021), pp. 104–114. ISSN: 1526-6125. DOI: https://doi.org/10.1016/j.jmapro.2021.05.033. URL: https://www.sciencedirect.com/science/article/pii/S1526612521003637.

[100] Sanna Turunen et al. "A review of rapid prototyping techniques for tissue engineering purposes". In: *Annals of medicine* 40 (Feb. 2008), pp. 268–80. DOI: 10.1080/07853890701881788.

[101] Robert Lancaster et al. "Structural Integrity of an Electron Beam Melted Titanium Alloy". In: *Materials* 9 (June 2016), p. 470. DOI: 10.3390/ma9060470.

[102] Tassilo Moritz and Saeed Maleksaeedi. "4 - Additive manufacturing of ceramic components". In: *Additive Manufacturing*. Ed. by Jing Zhang and Yeon-Gil Jung. Butterworth-Heinemann, 2018, pp. 105–161. ISBN: 978-0-12-812155-9. DOI: https://doi.org/10.1016/B978-0-12-812155-9.00004-9. URL: https://www.sciencedirect.com/science/article/pii/B9780128121559000049.

[103] Felicia F. Fashanu, Denis J. Marcellin-Little, and Barbara S. Linke. "Review of Surface Finishing of Additively Manufactured Metal Implants". In: *Proceedings of the ASME 2020 15th International Manufacturing Science and Engineering Conference (MSEC2020)*. Paper MSEC2020-8419. Virtual, Online, 2020.

[104] Subodh C. Subedi et al. "Towards the optimal design of support structures for laser powder bed fusion-based metal additive manufacturing via thermal equivalent static loads". In: *Additive Manufacturing* 57 (2022), p. 102956. DOI: 10.1016/j.addma.2022.102956.

[105] H. R. Javidrad and F. Javidrad. "Review of state-of-the-art research on the design and manufacturing of support structures for powder-bed fusion additive manufacturing". In: *Progress* ().

[106] Antonios Dimopoulos et al. “Support Structures Optimisation for High-Quality Metal Additive Manufacturing with Laser Powder Bed Fusion: A Numerical Simulation Study”. In: *Materials* 16.22 (2023), p. 7164. DOI: 10.3390/ma16227164.

[107] Omid Zarei et al. “Design of Easily Removable Lattice-Based Support Structures for L-PBF”. In: (2021). Preprints. DOI: 10.20944/preprints202102.0006.v1.

[108] Antonios Dimopoulos et al. “An Interactive Web-Based Platform for Support Generation and Optimisation for Metal Laser Powder Bed Fusion”. In: *Materials* 17.7 (2024), p. 1639. DOI: 10.3390/ma17071639.

[109] Fatima Zivic et al. “Biodegradable Metals as Biomaterials for Clinical Practice: Iron-Based Materials”. In: Jan. 2018, pp. 225–280. ISBN: 978-3-319-68024-8. DOI: 10.1007/978-3-319-68025-5_9.

[110] Cijun Shuai et al. “Biodegradable metallic bone implants”. In: *Materials Chemistry Frontiers* 3 (Jan. 2019). DOI: 10.1039/C8QM00507A.

[111] Humayun Kabir et al. “Recent research and progress of biodegradable zinc alloys and composites for biomedical applications: Biomechanical and biocorrosion perspectives”. In: *Bioactive Materials* 6.3 (2021), pp. 836–879. ISSN: 2452-199X. DOI: https://doi.org/10.1016/j.bioactmat.2020.09.013. URL: https://www.sciencedirect.com/science/article/pii/S2452199X20302334.

[112] Santanu Mandal et al. “Effects of multiscale porosity and pore interconnectivity on in vitro and in vivo degradation and biocompatibility of Fe-Mn-Cu scaffold”. In: *Journal of Materials Chemistry B* 9 (May 2021). DOI: 10.1039/D1TB00641J.

[113] International Organization for Standardization. *Mechanical testing of metals — Ductility testing — Compression test for porous and cellular metals*. Tech. rep. ISO 13314:2011. Geneva, Switzerland: ISO, 2011.

[114] International Organization for Standardization and ASTM International. *Additive Manufacturing of metals — Test artefacts — Compression validation specimens for lattice designs*. Tech. rep. ISO/ASTM 52959:2026. ISO/ASTM, 2026.

[115] Yue Du et al. “Design and statistical analysis of irregular porous scaffolds for orthopedic reconstruction based on voronoi tessellation and fabricated via selective laser melting (SLM)”. In: *Materials Chemistry and Physics* 239 (2020), p. 121968. ISSN: 0254-0584. DOI: https://doi.org/10.1016/j.matchemphys.2019.121968. URL: https://www.sciencedirect.com/science/article/pii/S0254058419307679.

[116] Valerio Lucarini. “Three-dimensional random Voronoi tessellations: From cubic crystal lattices to Poisson point processes”. In: *Journal of Statistical Physics* 134.1 (2009), pp. 185–206. DOI: 10.1007/s10955-008-9668-y.

[117] Tino Stanković and Kristina Shea. “Investigation of a Voronoi Diagram Representation for the Computational Design of Additively Manufactured Discrete Lattice Structures”. In: *Journal of Mechanical Design* 142.11 (May 2020), p. 111704. ISSN: 1050-0472. DOI: 10.1115/1.4046916. URL: https://doi.org/10.1115/1.4046916.

[118] Mohamed S El-Asfoury et al. “Orientation driven design and mechanical optimization of gyroid TPMS lattice structures”. In: *Scientific Reports* 16.1 (2026), p. 4373. DOI: 10.1038/s41598-026-35201-5.

[119] Syed Zahid Ahmad et al. “Recent Developments in Novel TPMS Lattice Materials: Design Optimization, Performance Control, and Applications in Biomimetic Scaffolds”. In: *Materials* 18.22 (2025), p. 5209. DOI: 10.3390/ma18225209.

[120] J.E. Santos et al. “LISBON TPMS TOOL: An open-source tool for the design of TPMS structures for engineering applications”. In: *Software Impacts* 24 (2025), p. 100747. ISSN: 2665-9638. DOI: https://doi.org/10.1016/j.simpa.2025.100747. URL: https://www.sciencedirect.com/science/article/pii/S2665963825000077.

[121] Jacob Cohen. *Statistical Power Analysis for the Behavioral Sciences*. 2nd ed. Hillsdale, NJ: Lawrence Erlbaum Associates, 1988.

[122] Hun Ban et al. “Study on 3D printing a fine quality bone-mimetic porous structure with minimized shape error in pore size: a parametric work on key laser parameters in SLM”. In: *The International Journal of Advanced Manufacturing Technology* 135 (Nov. 2024), pp. 4577–4594. DOI: 10.1007/s00170-024-14729-8.

[123] Yuzhu Wang et al. “Osseointegration of an innovative functionally gradient biomimetic scaffold based on Voronoi-Tessellation for the design of orthopaedic implants”. In: *Materials Technology* 40.1 (2025), p. 2481637. DOI: 10.1080/10667857.2025.2481637.

[124] D. Barba, E. Alabort, and R.C. Reed. “Synthetic bone: Design by additive manufacturing”. In: *Acta Biomaterialia* 97 (2019), pp. 637–656. ISSN: 1742-7061. DOI: https://doi.org/10.1016/j.actbio.2019.07.049. URL: https://www.sciencedirect.com/science/article/pii/S1742706119305380.

[125] Saran Seehanam et al. “Evaluating the effect of pore size for 3d-printed bone scaffolds”. In: *Heliyon* 10.4 (2024), e26005. ISSN: 2405-8440. DOI: https://doi.org/10.1016/j.heliyon.2024.e26005. URL: https://www.sciencedirect.com/science/article/pii/S240584402402036X.

[126] Y. Li, H. Jahr, K. Lietaert, et al. “Additively manufactured biodegradable porous iron”. In: *Acta Biomaterialia* 77 (2018), pp. 380–393. DOI: 10.1016/j.actbio.2018.07.011.

[127] Y. Li, H. Jahr, P. Pavanram, et al. “Additively manufactured functionally graded biodegradable porous iron”. In: *Acta Biomaterialia* 96 (2019), pp. 646–661. DOI: 10.1016/j.actbio.2019.07.013.

[128] D. Li, X. Wu, Y. Shao, et al. “Mechanical properties, degradation behavior, and biocompatibility of porous iron scaffold fabricated by laser powder bed fusion”. In: *Smart Materials in Manufacturing* 3 (2025), p. 100089. DOI: 10.1016/j.smmf.2025.100089.

[129] Karolina Planeta et al. “The assessment of the usability of selected instrumental techniques for the elemental analysis of biomedical samples”. In: *Scientific Reports* 11 (2021), p. 3704. DOI: 10.1038/s41598-021-82179-3.

[130] Francesco Baino and Seiji Yamaguchi. “The Use of Simulated Body Fluid (SBF) for Assessing Materials Bioactivity in the Context of Tissue Engineering: Review and Challenges”. In: *Biomimetics* 5.4 (2020), p. 57. DOI: 10.3390/biomimetics5040057.

[131] *Getting Started with Abaqus/CAE*. Dassault Systèmes. 2016.

[132] Christof J. J. Torrent et al. “Influence of Various Processing Routes in Additive Manufacturing on Microstructure and Monotonic Properties of Pure Iron—A Review-like Study”. In: *Metals* 14.5 (2024), p. 557. DOI: 10.3390/met14050557.

[133] Hai Qiu, Rintaro Ueji, and Tadanobu Inoue. “Yield-Point Phenomenon and Plastic Bands in Ferrite–Pearlite Steels”. In: *Materials* 16.1 (2022), p. 195. DOI: 10.3390/ma16010195.

[134] V. V. Gorbatenko, V. I. Danilov, and L. B. Zuev. “Plastic Flow Instability: Chernov–Lüders Bands and the Portevin–Le Chatelier Effect”. In: *Technical Physics* 62.3 (2017), pp. 395–400. DOI: 10.1134/S1063784217030094.

[135] Kerry S. Havner. “On the onset of necking in the tensile test”. In: *International Journal of Plasticity* 20.6 (2004), pp. 965–978. ISSN: 0749-6419. DOI: 10.1016/j.ijplas.2003.05.004.

[136] *Abaqus 2024 Documentation: Defining Plasticity in Abaqus*. Dassault Systèmes. 2024.

[137] Glen L. Niebur et al. “Convergence Behavior of High-Resolution Finite Element Models of Trabecular Bone”. In: *Journal of Biomechanical Engineering* 121.6 (1999), pp. 629–635. DOI: 10.1115/1.2800865.

Appendix A

# Supplementary Parametric Data

## A.1 Additional Voronoi Realisations

This appendix reports relative density $\rho_r$ and specific surface area $A$ for the three realisations of the Voronoi parametric study not adopted as reference in Section 3.3.1: ($i = 0.25$, Seed $= 42$), ($i = 0.25$, Seed $= 100$), and ($i = 0.40$, Seed $= 100$). As established in Section 3.3.1, the differences relative to the reference realisation ($i = 0.40$, Seed $= 42$; Tables 3.4 and 3.6) are statistically negligible, with both the irregularity factor and the random seed accounting for $\eta^2 < 10^{-4}$ of the total variance in either descriptor. The tables below are provided solely for transparency and reproducibility, and are not discussed individually.

Table A.1: Relative density $\rho_r$ (%) of the Voronoi lattice — realisation $i = 0.25$, Seed $= 42$.

| $n$ ($N$) | $D = 0.3$ mm | $D = 0.5$ mm | $D = 0.7$ mm |
|---|---|---|---|
| $n = 10$ (190) | 10.66 | 24.89 | 40.77 |
| $n = 12$ (276) | 14.32 | 32.61 | 51.35 |
| $n = 14$ (378) | 18.23 | 40.01 | 60.83 |
| $n = 16$ (496) | 21.76 | 46.02 | 68.11 |
| $n = 18$ (630) | 25.80 | 53.55 | 76.22 |
| $n = 20$ (780) | 30.47 | 60.73 | 82.88 |
| $n = 22$ (946) | 34.83 | 66.45 | 87.82 |
| $n = 24$ (1128) | 38.61 | 72.12 | 95.58 |
| $n = 26$ (1326) | 43.44 | 77.93 | 97.47 |
| $n = 28$ (1540) | 48.02 | 82.31 | 97.98 |
| $n = 30$ (1770) | 52.07 | 86.45 | — |

Table A.2: Relative density $\rho_r$ (%) of the Voronoi lattice — realisation $i = 0.25$, Seed $= 100$.

| $n$ ($N$) | $D = 0.3$ mm | $D = 0.5$ mm | $D = 0.7$ mm |
|---|---|---|---|
| $n = 10$ (190) | 10.78 | 25.13 | 41.09 |
| $n = 12$ (276) | 14.31 | 32.43 | 51.12 |
| $n = 14$ (378) | 18.32 | 40.04 | 60.68 |
| $n = 16$ (496) | 21.83 | 46.27 | 68.38 |
| $n = 18$ (630) | 25.70 | 53.48 | 76.14 |
| $n = 20$ (780) | 30.47 | 60.68 | 82.73 |
| $n = 22$ (946) | 34.98 | 66.72 | 88.36 |
| $n = 24$ (1128) | 38.62 | 72.27 | 95.81 |
| $n = 26$ (1326) | 43.42 | 77.93 | 97.48 |
| $n = 28$ (1540) | 48.05 | 82.28 | 97.97 |
| $n = 30$ (1770) | 52.11 | 86.50 | — |

Table A.3: Relative density $\rho_r$ (%) of the Voronoi lattice — realisation $i = 0.40$, Seed = 100.

| $n$ ($N$) | $D = 0.3$ mm | $D = 0.5$ mm | $D = 0.7$ mm |
|---|---|---|---|
| $n = 10$ (190) | 11.11 | 25.65 | 41.79 |
| $n = 12$ (276) | 14.60 | 32.84 | 51.54 |
| $n = 14$ (378) | 18.52 | 40.17 | 60.75 |
| $n = 16$ (496) | 22.17 | 46.97 | 69.02 |
| $n = 18$ (630) | 26.03 | 53.58 | 76.04 |
| $n = 20$ (780) | 30.67 | 60.68 | 82.77 |
| $n = 22$ (946) | 35.06 | 66.88 | 88.35 |
| $n = 24$ (1128) | 39.16 | 72.60 | 95.25 |
| $n = 26$ (1326) | 43.59 | 77.90 | 97.58 |
| $n = 28$ (1540) | 48.06 | 82.43 | 98.06 |
| $n = 30$ (1770) | 52.17 | 86.66 | — |

Table A.4: Specific surface area $A$ (mm$^2$) of the Voronoi lattice — realisation $i = 0.25$, Seed = 42.

| $n$ ($N$) | $D = 0.3$ mm | $D = 0.5$ mm | $D = 0.7$ mm |
|---|---|---|---|
| $n = 10$ (190) | 1522 | 1958 | 2072 |
| $n = 12$ (276) | 2000 | 2419 | 2358 |
| $n = 14$ (378) | 2480 | 2824 | 2568 |
| $n = 16$ (496) | 2894 | 3095 | 2622 |
| $n = 18$ (630) | 3354 | 3362 | 2535 |
| $n = 20$ (780) | 3831 | 3511 | 2366 |
| $n = 22$ (946) | 4242 | 3575 | 2080 |
| $n = 24$ (1128) | 4579 | 3563 | 1055 |
| $n = 26$ (1326) | 4971 | 3414 | 791 |
| $n = 28$ (1540) | 5255 | 3225 | 727 |
| $n = 30$ (1770) | 5489 | 2931 | — |

Table A.5: Specific surface area $A$ (mm$^2$) of the Voronoi lattice — realisation $i = 0.25$, Seed = 100.

| $n$ ($N$) | $D = 0.3$ mm | $D = 0.5$ mm | $D = 0.7$ mm |
|---|---|---|---|
| $n = 10$ (190) | 1538 | 1975 | 2083 |
| $n = 12$ (276) | 1998 | 2413 | 2356 |
| $n = 14$ (378) | 2482 | 2813 | 2546 |
| $n = 16$ (496) | 2904 | 3104 | 2627 |
| $n = 18$ (630) | 3346 | 3350 | 2536 |
| $n = 20$ (780) | 3835 | 3513 | 2367 |
| $n = 22$ (946) | 4255 | 3568 | 2006 |
| $n = 24$ (1128) | 4585 | 3575 | 1025 |
| $n = 26$ (1326) | 4974 | 3417 | 794 |
| $n = 28$ (1540) | 5259 | 3231 | 728 |
| $n = 30$ (1770) | 5486 | 2922 | — |

Table A.6: Specific surface area $A$ (mm$^2$) of the Voronoi lattice — realisation $i = 0.40$, Seed = 100.

| $n$ ($N$) | $D = 0.3$ mm | $D = 0.5$ mm | $D = 0.7$ mm |
|---|---|---|---|
| $n = 10$ (190) | 1575 | 2002 | 2107 |
| $n = 12$ (276) | 2021 | 2425 | 2360 |
| $n = 14$ (378) | 2494 | 2806 | 2547 |
| $n = 16$ (496) | 2929 | 3122 | 2618 |
| $n = 18$ (630) | 3348 | 3338 | 2556 |
| $n = 20$ (780) | 3825 | 3498 | 2367 |
| $n = 22$ (946) | 4232 | 3561 | 2031 |
| $n = 24$ (1128) | 4600 | 3560 | 1144 |
| $n = 26$ (1326) | 4942 | 3427 | 785 |
| $n = 28$ (1540) | 5228 | 3238 | 723 |
| $n = 30$ (1770) | 5460 | 2912 | — |